November 2011

Thermal and Mechanical Studies of Thin Spray-On Liner (TSL) for Concrete Tunnel Linings

Taesang Ahn, *University of Western Ontario*

Supervisor: Dr. Sean D. Hinchberger, *The University of Western Ontario*

A thesis submitted in partial fulfillment of the requirements for the Doctor of Philosophy degree in Civil and Environmental Engineering

THERMAL AND MECHANICAL STUIDES OF THIN SPRAY-ON LINER (TSL) FOR CONCRETE TUNNEL LININGS

(Spine title: Thermal and Mechanical Studies of TSL for Concrete Tunnel)

(Thesis format: Monograph)

by

Taesang Ahn

Graduate Program in Civil and Environmental Engineering

A thesis submitted in partial fulfillment
of the requirements for the degree of
Doctor of Philosophy

The School of Graduate and Postdoctoral Studies
The University of Western Ontario
London, Ontario, Canada

THE UNIVERSITY OF WESTERN ONTARIO
SCHOOL OF GRADUATE AND POSTDOCTORAL STUDIES

CERTIFICATE OF EXAMINATION

Supervisor

_____

Dr. Sean D. Hinchberger

Co-Supervisor

_____

Dr. K. Y. Lo

Examining Board

_____

Dr. Hesham El Nagger

_____

Dr. Timothy A. Newson

_____

Dr. Paul Wiegert

_____

Dr. James Archibald

The thesis by

Taesang Ahn

entitled:

Thermal and Mechanical Studies of Thin Spray-On Liner (TSL) for Concrete Tunnel Linings

is accepted in partial fulfillment of the
requirements for the degree of
Doctor of Philosophy

Date_____ _____

Chair of Examining Board

ABSTRACT

The thesis presents a summary of Thin Spray-On Liner (TSL) effects on concrete. Three aspects, fire insulation, adhesion strength on concrete surface and load carrying capacity (i.e. flexural strength) on segmental concrete liners, are presented. Small-scale to full-scale laboratory tests were conducted using ASTM standards or devised methods. The TSL effects on three aspects were then compared with the results for uncoated concrete specimens. Numerical analyses using TEMP/W for the thermal response of TSL and a FE program, ABAQUS for the mechanical response of TSL were respectively carried out and compared with the measured results. Additionally, numerical analyses in respect to the joint rotational stiffness for the modern joint and the flexible joint were performed. The TSL effect on the flexible joint was also evaluated.

Based on the results of this study, it is revealed that TSL is an excellent fire insulating material as well as a structural substrate material. The TSL coating can reduce the heat transmitted in the concrete during a fire. Also, the TSL coating can reduce concrete spalling and crack propagation during failure. The load carrying capacity increase of a segmental tunnel liner is also found.

Thin Spray-on Liner (TSL) could be a potential application in tunnel engineering as an insulating material as well as a substrate material.

KEYWORDS: fire in tunnel, adhesion strength, precast segmental concrete liner, full scale laboratory test, joint rotational stiffness, Thin Spray-On Liner (TSL), flexural strength

DEDICATION

Praise the Lord
Almighty God
Glorify Thy Name

ACKNOWLEDGEMENTS

I would like to express my hearty gratitude to my advisors, Dr. S. Hinchberger and Dr. K.Y. Lo, for their excellent guidance, constant encouragement and support throughout the duration of this thesis. It has been a pleasure to work with them for the past six years.

Genuine appreciation is expressed to the faculty, staff and fellows at the University of Western Ontario for their support, motivation, and friendship. In particular, I am extremely grateful to Mr. W. Logan, Mr. T. Stephan and Ms. M. Richard for their continuous assistance during this research. Thanks are also extended to Dr. S. Micic and Mr. Jae-Oh Lim for their assistance and friendship.

I would like to avail myself of this opportunity to acknowledge my debt of gratitude to Rev. Susan Lee and Ian Lee and Oakridge Presbyterian Church family for their generous help, constant encouragement, and most of all for the wonderful friendship they have extended to my family and me.

Finally, I would like to deeply thank my wife Yun-Kyung and daughter Angelina for their love, support and inspiration throughout this long journey. I also want to express my sincere gratitude and love to my parents in Korea, my mother Uk-Ja Kim, my father Ho-Bong Ahn and two sisters, Ok-Joo and Hye-young Ahn. With great pleasure and honour I dedicate this work to them.

TABLE OF CONTENT

LIST OF TABLES

LIST OF FIGURES

CHAPTER 4: THERMAL ANALYSIS OF TSL COATED CONCRETE SLABS

CHAPTER 5: MECHANICAL CHARACTERISTICS OF TSL: TENSILE AND ADHESION STRENGTH

CHAPTER 6: TSL EFFECT ON THE LOAD CARRYING CAPACITY OF SEGMENTAL CONCRETE LINERS

CHAPTER 7: NUMERICAL ANALYSIS OF JOINT ROTATIONAL STIFFNESS OF PRECAST SEGMENTAL CONCRETE LININGS

APPENDICES

LIST OF APPENDICES

APPENDIX *PAGE*

LIST OF ABBREVIATIONS, SYMBOLS AND NOMENCLATURE

ASTM	American Society of Testing and Materials
CB	Char Barrier
CDP	Concrete Damaged Plasticity
CSC	Concrete Smeared Cracking
Ch	Channel
EPDM	Ethylene Propylene Diene Monomer
FE	Finite Element
NFPA	National Fire Protection Association
PFR	Polypropylene Fibre Reinforced
PT	Preliminary Test
RC	Reinforced Concrete
RTRI	Railway Technical Research Institute of Japan
SJM	Simplified Joint Method
SFR	Steel Fibre Reinforced
TBM	Tunnel Boring Machine
TSL	Thin Spray-On Liner
TTC	Toronto Transit Commission

A	area [m^2]
D	distance between grips [mm]
E	initial tangent elastic modulus [Pa]
E_d	modulus of elasticity [Pa]
EI	bending rigidity [$Pa \cdot m^4$]
EI_e	effective bending rigidity [$Pa \cdot m^4$]
f'_c	uniaxial compressive strength [Pa]
f_{cu}	unconfined compressive strength at 28 days [Pa]

f_{b0} / f_{c0}	initial equibiaxial compressive yield stress to initial uniaxial compressive yield stress
$\mathbf{K}$	a matrix of coefficients related to geometry and material properties
K_c	ratio of the second stress invariant
k_x, k_y	thermal conductivity in x- and y-direction [W/m·^{o}C]
K_θ	the rotational joint stiffness [MN.m/rad/m]
L	length [m]
L	gauge length of narrow section [mm]
M	bending moments [N.m]
P	uniformly distributed line load
$\mathbf{Q}$	a vector of the heat flow quantities
Q	boundary flux
q	heat flux
$\mathbf{T}$	a vector of the temperature at nodes
T	initial thrust
T	thickness [mm]
t	time
W_c	width of narrow section [mm]
W_o	width overall [mm]
x	circumferential distance

α	thermal diffusivity [cm^2/s]
δ_v	vertical displacement
λ	capacity for heat storage[J/kg.°C]
ν	Poisson's ratio (lining)
ν	Poisson'r ratio (soil)
ρ	density [kg/m^3]
σ_{tf}	tensile failure stress [kN/m^2]
σ_y	initial yield stress [kN/m^2]

$\sigma_{y\,TSL}$	yield strength of TSL [MPa]
$\bar{\sigma}_{\max}$	maximum principal effective stress

CHAPTER 1

INTRODUCTION

1.1 GENERAL

Underground spaces are increasingly important, especially in major metropolises. Congestion at the surface leads engineers to consider underground structures such as subways, roads, and utility lines. However, like other facilities, these infrastructures, such as subway tunnels in cities are getting old. Therefore, those tunnels need to be reshaped, modified, refurbished or reinforced although they have been built at different times and with various techniques and materials.

Most modern subway tunnels have been constructed using a Tunnel Boring Machine (TBM) which is one of the important milestones in the field of tunnelling. Precast concrete lining is often accompanied with TBMs. In common with ageing concrete structures, appropriate monitoring, maintenance and repair are required to increase their life spans.

In cases of repairing or reinforcing, it is important to consider materials of use, especially if they are relatively innovative. Firstly, these innovative materials must meet some environmental and fire regulations. It would be beneficial to examine the influence on the existing structure including load carrying capacity, joint stiffness of the segmental tunnel lining, and usefulness of maintenance service.

In the 1970's, the Toronto Transit Commission (TTC) used precast concrete segmental linings to line new tunnels on both the Yonge and Spadina subway lines (i.e. North to Eglington). Since construction, the linings have experienced significant concrete degradation (i.e. spalling and delaminating) due to exposure to chloride in the groundwater. In 2003, the TTC embarked on a rehabilitation program to repair the linings and considered using Thin Spray-on Liners (TSLs) to preserve the linings. Therefore, TSLs were examined to meet the requirements of the TTC in respect of mainly remediating fire and spalling degradation. Further studies on determine the load carrying capacity of the segmental concrete lining and calculating joint rotational stiffness of the segmental lining due to the effect of a Thin Spray-on Liner (TSL) layer application were conducted. Consequently, the overall characteristics of TSL as a repairing material for the concrete tunnel were evaluated.

1.2 RESEARCH OBJECTIVES

The primary objectives of this research are to examine and evaluate a Thin Spray-on Liner (TSL) as an insulating material in respect of fire in tunnels and as a potential substrate material to reinforce concrete with respect to spalling, loading and joint rotational stiffness of concrete segmental linings, which was used in the Yonge and Spadina subway lines in Toronto, Canada. The following objectives to achieve these goals are devised through the research:

1) Measure the fire performance of a TSL using standard fire performance tests and determine the thermal response of a TSL subject to the planned fire (CAN/ULC-S102).
2) Conduct numerical analysis using Temp/W and compare the results with measured data.
3) Determine mechanical properties such as tensile strength and adhesion strength of a TSL.

4) Evaluate the load carrying capacity (i.e. flexural strength) of precast reinforced concrete tunnel lining segments similar to those used to construct TTC subway tunnels during the 1970's.
5) Develop a non-linear elasto-plastic finite element model using ABAQUS to simulate the structural response of TSL coated and uncoated precast RC tunnel lining segments.
6) Examine the feasibility of the FE model to determine the rotational joint stiffness (K_θ) using rectangular block models for both the modern joint type and the flexible joint type.
7) Investigate joint stiffness changes accounting for various components of the axial or circumferential joint.
8) Determine the range of the rotational joint stiffness for the various bending moments *(M)* associated with the initial thrust *(T)* on the linings.
9) Evaluate the effect of a TSL layer on the rotational stiffness of the flexible joint.

1.3 THESIS OULINE

This thesis has been prepared in a monograph format stipulated by the Faculty of Graduate Studies at the University of Western Ontario. This thesis consists of eight chapters. Three appendices, included at the end of the thesis, provide other pertinent information necessary for completeness of the thesis.

The following section describes the outline of each chapter. Three aspects including fire in tunnels and protection methods, testing the load carrying capacity of segmental tunnel linings (i.e. flexural strength of segmental tunnel lining), and numerical analysis of joint rotational stiffness of segmental tunnel lining are outlined.

Chapter 2 is the literature review on four subjects related to this research. Subjects include fires in tunnels and their accompanying damage, in particular concrete spalling and fire protection methods using various techniques. It is followed by various testing methods to examine load carrying capacities of tunnel linings. Lastly, numerical studies to calculate joint rotational stiffness of precast segmental concrete linings are presented in this chapter.

Chapter 3 focuses on a tunnel fire test according to CAN/ULC-S102-M88. It examines the TSL effect on fire using uncoated and TSL coated concrete slabs. The evaluation of the TSL effect is highlighted.

Chapter 4 presents Finite Element (FE) analysis using TEMP/W to simulate the fire test results presented in Chapter 2. Comparison of numerical results with the measured temperatures in TSL coated concrete slabs is described.

Chapter 5 presents the tensile behaviour of the TSL and adhesion characteristics of TSL layers. ASTM D683-08 for measuring tensile properties of plastics is used to measure the tensile strength of TSL. Additionally, a pull-off test, developed at Queen's University, is used to determine adhesion strength of TSLs. Three types of specimens were examined to determine the adhesion characteristics of TSLs. Optimal conditions for spraying TSL on the concrete structure are also discussed.

Chapter 6 consists of five flexural tests and FE analyses of TTC segmental concrete liners with uncoated and TSL coated concrete segments. Evaluation of the TSL was made based on test

results between uncoated and coated concrete segments. Results of three dimensional FE analyses using ABAQUS are presented and compared with the measured results in terms of displacement and strain.

In Chapter 7, joint rotational stiffness of two types of segmental linings, flexible joint (i.e. TTC liners) and modern joint types designed by Hatch Mott McDonald, are examined using FE program, ABAQUS. A three dimensional analysis using a simplified joint model was conducted. TSL effect on the joint rotational stiffness was also evaluated for the flexible joint.

Finally, Chapter 8 summarizes the major findings and conclusions based on the results of this study. Recommendations for further study with TSLs are suggested in the end of this chapter.

1.4 ORIGINAL CONTRIBUTIONS

The main contribution of the study is to test and evaluate a Thin Spray-On Liner (TSL) as a potential substrate material for the existing reinforced concrete tunnel linings. A feasibility study was performed using TSL coated concrete specimens including concrete slabs used for the tunnel fire test, concrete disks for the measurement of adhesive strength of TSL and full scale segmental concrete liners used for the flexural strength test to examine the TSL effect on load carrying capacity. Also, determination of the thermal and mechanical performance of TSL through use of FE analysis is another innovative contribution. In addition, non-linear elasto-plastic FE analysis accounting for all joint components provides useful information for the purpose of engineering design.

CHAPTER 2

LITERATURE REVIEW

2.1 INTRODUCTION

In this chapter, previous studies related to tunnel fire safety, various experiments to examine load carrying capacity of segmental tunnel linings and some numerical analyses associated with rotational joints in segmental tunnels are reviewed.

Firstly, tunnel fire related subjects are presented. They include several cases of fire accidents in tunnels and presentation of damage resulting from fire such as concrete spalling. Subsequently, fire protection methods in tunnels are presented. A Thin-Spray-On Liner (TSL) use, which is the focus of this study, is also described. Secondly, various experiments to determine load carrying capacities of tunnel linings are summarized. These include studies on bench-scale and a full-scale laboratory tests using precast concrete segment liners as well as fully assembled linings. Based on an extensive review, a full-scale flexural testing method is determined for this research. Finally, several numerical studies related to joint rotational stiffness of tunnel linings are reviewed.

2.2 FIRE IN TUNNELS

It has been reported (Haack, 1994) that there is increased risk of fires in transportation tunnels due to increased traffic volume, greater speeds in rail tunnels and the greater length of tunnels. Fire is one of the most critical risks to tunnel safety because it causes not only serious structural

damage but also loss of life. The main fire hazards are heat and smoke. Intense heat can cause damage to the lining or support structures (i.e., spalling of concrete, degradation of the reinforcement), and smoke is the primary cause of fatalities. Moreover, it has been reported that physical and chemical processes during fires can cause a reduction in the mechanical properties of rock or soil surrounding the tunnel structures (Erdakov and Khokhryachkin 2005).

Since 1990, there have been a number of major fires in road and railway tunnels world-wide. For example, the Mont Blanc Tunnel fire in 1999 caused damage to the tunnel structures which included: 1) serious spalling of over 900 m of the tunnel roof, 2) nearly 1 km of ceramic tiles falling, 3) safe refuges near the fire being severely damaged, and 4) 1.2 km of asphalt pavement being destroyed. The total estimated loss was 450 million Euros and it took 3 years to repair the tunnel (Ministry of the Interior, 1999).

Another example is the Channel Tunnel fire. Considerable damage occurred over a 480 m length of the Channel Tunnel structure. The damage included: 1) concrete spalling which caused a reduction in the lining thickness (on average 170 mm), and 2) the first layer of steel reinforcement ruptured in many places. The total loss in this case was 300 million Euros and it took 6 months to repair the damage. A 50 m long section of the Channel Tunnel had to be rebuilt or reinforced (Kirkland, 2002). In both preceding cases, the cost and time lost increased tremendously due to the lack of fire protection for the concrete structures. Table 2.1 summarizes major traffic tunnel fires and their characteristics.

2.2.1 Concrete Spalling Due to Fire

Concrete spalling is a common occurrence on the inner surface of tunnel linings. Spalling is defined as the deterioration of the concrete causing chunks to separate from the concrete structure. The spalling of concrete during a fire causes serious damage to concrete structures resulting in significant repair costs and risk to service life.

Fire induced spalling is primarily caused by: 1) rapid heating of concrete, 2) tensile strength affected by excessive strain on one side of the concrete tunnel linings, 3) rapid structure and volume change in the aggregate, and 4) pressure from the liberation of water vapor and gas from the aggregate and cement paste (Jansson and Bostrom, 2010). There are five categories of fire-induced spalling. They are namely violent spalling, progressive gradual spalling (or sloughing off), corner spalling, explosive spalling, and post-cooling spalling. The mechanism of fire-induced spalling can be caused by the combination of pore pressure changes due to evaporation of entrapped moisture, compression due to the increasing thermal gradient, internal cracking due to difference in thermal expansion, especially in the interface between aggregate and cement paste, cracking due to different thermal deformation (concrete-steel) and strength loss due to chemical transition (Promat, 2008). Spalling mechanisms and their causes are summarized in Table 2.2.

2.2.1.1 Violent spalling

Violent spalling is the separation of small or larger pieces of concrete from the cross section during which energy is released causing the rapid popping of pieces and small slices of concrete, producing a popping or cracking sound. This type of spalling is caused by pore pressure and

thermal gradients; internal cracking on the meso-level also influences this spalling process. The surface compression during heating can increase due to lateral restraint, reinforcement, pre-stressing, large concrete thickness and a high heating rate. Pore pressures are dependent on heating rate, moisture content, permeability, porosity and the presence of polypropylene fibres. However, an increased ductility of concrete by steel fibres has sometimes been reported to reduce the risk of this type of spalling (Fellinger and Both 1997).

2.2.1.2 Progressive gradual spalling

Progressive gradual spalling is caused by loss of strength due to internal cracking and chemical deterioration of the cement paste at the micro-level. This type of spalling is related to the attained temperature of the concrete instead of the heating rate. If the concrete is heated to a very high temperature, it will be too weak to carry its own weight, causing small pieces of concrete to fall without much sound. This type of spalling is likely to occur on a lining heated from below, since gravity will pull the cracked pieces of concrete from the cross section (Gawin et al. 2006).

2.2.1.3 Corner spalling

Corner spalling occurs when a corner of concrete breaks off at the location of a reinforcement bar. The unbalanced heating of concrete leads to an oval deformation of the concrete around the uniformly heated reinforcement bar. This difference in deformation causes splitting stresses in the concrete, leading to splitting cracks that can cause the corner of a column or slab to break off (Hertz, 2003).

2.2.1.4 Explosive spalling

Explosive spalling is the result of a combination of rising pore pressures and thermal gradients in the cross-section. At the front of heat penetration a “moisture clog”, which means an area with high pore pressure, develops inside the concrete. Part of the moisture is pushed further into the colder part of the concrete due to the pressure gradient at the back of the clog. If the heated surface is under compression due to a thermal gradient, the complete heated surface may be blown away with a loud bang. This type of spalling is especially likely to occur on structural members such as columns and beams when heated from more than one side. When moisture clogs are advancing into the concrete from all heated sides, at a given time, the moisture clogs will meet in the centre of the cross-section, giving a sudden rise in pore pressure which may cause large parts of the cross-section to explode. This type of spalling can also occur after a considerable burning time if the concrete surface has been protected with an insulating layers (Both, 1999).

2.2.1.5 Post-cooling spalling

Post-cooling spalling occurs after the fire is over, after cooling down or maybe even during extinguishment (Khoury, 2003). This type of spalling was observed with concrete types containing calcareous aggregate. The rehydration of CaO to $Ca(OH)_2$ after cooling, with an expansion of over 40%, explains this phenomenon. This occurs after cooling down, when moisture is again present on the concrete surface. The expansion due to rehydration causes severe internal cracking on the meso-level and thus completes the weakening of the concrete. Pieces of concrete keep falling down as long as there is water to rehydrate the CaO in the dehydrated zone.

2.2.2 Fire Protection

Various methods of fire protection to increase an insulating effect have been developed as the incidence of tunnel fires have increased. At present, there are no international standards for fire protection used in tunnels. However, a few countries, such as Germany and the Netherlands, have prescriptive standards which include the ZTV-RABT standard (Beard and Carvel, 2005) and the Rijkswaterstaat standard (Ministry for Public Works and Water Management, referred to as RWS). The requirements from RWS are:

1) Temperature of the steel reinforcements within concrete shall not exceed 250 °C to prevent sagging and collapse
2) Temperature of the concrete surface shall not exceed 380 °C to prevent spalling

There are various methods used to satisfy requirements such as those in the ZTV-RABT and RWS standards. For example, passive fire protection methods for concrete tunnels can be specified. Passive methods are classified as follow: i) cladding type, ii) secondary or sacrificial layer type, and iii) fireproofing. Other methods of minimizing the effect of fire are to increase the dimension of the components.

2.2.2.1 Cladding (Board) types

Protective panels such as mineral board are an example of cladding type fire protection. For example, silicate calcium fireproofing board attached to a thin aluminizing enameled steel plate can be considered for the interior finishing of concrete segments (see Figure 2.1). The thickness of the mineral board typically varies from 25 mm to 30 mm, and it is essential to ensure that the correct board thickness is chosen to give the required fire resistance in terms of duration of

protection. The advantages of this method are considered to be: 1) easy installation, 2) visual effects of fire damage are possible, and 3) excellent fire protection. However, it is also expensive. Such an approach has been utilized in the Akita central road tunnel in Japan and the Elbe tunnel in Germany (Ono, 2006).

2.2.2.2 Secondary layer types

Secondary layer types include the application of additional layers of concrete or cementitious material to the existing tunnel lining. One of these methods utilizes spray mortar. To apply spray mortar, steel wire mesh is fastened to the liner using weld pins and then the mortar is sprayed onto the tunnel lining as shown in Figure 2.2. The spray mixture usually consists of vermiculite and cement for fire protection. The thickness of the mortar spray varies from 10 mm to 50 mm.

Coatings such as the spray mortar described above are easy to repair if damaged, and consequently are widely considered to be the simplest and least expensive method of achieving acceptable fire resistance. Additionally, there is no risk of failure in case of fire. However, the disadvantages of this method can be: 1) longer construction time, 2) risk of water absorption that causes loss of thermal insulation, and 3) no visual access to the lining for inspection.

The Westerschelde Tunnel in the Netherlands was protected by spray mortar. In the repair of the Mont Blanc Tunnel following the 1999 fire, a refractory ceramic cementitious material called Fire Barrier was used to protect the linings (Beard and Carvel, 2005; Beard 2009).

2.2.2.3 Fireproof concrete

Fireproof concrete segments can be made by blending normal Portland cement with polypropylene fibers and aggregates comprising basaltic gravel and quartzite. These types of mixes have been shown to dramatically reduce the heat transmitted through concrete segments in the event of fire. The advantages of fireproof concrete are: 1) shorter construction time, 2) sufficient fire protection during construction, 3) free access for tunnel inspection, and iv) no problems for water seepage or cleaning. However, fireproof concrete cannot be applied to existing tunnels.

2.2.2.4 Thin Spray-on Liner (TSL)

The Toronto Transit Commission (TTC) is considering applying a type of Thin Spray-On Liner (TSL) to their subway lining segments to seal the inner tunnel surface. The TSL is being considered because other conventional coatings such as shotcrete and steel or mineral board cannot be applied due to the space limitations. Therefore, the primary benefit of the TSL is that it can be applied in 4 to 5 mm thick coatings to seal the inner tunnel surface, to limit oxygen availability, and to retain the loose concrete from falling on the track or trains if it develops. Although it is not considered as a fire retardant, it is necessary to examine the fire performance of the TSL.

The TSL to be considered in this thesis is a polyurea-based material referred to as RockWeb^{TM} was developed by Spray-on Plastics of Rockwood Ontario (see Figure 2.3). The form of RockWeb that was examined in this thesis also made use of a blend of vermiculite and graphite to confer fire protection capability. Certain types of TSL require the spray combination of two

liquid chemicals to create a polymer coating material with excellent bond strength to concrete. RockWeb is one such blend. The typical thickness of TSL coatings ranges from 1 mm to 5 mm. The advantages of TSL include: 1) ultrafast setting, 2) easy and fast installation and 3) limited rebound during spraying (Spray-on Plastics, 2000) and 4) consistent lining thickness. It is also reported that TSL improves explosion resistance of substrate materials such as rock during blasting operations (Archibald and Katsabanis, 2003).

2.3 TESTING PRECAST CONCRETE SEGMENTAL TUNNEL LININGS

Precast concrete segmental tunnel linings are generally thought to be durable and require minimal maintenance. However, serious maintenance problems can be caused by earthquakes, leakage through lining joints, increasing traffic in tunnels, or chemical attack from the groundwater or environmental pollution. Liner damage caused by earthquakes or concrete degradation due to chemical attack can decrease joint stiffness and reduce the load carrying capacity of tunnel linings. The factor of safety of a tunnel lining may gradually decease in time due to these effects, and thus, it is important to continually evaluate the load carrying capacity for the existing concrete segmental tunnel linings (He and Wu, 2005).

2.3.1 Previous Studies

This section summarizes a few studies that have focused on the strength of tunnel linings. Both full-scale testing and bench-scale testing have been performed by various researchers. However, as shown in the next sections, performing structural tests on full-scale and bench-scale linings is complicated by factors such as material defects, equipment limitations and methods of applying the load.

Table 2.3 summarizes several tunnel lining studies from the published literature including the lining dimensions, materials and reinforcement used, loading methods, major findings, and the load-carrying capacities. As shown in Table 2.3, the outer diameter of the studied tunnel linings ranged from 320 mm to 15,000 mm, and the thickness of the liners ranged from 40 mm to 650 mm. The loading methods ranged from applying a concentrated point load at the midpoint of the liner, to applying two equal-concentrated point loads or using multiple jacks to apply equivalent distributed loads.

2.3.2 Full Scale Tests

2.3.2.1 Nakamura et al. (1998)

Nakamura et al. (1998) introduced a new segmental tunnel lining system with mechanical joints and evaluated the effect of liner thickness and width on the load-carrying capacity. The lining design is a boltless composite steel-and-concrete structure that is connected using new mechanically shaped steel joints with a caulking groove. Differing from conventional RC segments, this segment comprises concrete with curved steel H-shape beams forming the ends and sides of each segment. One segment of 250mm thickness and 1200mm width and one with 200mm thickness and 1500 mm width were used to conduct bending tests with biaxial loading.

As shown in Figure 2.4, the two equal-concentrated loads were applied to the surface of the segments using a hydraulic jack and a load distribution beam. This study found there was a reduction in the integrated performance of the steel frame and concrete caused by a reduction in the load-carrying capacity of the filler concrete. The authors attributed the reduced load-carrying capacity to ineffective confinement of the filler concrete provided by the H-shaped steel beams compared to conventional reinforcement stirrups.

2.3.2.2 Mashimo et al. (2002)

Mashimo et al. (2002) performed full-scale tests on a semi-circular continuous lining ring (i.e. no joints) using three different loading cases. The three loading cases were applied in this study to approximately simulate different ground conditions. Figure 2.5 illustrates the loading types, which are labeled 'A', 'B', and 'C'. The primary objective of Mashimo et al. (2002) was to investigate the effect of steel fibre reinforcement (SFR) on the load-carrying capacity of concrete linings for various simulated ground loads and conditions. As shown by the following, however, these authors used different compressive strengths for the concrete linings leading to difficulty in interpreting the results.

Referring to Figure 2.5, loading type 'A' was an attempt to examine the influence of increased earth pressures at the ground due to weaker or loosened ground at the tunnel crown. Loading type 'B' simulated the effect of concentrated loads at the tunnel crown (i.e. due to loosened ground) in conjunction with loss of support or confinement of the lining ring at the tunnel shoulders. Finally, loading type 'C' was thought to represent a tunnel in very weak ground resulting in large uniform pressure acting on the lining.

Based on the load tests, the response of the tunnel linings to loading type 'A' was found to be dominated by the influence of axial forces rather than the bending moments induced by the increased loads at the crown. In contrast, for type 'B' loading, the liner response was found to be governed by bending at the tunnel shoulders. Lastly, loading was done in all of the sections until the specimen collapsed with loading type 'C'.

For loading type ‘A’, the collapse load was 330 kN/jack for the steel fibre reinforced specimens while a load of 390 kN/jack was required to collapse the specimen without reinforcement. The concrete compressive strength corresponding to the loads of 330 and 390 kN/jack was 20 MPa and 26 MPa, respectively. Consequently, the results indicate that the concrete compressive strength dominated and the steel fibre-reinforcing had a minimal effect. For the second loading case (type ‘B’), a collapse load of 110 kN/jack was observed for the unreinforced concrete specimens; the compressive strength of the concrete in this specimen was 27 MPa. The loading in the type ‘B’ tests varied from 120kN/jack to 160 kN/jack for the steel fibre reinforced specimens with compressive strengths of 24 and 27MPa, respectively. Based on these load test results, it was calculated that there was between 22% and 45% increase in the load-carrying capacity of the segments due to the fibre reinforcement.

Finally, the collapse loads were 250 kN/jack and 290 kN/jack for unreinforced and steel fibre reinforced segments subject to type ‘C’ loading. An additional 40 kN/jack was required to break the steel fibre reinforced segment compared to the unreinforced concrete.

Despite the puzzling results for the type ‘A’ loading tests, Mashimo et al. (2002) concluded that the load-carrying capacity of fibre reinforced concrete tunnel linings must be evaluated considering the ground conditions and lining materials.

2.3.2.3 Nishikawa (2003)

Nishikawa (2003) tested a prestressed precast concrete segmental tunnel lining, which is illustrated in Figure 2.6. Nishikawa (2003) examined the use of pre-stressing in an attempt to

reduce the volume of reinforcement and eliminate bolted joints, which reduced the manufacturing cost of the segments.

The bending strength at the joint was examined by applying two equal concentrated loads as shown in Figure 2.6 until the joint broke. For the prestressed linings, the load required to fail the jointed segments was 37.1 kN while the design bending strength of a segment with an single unbonded prestressing strand was 29.4 kN. As such, an adequate sufficient effect of the prestressing strands on the bending strength could be obtained. Furthermore, the horizontal displacement was restored to its initial state when the load was fully removed. The study verified that the prestress strands could provide high stability. However, these strands are only suitable for tunnels with a large diameter (i.e., more than 10 m) where deformation due to dead load is a problem.

2.3.3 Bench Scale Tests

2.3.3.1 He and Wu (2005), and Aruga et al. (2007)

The RTRI (Railway Technical Research Institute of Japan) developed and conducted tests on a bench-scale (1/30) model for double track tunnels to evaluate the structural performance of the concrete tunnel linings. Figure 2.7 illustrates the bench-scale model, which comprised the tunnel lining, a series of jacks, a ring-shaped reaction frame and fundamental supports. Each screw-type jack applied load to the ring through a loading plate, and comprised a cylindrical spring made of rubber and double threaded screw bolts as shown in Figure 2.7. The loading bolt consisted of an outer bolt connected to the reaction frame, and an inner bolt connected to the loading plate. The system was capable of applying eleven independent loads to simulate an oval-shaped load with

different magnitudes on each loading plate by adjusting the screws. An elastic reaction could be induced by fixing the outer bolt to the reaction frame except at the loading points. The longitudinal direction of the tunnel lining was constrained by springs. In addition, the bench-scale lining was 20mm wide, 10mm thick and had an outer diameter (OD) of 320 mm. The compressive strength of the concrete was 27 MPa.

Four cases were considered comprising reinforced concrete and plain concrete linings. In addition, damage consisting of a 20 mm wide by 10 mm deep chip was also evaluated. The load was applied on the crown of the lining. Displacement gauges were arranged on the inner surface of the lining at angles of approximately 0°, 5°, 45°, 90°, 135°, 175° and 180°.

According to the testing results from Aruga et al. (2007), the reinforced concrete lining and plain concrete lining maintained almost the same load carrying capacity. However, there was a significant improvement in the load-carrying capacity for the reinforced concrete after compressive failure occurred compared to the unreinforced lining. Aruga et al. (2007) attributed this to the steel reinforcement, which improved the post peak strength characteristics of the concrete compared to that of the plain concrete lining. For the cases where a deep chip or notch was introduced in the linings, both types of linings showed a significant decrease in the load-carrying capacity after the initial tensile crack occurred. However, the reinforced concrete segment again displayed better post-failure load capacity, whereas the unreinforced lining was more brittle. As a consquence, the durability of the reinforced concrete lining was shown to be greater than that of the plain concrete model. Also, the post-cracking behaviour of the reinforced concrete lining was substantially better.

2.3.3.2 Yan and Zhu (2007)

Yan and Zhu (2007) evaluated the fire safety of tunnel linings for different fire scenarios with a series of reduced-scale experiments on tunnel linings. Three types of concrete comprising Reinforced Concrete (RC), steel fiber reinforced (SFR) concrete and polypropylene fiber reinforced (PFR) concrete, were employed in the experiments. These test results showed the mechanical properties of the lining materials, especially the uniaxial compressive strength, elastic modulus and impermeability, deteriorate significantly after exposure to high temperatures:

1) compared with normal temperature conditions, high temperatures produce a significant decrease of load-carrying capacity and a significant increase in the displacement of segmental joints;
2) because of material deterioration caused by, thermal damage and thermal stress due to high temperatures, the load-carrying capacity and safety of the tunnel lining system decreases dramatically.

It was concluded that large displacement of the lining system might occur after a fire affecting the safety of the surrounding substructure.

2.3.4 Full-scale testing with full rings

2.3.4.1 Schreyer and Winselmann (2000)

The 4th Elbe Highway Tunnel of Germany is one of the largest tunnels in the world with an outer diameter of 13.75m. A full-scale full-ring test was carried out (Schreyer and Winselmann, 2000) during the design of this tunnel to evaluate the load carrying capacity and stability of the lining (see Figure 2.8). An additional objective of the study was to examine the joint tolerances and

allowances of the ring. The load test specimen had a width of 4000mm consisting of a full width ring (200mm) and two half width rings (100mm) bolted together in the longitudinal direction (see Figure 2.8). The OD of the specimen was 13750 mm and the thickness was 700 mm. The assembled lining rings were loaded using 96 jacks to simulate the anticipated earth and water pressures. One hundred and fifty displacement gauges were installed on the surface of the lining ring to measure the deformation of the rings (Schreyer and Winselmann, 2000).

2.3.4.2 Lu et al. (2006)

Similar to the Elbe Highway Tunnel lining tests, the Changjina Tunnel, the world's largest tunnel with an outer diamter of 15000 mm, a thickness of 1300 mm and a width of 2000 mm, was constructed in Shanghai, China. It was a shield-driven and stagger-jointed tunnel with contemporary wedge-shaped lining segments. A load test was performed on one lining ring in addition to measurement of the earth pressure acting on the lining and deformation during construction.

Figure 2.9 illustrates the load-test setup and loading positions around the rings. Each ring was composed of 10 segments. The test specimen comprised upper and lower 1-meter wide rings with a 2-meter wide middle ring. Adjacent segments were bolted together in the longitudinal direction and radial joints between segments were staggered.

Forty-four loading beams each with four loading points were placed around the ring. The load beam exerted four different magnitudes (i.e., P_1 to P_4) of pressure according to the diagram shown in Figure 2.9. Also, longitudinal forces were applied to the lining using jacks to simulate

jacking forces applied by a TBM during construction. A total of six load cases corresponding to two different depths (i.e., 15m and 27m) and three different coefficients of lateral earth pressure at rest (i.e., 0.68, 0.7 and 0.72) were examined. During the testing, longitudinal jack forces of 1500 kN and 3000 kN were applied corresponding to the simulated tunnel depths of 15 m and 27 m respectively. P_1 to P_4 varied between 1260 kN and 1084 kN in the case of the 15 m level while they were between 2240 and 1892 kN in the case of the 27 m depth. For each loading condition the authors measured strain in the reinforcing bars in segments, the concrete strains, the strains of the connecting bolts, and angle changes at the staggered joints. Also, the axial forces and bending moment distributions along the linings were plotted instead of measuring the load-carrying capacity of the linings.

2.4 JOINT ROTATIONAL STIFFNESS OF SEGMENTAL TUNNEL LININGS

A few numerical studies of the segmental tunnel linings have examined joint rotational stiffness related to its geometry because the analytical solution suggested by Muir Wood (1975) has been used for the tunnel design. For this reason numerous FE analyses using a continuous ring with a discounted rigidity applying the reduction factor have been widely employed using a ratio between effective bending rigidity (i.e. EI_e), and the bending rigidity (EI) of the tunnel lining (Koyama and Nishimura, 1988). However, for the last two decades, innovative approaches considering the interaction between the segments related to joint stiffness have been attempted. The following is a summary of a number of FE methods used in different simulations of joints in concrete segmental linings.

1) The flexural rigidity of the circular ring was assumed to be uniform throughout the lining. There was no allowance given for rigidity due to the existence of joints (Bull, 1944; and Morgan, 1961).
2) The reduction of rigidity was due to the presence of joints. A reduction factor was applied to the rigidity of the continuous lining structure (Peck et al. 1972; Muir Wood, 1975; *JSCE*, 1977; Einstein and Schwartz, 1979; and Koyama and Nishimura, 1988).
3) The lining ring was modified to a jointed ring, but the stiffness of the joint was ignored. Then, the joint was assumed to contain perfect pins (Lee et al. 2001).
4) The stiffness of the joints was considered to have a constant value (Blom et al. 1999; Hefny et al. 2004; Gruebl, 2006; Kramer et al. 2007; and El Nagger and Hinchberger, 2008).
5) Similar to method 4), the stiffness of joints was taken into consideration with a constant joint stiffness as well as non-equal values, and the performance of the tunnel linings was studied (Lee and Ge, 2001).

The methods mentioned above have different characteristics and they have been used in various projects. The first method is very simple but it may cause large errors. The second method seems to be reasonable. However, the reduction value can only obtained from the aid of empirical relationships established for various geological conditions or full-scale laboratory testing. The third method is the most comprehensive, which can be used to study the effect of stiffness of a joint on internal forces and displacement with soil resistance pressure to simulate different ground response conditions (Lee et al, 2001). The fourth method is extremely analytical for calculating the stresses and displacements on the lining using a number of joints. A limitation of

this method uses the same stiffness of joint disregarding the effects of various bending moments, thrust on the linings, and nonlinearity of the lining materials. The last method presents the mechanical behaviour of the joints by laboratory structural testing and an analytical solution for jointed ring structures which explains the effects of joint stiffness, joint distribution, the number of joints and non-equal joint stiffness on the performance of tunnel linings. However, it is extremely complicated and nonlinearity of the lining materials was not considered.

Most modern subway tunnel linings are designed with segmental linings comprising precast reinforced concrete segments. In addition to enabling higher construction rates compared to cast-in-place concrete linings, the joints between liner segments can reduce bending moments in the lining reducing the amount of flexural reinforcing steel required to resist loads due to the earth pressure. Currently, designers can use either closed-form analytical solutions (Muir Wood, 1975; Einstein and Schwartz, 1979; Blom, 2002; and El Naggar and Hinchberger, 2008) or Finite Element (FE) software to assess the moments and thrusts in jointed segmental tunnel linings. However, the rotational stiffness of liner joints is not well documented in the published literature.

Table 2.1 Summary of tunnel fires and consequences
(after Beard and Carvel, 2005 and Erdakov and Khokhryachkin, 2005)

Country	Year	Tunnel (city)	Length (m)	Fire sources	Duration	Consequence		
						People	Damage vehicles or trains	Structural damage
Canada	2000	Underground (Montreal)		Cable fire	6h			electrical system and severe smoke
Canada	2000	Metro (Toronto)		Railway train		2 dead	1 train	line closed 24h
Canada	1976	Christie (Toronto)		Station				> $3 million
Canada	1971	Henri Bourassa (Montreal)		Train		1 dead	1 train	
USA	2002	Ted Williams (Boston)	2,600	Electrical compartment				
USA	2001	Howard St. (Baltimore)	2,253	Cargo train	12h		60 trains	Severe spalling damaged
USA	1992	Metro (New York)		Metro car		86 injured	1 metro car	
USA	1985	Grand Central Station (New York)		Station fire				Severe station damage 3 million loss
USA	1982	Caldecott (Oakland)	1,028	1 car 1 coach 1 lorry	2 .8h	7 dead 2 injured	3 lorries 1 coach 4 cars	580m serious damage
USA	1971	Underground (Boston)		Metro car		34 injured	1 metro car	
South Korea	2003	Subway Station (Daegu)		Train attack	24h	195 dead 140 - injured	6 carriers	Severe concrete damage
Switzer-land	2001	St. Gotthard	16,918	Lorry	48h	11 dead	13 lorries 4 vans 6 cars	collapse 250 m of tunnel lining
Austria	2000	Kitzsteinhorn	3,300	Passenger train	12h	155 dead	1 train	closed 1 year
France-Italy	1999	Mont Blanc	11,600	Lorry	53h	39 dead	23 lorries 10 cars	serious tunnel damage
France-UK	1996	Channel Tunnel	51,000	HGV carrier	7h		1 HGV carriers 10 HGV's	extreme spalling

Table 2.2 Summary of spalling mechanisms induced by fire
(after Breunese and Fellinger, 2003)

	Pore pressure due to evaporation	**Compression due to thermal gradient**	**Internal cracking due to thermal expansion**	**Cracking due to different thermal deformation**	**Strength loss due to chemical transition**
Violent spalling	Y	Y	Y		
Sloughing off					Y
Corner spalling				Y	
Explosive spalling	Y	Y	Y		
Post-cooling spalling			Y		Y

Table 2.3 Summary of testing of tunnel linings

Dimension (mm)	# of Tests	Materials and Reinforcement	Loading Method	Objectives	Load Carrying Capacity (ultimate)	Reference
A:1200(w) x 200(t) B:1500(w) x 250(t)	4	Steel plate & Unreinforced and Reinforced Concrete	One segment subjected to two equal concentrated loads	Evaluated reduction of the confining effect due to an increase of width and thickness.	[A] 512, [B] 518 kN (unreinforced) [A] 784, [B] 785 kN (reinforced)	Nakamura et al. (1998)
[1]O.D: 9700 mm [2]W:1000 mm [3]T: 300 mm	7	Concrete (*f'c* 12-28MPa) Unreinforced, Steel-fibre reinforcement, or vinyl reinforcement	Half ring subjected to 3 types of radial loading (2 jacks per a segment)	Examined three types of loadings A, B and C, along with the effect of steel fibre reinforcement	A:330 & 390 kN/jack B:110,120 &160 kN/jack C:250 & 290 kN/jack	Mashimo et al. (2002)
O.D:3550 mm W:1000 mm T: 150 mm	2	Concrete steel reinforcement and prestressing strands	One segment subjected to two equal concentrated loads	Examine the benefits of prestress (i.e. enabled the elimination of bolt joint, reduced the volume of reinforcement and improved load-carrying capacity).	Baseline load-carrying capacity: 29.4 kN Prestressing: 37.1 kN	Nishikawa (2003)
O.D: 320 mm W:100 mm T: 40 mm	4	Unreinforced concrete and reinforced (stainless steel wire)	One concentrated load on the crown	Bench scale tests to evaluate the effect of partial loss and simulated oval shape earth pressure	Crack loads: <1 kN Load-carrying capacity: < 2kN	He & Wu (2005) Aruga et al. (2006)
O.D: 15000 mm W: 13000 mm T: 650 & 2000 mm	1	Reinforced concrete	Distributed loads using 44 jacks	Examine the effects of staggered-jointed rings and axial force in longitudinal direction of lining.	Not determined	Lu et. al (2006)
[4]I.D:1800 mm [5]L: 10000 mm	33	Reinforced concrete, steel fibre and polypropylene fibre reinforcement	One segment subjected to a point load before and after exposure to fire	To study the effect of fire on the load carrying capacity of linings	Not available	Yan and Zhu (2009)

NOTE: [1]O.D. - outer diameter; [2]W - width; [3]T - thickness; [4]I.D. - inner diameter; [5]L - tunnel length; RC- Reinforced Concrete

Figure 2.1 Tunnel fire protection: cladding type (board type)

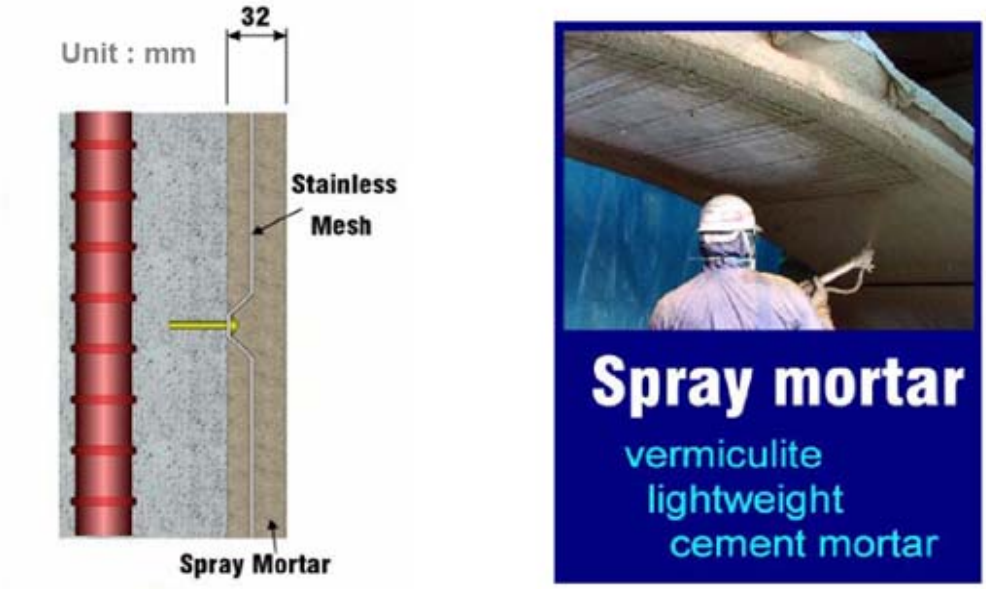

Figure 2.2 Tunnel fire protection: Secondary layer type (spray mortar)

a) Spraying b) TSL coated concrete slab

Figure 2.3 Thin Spray-on Liner (TSL)

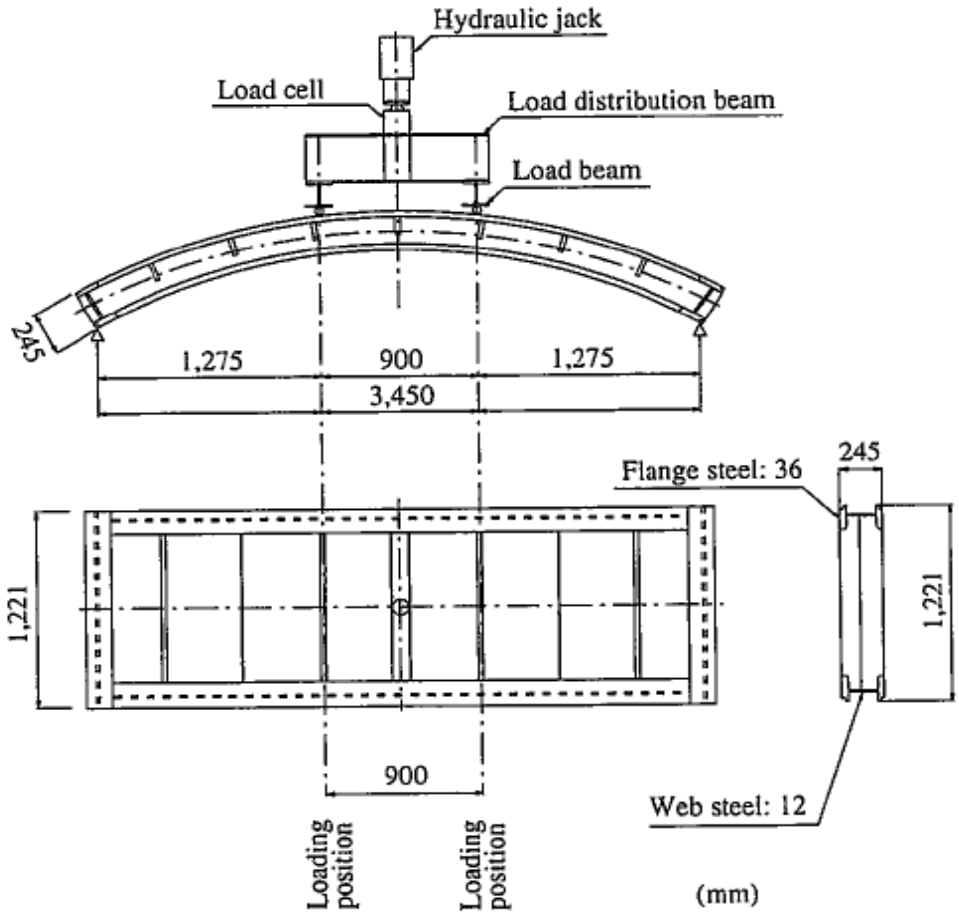

Figure 2.4 A schematic diagram of the bending test (Nakamura et al. 1998)

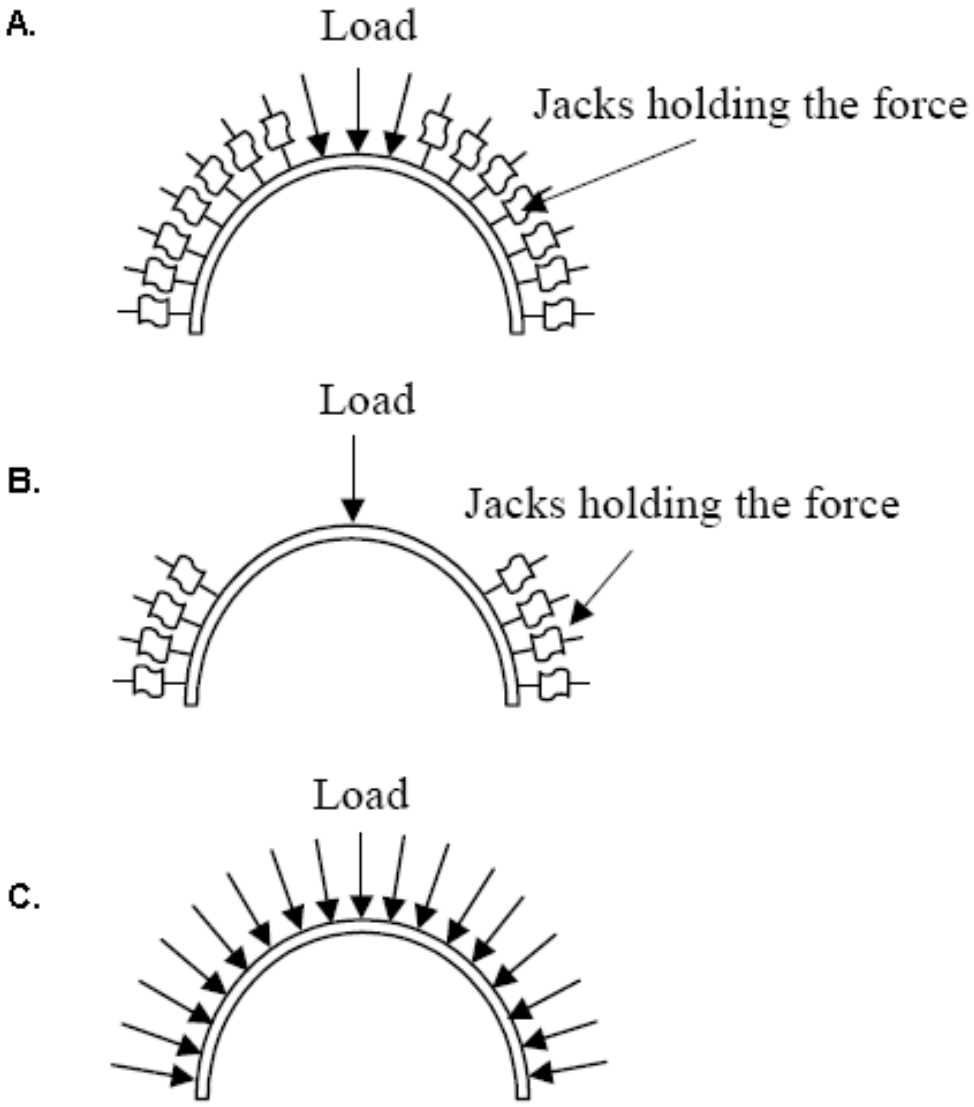

Figure 2.5 Three loading types simulated ground conditions (Mashimo et al. 2002)

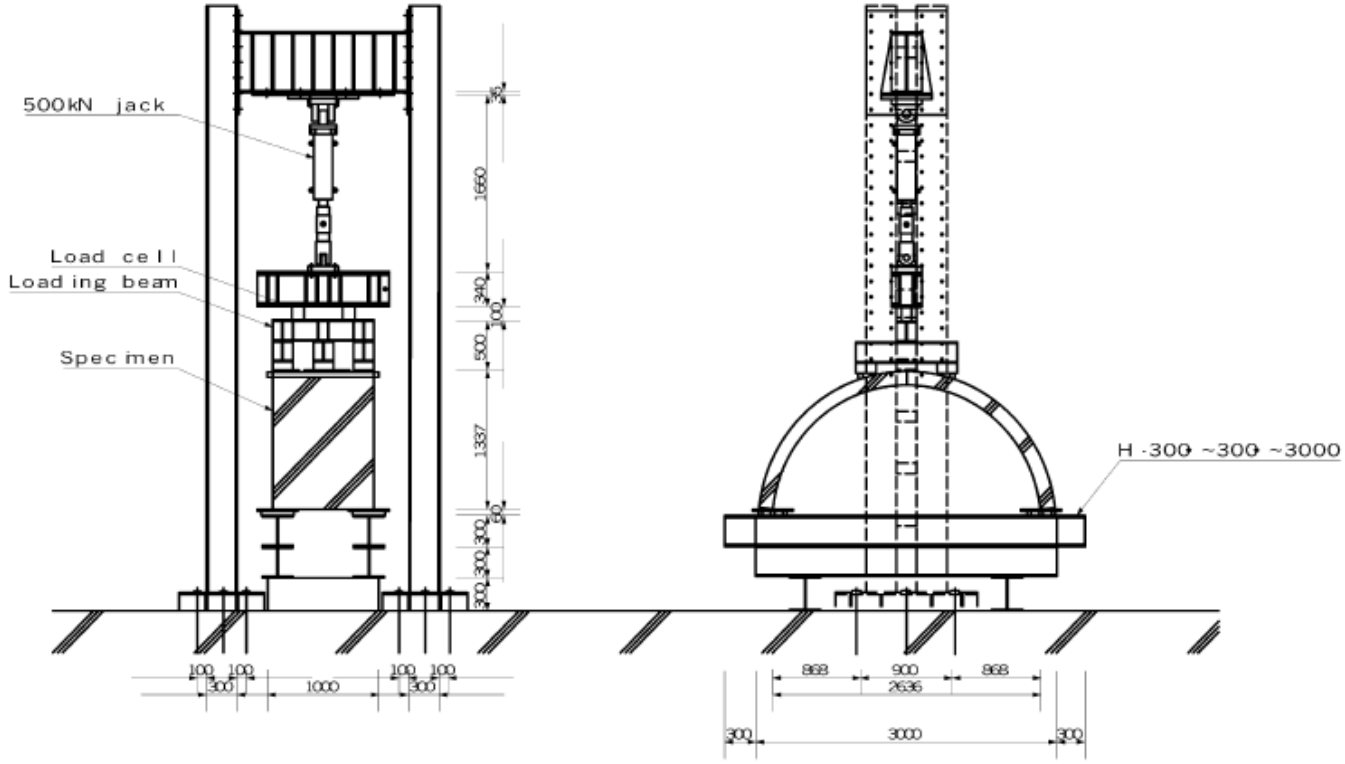

Figure 2.6 A flexural (bending) test setup (Nishikawa, 2003)

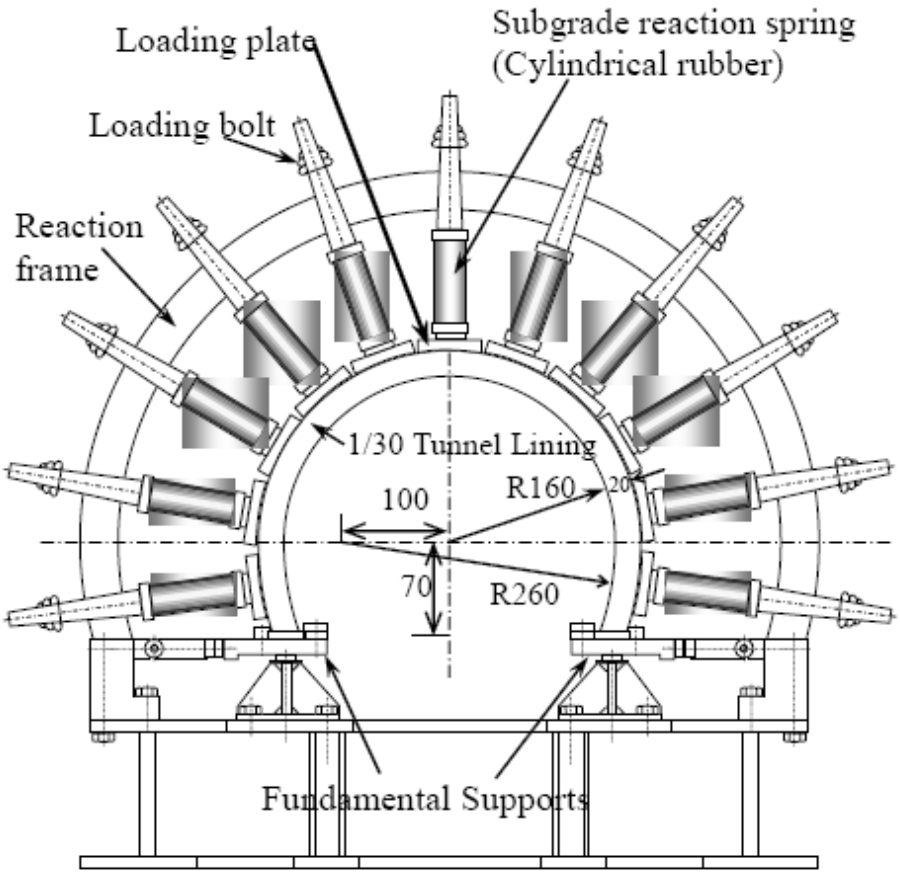

Figure 2.7 A bench-scale test setup for double track tunnels
(He and Wu, 2005; Aruga et al. 2007)

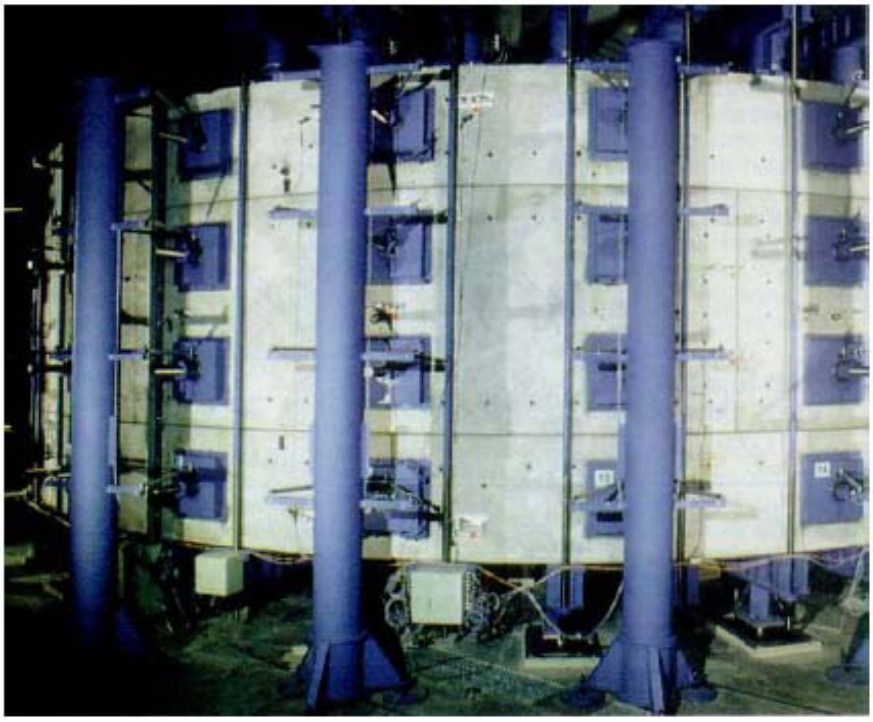

Figure 2.8 The 4th Elbe highway tunnel lining test (Schreyer and Winselmann, 2000)

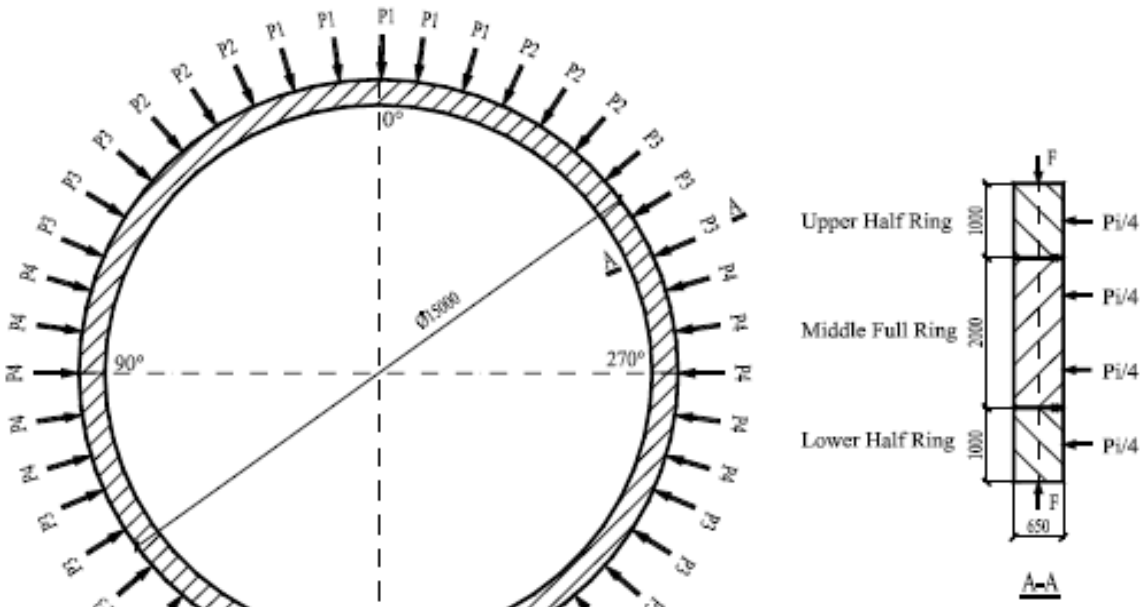

a) layout of loading

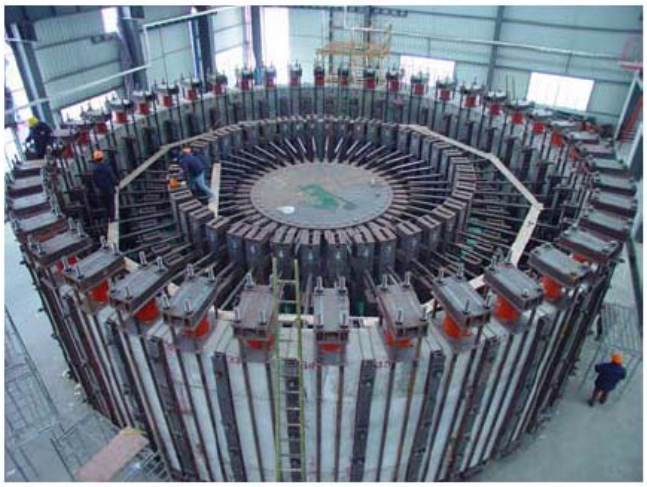

b) Test setup

Figure 2.9 Layout of loading plan and test setup

CHAPTER 3

TUNNEL FIRE TESTS ON THIN SPRAY-ON LINER (TSL)

3.1 INTRODUCTION

The use of construction materials for subway tunnels is regulated under codes such as the National Fire Protection Association code (i.e. Standard for Fixed Guideway Transit and Passenger Rail Systems) (NFPA 130, 2000). NFPA 130 covers fire protection requirements for passenger rail, underground, surface and fixed transit systems including trainways, transit stations, vehicles, and storage areas. The purpose of the standards is to establish minimum requirements for tunnel and transit fire safety. In NFPA 130, fire safety is achieved through facility design, operating systems, hardware including construction materials and vehicles, and software. The level of desired fire safety must be integrated with required standards of each subsystem (NFPA 130, 2000). For example, construction materials used in underground tunnels (e.g. trainways) are required to be non-combustible. Also, an engineering analysis of potential fire exposure hazards to the structure must show that the life safety risk is acceptable. Nevertheless, the code does provide for limited use of combustible materials. Hence, in accordance with NFPA 130, the combustion characteristics of TSL must be assessed (i.e. flame spread classifications (FSC) and smoke index).

This chapter examines the fire performance of a candidate Thin Spray-On Liner (TSL). The TSL is a limited-combustible material, which is being considered for use in the Toronto Transit

Commission (TTC) subway tunnels. In order to examine the fire performance of this TSL, two preliminary tunnel tests were conducted according to CAN/ULC-S102-M88 (*Method of test for surface burning characteristics of building materials and assemblies,* Laboratories of Canada, 2003) at Bodycote Laboratories of Canada. After the preliminary tests were performed, two detailed instrumentation tunnel tests were conducted. The detailed instrumentation tunnel tests were also performed according to CAN/ULC-S102-M88 (Laboratories of Canada, 2003). In addition, the concrete slabs used in the tunnel tests were instrumented with thermocouples to monitor the concrete temperatures.

The objectives of the research reported in the following sections was to measure the fire performance of the Thin Spray-On Liner (TSL) using standard fire performance tests and to provide data that could be used to determine the thermal response of a TSL subject to direct flame exposure and high temperatures. A series of thermal and mechanical tests were carried out to evaluate the TSL with a substrate material of reinforced concrete.

3.2 METHODOLOGY

3.2.1 CAN/ULC-S102-M88 Test

The surface burning characteristics of building materials are typically studied using the test standard CAN/ULC-S102-M88, which is similar to ASTM E84, *Standard Test Method for Surface Burning Characteristics of Building Materials* (ASTM, 2011). This test method is probably the most commonly applied fire test standard and the most common test method used to characterize flammability of plastics (Troitzsch, 2004). The main purpose of the test is to determine the burning behavior of surface coatings relative to red oak.

Figure 3.1 illustrates the CAN/ULC-S102-M88 test apparatus. The test tunnel consists of a 450 mm wide, 300 mm deep and 7600 mm long chamber. It has two gas burners located 190 mm below the specimen and 300 mm from the upstream end of the tunnel. Typical test duration is 10 minutes. A test is conducted to obtain a flame spread index and a smoke-developed index. An air ventilation system controlling the air flow in the chamber is located in the end of the tunnel.

The test specimen must be at least 50 mm wider than the interior width of the test chamber (i.e. 450 mm) and less than 7300 mm in length. Specimens must be representative of the material or assembly to be tested. The specimen thickness must be less than 50 mm or the depth of thermal involvement during the test (Laboratories of Canada, 2003).

The test procedure is summarized as follow: (Laboratories of Canada, 2003)

1) Preheat the test chamber until the temperature indicated by the thermocouple at 7090 mm reaches 85 ± 5 °C. Then let the chamber cool to a temperature of 40 ± 3 °C at 4000 mm from the upstream end.
2) The test specimens are placed at the top of the tunnel on the test chamber ledges which are covered with 3 mm thick by 40 mm wide woven asbestos tape. A lid or cover is positioned over the specimen, and the specimen coating side is down and exposed to the flame source or burner.
3) After the specimens are mounted, the test chamber operates for 120 seconds prior to the application of the test flame. Air is supplied to the chamber at a constant flow velocity of 1.2 m/s using forced ventilation.

4) Then the burner is lit and with the room darkened and the lab technician observes and records the position of the flame front at 15 second time intervals. The test duration is 10 minutes.
5) Automatically record the temperature measured by the thermocouple near the vent end at intervals not longer than 15 seconds. Also record the gas pressure and the photoelectric cell output every 15 seconds.
6) When the test is ended, the gas supply is turned off and any smouldering or continued burning is observed within the test chamber. The specimen is removed for further examination after the test chamber has cooled enough to allow handling of the segments.
7) The primary data recorded during the test includes the flame spread distance, exhaust temperature, and photoelectric cell measurements. This data is used to determine the flame spread index and smoke development classification.

3.2.2 Test History

First, two preliminary tunnel tests were conducted at the Bodycote commercial fire test laboratory in Mississauga, Ontario, Canada. For the preliminary tests, ten 500mm x 1220mm x 38mm (width x length x thickness) reinforced concrete slabs were constructed in the University of Western Ontario (Western) structure lab. The slabs were instrumented by installing twelve Type-K thermocouples at various depths in the concrete. After the preliminary tests, two more detailed instrumented tunnel tests were performed at Bodycote in 2006. The detailed instrumentation tests were conducted using concrete slabs coated with a 4 mm thick layer of TSL. In addition, the slab thickness was increased from that used in the preliminary tests to minimize variations in the slab thickness and to ensure proper placement of the wire reinforcement mesh

and thermocouples. The detailed test had 50 thermocouples installed at various locations and depths as described in the following section.

3.2.3 Preparation of Test Specimens

3.2.3.1 Test specimens

The concrete slabs were prepared using the following methodology:

1) All slabs were reinforced with a light (3mm thick) wire mesh. The concrete was placed in the plywood formwork and consolidated using a vibrating compactor.
2) Thirteen concrete cylinders were cast during the slab construction. Since the tests were intended to simulate the response of TSL during a fire in the TTC tunnels, the slabs were made using 40 MPa concrete, which is the strength of the concrete used for the TTC linings. Standard compression tests were conducted on the concrete specimens according to ASTM C873-04 (ASTM C873-04e1, 2003).
3) The concrete slabs were cured at room temperature and the surface of each was covered with burlap and wetted down periodically for 3 days. After that, the concrete slabs were moved into a steam curing room for 24 days.
4) The concrete slabs were then transported to Spray-On Plastics in Rockwood, Ontario, Canada, where they were sandblasted on one side and coasted with approximately 4mm. of TSL applied in successive lifts.
5) During spraying of the TSL, the nozzle height was held between 80 cm to 100 cm from the surface of concrete slabs (see Figure 2.3). A primer layer was applied first using a pressure of 500 psi and the TSL was applied after the primer was cured using spray

pressures that varied between 2300 to 2500 psi. These parameters were required to maintain a relatively uniform thickness of the TSL on each slab.

6) The slabs were subsequently stacked on pallets and stored at Spray-On Plastics until the tunnel tests. The spraying occurred on August 28, 2006 and CAN/ULC-S102-M88 tests were done on September 6, 2006

3.2.4 Installation of Thermocouples

Prior to conducting the CAN/ULC -102-M88 tests, 3 mm diameter holes were drilled in some of the slabs from the back side to the depth illustrated in Figure 3.2 for the preliminary tunnel tests and Figure 3.3 for the detail instrumented tunnel tests. The holes were drilled using a heavy duty hammer drill with a 3 mm diameter drill bit, and then cleaned out using compressed air. A small dowel was inserted into each hole to confirm its depth. The TSL coated concrete slabs were transported to Bodycote on September 5, 2006 for the tunnel tests. Tests were also performed on uncoated slabs as a benchmark for studying the effect of TSL on the concrete temperatures in the tunnel fire tests.

Type-K thermocouples were inserted into the pre-drilled holes and held in place using thermal putty. For each test, the instrumented slabs were placed in the CAN/ULC-102-M88 tunnel test chamber. The thermocouples were connected to a computer controlled data-logging system and the tunnel test was subsequently conducted for 30 minutes. Temperature readings were retrieved at 10 second intervals during the tests. Prior to the tunnel tests, each thermocouple was checked by inserting the thermocouple tip into boiling water and comparing the recorded temperature

with that measured using a standard thermometer. All thermocouples matched with the thermometer readings.

3.2.5 Instrumentation Layout

3.2.5.1 Preliminary tunnel tests

Figure 3.4 shows the instrumentation plan for the preliminary tests which are hereafter labeled PT-1 and PT-2. PT-1 was conducted using six uncoated concrete slabs (i.e. no TSL) while PT-2 had six TSL coated concrete slabs. Three sites were monitored as illustrated in Figure 3.4. The sites are labeled 1-3 and were located at 450mm, 1560mm and 2360mm from the flame source. Table 3.1 presents the temperature monitoring positions relative to the flame source and the depth of the thermocouples into the slabs. Each site had 4 thermocouples installed as illustrated in Figure 3.2.

3.2.5.2 Detailed instrumentation tests

Fifty-two thermocouples were installed in the slabs to monitor temperatures in the slabs during the detailed CAN/ULC-S102-M88 tests. Figure 3.5 and Figure 3.6 shows the instrumentation plan for the detailed instrumented tests, which are labeled ITT-1 and ITT-2. Concrete and air temperatures were measured using Type-K thermocouples installed at points labeled 1 to 50 in Figures 3.5 and 3.6. Four of the thermocouples labeled T1 to T4 were installed to measure the tunnel chamber temperatures. Four transverse sections were monitored during each test, as shown in Figure 3.5 and Figure 3.6. The four sections include:

1) Site 1 located 750 mm from the upstream end of the tunnel chamber;
2) Site 2 located 1560 mm from the upstream end;
3) Site 3 located 2360 mm from the upstream end;

4) Site 4 was situated 4265mm from the upstream end during ITT-1 and 3047 mm from the upstream end during ITT-2.

It can be seen from Figure 3.5 that up to four thermocouples were installed at each of the monitoring points. At locations where four monitoring points were installed (e.g. see points 3,4,5,6 at Section 1 in Figure 3.6), the thermocouple tips were situated at depths of 3 mm, 25 mm, 37 mm and 47 mm measured from the outer surface of the concrete slabs that was not exposed to flame. At locations with two monitoring points (e.g. see the points 1, 2 at Section 1 in Figure 3.5), the thermocouple tips were installed at depths of 3 mm and 47 mm from the top of the slabs. When only one thermocouple was installed, the tip was located at the midpoint of the concrete slabs (e.g. see the point 17 and 18 in Figure 3.5). The four thermocouples used to measure the tunnel chamber temperature were situated at least 50mm below the inner surface of the concrete slabs.

3.3 RESULTS

3.3.1 Preliminary Test Results

Figures 3.7 to 3.9 summarize the measured temperature versus time during the preliminary tests at Site 1 to Site 3. As described previously, twelve thermocouples were installed at various depths and monitored during the 30 minute CAN/ULC-S102-M88 tests, which included an additional 5 minutes after extinguishing the flame. All results presented are between 0 minute and 25 minutes at one minute intervals because some thermocouples did not work after the 25 minutes of tests. Presenting the results with one minute intervals is sufficient to evaluate the temperature profiles of the tests. Temperature profiles with depths in the slab are plotted in Figures 3.10, 3.11 and 3.12. Also, Figures 3.13 to 3.14 present longitudinal temperature profiles with distance from the upstream end of the slabs.

3.3.1.1 Temperature difference in coated versus uncoated slabs by time

Referring to Figure 3.7, it can be seen that the temperature increases as time increases at all thermocouples. In addition, the temperatures in the uncoated concrete slabs increase more rapidly than at the corresponding point in the TSL coated slabs. For example, the temperature difference at Ch. 1 between the uncoated slab and TSL coated slab after 5 minutes was 20 °C and the difference increased to 120 °C after 25 minutes of testing. The temperature difference between uncoated and coated slabs also increases as the distance from the thermocouple and inner surface decreases. For example, the temperature difference at Ch. 4 between the uncoated slab and TSL coated slab after 5 minutes was 230 °C and it increased to 350 °C after 25 minutes of testing.

Figure 3.8 presents the temperatures measured at Site 2 during tests PT-1 and PT-2. The temperatures measured at Ch.5 and Ch.6 show a similar pattern to those measured at Ch.1 and Ch. 2. But the temperature differences between the uncoated slab and the coated slab are smaller than those at Site 1. Considering Ch. 5 and Ch. 6, the temperature difference was 25 °C and 35 °C after 4 minutes of testing and it increased to 40 °C and 51 °C after 20 minutes of testing, respectively. It can be calculated that the temperature difference at Ch. 7 increased from 28 to 78 °C between 4 minutes and 20 minutes of testing. Also, the temperature differences between 4 minute and 20 minutes of testing at Ch. 8 were approximately 140 °C and 165 °C.

It can be seen that the temperature differences decreased at monitoring locations farther from the flame source (see Figure 3.9). Therefore, there was only 14 °C and 18 °C difference at Ch. 9 and 10 after 25 minutes of testing. The maximum temperature difference was 37 °C at Ch. 11 during the test. Lastly, Ch.12 failed to measure the TSL effect on temperature due to improper installation of the thermocouples.

3.3.1.2 Temperature difference in coated versus uncoated slabs by depth

It can be seen from Figure 3.10 for Site 1 that the maximum concrete temperature was 617 °C on the inner surface of the uncoated concrete slab, while the TSL coated concrete temperature reached 255 °C at 25 minutes at the same location. The TSL coated concrete temperatures on the inner surface were 284 °C, 319 °C, 365 °C , 380 °C and 411 °C lower at 5 minutes, 10 minutes, 15 minutes, 20 minutes and 25 minutes after starting the test, respectively. At monitoring points located 18 mm to 22 mm from the inner surface (i.e. the middle of the slabs), the TSL coated concrete temperatures were 50% lower compared to the uncoated concrete

temperatures. Similar results can be found at the observation points located 5 mm from the inner surface of the slabs. From Figure 3.10, it can be also seen that the temperatures of the uncoated concrete slab exceeded 380 °C which is the safety limit (i.e. concrete surface temperature criteria) suggested by the RWS standards.

At Site 2 (see Figure 3.11), the temperatures at the inner surface of the concrete slabs were 325 °C for the uncoated concrete and 139 °C for the TSL coated concrete after 25 minutes of testing. As a result, the concrete temperature at the inner surface of the uncoated concrete slabs came close to the safety limit while the TSL coated temperature did not. (i.e. 140 °C after 25 minutes of testing). As shown in Figure 3.11, all other temperatures in either the uncoated or TSL coated concrete slabs were below 380 °C. Additionally, the temperatures measured at Site 3 were below the safety limit (380 °C) by the RWS standards as shown in Figure 3.12. Also, the largest temperature difference at the inner surface of the concrete was 120 °C after 25 minutes of the tests.

3.3.1.3 Temperature difference in coated versus uncoated slabs by distance

Figures 3.13 to 3.16 summarize the longitudinal temperature distribution at the outer surface of slabs, midpoint of slabs and inner surface of slabs during the tests, respectively. Figure 3.16 shows the temperatures in the TSL. It can be seen that the temperatures decrease as the monitoring positions are located farther from the flame source.

Figure 3.13 shows the concrete temperatures at the outer surface of the slabs. At the outer surface, measured temperatures at Site 1, 2 and 3 were below the RWS safety limit for both the uncoated

concrete slabs and TSL coated concrete slabs. The temperature difference between Site 1 and Site 3 ranged from 5 °C to 130 °C for the uncoated concrete during the 25 minutes of the test. On the other hand, for the TSL coated concrete, the maximum temperature difference between Site 1 and Site 3 was 18 °C.

Figure 3.14 illustrates the longitudinal temperatures at the midpoints of the uncoated and TSL coated concrete slabs during 25 minutes of testing. As seen in Figure 3.14, for the uncoated concrete, the temperatures at Site 1 were 271 °C at 20 minutes and 326 °C at 25 minutes. In contrast, all measured temperatures at the midpoint of the TSL coated concrete were below 130 °C which does not exceed the RWS safety limit.

Temperatures measured at the inner surface of the uncoated and TSL coated concrete are presented in Figure 3.15. It shows that the uncoated concrete surface temperature exceeded the RWS requirement for spalling prevention (380 °C) at 5, 10, 15, 20 and 25 minutes after the start of the test. However, the maximum TSL coated concrete temperatures varied from only 131 °C at 5 minutes to 205 °C at 25 minutes, respectively. As shown in Figure 3.13 to 3.15, temperatures in the TSL coated slabs are significantly lower than the temperatures at the corresponding time and depth in the uncoated slabs.

Lastly, the temperatures measured just inside the sprayed TSL are presented in Figure 3.16. Surprisingly, the results in this figure suggest that the temperatures measured at Site 3 were higher than those at Site 2 for 10 minutes and 20 minutes of burning time. These results are thought to reflect the effect of exfoliation of the TSL at sites 1 and 2, whereas the TSL relatively

did not exfoliate at Site 3. Thus intact TSL layer having higher thermal conductivity character than that of partially exfoliated layer at Site 2 caused lesser temperature differences at Site 3. The detailed explanation about the exfoliation of TSL can be found in Section 3.3.3.3.

3.3.2 Detailed Instrumentation Test Results

Temperature measurements during the detailed instrumented tunnel tests are presented in this section. Generally, the temperature readings were repeatable and well controllable during ITT-1 and ITT-2 except for the following cases:

1) Thermocouples installed at the edges of the concrete slabs were shielded by the tunnel slab supports (a steel angle with an asbestos bearing pad). This was not foreseen prior to testing and as such, data from thermocouples P1, P2, P15, P16, P19, P20, P33, P34, P36, P41, P42, P45, P46, P49 and P50 were not representative of the thermal regime in the concrete slabs.
2) Half of the thermocouples installed to measure the tunnel chamber temperature did not work properly. It is because that the testing tunnel edges prevent heat transmittance to concrete slabs.

The following sections present temperature versus time only because: 1) no test was conducted with uncoated concrete slabs, 2) temperatures versus time plot would be the most comprehensive presentation of the tunnel fire test based on the results from the preliminary tests, and 3) an objective of the detailed instrumentation tests is to evaluate the TSL effect on selected locations in terms of time. Additionally, the measured temperatures are compared with calculated temperatures by Finite Element Analysis (FEA) in Chapter 4.

3.3.2.1 Tunnel air temperature

Air temperatures in the tunnel recorded during ITT-1 and ITT-2 are plotted in Figure 3.17. During ITT-1, thermocouples T1, T2 and T3 were damaged as mentioned above and data was not recorded. The thermocouple at T4 was damaged during ITT-2. Therefore, only the tunnel air temperatures at Site 1 (i.e. thermocouple T1), Site 2 (i.e. thermocouple T2) and Site 3 (i.e. thermocouple T3) from ITT-2 and the tunnel air temperatures at Site 4 (i.e. thermocouple T4) from ITT-1 were presented.

As can be seen in Figure 3.17, the temperature at Site 1 (T1) increased to 430 °C immediately after flame ignition. After that, temperatures slowly increased from 430 °C to 530 °C between 2 minutes and 10 minutes of the test. The TSL started combusting and increasing the air temperature at Site 1 to 616 °C. After the TSL combusted, the air temperature decreased to 500 °C. A similar pattern for the air temperature at Site 2 and Site 3 can be observed. On the other hand, the air temperature at Site 4 steadily increased from 26 °C to 100 °C.

3.3.2.2 Temperatures at Site 1

Figures 3.18 to 3.21 show concrete temperatures at Site 1 during ITT-1 and ITT-2. As previously discussed, thermocouples at P1, P2, P15 and P16 were shielded by the tunnel slab supports and as such did not provide data consistent with heat flow through the slabs. ITT- 1 and ITT-2 were performed with consistent ranges from an initial tunnel temperature (22 °C) to 120 °C for in 15 minutes. All figures summarize the upper bound and lower bound of the measured temperatures at each monitoring position.

Figure 3.18 presents the concrete temperatures measured at the inner surface of the concrete slab (i.e. the observation depth of 47mm from the outer edge of the slab; thermocouples at P3, P7 and P11). It can be seen that the temperature differences between the upper bound (up to 120 °C) and lower bound (up to 90 °C) is approximately 30 °C after 15 minutes of testing. According to the response of thermocouples P3, P7 and P11 during Test 2, temperatures did not significantly change after 8 minutes while the temperatures during ITT-1 kept increasing as seen in Figure 3.18.

As seen in Figure 3.19, the temperatures increased linearly between 2 minutes and 15 minutes of testing. It also shows that P12 (ITT-2) records the upper bound temperatures being somewhat higher than temperatures of the other monitoring points including P4, P8 (ITT-1and ITT-2) and P12 (ITT-1). The maximum temperature at 15 minutes was 90 °C for the upper bound and 80 °C for the lower bound, respectively. The observation depth was 37.5mm from the outer edge of the slab and 12.5mm from the inner edge of the slab.

As seen in Figures 3.20, the temperatures at the midpoint of the slab slowly increase as time increases. The temperature difference between the upper bound and lower bound after 15 minutes was 8 °C and the maximum upper bound temperature was 70 °C.

The temperatures measured at the outer surface of the concrete slab (i.e. a depth of 3mm from the outer edge of the concrete slab) are presented in Figure 3.21. The temperature increases from 23 °C to 49 °C during the 15 minutes of the test. The temperature between the upper bound and lower bound was only 4 °C.

3.3.2.3 Temperature at Site 2

Figures 3.22 to 3.25 present concrete temperatures measured at Site 2 during ITT-1 and ITT-2. Monitoring points P19, P20, P33 and P34 were not functioning due to the shielding of the tunnel supports as discussed previously.

Temperatures observed at the inner surface of the slab (i.e. a depth of 47 mm) at Site 2 can be seen in Figure 3.22. There were no significant temperature changes during the first minute where it can be an initial heating period and the temperatures gradually increased at a rate of 7.5 °C/min between 2 minutes and 10 minutes. The temperature gradients were then reduced from 7.5 °C/ min to 2 °C/min. The maximum temperature was recorded at 100 °C according to the upper bound.

Figure 3.23 presents the concrete temperatures observed at a depth of 37.5mm from the outer edge of the concrete slab. Temperatures at P22 are the upper bound and temperatures at P30 are the lower bound. The highest temperatures for the upper bound and the lower bound at 15 minutes of testing were 80 °C and 65 °C, respectively. Approximately 4 minutes was taken to heat up the thermocouples located at the midpoint of the slabs, as presented in Figure 3.24. It also can be seen that the temperatures reached 58 °C at a temperature gradient of 4 °C/min. The maximum temperature for the lower bound was 50 °C.

Thermocouples observed at the outer surface of the slab (i.e. at a depth of 3 mm from the outer edge of the slab) required 7 minutes of the initial heating period to register any rise and the temperature increased to 40 °C after 15 minutes of testing as presented in Figure 3.25.

3.3.2.4 Temperatures at Site 3

Figures 3.26 to 3.28 summarize the concrete temperature measured at Site 3 during ITT-1 and ITT-2. Thermocouples at P19, P20, P33 and P34 were shielded by the tunnel supports and as such did not provide data representative of heat flow through the slabs.

Figure 3.26 presents the temperature measured at the inner surface of the slab. There is a bit of difference in temperatures between the upper bound and the lower bound. The temperature differences vary from 5 °C to 20 °C corresponding to times of 2 minutes and 10 minutes after test initiation. The temperature difference decreases to 12 °C after 15 minutes of test.

From Figures 3.27 and 3.28, as the observation location moves to the outer surface of the slab, the temperature differences between the upper bound and the lower bound become smaller. The temperatures measured at the slab midpoint after 15 minutes of test range from 45 °C to 55 °C. Additionally, Figure 3.28 shows the temperature measured at the outer surface of the slab. The temperature differences from the upper bound and the lower bound is less than 1 °C.

3.3.2.5 Temperatures at Site 4

The concrete temperatures at Site 4 are presented in Figure 3.29. As noted for the other monitoring sites, thermocouples at P45, P46, P49 and P50 had no data consistent with heat flow through the slabs. Thermocouples at P47 and P48 are both plotted in Figure 3.29 corresponding to the temperatures measured at depths of 47 mm and 3 mm from the outer surface, respectively.

The temperatures measured at the depth of 47mm from the top of the concrete slab shows quite a gap between ITT- 1 and ITT- 2. At 15 minutes, the temperature difference is approximately 20 °C. Such a difference can be caused by variation of the TSL layer thickness and local differences in density. The consistent measured temperatures at P48 are presented in Figure 3.29.

3.3.3 Evaluation of TSL Effect

The measured temperatures in the TSL coated concrete (i.e. PT-1, ITT-2 and ITT-2) were plotted against the measured temperatures in the uncoated concrete (i.e. PT-2) to evaluate the TSL effect during the tunnel fire tests. The evaluation presents temperature differences in terms of depth of slabs and time. The evaluation with the depth of slabs has been made at 5 minutes, 10 minutes and 15 minutes after test initiation because the results from ITT-1 and ITT-2 were only considered for the 15 minutes of testing. Three locations, including the outer surface, midpoint and inner surface of slabs, have been evaluated during the 15 minutes periods of testing.

3.3.3.1 Temperature difference by depth

Figures 3.30 to 3.32 illustrate temperature differences between the TSL coated concrete and the uncoated concrete at Site 1, Site 2 and Site 3 at the 5 minute, 10 minute and 15 minute marks.

It can be seen from Figure 3.30 that the effect of TSL coating for fire insulation becomes larger as time increases. The temperatures at the inner surface of the slabs decrease approximately 69 % to 73 % due to the TSL coating. Also, a 60% temperature reduction can be seen at the midpoint of the concrete slab.

From Figure 3.31, the temperature difference, presented as the hatched area, is significantly reduced compared to the area at Site 1. The temperature reduction rates are approximately 60 % at the inner surface of the slab and about 50 % at the midpoint of the slab. From Figure 3.32, the temperature reduction rates are approximately 63 % at 5 minutes, 47 % at 10 minutes and 50 % at 15 minutes at the inner surface of the slab. Reduction rates of 20 %, 35 % and 40 % for 5 minutes, 10 minutes and 15 minutes of the test can be calculated at the middle of the slab.

To conclude, the TSL coating significantly reduces the heat transmitted through the concrete. As a result, the temperature in the concrete slab can be reduced up to 70 % by the insulating effect of an applied TSL coating.

3.3.3.2 Air temperature difference by time

Figure 3.33 shows air temperature differences measured with the TSL coated concrete slabs (from PT-1, ITT-1 and ITT-2) and the uncoated concrete slabs (from PT-2) at Site 1, Site 2 and Site 3 during 15 minutes of testing. The temperature difference is presented as the hatched area. As seen in Figure 3.33 a), the air temperatures measured with the TSL coated concrete slabs during ITT-2 are higher than these measured with the uncoated concrete slabs during PT-1. The same results can be observed at Site 2 and Site 3 in Figures 3.33 b) and 3.33 c), respectively. Immediately after ignition, the air temperature difference in the tunnel is approximately 150 °C due to the TSL combusting (1st combusting). This difference decreases to zero at 8 minutes as the tunnel temperature measured with the uncoated concrete slabs increases. On the other hand the air temperature measured with the TSL coated concrete slabs is constant with some fluctuation. Between 10 minutes and 14 minutes, there is another combusting process (2nd

combusting). In this period, the air temperature difference is approximately 100 °C. After 14 minutes of testing, the air temperature in the tunnel becomes similar for both cases.

A similar pattern can be observed at Site 2. The air temperature differences measured with the TSL coated and uncoated concrete slabs are ranged from 100 to 250 °C. The largest difference, of 250 °C, was observed immediately after flame ignition. The smallest differences can be measured at the 8 minute mark of the test. In contrast to the results at Sites 1 and 2, the air temperature differences are constant and approximate 220 °C at Site 3.

3.3.3.3 Observation of TSL coating before and after the fire test

It was observed that the intact TSL was damaged by combustion during the tunnel fire tests. The TSL combustion occurs immediately after the ignition. During and after the fire tests, TSL forms two layers depicted in Figure 3.34 b). These are the intact TSL and the exfoliation of TSL (referred to a char barrier). The exfoliation process can explained as follows. When powdered graphite and/or vermiculite are homogeneously mixed into the TSL substrate and are exposed to high temperature, they undergo a physical change that includes large volumetric growth through release of water of hydration, creating a highly porous and lower density matrix that possesses low thermal conductivity. The char barrier, therefore, must be taken account for the FE analysis as an additional layer because it would have different thermal and physical properties. Additional information about the char barrier is presented in Chapter 4. In addition, the exfoliation of TSL can be also observed at both Site 1 and Site 2. However, no exfoliation was observed at Site 3. The locations of exfoliation can be found in Appendix B.

3.4 SUMMARY AND CONCLUSIONS

Two preliminary tunnel tests (PT-1 and PT-2) and detailed instrumented tunnel tests (ITT-1 and ITT-2) were conducted to determine thermal characteristics of TSL in a tunnel fire and the possibility of TSL fire protection for existing concrete tunnels. TSL appears to have an insulating effect on the concrete slabs. Uncoated slabs exceed 380 °C at several locations where the temperatures of the coated slabs are less than 260°C. Based on the results from the preliminary tunnel tests and the detailed instrumented tunnel tests, it can be concluded as follows:

Preliminary Tunnel Tests

1) The highest uncoated concrete temperature recorded was 617 °C after 25 minutes of testing. After 25 minutes, thermal cracks and spalling were observed on the first uncoated concrete slab.
2) On the other hand, TSL coated concrete temperatures were recorded at less than 240 °C at Site 1, Site 2, and Site 3. Also, there was no observation of thermal cracks and spalling but extreme burning on the TSL surface could be found.
3) The TSL spray with a thickness of 4mm prevented concrete structures from thermal cracks or spalling during a fire producing a temperature less than 700 °C.

Detailed Instrumented Tunnel Tests

1) TSL combusting causes the increase of the air temperature in the tunnel.
2) The detailed instrumented tunnel tests provide a comprehensive understanding of thermal distribution or heat propagation through the TSL coated concrete slabs.

3) TSL can protect concrete structures against fire and keep the concrete surface temperature under 380 °C which is the RWS safety limit for concrete surfaces.

Based on the evaluation of TSL effects during the CAN/ULC-S102-M88 test, it can be concluded that:

1) The insulation effect of a TSL coating causes significant reduction of the temperature transmitted to the concrete slab.
2) This experimental study shows that a TSL has excellent characteristics as an insulating material for existing concrete tunnels.

Table 3.1 Monitoring positions of thermocouples for the preliminary tests (PT-1 and PT-2)

TEST	SITE 1 (750mm)	SITE 2 (1560mm)	SITE 3 (2360mm)
PT-1 TSL coated slabs (avg. thickness 38mm+ 4mmTSL)	Ch.1. 5mm Ch.2 20mm Ch.3 38mm Ch.4 42mm	Ch.5 4mm Ch.6 22mm Ch.7 38mm Ch.8 42mm	Ch.9 4mm Ch.10 22mm Ch.11 35mm Ch.12 42mm
PT-2 Uncoated concrete slabs (avg. thickness 38mm)	Ch.1 5mm Ch.2 19mm Ch.3 30mm Ch.4 38mm	Ch.5 4mm Ch.6 20mm Ch.7 30mm Ch.8 38mm	Ch.9 4mm Ch.10 20mm Ch.11 30mm Ch.12 38mm

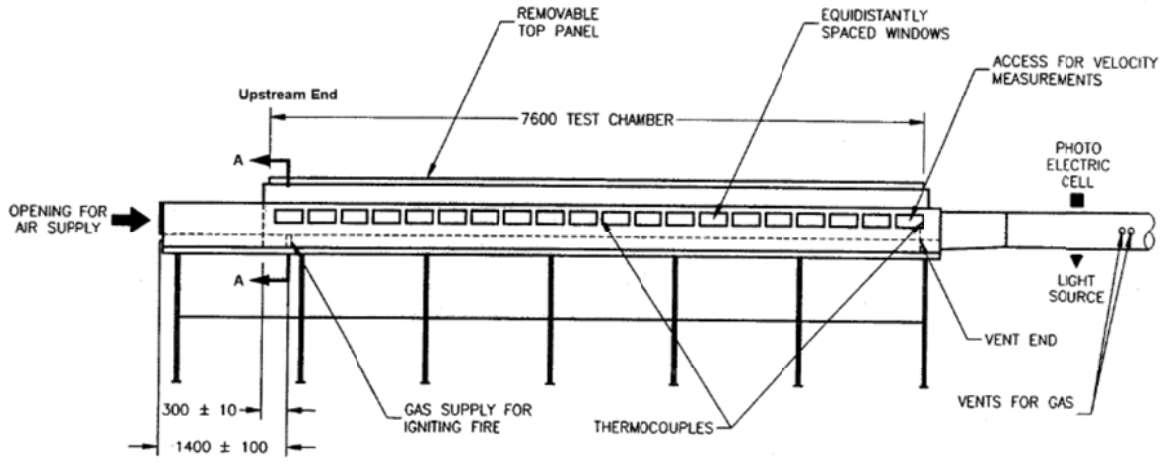

a) Side view

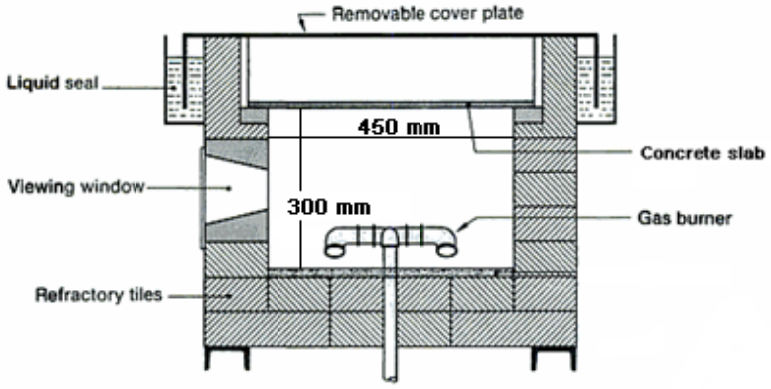

b) Section A-A

Figure 3.1 Schematic diagrams of CAN/ULC-S102-M88 testing tunnel
(Laboratories of Canada, 2003)

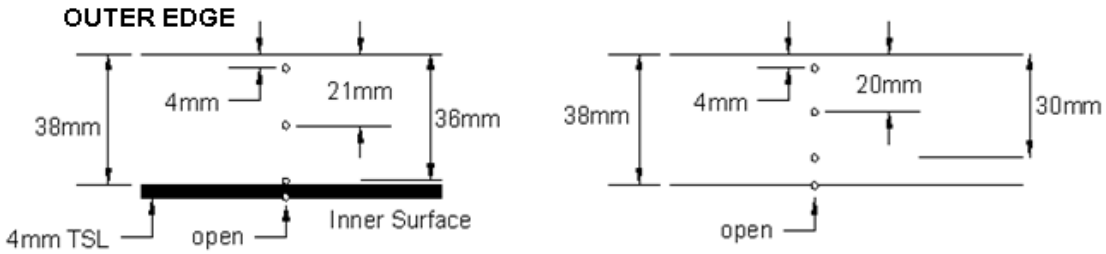

(a) Coated Concrete Slab (b) Uncoated Concrete Slab

Figure 3.2 Average thermocouple positions for the preliminary tunnel tests (PT-1 and PT-2)

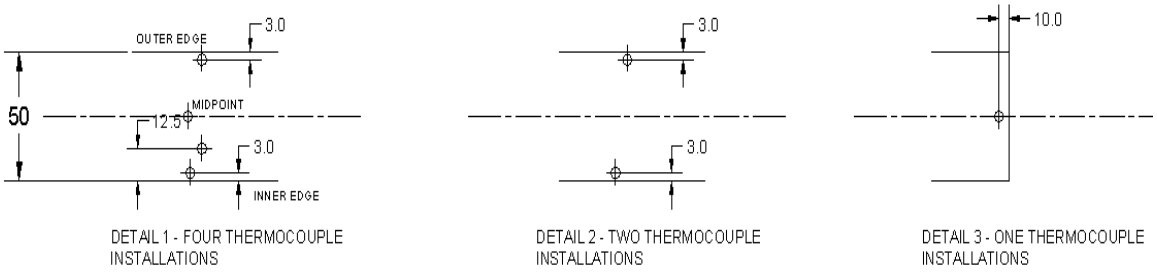

Figure 3.3 Thermocouple positions for the detailed instrumented tunnel tests (ITT-1 and ITT-2)

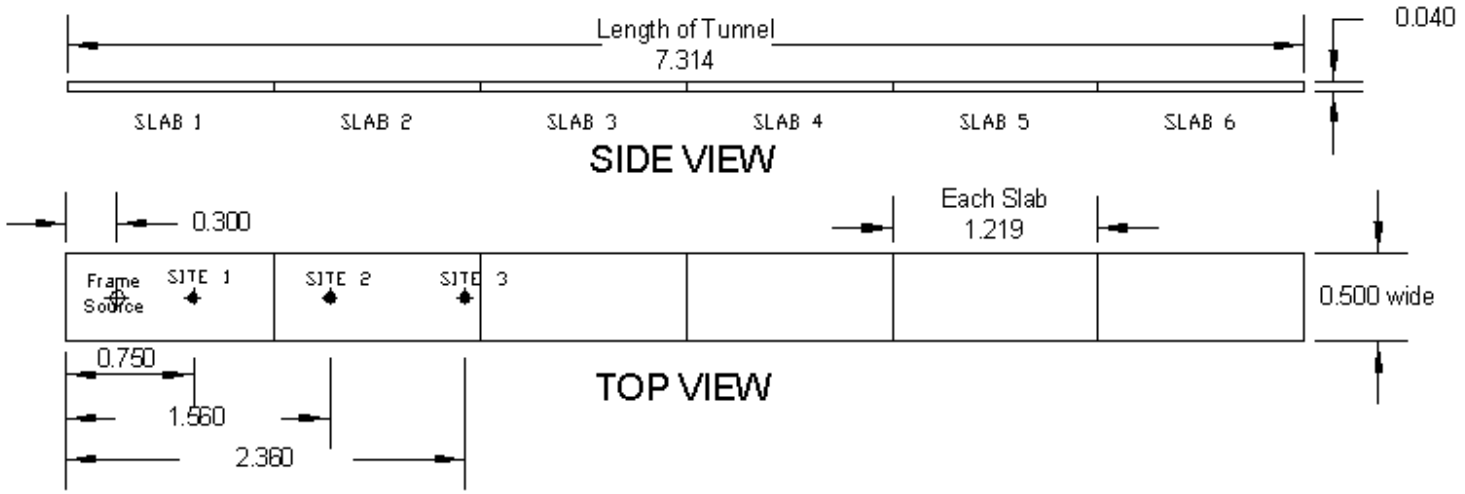

Channel Sequence (From Top to Bottom)

SITE	Channels
1	1,2,3,4
2	5,6,7,8
3	9,10,11,12

Unit = meter

Figure 3.4 Instrumentation plan for PT-1 and PT-2

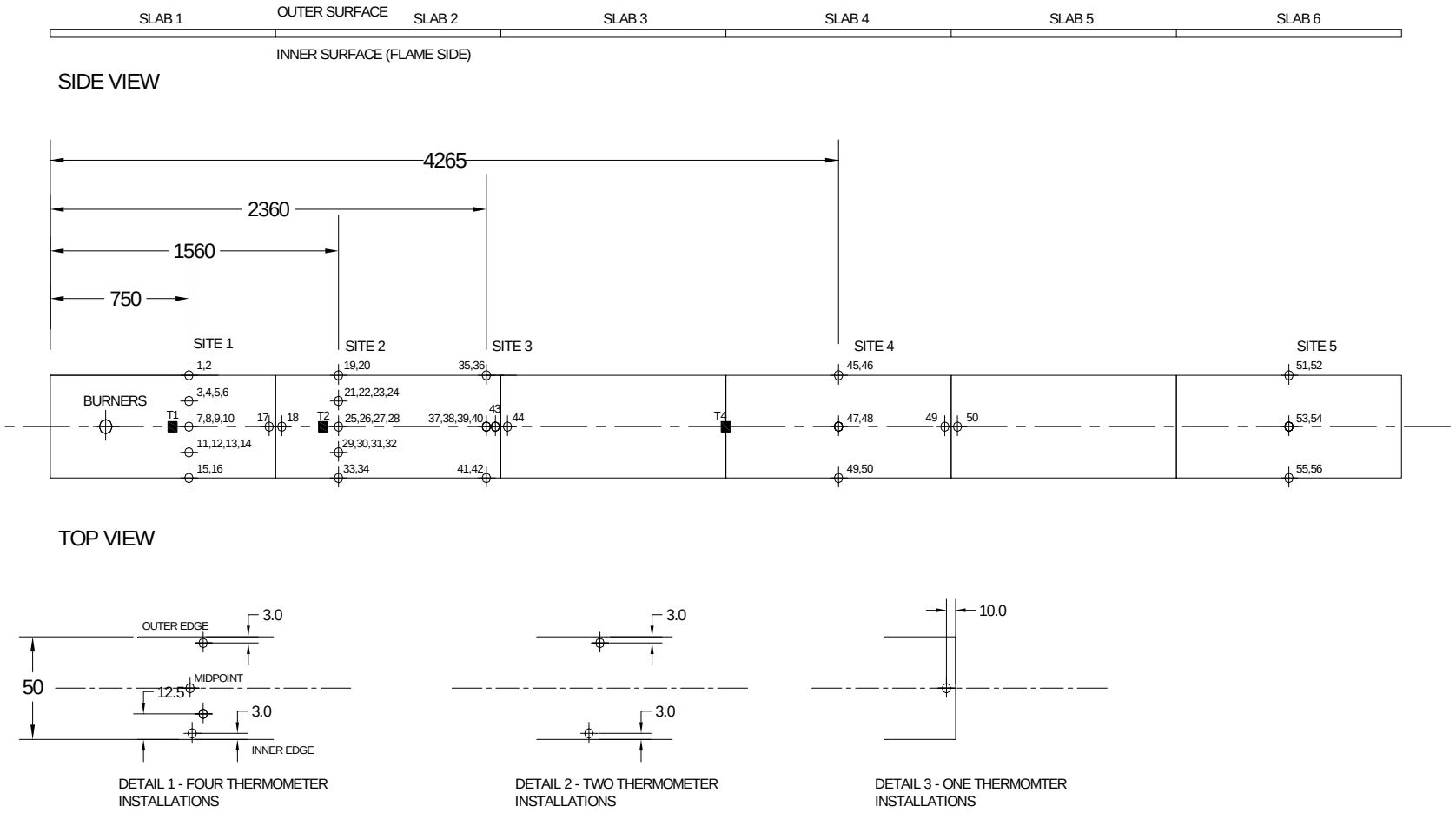

Figure 3.5 Instrumentation plan for ITT-1

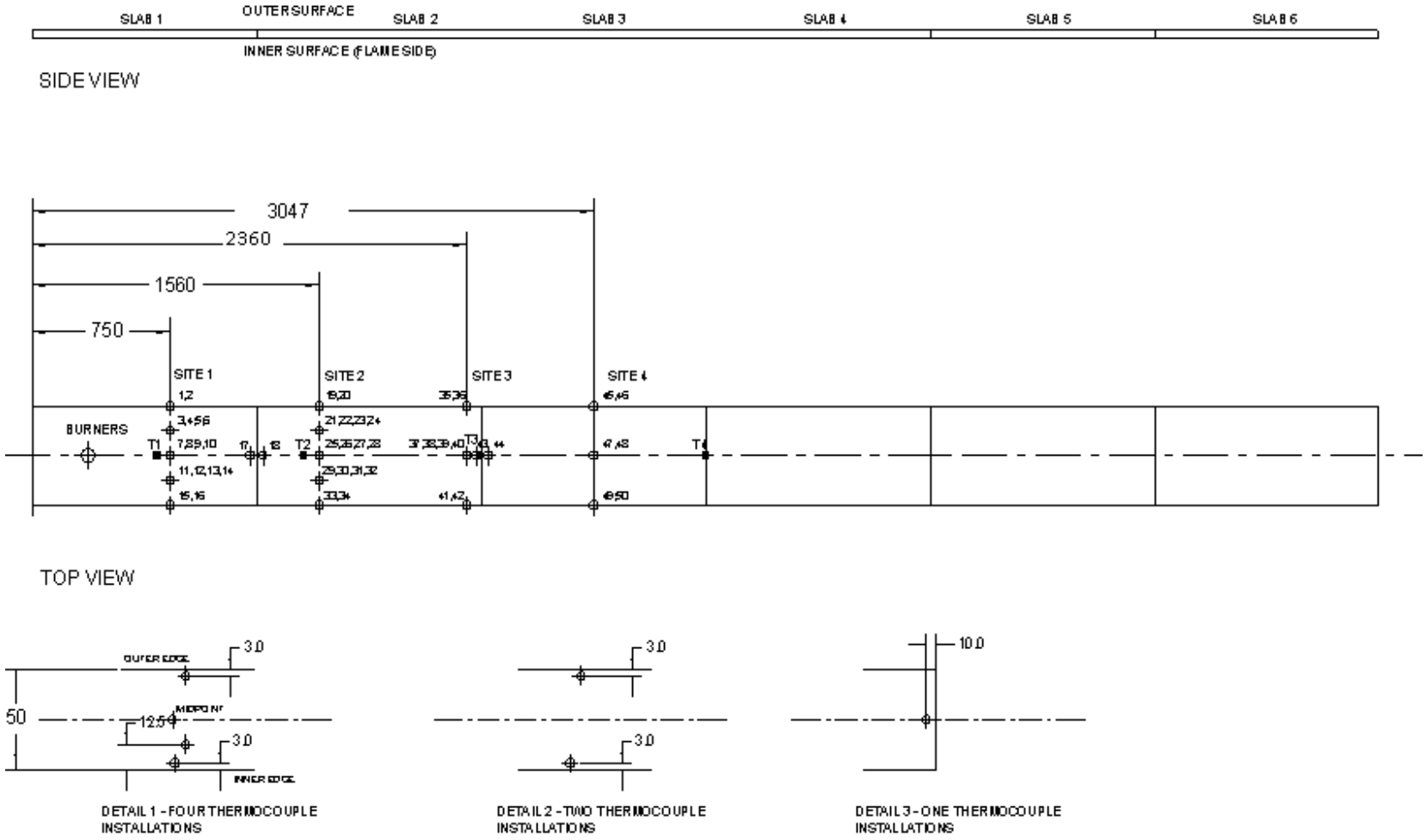

Figure 3.6 Instrumentation plan for ITT-2

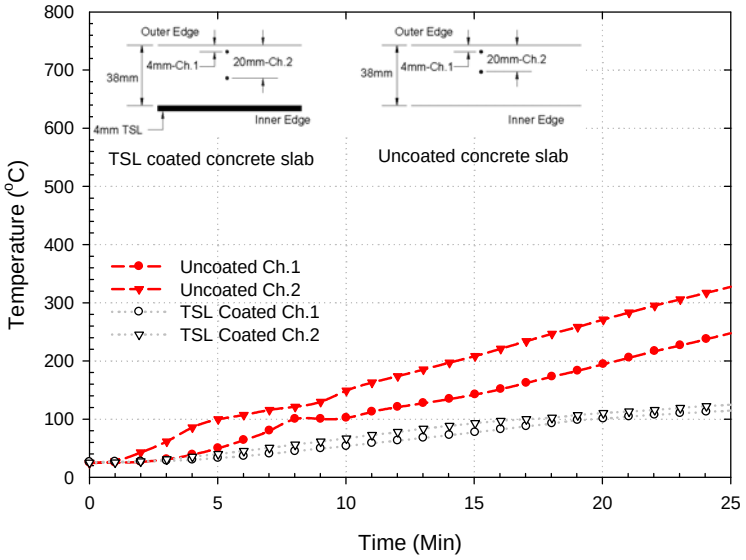

(a) Ch.1 and Ch.2

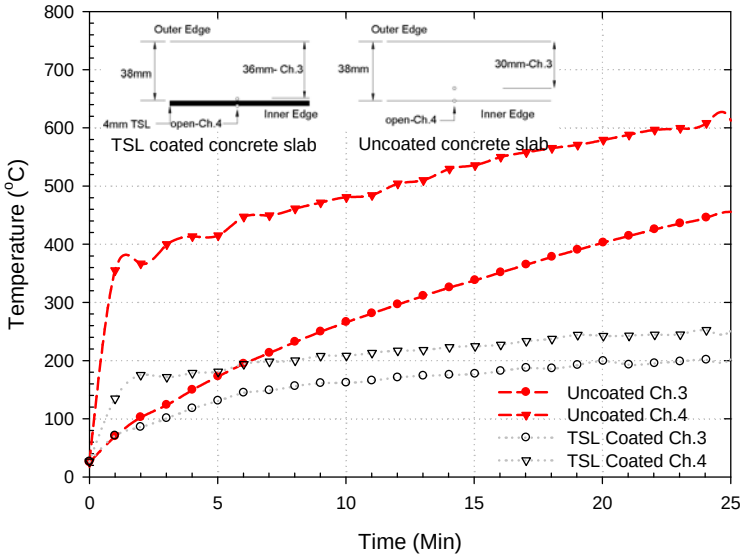

(b) Ch.3 and Ch.4

Figures 3.7 Temperatures versus time at site 1 for PT-1 and PT-2

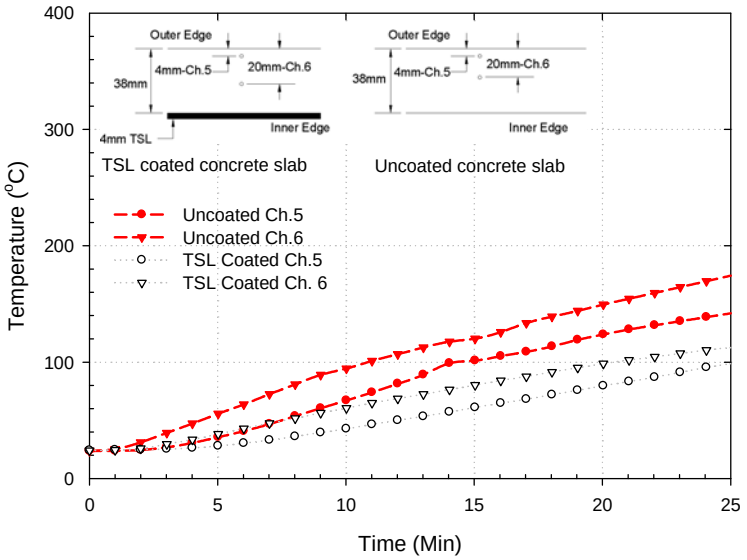

(a) Ch.5 and Ch.6

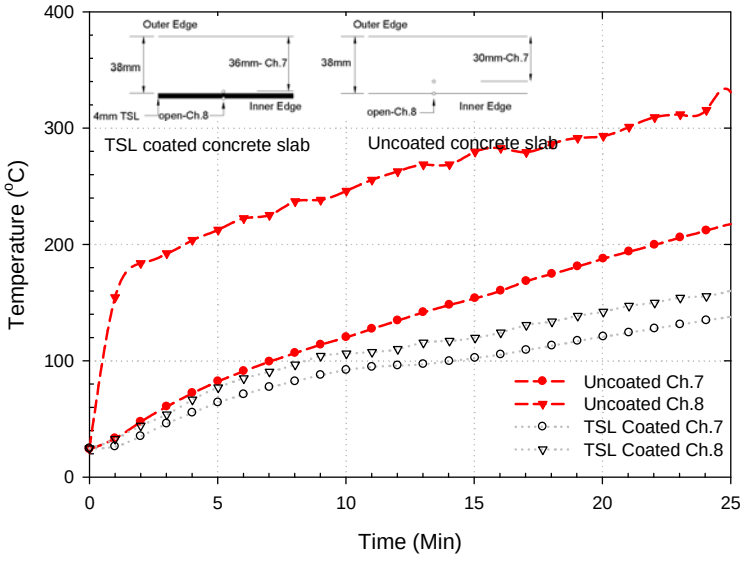

(b) Ch.7 and Ch.8

Figures 3.8 Temperatures versus time at site 2 for PT-1 and PT-2

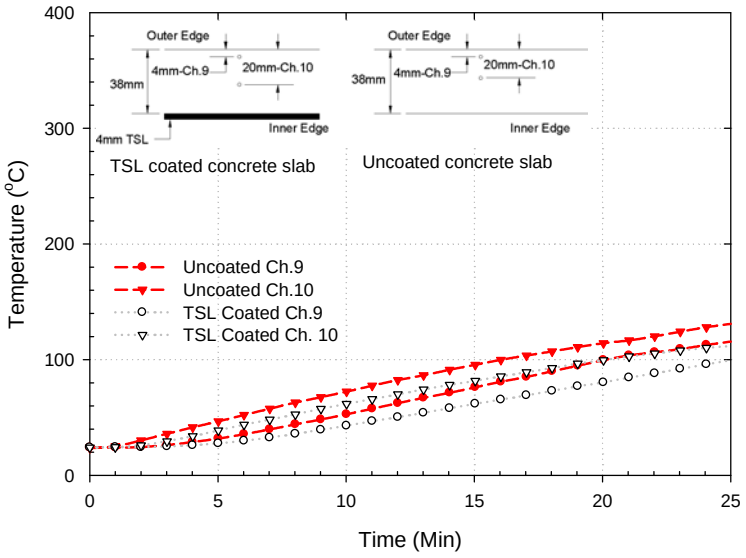

(a) Ch. 9 and Ch.10

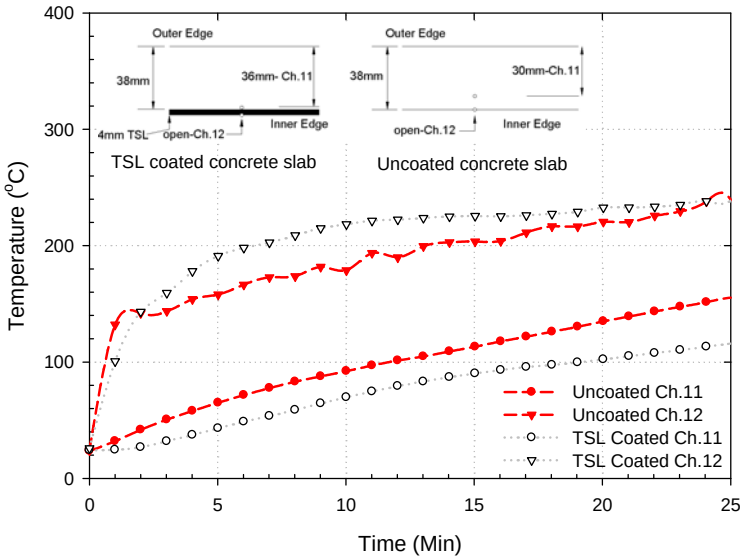

(b) Ch. 11 and Ch. 12

Figures 3.9 Temperatures versus time at site 3 for PT-1 and PT-2

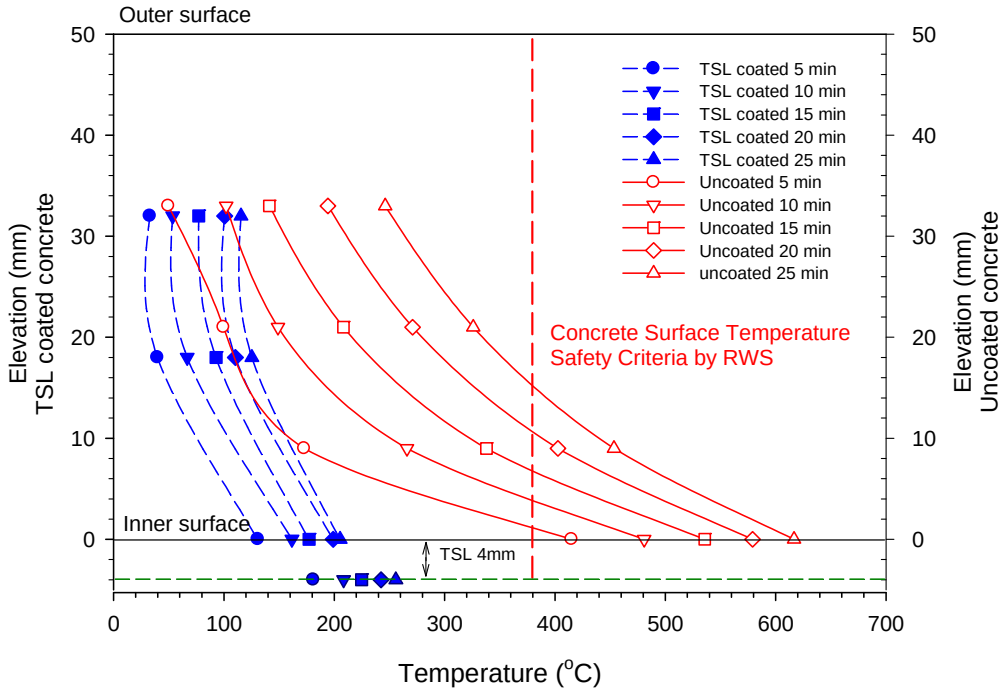

Figure 3.10 Temperatures versus depth at site 1

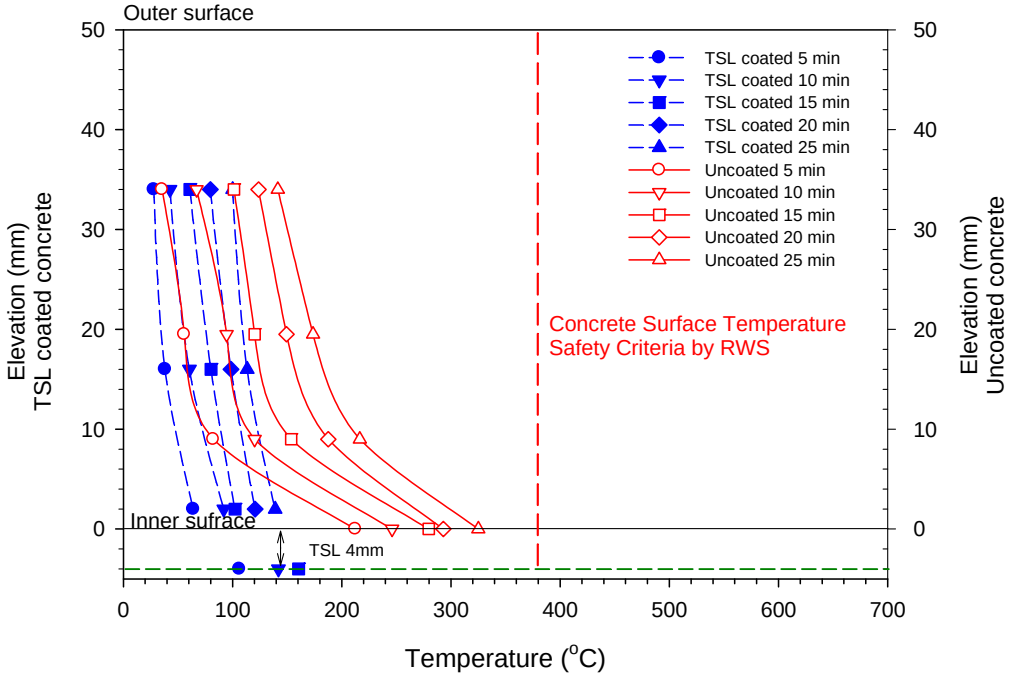

Figure 3.11 Temperatures versus depth at site 2

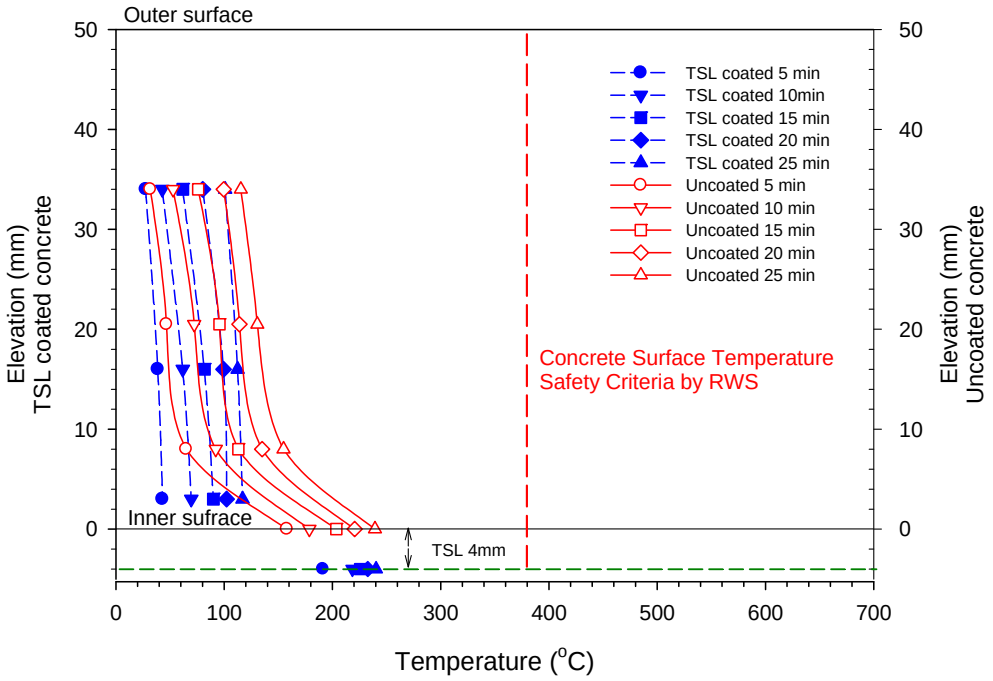

Figure 3.12 Temperatures versus depth at site 3

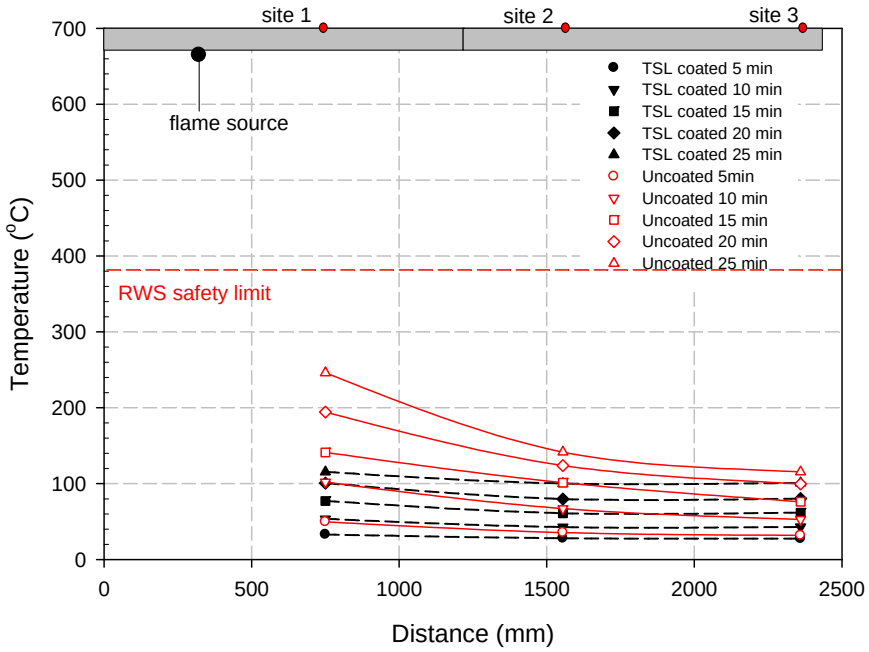

Figure 3.13 Longitudinal temperature distribution: outer surface (i.e. top of slabs)

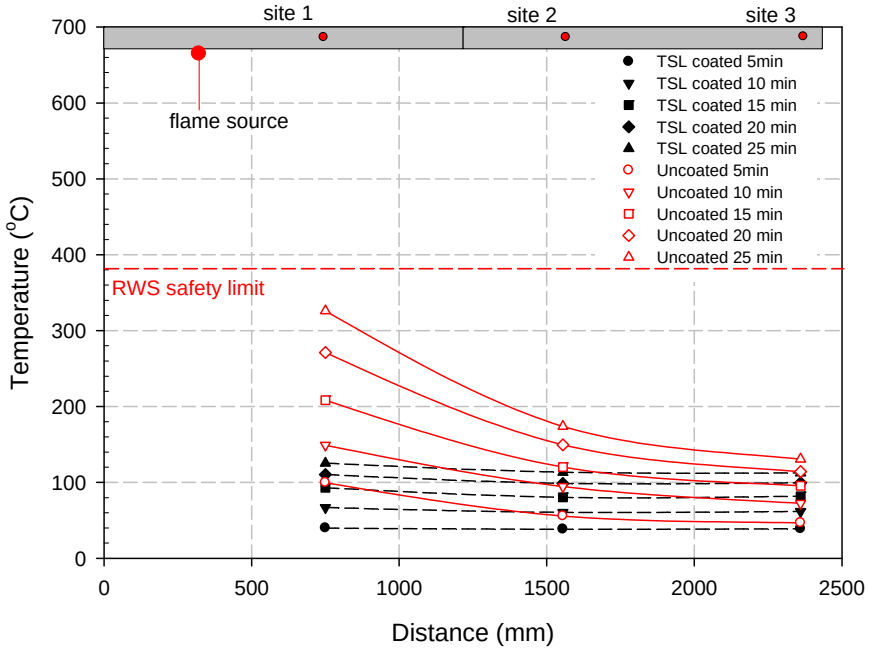

Figure 3.14 Longitudinal temperature distribution: midpoint of slabs

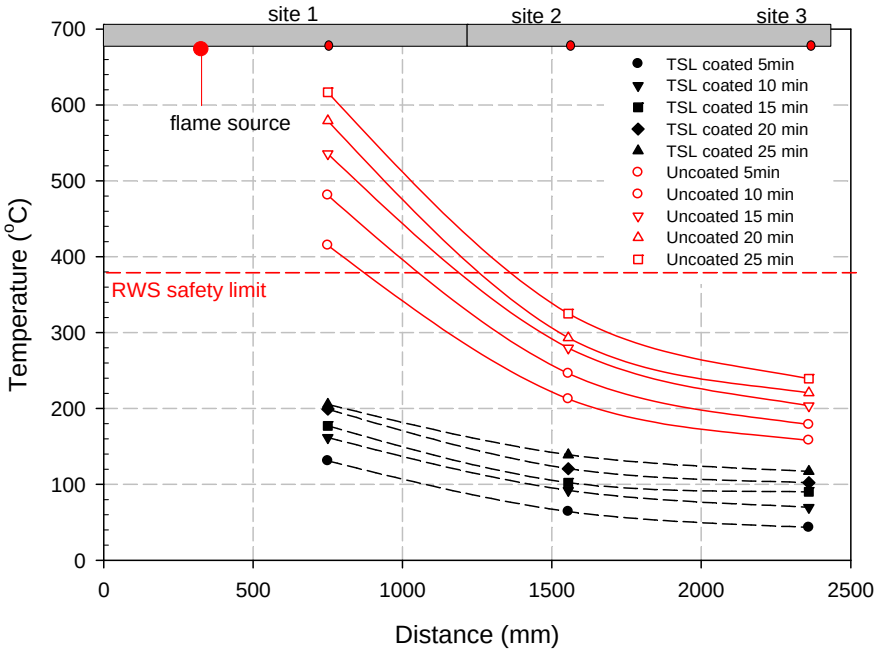

Figure 3.15 Longitudinal temperature distribution: inner surface (i.e. exposed to flame source)

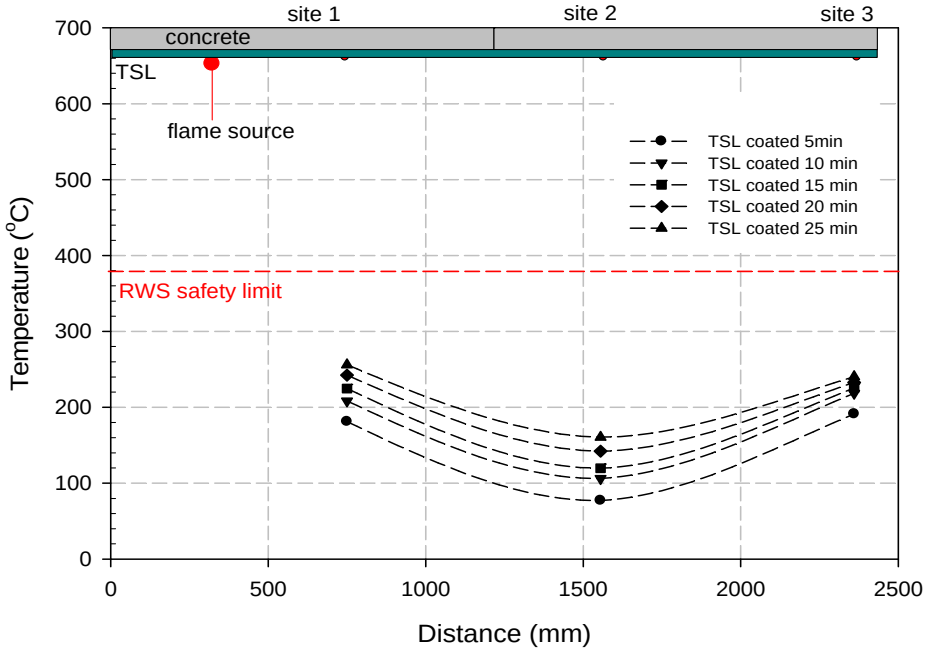

Figure 3.16 Longitudinal temperature distribution: in TSL

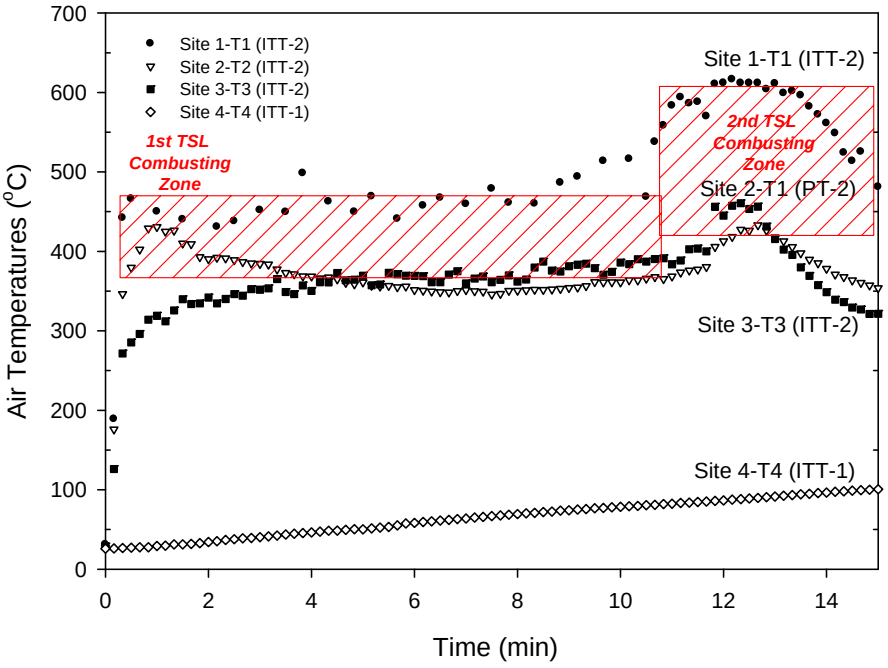

Figure 3.17 Tunnel air temperatures during ITT-1 and ITT-2

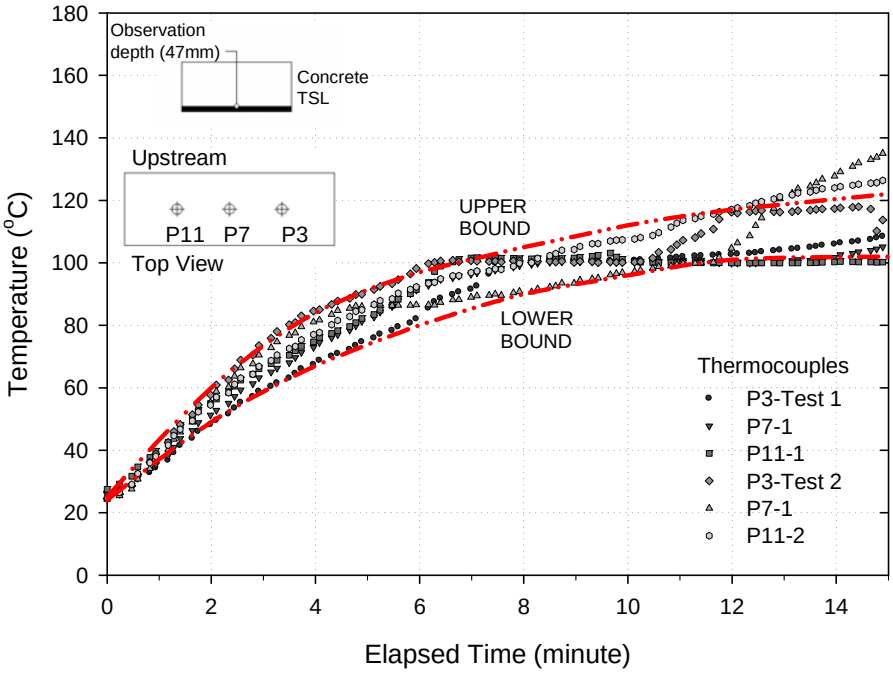

Figure 3.18 Concrete temperatures for ITT-1 and ITT-2 at thermocouples P3, P7 and P11 located at a depth of 47mm from outer edge of concrete slab – site 1

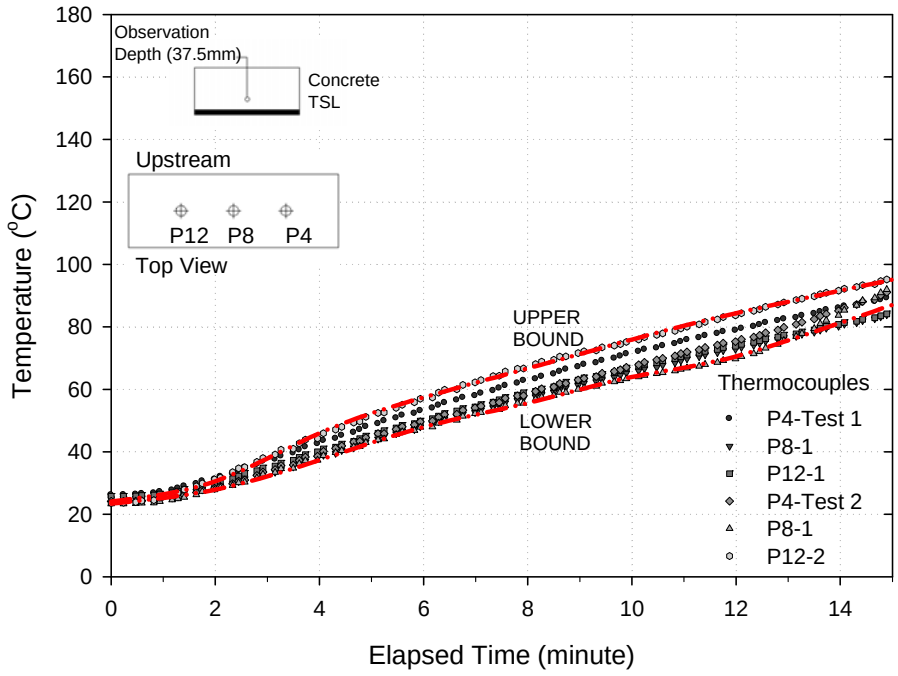

Figure 3.19 Concrete temperatures for ITT-1 and ITT-2 at thermocouples P4, P8 and P1 located at a depth of 37.5mm from the top of concrete slab – site 1

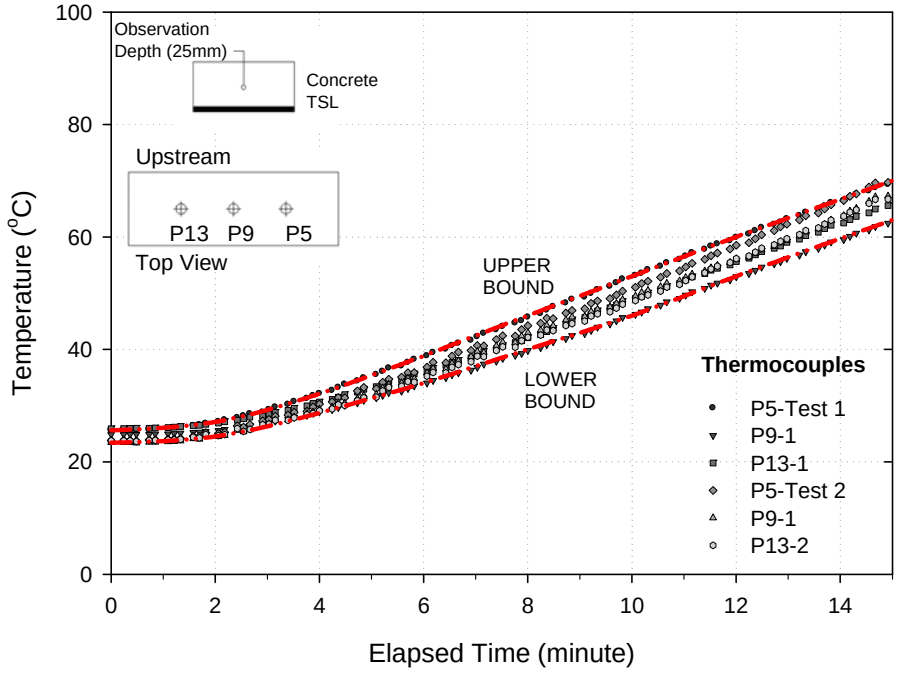

Figure 3.20 Concrete temperatures for ITT-1 and ITT-2 at thermocouples P5, P9 and P1 located at a depth of 25mm from the top of concrete slab – site 1

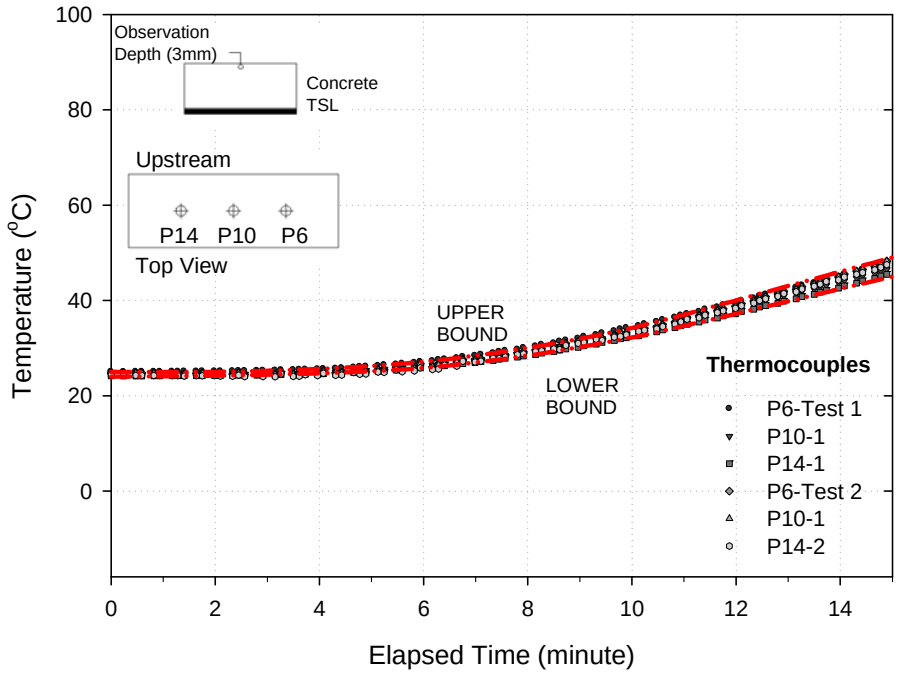

Figure 3.21 Concrete temperatures for ITT-1 and ITT-2 at thermocouples P6, P10 and P14 located at a depth of 3mm from the top of concrete slab – site 1

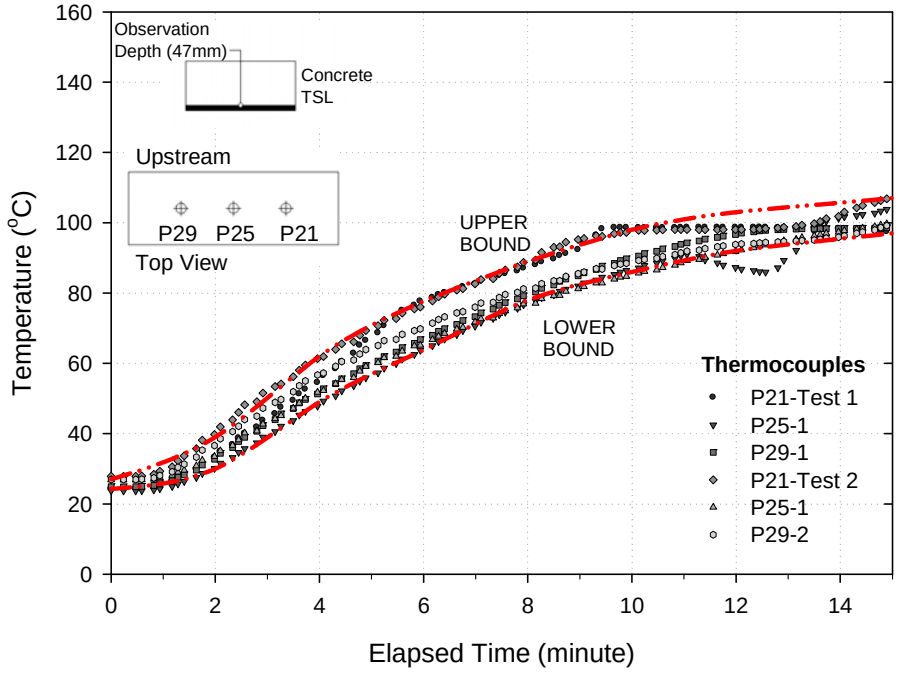

Figure 3.22 Concrete temperatures for ITT-1 and ITT-2 at thermocouples P21, P25 and P29 located at a depth of 47mm from the top of concrete slab – site 2

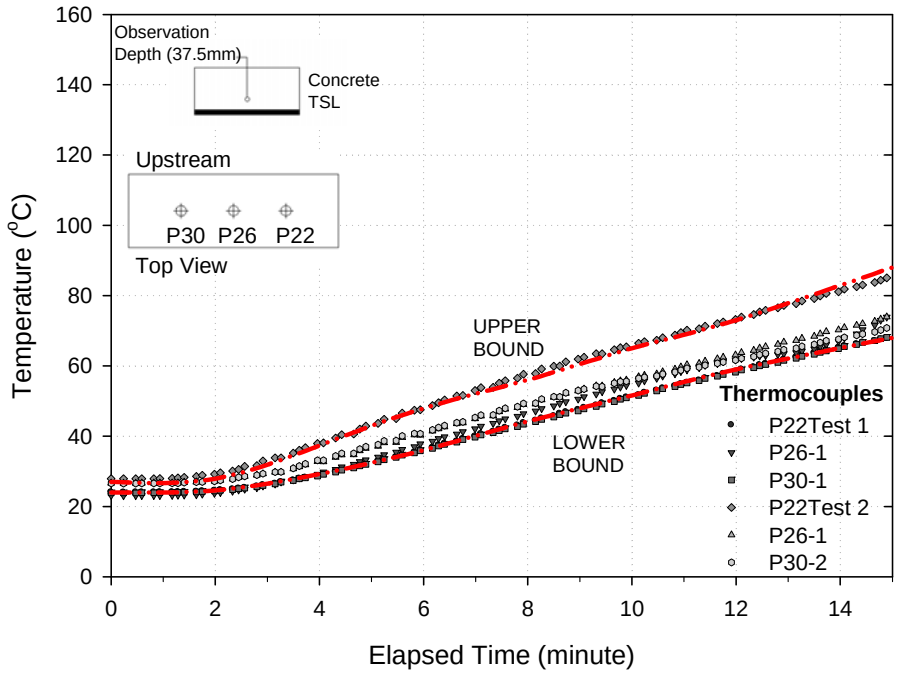

Figure 3.23 Concrete temperatures for ITT-1 and ITT-2 at thermocouples P22, P26 and P30 located at a depth of 37.5mm from the top of concrete slab – site 2

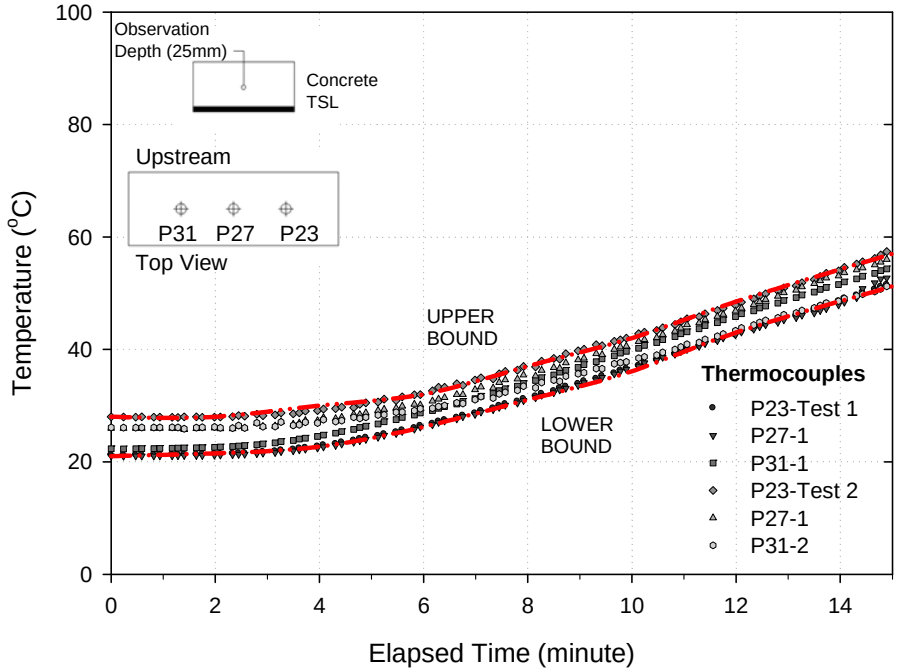

Figure 3.24 Concrete temperatures for ITT-1 and ITT-2 at thermocouples P23, P27 and P31 located at a depth of 25mm from the top of concrete slab –site 2

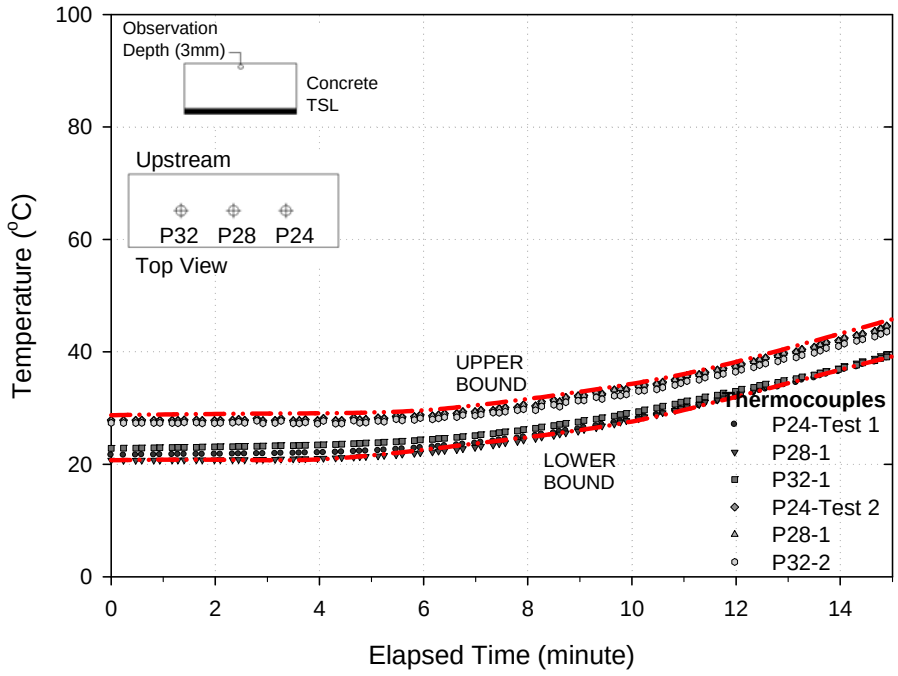

Figure 3.25 Concrete temperatures for ITT-1 and ITT-2 at thermocouples P24, P28 and P32 located at a depth of 3mm from the top of concrete slab – site 2

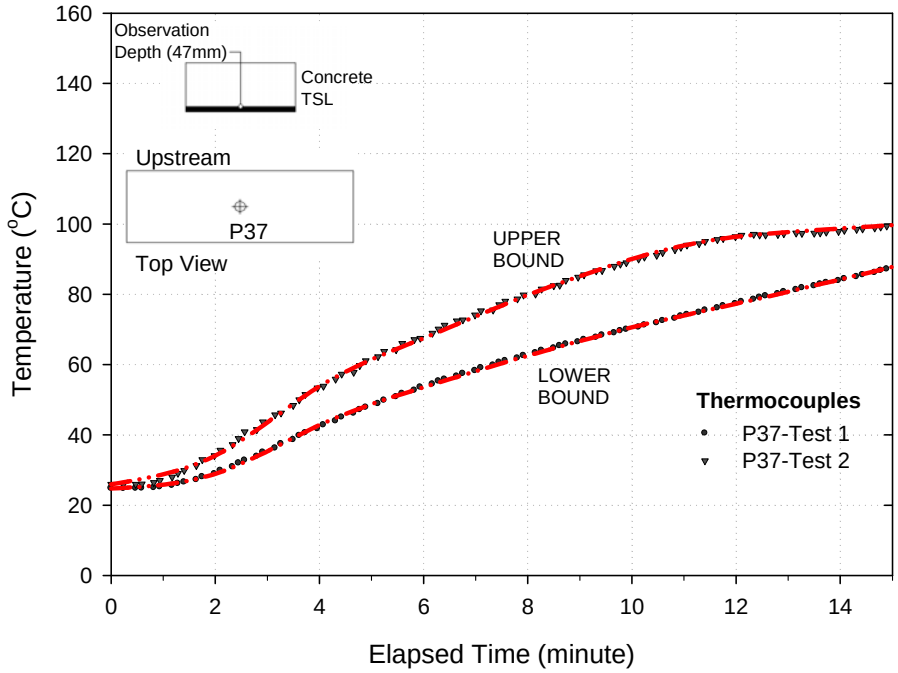

Figure 3.26 Concrete temperatures for test 1 and test 2 at thermocouples P37 located at a depth of 47mm from the top of concrete slab – site 3

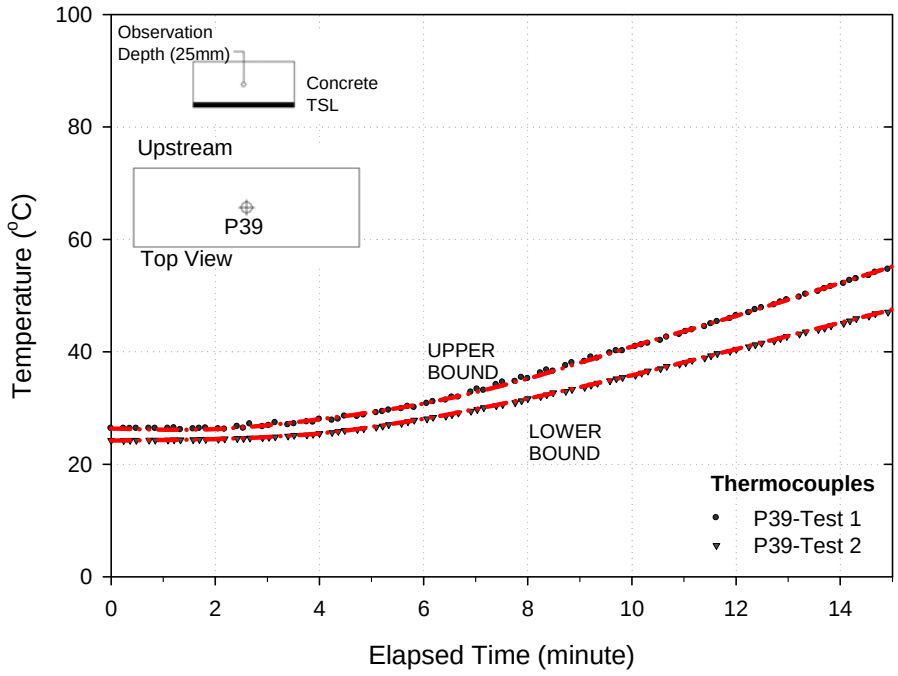

Figure 3.27 Concrete temperatures for test 1 and test 2 at thermocouples P39 located at a depth of 25mm from the top of concrete slab – site 3

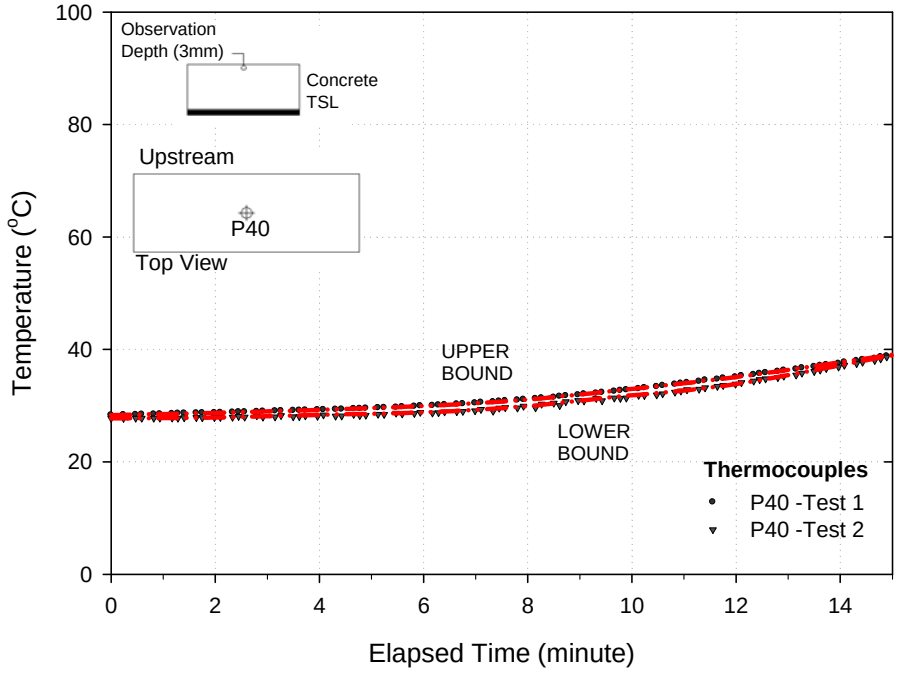

Figure 3.28 Concrete temperatures for test 1 and test 2 at thermocouples P40 located at a depth of 3mm from the top of concrete slab – site 3

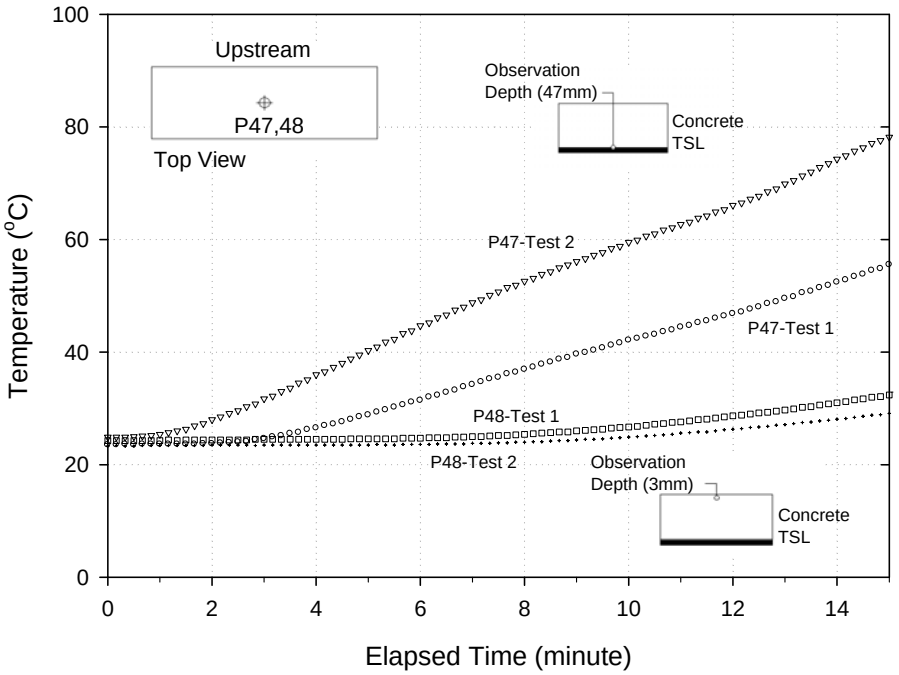

Figure 3.29 Concrete temperatures for ITT-1 and ITT-2 at thermocouples P47 (47mm depth) and P48 (3mm depth from Outer Edge) located at site 4

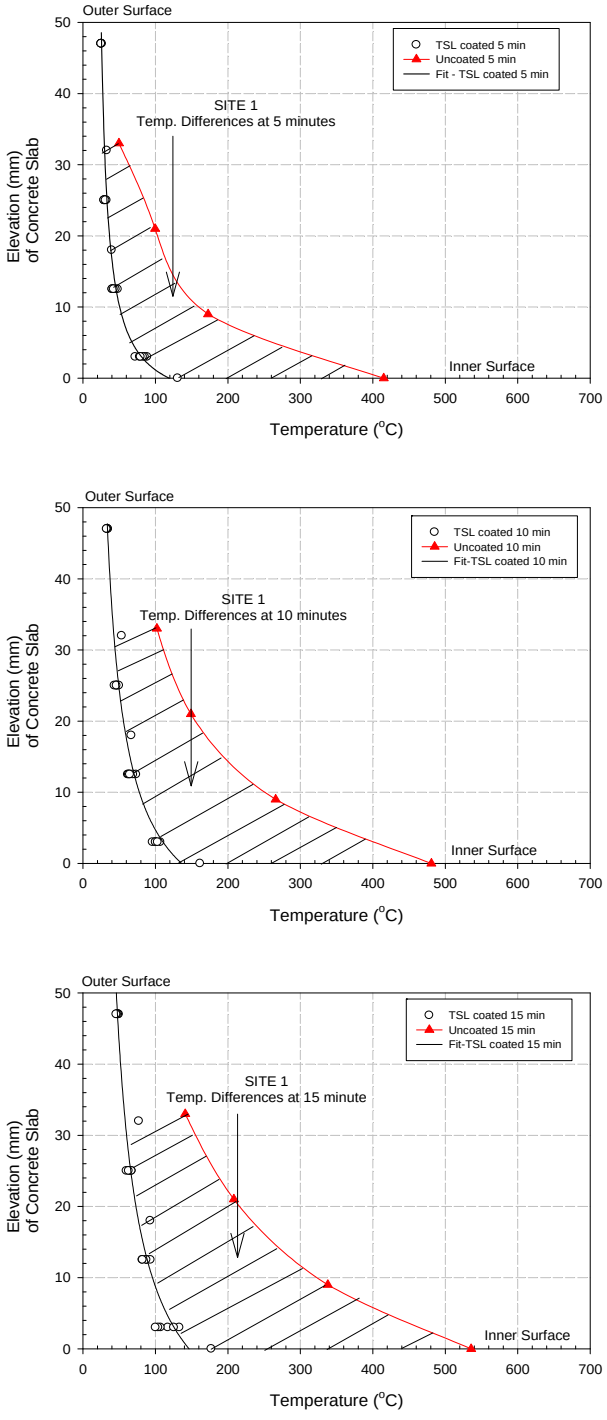

Figure 3.30 Temperature differences between TSL-coated concrete and uncoated concrete at site 1 (top to bottom: 5min, 10min and 15min)

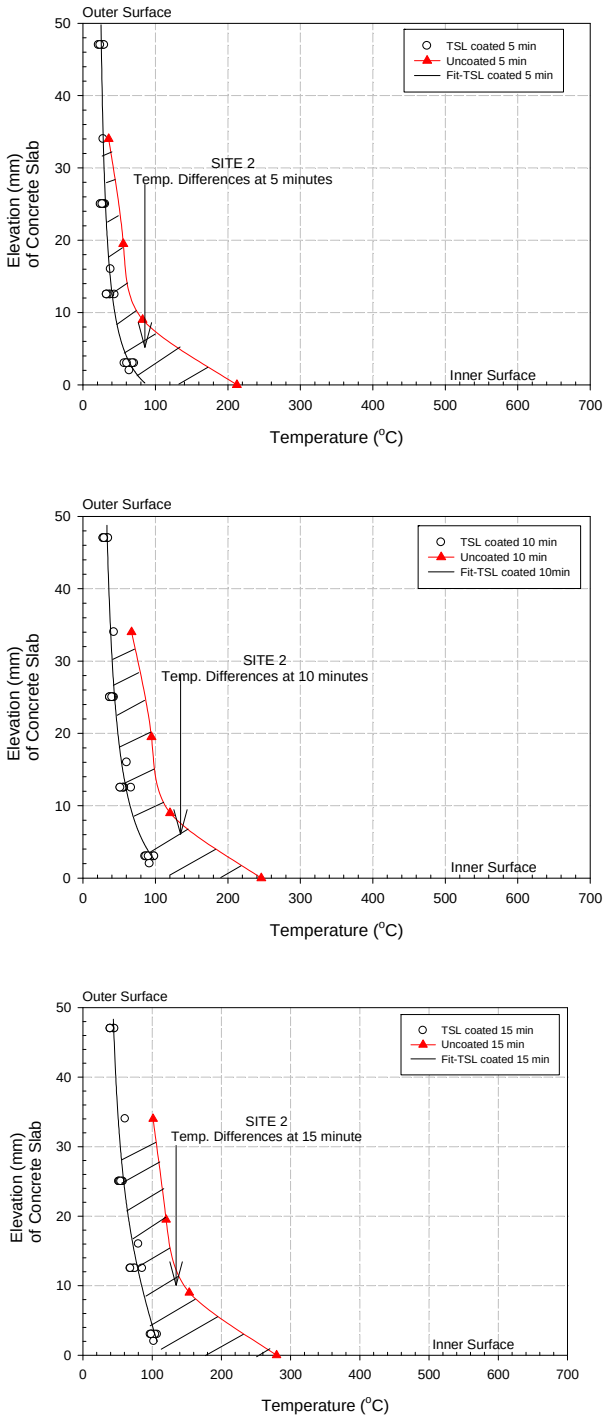

Figure 3.31 Temperature differences between TSL-coated concrete and uncoated concrete at site 2 (top to bottom: 5min, 10min and 15min)

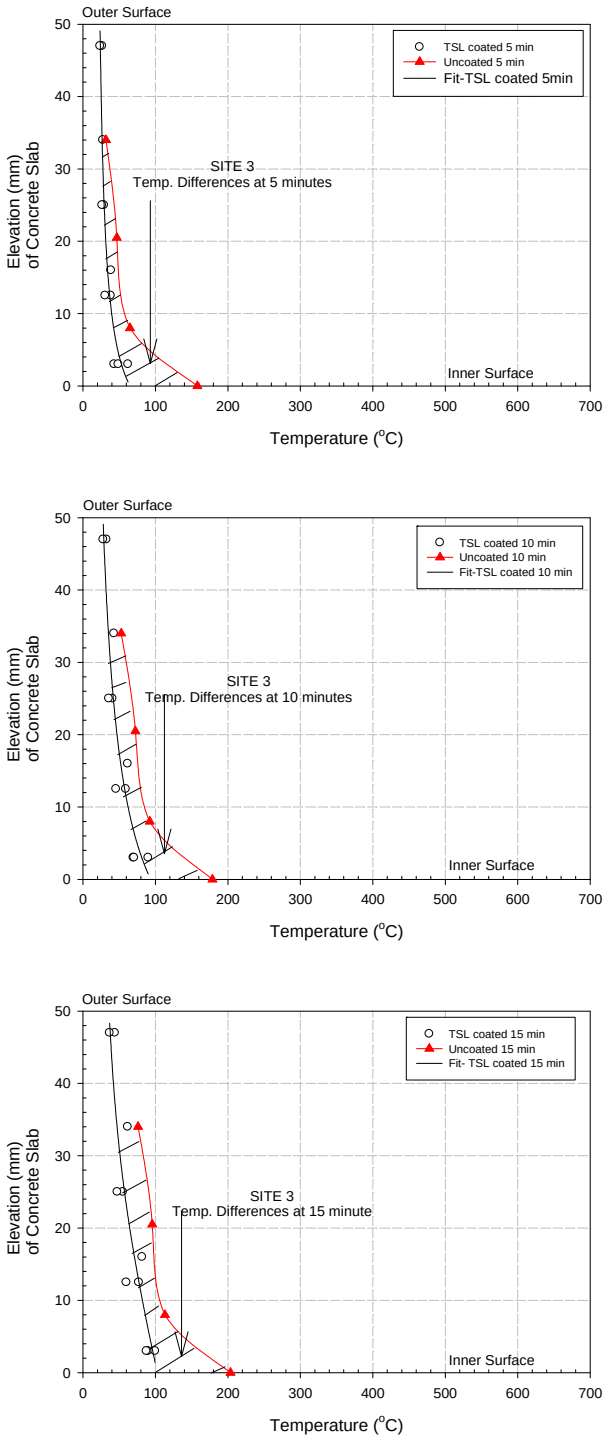

Figure 3.32 Temperature differences between TSL-coated concrete and uncoated concrete at site 3 (top to bottom: 5min, 10min and 15min)

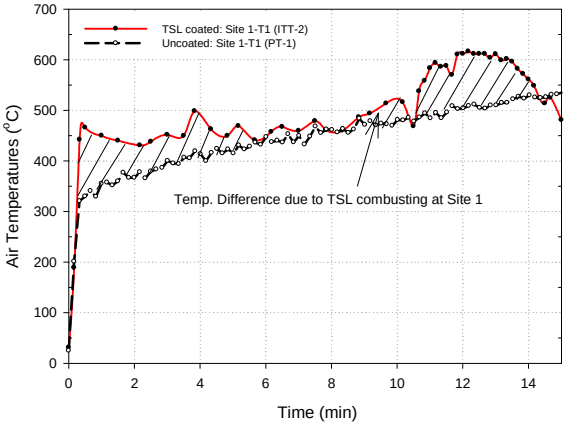

a) Site 1

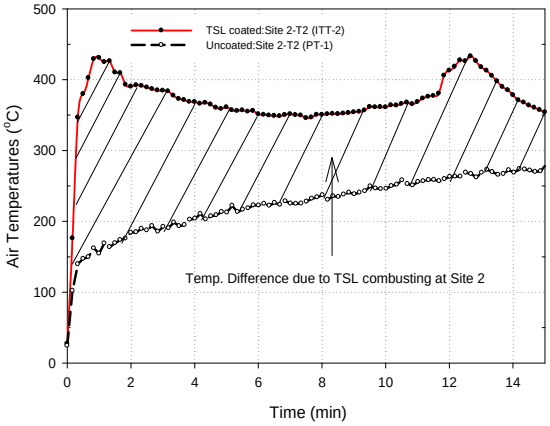

b) Site 2

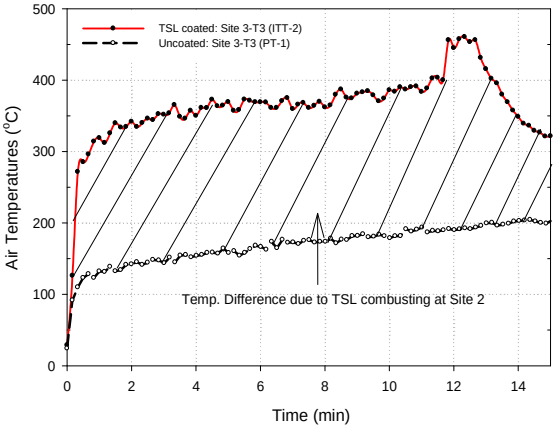

c) Site 3

Figure 3.33 Air temperature difference measured with the TSL coated concrete and the uncoated concrete at sites 1, 2 and 3

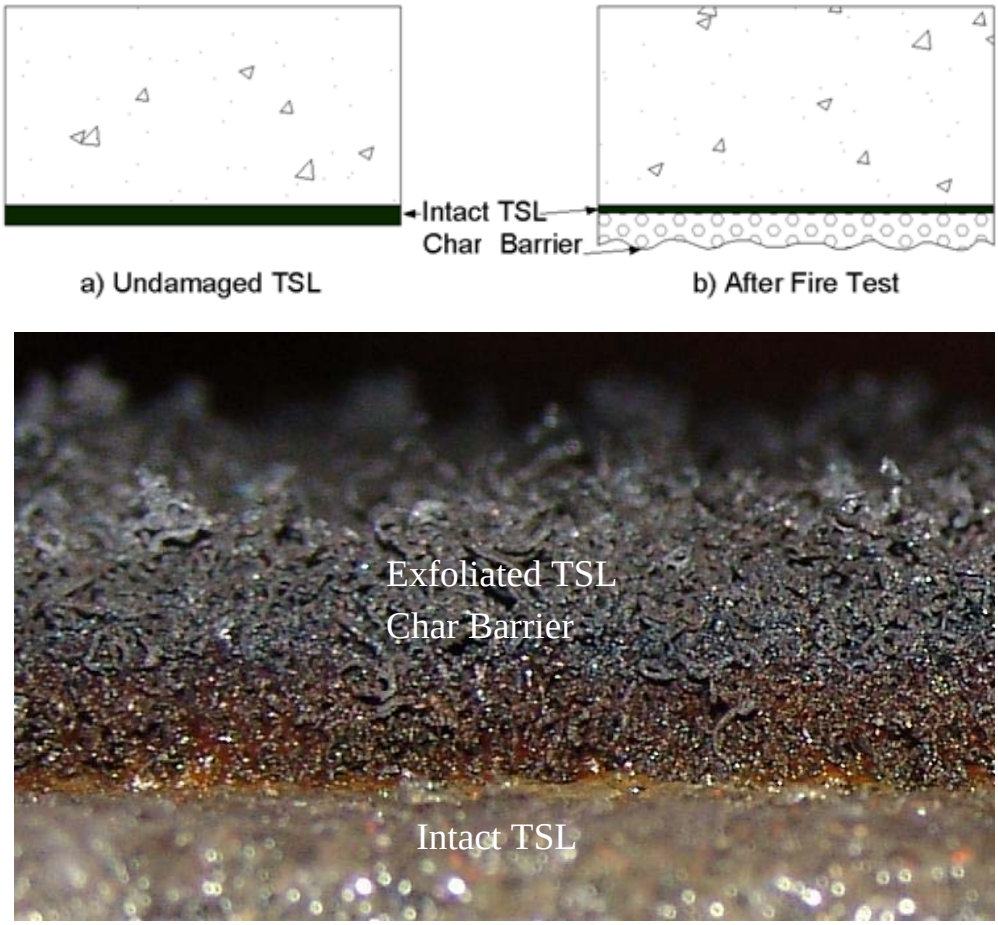

Figure 3.34 Observation of the TSL before and after the fire tests

CHAPTER 4

THERMAL ANALYSIS OF TSL COATED CONCRETE SLABS

4.1 INTRODUCTION

This chapter presents results of thermal finite element (FE) analyses of TSL coated concrete slabs during the standard CAN/ULC-S102-M88 tunnel fire tests. The finite element software Temp/W was used to interpret the fire test results reported in Chapter 3. The primary objectives of the analyses were to interpret the concrete and tunnel temperatures reported in Chapter 3 for uncoated concrete slabs during standard fire tests (CAN/ULC-S102-M88) and to determine the thermal properties of the TSL and the char barrier that forms on exposure to flame. The following sections in this chapter (a) describe the numerical methodology, (b) compare numerical results with the measured temperature performance of uncoated concrete slabs during the fire tests, and (c) summarize the conclusions.

4.2 METHODOLOGY

Numerical modeling with Temp/W requires specification of the thermal properties of the materials to be modelled as well as the boundary conditions and geometry of the problem to be analyzed. Thermal properties such as thermal conductivity and volumetric heat capacity can be measured using laboratory tests, whereas the boundary conditions are governed by the test set up and conditions. This section summarizes the background theory of the TEMP/W FE program and the requirements of input parameters for FE analysis are described in detail.

4.2.1 General Theory

Temp/W is a commercial finite element program that can be used to model transient conductive heat transport in solid materials as a result of temperature time-histories applied at the material boundaries. There are two primary material properties that govern heat conduction in materials, namely thermal conductivity and volumetric heat capacity or specific heat capacity. Conduction is defined as the flow of heat in a body due to thermal gradients in the body. For one-dimensional heat flow, the equation governing heat flux is:

$$\boldsymbol{q} = -\boldsymbol{k}\frac{\partial \boldsymbol{T}}{\partial \boldsymbol{x}} \qquad [3.1]$$

where, $\boldsymbol{q}$ is the flux, $\boldsymbol{k}$ is the thermal conductivity, $\boldsymbol{T}$ is temperature and $\boldsymbol{x}$ is distance. Consequently, the quantity of heat flowing through a body is equal to the material thermal conductivity times the temperature gradient.

For 2-dimensional transient heat flow problems, the governing differential equation is:

$$\frac{\partial}{\partial \boldsymbol{x}}(\boldsymbol{k}_x \frac{\partial \boldsymbol{T}}{\partial \boldsymbol{x}}) + \frac{\partial}{\partial \boldsymbol{y}}(\boldsymbol{k}_y \frac{\partial \boldsymbol{T}}{\partial \boldsymbol{y}}) + \boldsymbol{Q} = \boldsymbol{\lambda}\frac{\partial \boldsymbol{T}}{\partial \boldsymbol{t}} \qquad [3.2]$$

where $\boldsymbol{k_x}$ and $\boldsymbol{k_y}$ are thermal conductivity in the x- and y- directions, respectively, $\boldsymbol{Q}$ is applied boundary flux, $\boldsymbol{\lambda}$ is capacity for heat storage; and $\boldsymbol{t}$ is time. The equation on the left hand side expresses the difference between the incoming and the outgoing heat flux in an element at a point in time. This is equal to the change in stored heat energy represented by the right-hand-side of the equation (Krahn, 2004).

4.2.2 Thermal Properties of TSL

Thermal conductivity, thermal diffusivity, and differential scanning calorimeter tests were performed on TSL specimens by Anter Laboratories Inc. in Pitsburgh, PA. Table 4.1 summarizes the thermal properties of TSL.

The thermal conductivity was measured according to ASTM E1530 (ASTM E1530-06, 2006) on three TSL specimens labelled TSL-S1, TSL-S2 and TSL-S3. The specimens were 2.54 mm long by 2.54 mm wide by 3 mm thick. Thermal diffusivity tests were performed according to the flash method (ASTM E1461-01) on disc specimens (31.75mm diameter by 4mm thick) labelled TSL-S4, TSL-S5 and TSL-S6. Thermal diffusivity, $\boldsymbol{\alpha}$, is equal to

$$\boldsymbol{\alpha = k/\rho c_p} \qquad [3.3]$$

where k is the thermal conductivity, $\boldsymbol{\rho}$ is density and c_p is the specific heat capacity. The thermal diffusivity varies from 0.0014 to 0.0017 m. Finally, differential scanning calorimeter tests were performed on specimens TSL-S4 and TSL-S5 according to ATSM E1269 to measure the specific heat capacity. Based on this test, c_p varies from 1528 to 2197 J/kg°C.

Based on the test results summarized in Table 4.1, the thermal conductivity of the TSL material tested is 0.15 W/m·^{o}C and the volumetric heat capacity is 2.0 MJ/m^3 °C. For analysis purposes, the intact TSL was given a density of 1050 kg/m^3.

4.2.3 Thermal Properties of Concrete

It is reported that the thermal properties of concrete, in particular thermal conductivity and volumetric specific heat capacity, are dependent upon moisture content, aggregate type, permeability, density and temperature (Eurocode, 2004; Kodur and Khaliq, 2011). Specifically, the thermal conductivity of concrete decreases approximately from 2.0 to 1.0 W/m°C as temperature increases from 0 to 600 °C. Volumetric specific heat capacity is highly sensitive to moisture content, aggregate type, test conditions and measurement techniques used in experiments rather than concrete temperature (Harmathy and Allen, 1973; Kodur and Sultan, 1998; Eurocode, 2004; and Kodur and Kahliq, 2011). The volumetric heat capacity of concrete ranges between 1.8 MJ/m^3 °C and 2.0 MJ/m^3 °C at temperature ranging from 0 to 600 °C.

Although the thermal properties of concrete vary with temperature, thermal conductivity and volumetric heat capacity of concrete at temperatures between 20 °C to 600 °C can be assumed as constant. The thermal conductivity of 1.3 W/m°C and the volumetric heat capacity of 1.9 MJ/m^3 °C are used in this analysis.

4.2.4 Test Geometry and FE Models

4.2.4.1 Test geometry

Figure 4.1 shows the test geometry of TSL coated concrete slabs. Figure 4.1 includes the cross-sections of the TSL coated slab before and during/after the fire test. A slab is 500mm wide, 1220 mm long and 50mm thick. The CAN/ULC-S102-M88 tunnel test requires six slabs being situated on top of the testing chamber as described in Figure 3.1 in Chapter 3. The total length of the

slabs is 7320 mm. Temperature monitoring positions are located at 750 mm, 1560 mm, 2360 mm and 3050 mm from the upstream end of the testing chamber.

4.2.4.2 FE model

The FE mesh comprised 3 layers as illustrated in Figure 4.2. The modeled layers include: a 50 mm thick concrete slab, 2mm of intact TSL on the concrete and a 6 mm thick char layer over the intact TSL. As discussed in Chapter 3 and illustrated in Figure 3.34, a char barrier forms during the CAN/ULC-S102-M88 tunnel tests. Based on physical measurements taken after each test, the char barrier was found to be on average 6 mm thick and the intact TSL was only 2 mm thick beneath the char layer.

The FE mesh comprised 700 rectangular quadrilateral elements and 2550 nodes. The concrete was sub-divided into 4 rows of elements and the TSL and char barrier were modeled using 1 row of elements. The finite element geometry matched the test geometry illustrated in Figure 4.2.

4.2.5 Boundary Conditions

In this study, temperature boundary conditions were used. As described in Chapter 3, the temperatures were measured during the CAN/ULC-S102-M88 tunnel tests using thermocouples situated in the concrete but also at the inner surface to measure air temperatures during the CAN/ULC-S102-M88 test tunnel and at the outer surface of the test slabs. Figures 4.3 and 4.4 show the interpreted boundary temperatures at various times during the tests for the inner and outer concrete surfaces, respectively. Tables 4.2 and 4.3 provide additional temperature

measurements at various times and distances from the left-hand side of the model. These boundary temperatures were specified in the FE models.

4.2.6 Summary of Analyses

The primary objective was to back calculate the thermal properties of the char barrier from the temperature distribution in the concrete slabs during the CAN/ULC-S102-M88 tunnel tests. This was done by varying the thermal properties of the char layer until there was reasonable or satisfactory agreement between measured and calculated temperatures at the various monitoring points in the concrete.

Three computation runs or trials were performed as summarized in Table 4.4. For all trials, it was assumed that the specific heat capacity of the char layer is equal to that of TSL (i.e. 2 kJ/kg °C) and the density was equal to that of air (1 kg/m^3). The resultant volumetric heat capacity was 0.002MJ/m^3°C. The thermal conductivity of the char barrier was assumed to be 0.10, 0.12, and 0.15 W/m^oC for Trials A, B and C, respectively. As discussed in the following section, the thermal properties of the char layer are assumed to be equal to those in the run that best matches the measured concrete temperatures during the test.

4.3 RESULTS

Using the given parameters summarized in Table 4.4, numerical analyses were performed and compared to the measured temperatures during instrumented tunnel tests (see ITT-1 and ITT-2 in Chapter 3). All monitoring points in the concrete were considered except the position at a depth of 3 mm from the top of the slabs. The temperature did not change significantly during the tests at this location and it was therefore ignored in the following assessment.

Figures 4.5 to 4.11 compare the measured temperatures during ITT-1 and ITT-2 with calculated temperatures from Trials A, B and C corresponding to thermal conductivities of 0.1, 0.12 and 0.15 W/m·°C for the char layer. As shown in the figures, the calculated temperatures corresponding to a thermal conductivity of 0.1 W/m^3·°C lie near the lower bound of the measured temperatures except for the temperatures at a depth of 50 mm from the top of the slab at Site I. In contrast, the calculated temperatures corresponding to the thermal conductivity of 0.15 W/m^3·°C plot near the upper bound of the measured temperatures. The calculated temperatures corresponding to a thermal conductivity of 0.12 W/m^3·°C lie within the measured temperature ranges except at a depth of 50 mm from the top of the slab at Site-T1 as illustrated in Figure 4.5. However, for the remainder of the sites, the Trial B results agree satisfactorily with the measured temperatures versus time during the tunnel fire tests.

4.4 SUMMARY AND CONCLUSIONS

This chapter has described the results of thermal finite element analyses that were performed to estimate the thermal conductivity of the char layer that forms during CAN/ULC S102-M88 tunnel tests on TSL coated concrete slabs. The FE analyses were performed using the commercial software Temp/W. Linear analyses were performed using constant specific heat capacity and thermal conductivity for concrete, TSL, and the char barrier. In addition, two different types of geometry have been used in this study. The finite element models considered the exact geometry of the CAN/ULC S102 tunnel tests and, based on the results, the following conclusions can be made:

1) The linear FE analysis using constant thermal properties for the materials and time-dependent temperature boundary conditions corresponding to those measured during the tests presents very good agreement to the measured concrete temperatures with TSL coating. The calculated temperatures versus time and with depth are close to the measured temperatures.
2) The thermal conductivity of the char barrier is in the order of 0.12W/m°C corresponding to a volumetric heat capacity of 0.002MJ/m^3°C. The thermal conductivity of the char barrier is not that different from the TSL (i.e. 0.15W/m°C).
3) The analysis confirms the conclusion that the TSL causes a reduction in temperature in concrete slabs during 20 minutes of fire exposure testing in CAN/ULC S102-M88 tunnel tests due to its insulating effect (i.e. its thermal conductivity is 1/10^{th} that of concrete).

Table 4.1 Thermal conductivity of TSL for various temperatures

Sample	Temperature (°C)	Thermal Diffusivity (cm^2/s)	Thermal Conductivity ($W/m \cdot {}^oC$)	Specific Heat Capacity ($J/kg.{}^oC$)
TSL-S1	28		0.14	
	102		0.15	
	153		0.16	
TSL-S2	28		0.14	
	102		0.15	
	153		0.16	
TSL-S3	28		0.15	
	102		0.16	
	154		0.18	
TSL-S4	25	0.0016		
	50	0.0015		
	100	0.0015		
	150	0.0015		
TSL-S5*	25	0.0016		1528
	50	0.0016		1713
	100	0.0015		2104
	150	0.0014		2111
TSL-S6*	25	0.0017		1559
	50	0.0017		1737
	100	0.0015		2081
	150	0.0014		2197

* *The specific heat capacity results were obtained from differential scanning calorimeter tests.*

Table 4.2 Temperature boundary condition – inner model surface

Time (min)	Distance from left-side of Model			
	750mm	1560mm	2360mm	3050mm
0	25	25	25	25
2	350	267	179	50
4	410	314	213	65
6	450	349	242	85
8	470	366	256	95
10	480	378	269	110
12	510	402	287	120
14	530	419	302	130

Table 4.3 Temperature boundary condition – outer model surface

Time (min)	Distance from left-side of Model				
	750mm	1560mm	2360mm	3050mm	4265mm
0	24.5	24.3	24.4	24.3	23.3
2	24.7	24.4	24.4	24.4	23.5
4	25.3	24.7	24.5	24.5	23.5
6	26.0	25.2	25.5	24.7	23.6
8	29.5	28.2	27.0	25.9	24.0
10	34.1	32.0	29.9	28.1	24.9
12	39.0	36.1	33.3	30.8	26.5
14	47.5	43.2	38.9	35.2	28.8

Table 4.4 Trial analysis to determine the thermal properties of the char barrier

Trials	Materials	Thermal Conductivity (W/m·°C)	Volumetric Heat Capacity (MJ/m^3 °C)	Layer Thickness (mm)
Trial A	Concrete	*1.3	1.9	50 mm
	TSL	0.15	2.0	2 mm
	Char Barrier	0.10	0.002	6 mm
Trial B	Concrete	1.3	1.9	50 mm
	TSL	0.15	2.0	2 mm
	Char Barrier	0.12	0.002	6 mm
Trial C	Concrete	1.3	1.9	50 mm
	TSL	0.15	2.0	2 mm
	Char Barrier	0.15	0.002	6 mm

**Thermal conductivity of concrete varies depending on concrete temperature*

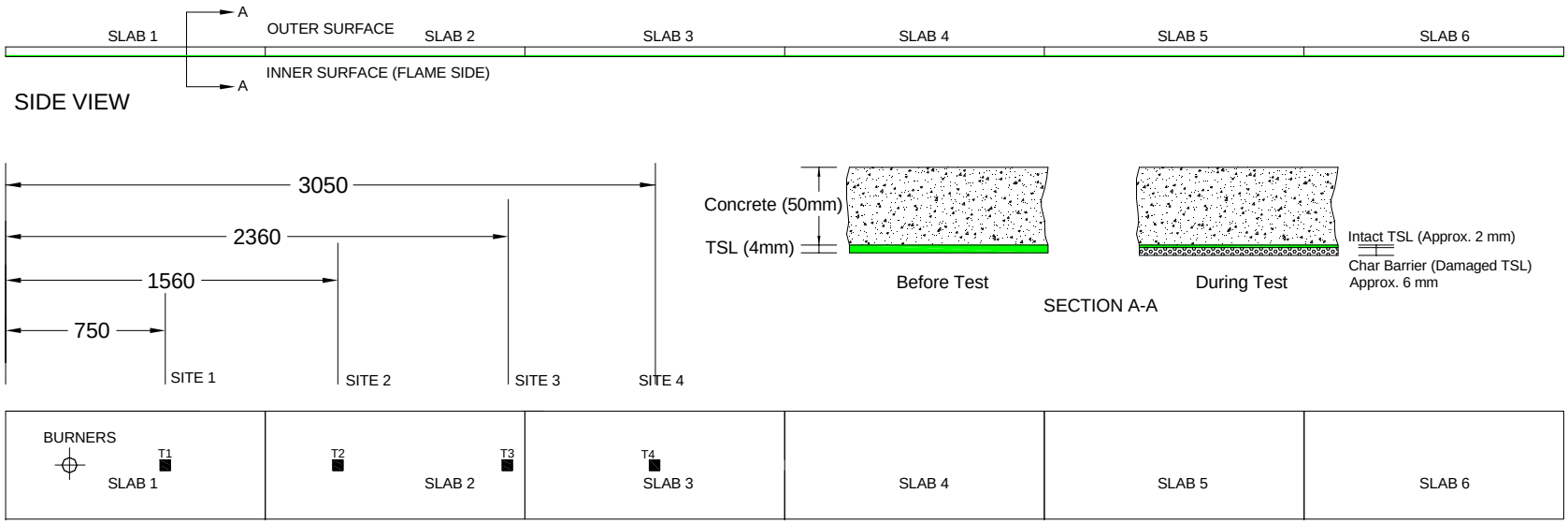

Figure 4.1 Test geometry and profile of TSL coated slab

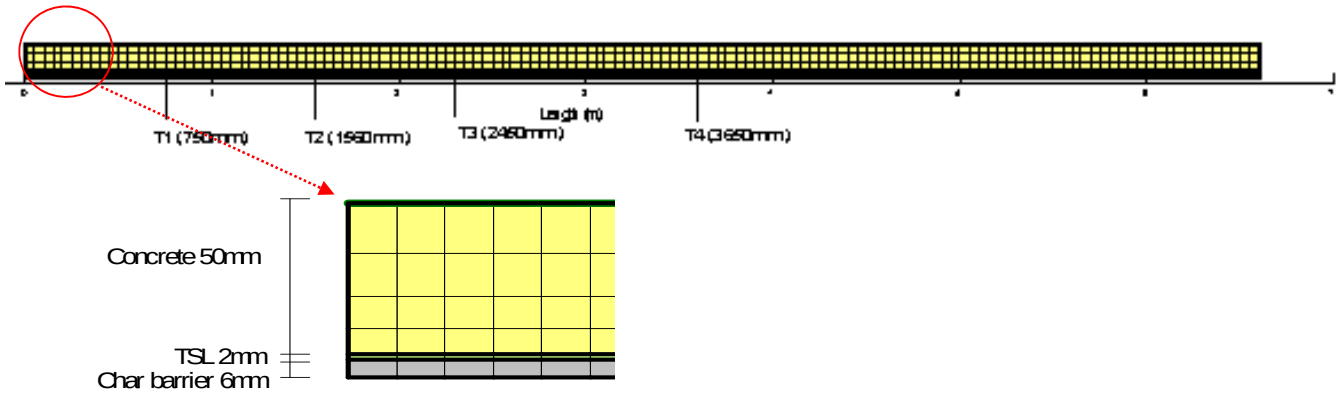

Figure 4.2 Finite element mesh

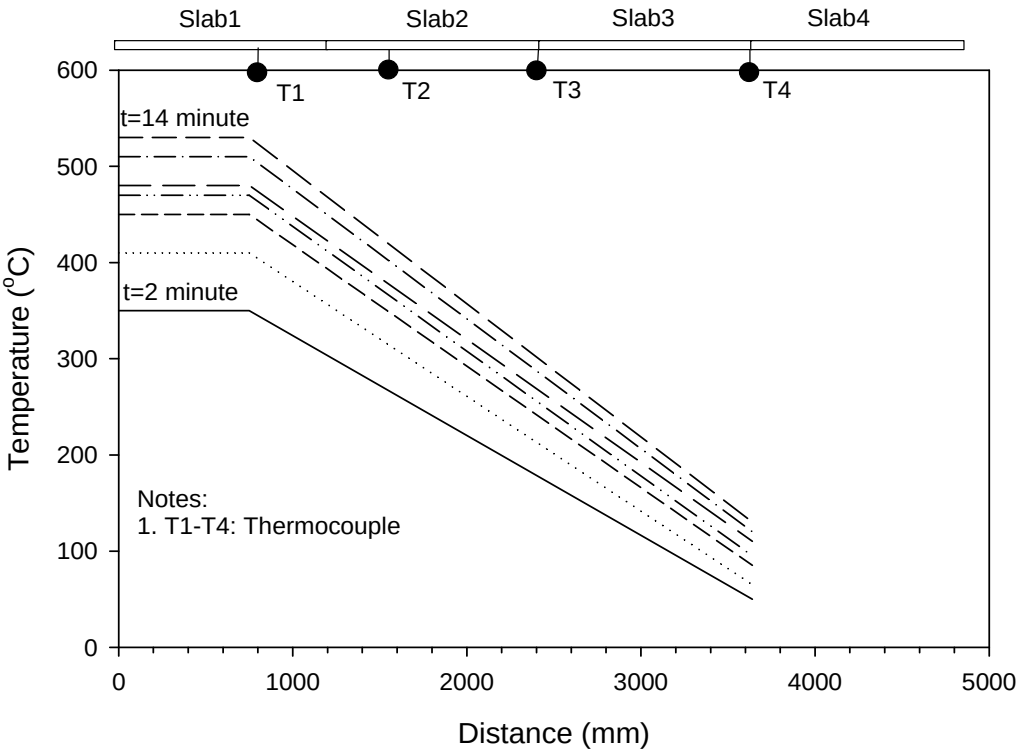

Figure 4.3 Air temperature boundaries in the tunnel

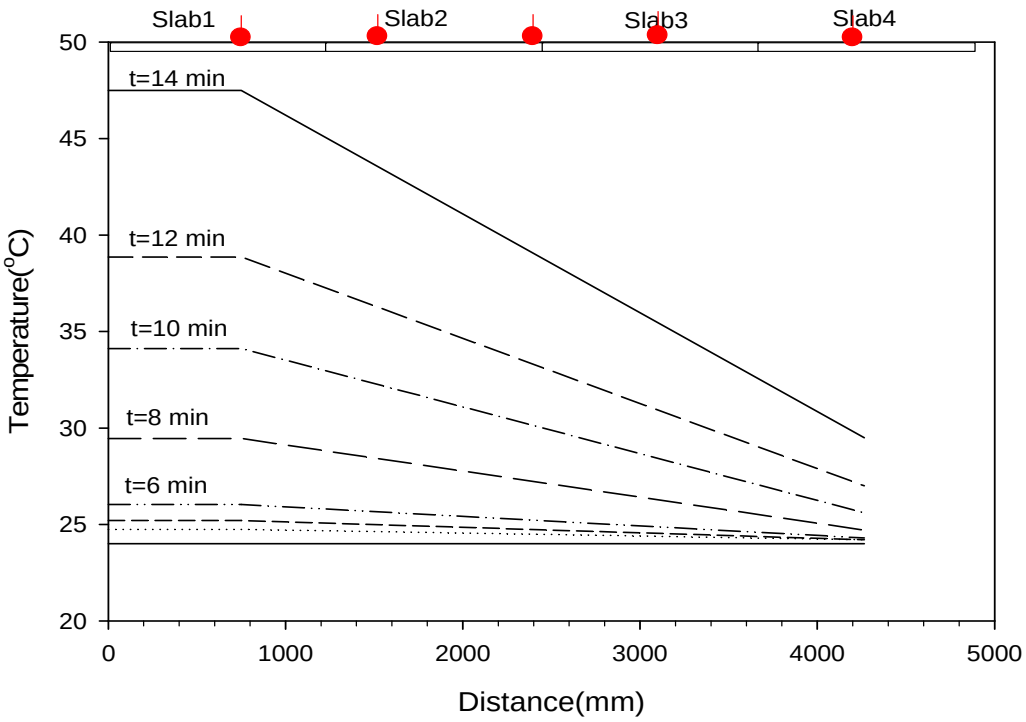

Figure 4.4 Outer concrete surface temperature boundaries

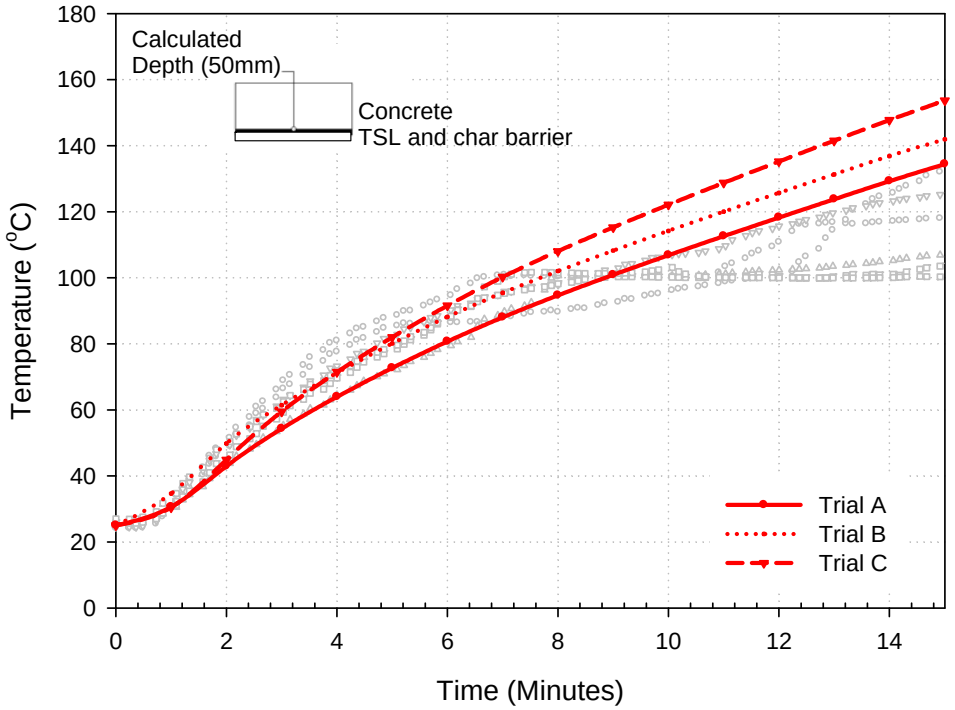

Figure 4.5 Calculated and measured temperatures-50 mm from the top of the slab (Site T1)

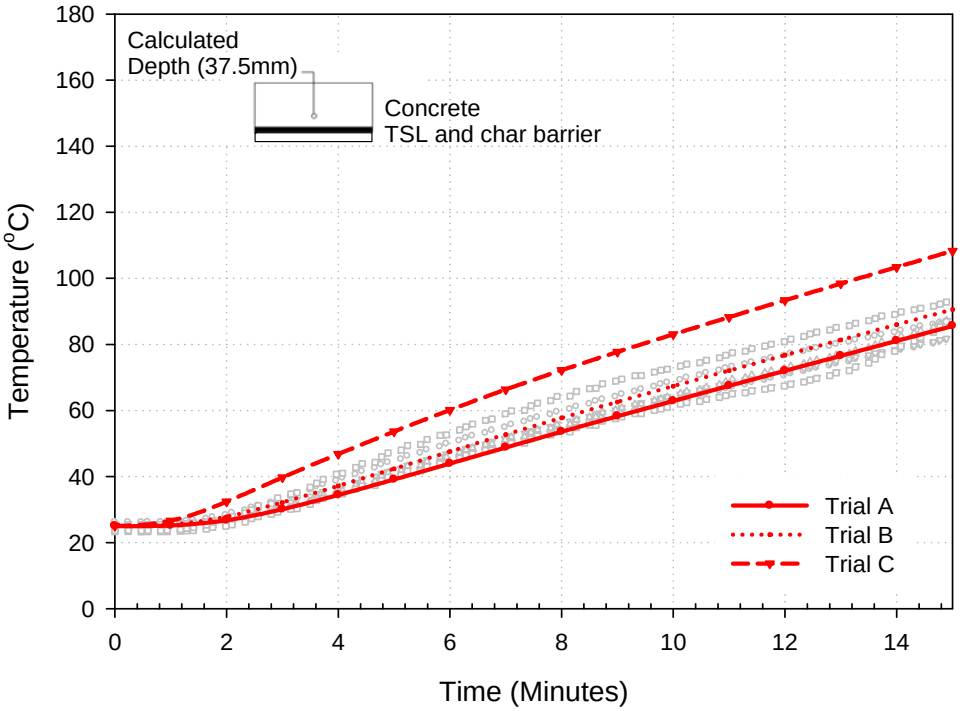

Figure 4.6 Calculated and measured temperatures-37.5 mm from the top of the slab (Site T1).

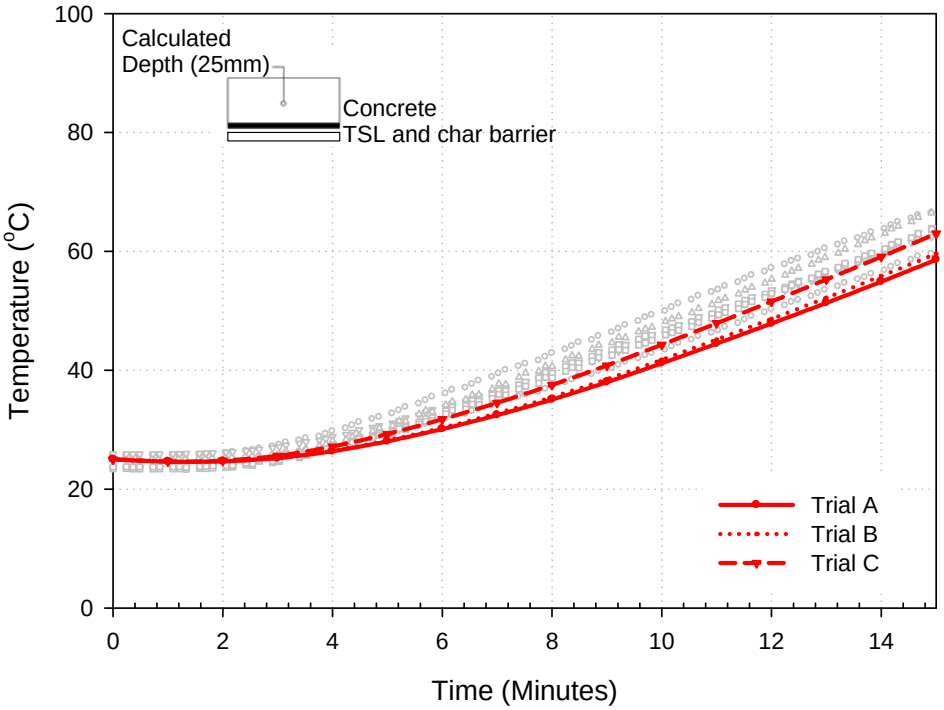

Figure 4.7 Calculated and measured temperatures-25 mm from the top of the slab (Site T1)

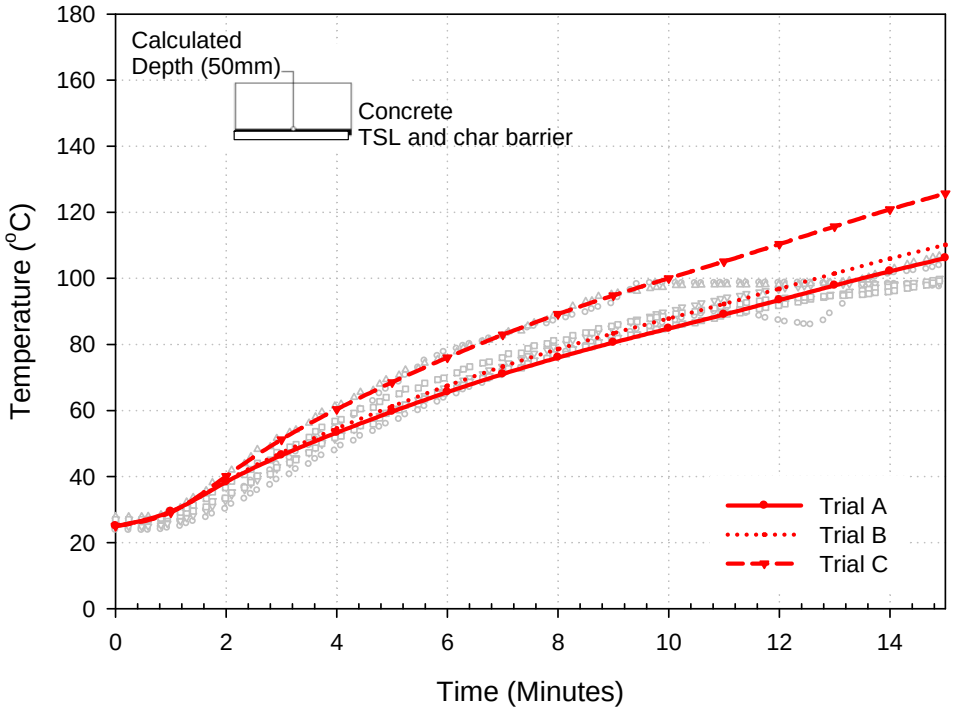

Figure 4.8 Calculated and measured temperatures-50 mm from the top of the slab (Site T2)

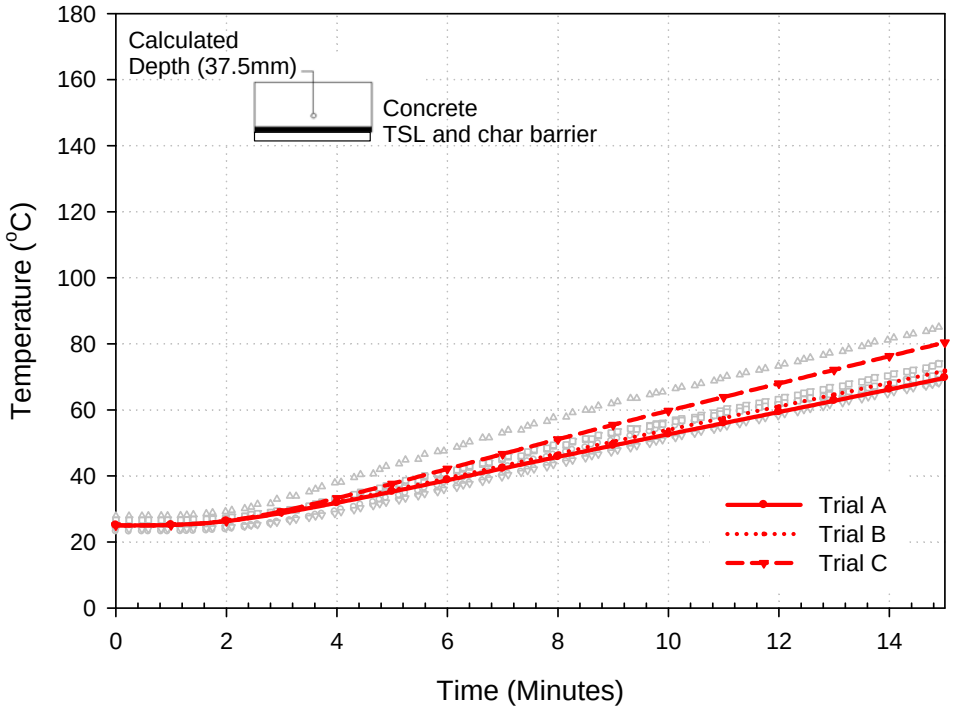

Figure 4.9 Calculated and measured temperatures-37.5 mm from the top of the slab (Site T2).

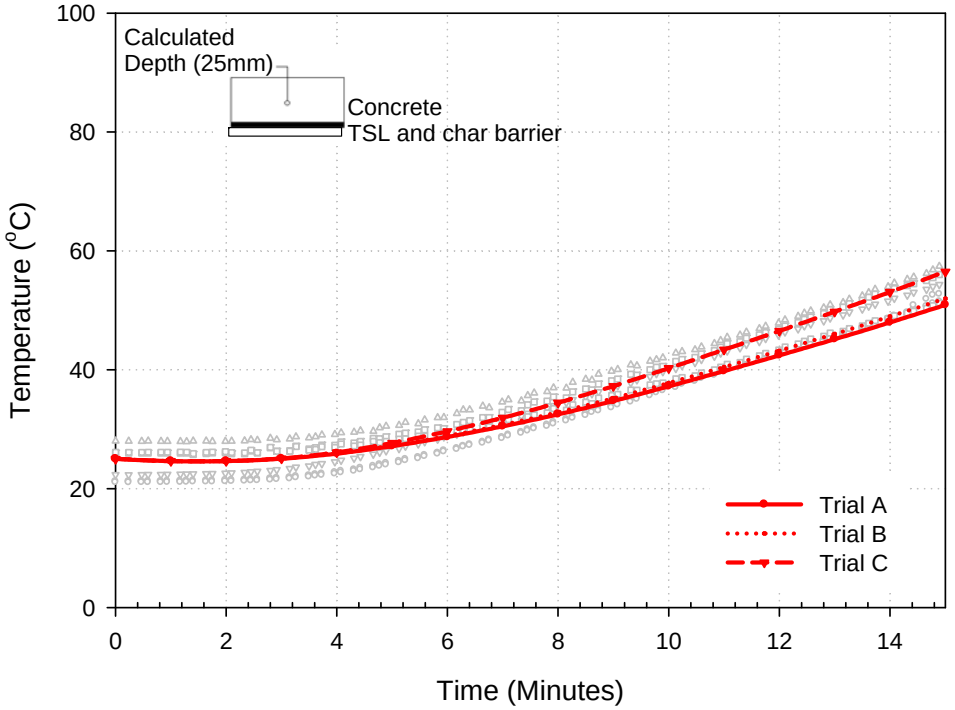

Figure 4.10 Calculated and measured temperatures-25 mm from the top of the slab (Site T2).

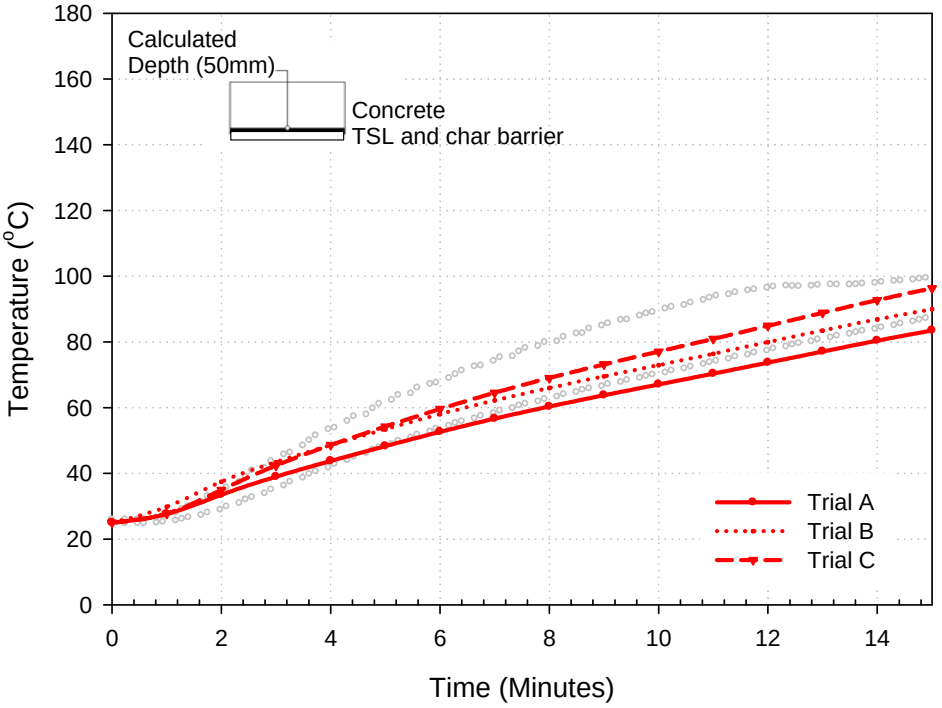

Figure 4.11 Calculated and measured temperatures-50 mm from the top of the slab (Site T3).

CHAPTER 5

MECHANICAL CHARACTERISTCS OF TSL: TENSILE AND ADHESION STRENGTH

5.1 INTRODUCTION

It is important to understand the mechanical behaviour of a TSL as a substrate material for reinforced concrete tunnel linings. As presented in Chapter 3, the TSL was proven to be a potential fire protection agent presenting superior characteristics during the tunnel fire tests (i.e. CAN/ULC S102-M88). For instance, the TSL used in this work significantly reduced heat transfer through concrete structures during the CAN/ULC S102-M88 tunnel tests. Also, some TSL remained intact and in place after the fire tests implies that TSL can control concrete spalling during and after a fire.

Fire-induced spalling can result from various mechanisms but it is principally caused by excessive heating of concrete during fires (Breunese and Fillinger, 2004). The potential of a TSL as a fire insulation agent has been assured as a result of the tunnel fire tests. Hence, to decrease concrete spalling without substantial failure may require adequate adhesion strength to reduce or prevent concrete debris or crack propagation before or after a fire.

The main objectives of the experiments presented in this chapter are to: i) determine the TSL mechanical properties including the tensile strength and the modulus of elasticity, ii) evaluate TSL adhesion strength under different curing conditions in the concrete or the grout, and iii)

examine TSL adhesion strength. A series of evaluating procedures will provide a comprehensive perspective as to whether this TSL can be a good substrate material for concrete tunnel linings.

This chapter describes and presents the experimental approaches to evaluate TSL suitability as a substrate material with regard to the spalling and delaminating of concrete. The possibility of reducing concrete spalling or delaminating was determined through tensile testing and adhesion strength testing. At the end of this chapter, the experimental results and conclusions are delineated.

The following sections present the TSL tensile strength tests and the TSL adhesion strength tests. The tensile strength tests were performed using a standard test method for tensile properties of plastics (ASTM D638-08) while the adhesion strength tests were conducted using a developed method (Archibald and Nicholls, 2001).

5.2 METHODOLOGY

5.2.1 Tensile Test (ASTM D683-08)

The tensile strength of TSLs, one of the most important mechanical properties related to the decrease of concrete spalling, was evaluated using a standard test method for plastic materials followed by ASTM D683-08. The objective of this testing was to determine TSL stress-strain (nominal) characteristcs including tensile strength at nominal yield or break load and the modulus of elasticity (E_d). A total of four specimens were prepared in accordance with ASTM standards and tested.

ASTM D683-08 is a test method to determine the tensile properties of unreinforced plastics in the form of a dumbbell-shaped test specimen illustrated in Figure 5.1. This test method is designed to produce tensile properties for the control and specification of plastic materials. These data may be useful for qualitative characterization and for research and development (ASTM D638-08, 2008). Tensile properties obtained through this method can provide useful data for the purpose of engineering design.

5.2.1.1 Test specimen preparation

The shape and essential dimensions of the dumbbell-shaped specimen (Type-I) are also presented in Figure 5.1. According to ASTM D683-08, the Type-I specimen is recommended for semirigid plastics with a thickness of 7 mm or less. Detailed demensions for the TSL specimens are described in Table 5.1.

5.2.1.2 Test procedures

A MTS machine at the Geotechnical Research Centre (GRC), the University of Western Ontario, was used to perform the tensile tests on the TSL specimens. The testing setup can be seen in Figure 5.2. Before implementing the tests, the width (W_c) and thickness (T) of each specimen were measured to the nearest 1/100 mm using a digital caliper. The measurement of width and thickness at the centre of each specimen and within 5mm of each end of the gage length (L) was considered and an average of these three measuremnts was taken.

The tensile test specimen was held in such a way that slippage relative to two grips was prevented as much as possible. Thus, a specimen was positioned between the two fixed grip

guards which are desinged to hold thin plastic materials for tensile testing. Once the specimen was firmly gripped, the actuator began loading the specimen. The loading rate was set at 5mm per minute as recommended in ASTM D638-08. Loads and displacements were automatically recorded by the data-logger every two seconds.

5.2.2 Adhesion Strength Test

A pull-off test is designed to assess the bond strength properties of the interface between a TSL and concrete or concrete-like surface (i.e. grout). If adequate adhesion bonds exist, the TSL coated liners can potentially transfer or carry an extra load. Another expectation for a TSL is that TSL coated liners can prevent or reduce spalling in the event of failure.

5.2.2.1 Test specimen preparation

Adhesion strength tests were conducted to evaluate TSL adhesion capability. The test arrangement and detailed components used in these tests are illustrated in Figure 5.3. Ten concrete specimens and five Sika grout specimens were produced. Each specimen is 38 mm in thickness and 300 mm in diameter. Two curing conditions, room conditions and 100% relative humidity conditions, were used for curing the specimens. The following steps were considered during the preparation of the specimens:

1) For the first three days after casting, the specimen surfaces were covered with wetted burlap.

2) After three days, half were placed in the normal storage area under room conditions (e.g. room temperature) while the other half was moved into a concrete curing room (100% relative humidity) for 28 days.
3) After 28 days of curing, the unconfined compressive strengths (*f'c*) of concrete and Sika grout were measured using standard cylinders (i.e. 76.2mm x 15.24mm). The average unconfined compressive strength of concrete was 30MPa while the unconfined compressive strength of Sika grout was 56 MPa.
4) Among ten concrete specimens, one side of two concrete specimens cured in room conditions and three specimens cured in 100% humidity conditions were painted with ocean fire-retardant paint. The other five concrete specimens and the Sika grout specimens were not painted. Table 5.2 summarizes material and curing conditions for all specimens.

5.2.2.2 Test procedures

There is no proper standard test method to evaluate global adhesion strength of spray-on lining material except for the method developed by Archibald (Archibald, 1992 and Tannant et al. 1999). In this test method, a circular perforated steel plate was used and placed on the test surface before spraying with TSL. The size of a circular perforated steel plate (referred as a pull plate) was 100 mm in diameter by 3.2 mm thick. Prior to spraying the TSL, one side of each non-painted specimen was sand-blasted to sustain similar surface conditions. At least an initial 1-mm of coating (i.e. primer) was applied through all perforated holes on each plate. The pull plate had to be over-cored to insure that only the adhesion bond associated with the area beneath the pull plate actually measured the adhesion strength during the pull-off testing. After the TSL primer

seeped into the perforated holes, a second spraying was immediately done so that the TSL coating became a total of 4 mm thick. The sprayed specimen can be seen in Figure 5.4(a). After 45 days of curing TSL, all specimens were ready to be tested using the MTS machine.

In order to evaluate the TSL bonding between the specimen surface and TSL coating including the primer coating, a kerf cut around the pull plate up to the concrete or Sika grout surface was done just before testing (See Figure 5.4(b)). Tests were then conducted in all cases until full release of the adhesion contact between the pull plate and specimen surface occurred. The pulling rate of 0.5 mm/min was selected to evaluate the possible residual adhesion strength after the peak strength was achieved. Figure 5.5 presents the adhesion strength test setup and the pull plate being pulled by the MTS machine.

5.3 RESULTS

5.3.1 Tensile Test

The load-elongation curves for tensile force on a TSL sample can be seen in Figure 5.6. During testing samples, TT-1 and TT-2 reached the maximum displacement of the MTS machine (i.e. 100 mm for TT-1 and 120 mm for TT-2, respectively) while TT-3 and TT-4 were broken at elongations of 72 mm and 70 mm, respectively. As seen in Figure 5.6, samples TT-3 and TT-4, which are 1.07 g/cm^3 in density, present less elongation compared to TT-1 which is 1.01 g/cm^3 in density. The difference in density states that is most likely due to graphite inclusions used to confer non-flammable character. It can be known that specimens containing more graphite cause less elongation. In other words, the ductile characteristics of TSL are dependent on the density of the TSL.

The load-elongation curves were converted to the nominal stress-strain curves as presented in Figure 5.7. As shown in Figure 5.7, TSL nominal stress-strain curves show nearly an elastic-perfectly-plastic behaviour. However, a realistic behaviour of a TSL is expected to have more strain-hardening. It is because the cross-sectional area of a specimen decreases as load increases. However, the correction of cross-sectional area would be minimal in the linear elastic zone of the material.

The true stress-strain curve of a TSL could not be determined using ASTM D683-08 because the changes in width and thickness of test samples during the test cannot be measured. However, the modulus of elasticity which is the ratio of nominal stress to corresponding strain below the proportional limit of a material can be determined from the nominal stress-strain curve because

the effect of area correction is small. For the determination of yield strength ($\sigma_{y\ TSL}$), ASTM D683-08 specifies the stress determinate by an offset of 0.2% strain from the initial linear portion of the load-elongation curves as shown in Figure 5.7.

The results of four tensile tests and the average of four tests are shown in Figure 5.7. A modulus of elasticity of 100 MPa was calculated from the average curve presented. Similarly, tensile strength at yield from the figure is evaluated to be 3.8 MPa. However, it is difficult to determine the true yield point for plastics because of their visco-elastic characteristics. Therefore, it is not common to determine the exact yield point from the stress-strain curves. For this reason, plastic yield points are typically estimated as a yield range (Mascia, 1989). The yield range of this TSL material can be found between the stress of 4 MPa and 6 MPa.

5.3.2 Adhesion Strength Test

All test results are presented in Table 5.3 to Table 5.5. Also, load-displacement curves of each test were plotted in Figures 5.9, 5.11 and 5.13. It was assumed that an ideal failure at the interlayer (i.e. TSL and specimen surface at perforated holes) took place. Thus, the adhesion strength was calculated using the total area of the plate. However, three specimens, C-5, SG-5 and PC-5 failed to measure the adhesion strength due to the excessive kerf cut.

5.3.2.1 Specimen-concrete

Table 5.3 summarizes the adhesion strength testing results for the concrete specimens (i.e., C-1 to C-5). The maximum adhesion strength ranging between 480 kPa and 502 kPa was exhibited by the concrete specimens cured in room conditions (C-1 and C-2). It was the highest strength

and tenacity of bond developed as seen from Figure 5.5. On the other hand, for concrete specimens cured in 100% humidity conditions, the maximum adhesion strength ranged between 280 kPa and 333 kPa. It indicates that concrete cured under 100% relative humidity curing conditions may result in lower adhesion strength.

Figures 5.8(a) through 5.8(d) show the surfaces of the fully separated pull plate surfaces of the concrete specimens. Figures 5.8(a) and 5.8(b) present the pull plate surfaces released from the concrete specimen surfaces cured in room conditions while Figures 5.8(c) and 5.8(d) show the pull plates separated from the specimens cured in 100% humidity conditions. As seen in the figures, the pull plate surfaces from specimen C-3 and C-4 have a smoother surface than the plate surfaces from specimen C-1 and C-2. As a result of the separated surface conditions, either rough or smooth, it can be inferred that the adhesion strength of TSL is dependent upon the moisture content of the specimen (i.e. concrete or grout) due to different curing conditions.

As seen in Figure 5.9, the residual adhesion strength can be quantifiable, after the peak load, at a load of 3.5kN, 3.2kN, 2kN and 0.3 kN for C-1. A similar pattern can be also found at a pull load of 3.5kN, 3kN and 0.5kN for C-2. The maximum displacements at the peak for C-1 and C-2 are 0.5 mm and 0.8 mm, respectively. Specimens C-3 and C-4, which were cured in 100% humidity conditions, do not present significant residual adhesion bond strength. For these samples, the displacements at the peak load of 2.6 kN and 2.2 kN are observed at 0.4 mm and 0.6 mm. It can be seen that there are no major differences between two groups of samples with respect to the displacement at the peak loads. The displacement at the peak loads ranges from 0.4 mm to 0.8 mm. Once again, it can be seen that the curing conditions (in other words, moisture content of

specimens) in the concrete would be a critical parameter to determine the adhesion strength of TSL.

5.3.2.2 Specimen-Sika grout

Table 5.4 summarizes the adhesion strength testing results for the Sika grout specimens (i.e., SG-1 to SG-5). The maximum adhesion strengths were evaluated at 471 kPa and 413 for SG-1 and SG-2 respectively. However, the maximum adhesion strength for SG-3 and SG-4 cured in wet conditions ranged from 172 and 185 kPa. Although the 100% humidity curing conditions can increase the strength of concrete or grout, it can induce a decrease in the adhesion strength at the interface.

The manner, in which the TSL adhesion strength loss occurs shown in Figures 5.10(a) through (d), was consistent except in SG-4. The perforated holes can clearly be seen in Figures 5.10(a), 5.10(b) and 5.10(c) but not in Figure 5.10(d). Differing from the separated pull plate surfaces of the concrete (refer to Figure 5.8) specimens, the surfaces of Sika grout specimens appeared uniform. Also, a full surface failure of the interface beneath the pull plate was observed with minimal material remaining attached to the Sika grout. Therefore, consistent ranges of the adhesion strength for all samples can be obtained.

Figure 5.11 illustrates the load and displacement curves during the adhesion strength tests between the pull plate and Sika grout specimen surfaces. The peak loads of the specimens cured in room conditions were measured between 3.2 kN and 3.7 kN. On the other hand, the peak loads for SG-3 and SG-4 cured in 100% humidity conditions ranged from 1.4 kN to 1.5 kN. The

displacements at the peak load for each specimen were 0.9 mm for SG-1, 0.6 mm for SG-2, and 0.4 mm for both SG-3 and SG-4. A large amount of residual adhesion strength was observed in SG-1 testing at displacements ranging from 1.4 mm to 2 mm. It can be explained that an existing localized bond carried the load after losing global bond strength. For the other cases, they showed a regular progressive loss of adhesion strength at various pull loads up to a displacement of 1.0 mm. A full release between the pull plate and sample surfaces varied from 1.2 mm to 5 mm.

5.3.2.3 Specimen-Painted Concrete

Table 5.5 summarizes the adhesion strength testing results for the painted concrete specimens (i.e. PC-1 to PC-5). The maximum adhesion strength for a concrete specimen cured in room conditions and painted by the ocean fire-retardant (i.e., PC-1), was 154 kPa. The maximum adhesion strength measured with PC-1 was only 30% of the maximum adhesion strength of the unpainted concrete specimen (C-1). In the case of being cured in 100% humidity conditions, very low adhesion strengths between 14 kPa to 69 kPa were obtained.

Figure 5.12 illustrates the separated pull plate surfaces for the painted concrete specimens (i.e. PC-1 to PC-4). The adhesion strength varied with the location of the separation surface in the pull-off tests as shown in Figure 5.12. The separated plate surfaces observed in PC-1, PC-2 and PC-4 present traces of the paint and concrete while PC-4 shows only a trace of the paint.

Figure 5.13 presents the pull load versus the displacement of the pull plate for these tests. Specimen PC-1, cured in room conditions shows the maximum pull load of 1.2 kN and the

displacement at the peak load is 0.5 mm. There is no significant residual adhesion strength. PC-2 shows a peak load of 0.54 kN at a displacement of 0.4 mm. After the peak for PC-2, the residual adhesion strength of 0.25 kN at 0.5 mm in displacement is observed. For specimens PC-3 and PC-4, relatively low adhesion strengths ranging from 0.1 kN to 0.2 kN were presented. PC-3 shows a broad range of residual adhesion strength at displacements between 0.5 to 2.0 mm while no residual adhesion can be found for PC-4. A full loss of adhesion contact occurred at 3.8 mm for PC-2 and PC-3 while at 1.5 mm, full detachment occurred for PC-4. PC-1 had full separation at a displacement of 0.9 mm.

5.4 SUMMARY AND CONCLUSIONS

In this chapter, a series of tests have been completed using ASTM D683-08 for the tensile test and the recommended testing suggested by Archibald (1992, 2000, and 2001) for the adhesion strength test. Adhesion and tensile strengths, which are important mechnical properties for tunnel supports, were evaluated. These tests can be used successfully to measure the adhesion and tensile strength of the TSL. Measured support chracteristics and immediate mobilization of high tensile strength liners may prevent gradual or sudden spalling developed in a fire. Therefore, the TSL, not only as a fire retardant but also as a substrate material, shows considerable promise for providing rapidly-deployable and effective support, either in conjunction with conventional support or in a stand-alone fashion.

The testing results provide the following conclusions:

1) Measurement by the ASTM D638-08 method showed that TSL tensile yield strength is between 4 MPa and 6MPa and the modulus of elasticity of TSL is to be 100 MPa.
2) The adhesion strengths for C-1, C-2, SG-1 and SG-2 cured in room conditions ranged from 413 kPa and 502 kPa. On the other hand, the adhesion strengths for C-3, C-4, SG-3 and SG-4 cured in 100% relative humidity were measured at between 172 kPa and 333 kPa. The adhesion strength for PC-1 cured in room conditions was 157 kPa while a range from14 kPa to 69 kPa was measured for PC-2, PC-3 and PC-4. Additionally, the displacements at the peak load consistently ranged from 0.5 to 0.9 mm.
3) The primary influences affecting adhesion strength of a TSL are the moisture content of the concrete or grout which it is sprayed onto and the surface roughness character (i.e.

painted and unpainted surfaces). To improve the adhesion strength of the interlayer bonded by TSLs, the contact area should be clean and the moisture content minimized.

4) If a TSL is sprayed on a painted surface of a concrete structure, the possiblility of significant loss of adhesion strength must be considered.
5) Based on testing results presenting relatively high tensile strength as a polymer and relatively high adhesion strength, it is possible to use the TSL as a substrate material for the reduction or prevention of spalling due to either fire or excessive unexpected extra loading.

Table 5.1. Type I- essential dimensions of the specimens

Specimen	T(mm)	Wc (mm)	A (mm^2)	Spray date	Density (g/cm^3)
TT-1	3.25	16.74	54.41	Aug 28, 2006	1.06
TT-2	4.09	16.00	65.49	Aug 28, 2006	1.01
TT-3	3.75	17.31	64.91	Oct 8, 2009	1.07
TT-4	3.75	15.25	57.19	Oct 8, 2009	1.07

Table 5.2 Specimens used in the adhesion strength tests

Specimen	Material (f'_c)	Curing Conditions
C-1	Concrete (30MPa)	Room conditions
C-2	Concrete (30MPa)	Room conditions
C-3	Concrete (30MPa)	100% humidity conditions
C-4	Concrete (30MPa)	100% humidity conditions
C-5	Concrete (30MPa)	100% humidity conditions
SG-1	Sika Grout (56MPa)	Room conditions
SG-2	Sika Grout (56MPa)	Room conditions
SG-3	Sika Grout (56MPa)	100% humidity conditions
SG-4	Sika Grout (56MPa)	100% humidity conditions
SG-5	Sika Grout (56MPa)	100% humidity conditions
PC-1	Painted Concrete (30MPa)	Room conditions
PC-2	Painted Concrete (30MPa)	100% humidity conditions
PC-3	Painted Concrete (30MPa)	100% humidity conditions
PC-4	Painted Concrete (30MPa)	100% humidity conditions
PC-5	Painted Concrete (30MPa)	Room conditions

C: Concrete; SG: Sika Grout; and PC: Painted Concrete

Table 5.3 Adhesion strength of TSL for the concrete surface

Concrete	Curing Condition	Max. Load (kN)	Pulled Area (m^2)	Strength (kPa)
C-1	Room	3.940	0.007854	502
C-2	Room	3.754	0.007854	478
C-3	100% humidity	2.205	0.007854	281
C-4	100% humidity	2.619	0.007854	333
C-5	100% humidity	No Data	0.007854	No Data

Table 5.4 Adhesion strength of TSL for the Sika grout surface

Sika Grout	Curing Condition	Max. Load (kN)	Pulled Area (m^2)	Strength (kPa)
SG-1	Room	3.707	0.007854	471
SG-2	Room	3.245	0.007854	413
SG-3	100% humidity	1.453	0.007854	185
SG-4	100% humidity	1.348	0.007854	172
SG-5	100% humidity	N.A	0.007854	No Data

Table 5.5 Adhesion strength of TSL for the ocean fire-retardant painted concrete surface

Painted Concrete	Curing Condition	Max. Load (kN)	Pulled Area (m^2)	Strength (kPa)
PC-1	Room	1.207	0.007854	154
PC-2	100% humidity	0.544	0.007854	69
PC-3	100% humidity	0.108	0.007854	14
PC-4	100% humidity	0.207	0.007854	26
PC-5	Room	No Data	0.007854	No Data

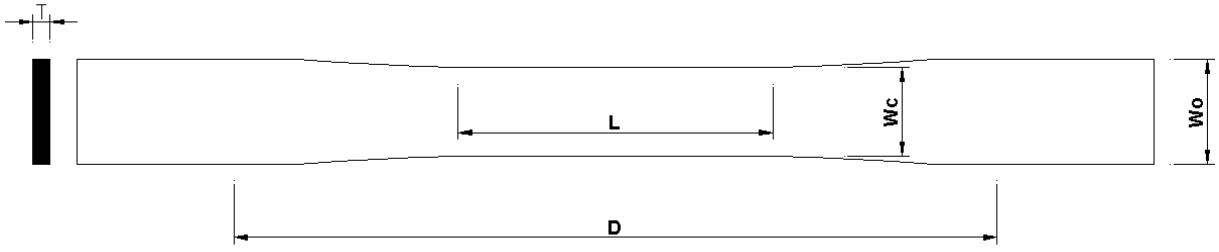

Figure 5.1 Type-I specimen: Detailed dimensions in ASTM D638-08

Notes: Wo= width overall (19mm), Wc= width of narrow section (16mm), L= gauge length of narrow section (57mm), D=distance between grips (115mm) and T= thickness (less than 7 mm)

Figure 5.2 Tensile strength test setup

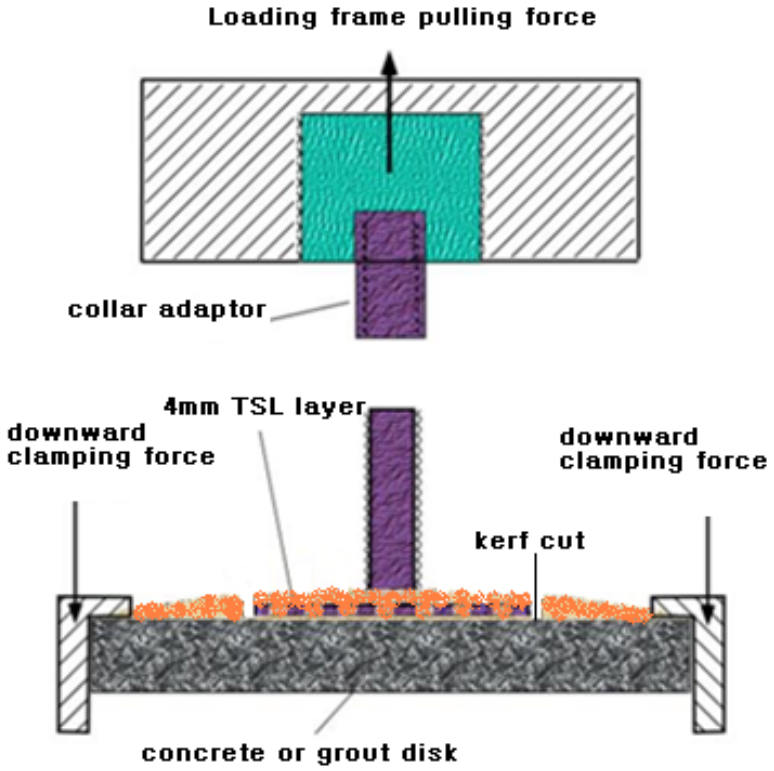

Figure 5.3 Pull-off testing diagram for the adhesion strength test
(after Archibald, 2000)

a) TSL sprayed specimens b) The kerf cut around the pull plate

Figure 5.4 TSL sprayed specimens for the adhesion strength testing

Figure 5.5 The adhesion strength testing setup and pull plate being pulled

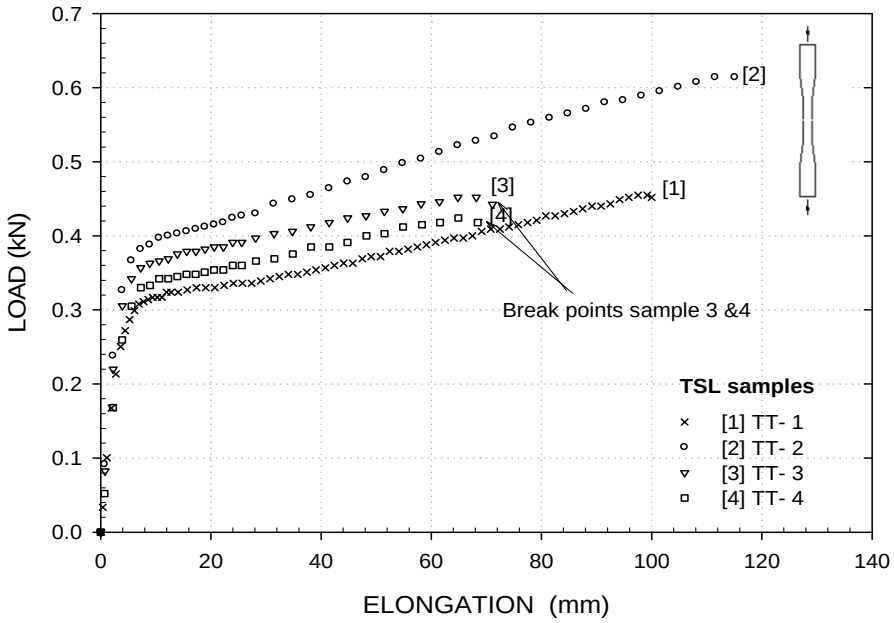

Figure 5.6 Load-displacement curves for the TSL tensile tests

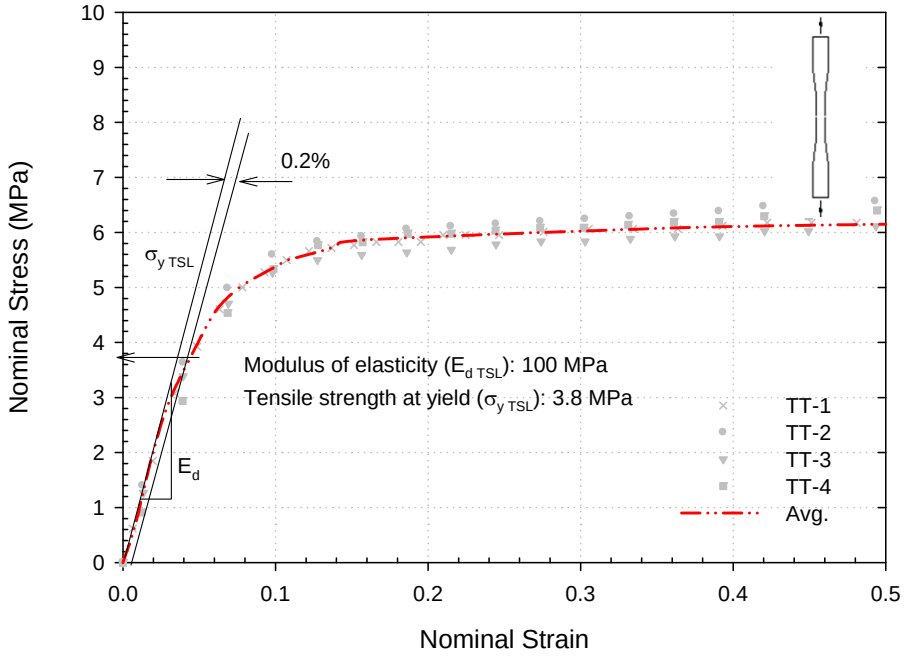

Figure 5.7 Nominal stress-strain curve of TSL

Figure 5.8 Pulled plate surfaces on concrete: a) C-1, b) C-2, c) C-3 and d) C-4

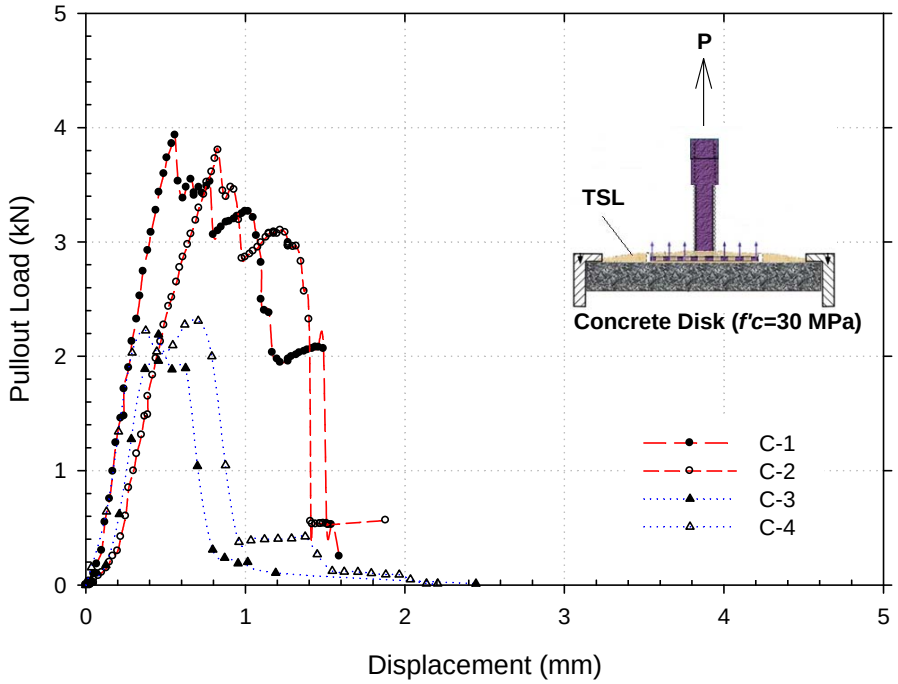

Figure 5.9 Load-displacement test data for TSL sprayed on the concrete specimens

Figure 5.10 Pulled plate surfaces on Sika grout: a) SG-1, b) SG-2, c) SG-3, and d) SG-4

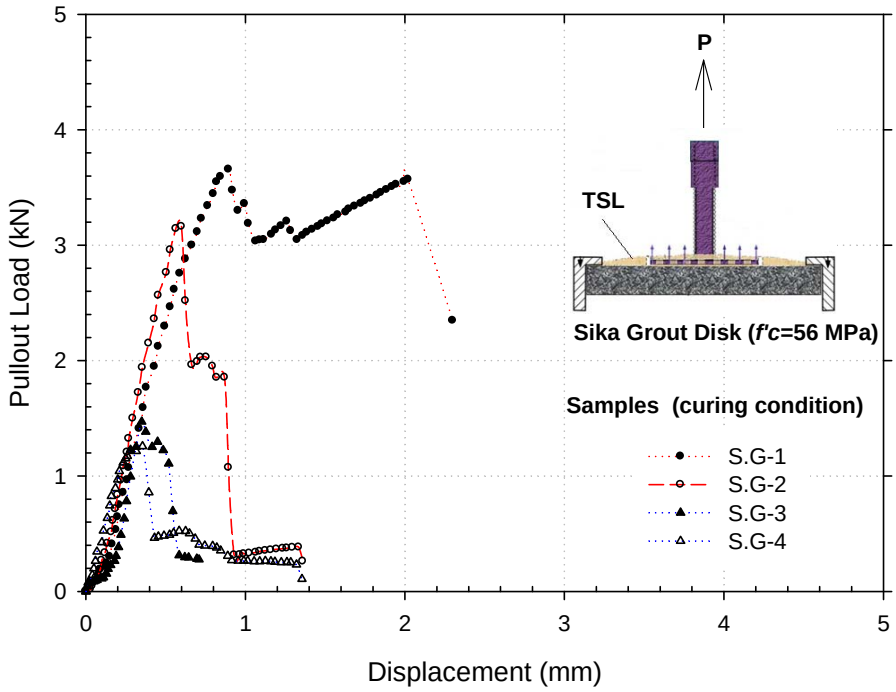

Figure 5.11 Load-displacement test data for TSL sprayed on the Sika grout specimens

Figure 5.12 Pulled plate surfaces for painted concrete: a) PC-1, b) PC-2, c) PC-3 and d) PC-4

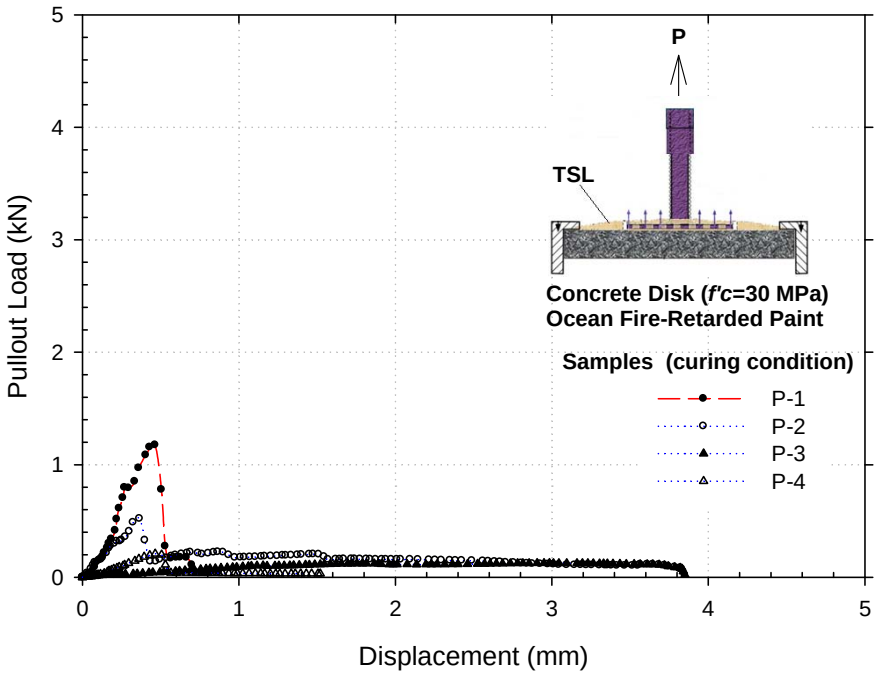

Figure 5.13 Load-displacement test data for TSL sprayed on the painted concrete specimens

CHAPTER 6

EVALUATION OF TSL EFFECT ON THE LOAD CARRYING CAPACITY OF SEGMENTAL CONCRETE LINERS

6.1 INTRODUCTION

Precast concrete segmental tunnel linings are generally thought to be durable and require minimal maintenance. However, serious maintenance problems can be caused by earthquakes, leakage through lining joints, increasing traffic in tunnels, or chemical attack from the groundwater or environmental pollution. Liner damage caused by earthquakes or concrete degradation due to chemical attack can decrease joint stiffness and reduce the load-carrying capacity of tunnel linings. The factor of safety of a tunnel lining may gradually decrease as time passes due to these effects, and thus, it is important to evaluate the load carrying capacity for the existing concrete segmental tunnel linings (He and Wu, 2005).

The preceding section (see chapter 2) summarized the published literature dealing with load tests on segmental concrete tunnel linings. Thus far, published studies have attempted to investigate the effect of joint tolerances, steel and polymer-fibre reinforcement, concrete prestressing, and composite behaviour on the load-displacement response and structural capacity of tunnel linings. However, no studies have examined the response of conventional precast reinforced concrete (RC) segments coated with TSLs. Accordingly, the overall benefits of applying a TSL to precast RC tunnel lining segments will be demonstrated at the end of this chapter.

The objectives of this portion of the study are to:

1) evaluate the moment resistance of precast reinforced concrete tunnel lining segments similar to those used to construct TTC subway tunnels during the 1970's (Yonge and Spadina Line Extensions),
2) investigate the effect of a TSL on the load carrying capacity of the linings subject to the same loading,
3) develop a non-linear elasto-plastic finite element model using ABAQUS to simulate the structural response of the TSL coated and uncoated precast RC tunnel lining segments; and,
4) investigate the effect of a TSL on the crack development and propagation during the tests.

6.2 METHODOLOGY

6.2.1 TTC Segmental Concrete Liners

Figures 6.1 and 6.2 illustrate the dimensions of the precast RC segmental tunnel linings used to extend the TTC Yonge and Spadina subway lines during the 1970's. In this study, six full-scale TTC segments were fabricated and five were used to perform simply supported flexural tests. Three segments were sprayed with TSL to achieve a coating of thickness 3.5 mm, 4.0 mm or 4.2 mm, respectively. The other two segments were uncoated and their response during flexural testing was used as a benchmark for the TSL coated segments. As illustrated in Figure 6.1, the TTC tunnel linings consist of 8 segments and a key piece, which are bolted together to form rings; the rings are bolted together in the longitudinal direction to form the tunnel lining. The tunnel lining has an outer diameter of 5000 mm and the segments have a width of 610 mm, thickness of 150 mm and length of approximately 1800 mm.

The segments have three bolt pockets, which enable the segments to be bolted together during construction. There are two end 350×350×100mm (L×W×D) bolt-pockets situated 120 mm from the end of each segment and approximately 130 mm from the left and right sides. The third pocket is situated at the middle of the segments. The middle bolt-pocket is 150×350×100mm (L×W×D). The end bolt-pockets provide access to steel ferrule-lined bolt holes, which enable installation of two circumferential bolts and two longitudinal bolts at the end of each segment. The middle-pocket provides access to install two longitudinal bolts only.

The segment flexural steel consists of four 12mm diameter steel bars embedded in the outer ribs of the segment and oriented in the circumferential direction as shown in Figure 6.2. The segments are further reinforced with stirrups to provide confinement for the concrete and shear resistance. The unconfined compressive strength of the concrete was 40 MPa.

6.2.2 Simply Supported Flexural Test

Figure 6.3 illustrates the test setup. Referring to the right side of Figure 6.3, the segments were placed concave side down and supported at each end using L-section (L150×150×12.5mm) beams resting on steel plates at the right end and on a steel plate on roller bars at the left end. Two H-beams were placed horizontally at the right end of the segment as struts to prevent horizontal displacement, while the other end was free to move.

A single point-load was applied at the mid-span of the segment using a computer-controlled hydraulic actuator (MTS hydraulic actuator; Model No. 204.71) with a 250kN load capacity and maximum stroke of 150 mm. The actuator was suspended from a stiff reaction frame and the

actuator load was spread onto the segment using a 600 mm long hollow structural steel section (75×75×12.5mm) and a 620×110×25.4mm steel plate; both were placed on the segment at the mid-span giving a loaded area of 67100 mm^2.

6.2.2.1 Instrumentation plan

Figure 6.4 shows the instrumentation plan including the segment dimensions and the positions of strain gauges (labeled S-) and displacement transducers (labeled D-). As shown in Figure 6.4, eight strain gauges and eight displacement transducers were used to measure the strain and displacement at the segment extrados and above the centre of the side bolt pockets. All strain gauges were located on the outer surface (extrados) of the segment to measure the compressive strains. The tensile strains at the segment intrados were not measured because it was considered that high tensile strains would occur during the test due to cracking and that the cracking would damage the gauges. The strain gauges (Showa and N11-FA-30-120-11) are denoted by S-1 to S-8 in Figure 6.4. The gauge length was 30 mm, sensitivity was 1 με and the measurable strain was 2% to 4% maximum. Similarly, the displacement transducers (Penny & Giles; HLP190/FS1/100/4K) are labeled D-1 to D-8 and have a maximum tolerance of 0.01mm. Figure 6.5 shows the testing setup associated with the full instrumentation.

6.2.3 Test Procedures

The following summarizes the test procedures used to determine the load-displacement response of TTC segmental concrete liner with or without TSL coating:

6.2.3.1 Segment preparation

1) All segments were constructed using wooden forms according to Figures 6.1 and 6.2 using 45MPa concrete supplied by Lafarge, London, Ontario.
2) For each segment, rebar was placed in the forms using spacers to ensure the steel was positioned correctly. Then, concrete was placed into the forms by hand (i.e. using wheel barrows and shovels) and vibrated to consolidate the concrete. After placing the concrete, the segments were cured at room-temperature in their wooden forms for about 6 months.
3) After curing, the segments were removed from their forms and stored in the Structures Lab at the University of Western Ontario for 3 years after which the segments had been abraded and some hairline cracks on the inner surface of the segments had developed.
4) Three segments were then transported to Spray-on-Plastics Inc. in Milton to apply a TSL coating. The inner surface of each segment was sand blasted prior to applying the TSL coating.
5) TSL was sprayed in three consecutive layers and allowed to cure for several minutes.
6) After spraying the TSL, the thicknesses of three random locations were measured to check that TSL layer did not exceed 4.5 mm in thickness.
7) The TSL sprayed concrete segments were then transported back to the University of Western Ontario and the TSL was allowed to cure for 7 days at room temperature in the Structures Lab.

8) For each load test, the segment was carefully lifted using a 20-Ton capacity overhead crane and positioned beneath the load frame and actuator. Then, the L-beams were placed on both edges. One end was fixed by two H-beams anchored on the floor and the other end was placed on rollers.

6.2.3.2 Load test

1) For each test, the segment was situated on the L-beams and leveled.
2) The load plate and hollow square structural steel section were positioned at the middle of the segment and the actuator was brought into contact with the load plate.
3) The actuator was then set at a displacement rate of 0.2 mm/min and the segment was loaded.
4) When the load reached 20 kN, the segment was unloaded at a constant rate of displacement (0.2mm/min) until the load was reduced to 5kN.
5) Following unloading, the segment was re-loaded at 0.5mm/min until either the specimen failed as indicated by a significant loss of load resistance or the maximum actuator stroke (150mm) was reached (Tests 2 and 5 only).
6) During the test, cracks were marked and the entire test was videotaped (for only Test 2 and Test 5 which are reached a full displacement).

6.3 NUMERICAL ANALYSIS

In order to study the load-displacement response of the TTC lining segments with and without a TSL, a Finite Element (FE) model was developed using the commercial software ABAQUS. This section summarizes the FE procedures.

6.3.1 Finite Element (FE) Model

Figure 6.6 illustrates the 3-D finite element mesh. The FE mesh comprised 12599 10-noded tetrahedron elements for the uncoated and 16050 10-noded tetrahedron elements for the TSL coated segments. The circumferential flexural steel rebar (d=12 mm) in the segment rigs (see Figure 6.2) was modeled using an embedded rebar element model in ABAQUS. This model assumes the rebar is fully bonded to the concrete ensuring strain compatibility and it does not require modeling of the detailed shape of the reinforcement. Furthermore, the influence of the stirrups is also taken into consideration in this model. The reinforcement is modeled by modifying the stress-strain response of the 'reinforced' elements to reflect the effect of the flexural steel. Elements which have flexural steel were assigned a percentage of steel (2%) based on Figure 6.2.

6.3.2 FE Model Parameters: Concrete

There are two concrete constitutive models in ABAQUS: (i) a concrete smeared cracking (CSC) model and (ii) a concrete damaged plasticity (CDP) model. Each model is designed to provide a general capability for modeling plain and reinforced concrete (Pevsner et al, 2005). Both models were investigated by the author and the CDP model was used in this thesis because the CSC model was found to have trouble converging after the concrete yielding and, as discussed in the

preceding sections, one of the main objectives of this research was to interpret the load-deflection responses until the peak strength.

The CDP model is a continuum plasticity-based damaged model, which is able to simulate the non-linear stress-strain response of quasi-brittle materials such as concrete. The model is based on the theories of isotropic damaged elasticity (Bazant and Kim, 1979; Ortiz, 1985; Lubliner et al., 1989; Imran and Pantazopoulu, 2001; Ananiev and Ozbolt, 2004; Kratzig and Polling, 2004; Menzel et al., 2005) and isotropic plasticity (Chen and Chen, 1975; William and Warnke, 1975; Dragon and Mroz, 1979; Chen and Buyukozturk, 1985; Onate et al. 1988; Voyiadjis and Abu-Lebdeh, 1994; Karabinis and Kiousis, 1994; Este and Willam, 1994; Menetrey and Willam, 1995; Grassl et al. 2002). The CDP model simulates (1) the stress-strain response of concrete for arbitrary and cyclic loading, (2) stiffness recovery effects under cyclic loading, (3) tensile cracking and compressive crushing of the concrete material, and (4) strain-hardening or softening of the yield and failure surface under tension and compression loading (Lubliner et. al. 1989). The concrete material properties and FE parameters for the CDP model are summarized in Table 6.1. The following paragraphs summarize the modeled stress-strain response of concrete based on the material parameters listed in Table 6.1.

The stress-strain response of concrete in the CDP model is governed by a series of analytical equations. The concrete strain at the peak compressive stress is defined using an equation proposed by De Nicolo et al. (1994) and the stress-strain response is defined using the equations of Carreira and Chu (1985). For concrete with an unconfined compressive strength, f_c' of 40 MPa, the axial strain at failure is (De Nicolo et al. 1994):

$$\varepsilon_o = 0.00076 + [(0.626 f'_c / f^* - 4.33) \times 10^{-7}]^{\frac{1}{2}} \qquad \text{[Eq. 6.1]}$$

where ε_o is the axial strain at the peak stress, f'_c is the unconfined compressive strength, and f^*=1 MPa. De Nicolo et al. (1994) have shown that Eq. 6.1 agrees with the measured compressive strength (f'_c) and strain at f'_c (ε_o) for concrete with an f'_c between 10 MPa and 100 MPa. Given ε_o , the stress at any strain ε below f'_c is (Carreira and Chu, 1985):

$$\sigma_c = f'_c \beta(\varepsilon / \varepsilon_o) / \beta - 1 + (\varepsilon / \varepsilon_o)^{\beta} \qquad \text{[Eq.6.2]}$$

where σ_c is the stress at ε , ε is the arbitrary normal strain , and β is an empirical parameter based on the equation $[f'_c/32.4]3+1.55$. In the CDP model, the concrete stress-strain response is governed by Eqs. 6.1 and 6.2 and the modeled stress-strain behaviour of 40MPa concrete is plotted in Figure 6.7. The parameter β in Eq. 6.2 has been calibrated to give an initial elastic modulus equal to (Mander et al. 1988):

$$E = K_1 K_2 33500 (\frac{\sigma'_c}{60})^{1/3} (\frac{\rho}{2.4})^2 \qquad \text{[Eq. 6.3]}$$

where, K_1 and K_2 are constants, and $\sigma_c' = 2f'_c(\varepsilon/\varepsilon_o) - f'_c(\varepsilon/\varepsilon_o)^2$ and ρ = density of concrete (g/cm^3).

6.4 RESULTS

6.4.1 Measured Displacement

Results from Test 1 and Test 2, corresponding to the uncoated segments, are presented in Figures 6.8(a) to 6.8(d). Test 1 was only conducted until the maximum displacement (at D-3) reached 20 mm, whereas Test 2 was carried out until the maximum displacement exceeded 120 mm. The results show that the two segments have quite similar load-deflection responses and capacities. As a consequence, the resultant load-displacement response summarized in Figures 6.8(a) to (d) are considered to be suitable for use as benchmark tests to evaluate the influence of TSL on the segment capacity.

Figures 6.9(a) to 6.9(d) show the results from Test 3, Test 4, and Test 5 corresponding to the segments that were coated with TSL. As shown in these figures, the results from Test 4 and Test 5 present quite consistent load-displacement relationships while the load-displacement result from Test 3 shows slightly lower flexural strength (about 14% lower). Such variations are probably due to variations in the quality of construction and curing of the segments. As seen in Figure 6.9(b) and 6.9(c), the load-carrying variations occurred after the concrete yielded (i.e., 50kN). For instance, a load of approximately 53 kN is required to maintain a displacement of 20 mm in Test 3 while a load ranging from 60 kN to 65 kN is required to keep the same displacement in Test 4 and Test 5 (see Figure 6.9 (b)). It is evident that the thickness of TSL coating may affect the load-carrying capacity after the concrete yields. The segments used in Test 4 and Test 5 have a TSL thickness of 4.0 mm and 4.2 mm, respectively, but the TSL thickness was 3.5 mm for the segment used in Test 3. Based on the preceding discussions, the

results from Test 4 and Test 5 are used to examine the TSL effect on the load-carrying capacity compared to the benchmark results from Test 2 in Section 6.4.2.

6.4.2 Measured strain

Figures 6.10 (a) to (c) summarizes the strains measured during the benchmark tests (i.e. uncoated segments) and Figures 6.11(a)-(c) show the corresponding strains measured during tests on the TSL coated segments (i.e. Test 3, Test 4 and Test 5). As noted above, Test 1 was terminated at a displacement of 20 mm and Test 2 was conducted until the maximum displacement exceeded 120mm.

Figures 6.10 (a) through (c) summarize strains measured on uncoated concrete segments in Test 1 and 2. Referring to Figures 6.10, the strains measured at S-1 through S-3 in Test 1 and Test 2 and S-6 through S-8 in Test 1 show good agreement with maximum strains between 250 and 300 με. Substantial variations for gauges S-6 and S-8 can be seen in Figure 6.10 (b). For example, the strain difference at S-6 in Test 1 and Test 2 is approximately 500 με when the load is 50kN. Strains at the middle of the segment ribs are summarized in Figure 6.10 (c). The difference in strain at S-4 to S-5 reduces as the load increases and shows a good match at loads between 50kN and 62 kN. At a load of 62kN, which is considered to be the ultimate load, the strains at S-4 to S-5 reached approximately 3000 με. Figures 6.11 (a) to (c) present the strains measured in Test 3, Test 4, and Test 5 using the segmental concrete liners with the TSL coating. Referring to Figure 6.11(a), strains measured at S-1, S-2 and S-3 in Test 3 and Test 4 experienced a similar amount of strain until the load reached 40 kN. And then, a minimal change in strain from Test 4 can be found when the load was higher than 40 kN. In Test 5, the strains at S-1 and S-3 were

recorded at slightly lower level than the strains measured at the same places in Test 3 and Test 4. A similar pattern can be observed at S-2 in all tests. The strain changes at S-6, S-7 and S-8 presented in Figure 6.11 (b) show a similar trend to the strains measured at S-1 to S-3. Strains at S-4 and S-5 in Test 3, Test 4 and Test 5 did not demonstrate consistency under the load of 40 kN except for strains at S-4 in Test 4 and Test 5. However, strain gauges in the middle of the segments, S-4 and S-5, presented substantial differences at loads between 30 kN and 60 kN. The difference is approximately 300% which might be related to the difference of the failure mechanism or an unbalanced load distribution.

To conclude, the displacements and strains measured in Test 4 and selected data from Test 5 were used for the comparison which examined the TSL effect on load-carrying capacity of the segmental concrete liners.

6.4.3 Evaluation of the TSL effect

6.4.3.1 Displacement comparison

Figure 6.12 compares the load-displacement behaviour of the concrete segments with and without the TSL coating. The displacements correspond to gauge point D-3, which is situated just beside the loading zone. As shown in this figure, the load-displacement response of the uncoated segment (i.e. Test 1) and the TSL coated segments (i.e. Tests 4 and 5) are similar up to Point ‘B’, related to the points of concrete yielding. After Point ‘B’, it can be seen that the TSL coated segments have slightly higher load capacity compared to the uncoated segment. For instance, at a displacement of 30 mm, the corresponding load for the uncoated concrete segment was about 61 kN while the corresponding load for the TSL coated segment was 65 kN. Also, the

peak load (i.e. Point C_1) for the uncoated concrete segment was 63 kN while the peak loads (C_2) for the TSL coated segments were between 65 kN and 68 kN for Tests 5 and 4, respectively. Also, the load and displacement corresponding to yielding of the reinforcing steel rebar (i.e. Points A_1 or A_2) varied from 44 mm at 67 kN to 58 mm at 61 kN for the TSL coated and uncoated segments, respectively. After reaching the ultimate load, differences in the load-carrying capacity of the uncoated and the TSL coated segments gradually decreased.

Figure 6.13 illustrates the load-displacement curves at D-1 and D-2. Although there are some variations in the load-displacement curves at loads less than 50 kN, the overall load-displacement behaviour was similar to the results at D-3 shown in Figure 6.12. The peak load for the TSL coated segments was about 5 kN higher than the peak load for the uncoated segments. In addition, the displacement at the peak load was 20 mm for both coated and uncoated cases.

Figure 6.14 presents the load-displacement curves at D-4 and D-5. Referring to Figure 6.14, the displacement was about 24 mm at D-4 and D-5 at the peak load. No significant differences can be found in the load-displacement patterns at D-4 and D-5 compared with the response at D-1 and D-2 except that the displacements were larger at D-4 and D-5 at the peak load (24mm) compared to D-1 and D-2 (20mm). This difference could be due to the influence of the TSL coating, which has a rough finish that may have caused some minor variation of the dial gauge readings as the segments moved laterally (i.e. the roller support permitted some very small lateral movement).

Finally, the horizontal displacements during the tests at D-8 are presented in Figure 6.15. The TSL effect can be clearly seen in this figure. Despite slightly higher loads being applied to the TSL coated segments, the maximum horizontal travel distance recorded for the TSL coated segment was 45 mm while the horizontal travel distance for the uncoated concrete segment was 55 mm. This behaviour indicates that the TSL carried tensile stress of the segments.

Based on the preceding results and discussion, it is confirmed that (i) application of a TSL coating to the segments increases the load carrying capacity (i.e. flexural strength) of the segment, and (ii) the tensile stiffness is increased most notably after concrete cracking is initiated at the segment intrados leading to non-linear load-displacement behaviour.

6.4.3.2 Strain comparison

Figure 6.16 summarizes the strains measured at S-4 and S-5 for both the uncoated and TSL coated segments. Strains at S-4 in Test 1 and 2 were used as a benchmark. Generally, higher strains were measured at the extrados of the TSL coated segments at the same load compared with the uncoated segments. For example, compressive strains in the uncoated segments were about 600 με at a load of 50kN compared to 1000, 1450 and 1700με for the coated segments. This is difficult to explain since higher compressive strain at the segment extrados should be accompanied by larger flexural deflections. In this case, however, the measured deflections were similar if not slightly lower for the TSL coated segments compared with the uncoated segments. These results suggest that the TSL may increase compressive strains in the segment during loading but reduce the flexural strains.

Figure 6.17 presents the strains measured at strain gauges S-1, S-3, S-6 and S-8. Again, as seen above with respect to Figure 6.16, the measured strains were higher in the coated segments compared to the uncoated segments. The maximum compressive strains measured at the extrados of the uncoated segments were between 240 με and 320 με at a load of 60 kN while the corresponding strains in the TSL coated segments were between 760 με and 840 με. Again, it is hypothesized that the TSL may be improving the flexural performance of the segments by increasing the overall level of compression in the segments and simultaneously reducing the flexural strains (i.e. the difference between the strain at the extrados and intrados). This hypothesis will be assessed in Section 6.4.3, which summarizes the results of FE analysis.

To conclude, Figure 6.18 plots the measured strains at S2 and S7, which are situated above the bolt pockets. As shown in this figure, there is negligible difference between the strain measured at the centerline of the coated and uncoated segments above the two bolt pockets. Comparing Figures 6.17 and 6.18, it can be seen that the concrete strains in the uncoated segments are comparable at the segment edges (S1 and S3 and S4 and S6) and centerline (S2 and S7). For the coated TSL segments, the strains at S2 and S7 are similar to the uncoated strains at the same load; however, the compressive strains along the edges are 2.5 to 3-times higher. This suggests that the TSL does not play a significant role in the thinner sections where there are bolt pockets. The maximum effect of the TSL appears to be over the segment ribs at the edges of each segment where the liner thickness is 150mm. The behaviour in Figures 6.17 and 6.18 appears to support the phenomenon that the TSL increases the level of compressive load in the ribs along the segment borders and reduces the flexural strains in the segments.

6.4.4 FE Analysis Results

FE results using ABAQUS are compared to the experimental results in Figures 6.19 to 6.24. Due to the segment symmetry, calculated displacements at D-1 and D-2 were the same as those calculated at D-4 and D-5. Additionally, the calculated strains at S-1 and S-3, S-4 and S-5, and S-6 and S-8 were also the same. Thus, the displacements computed at D-1, D-3, and D-4 and the strains calculated at S-1, S-2 S-4, S-6 and S-7 were compared with those measured from the tests. Additionally, post-failure behaviour could not be predicted because FE calculations did not converge after the steel rebar reached its yield limit.

6.4.4.1 Comparison with measured displacements

Figure 6.19 compares the calculated and measured load-deflection response of the TSL-coated and uncoated segments. Referring to Figure 6.19, it can be seen that the experimental and FE results matched quite well. The FE load-deflection curve has a steeper slope than the experimental results at the initial loading stages up to 40 kN load. In general, the FE model exhibited a stiffer response than the actual segments up to 20mm of displacement. After reaching 40kN, the FE model response becomes highly nonlinear and the gap between the measured and FE load-deflection curves decrease. In the nonlinear zone, concrete yielding occurred and the steel rebar began to carry the load. The FE calculations were then stopped when the steel yielded at 63 kN and 66 kN for the model with a TSL layer and without the layer, respectively. At these loads, the FE model was unable to converge. Figure 6.20 compares the calculated and measured response at D-1 and D-4 where similar trends can be observed.

To conclude, Figure 6.21 shows the calculated and measured horizontal displacement at D-8 Based on this figure, it is clear that the horizontal displacement behaviour of the uncoated and TSL coated segments can be predicted using ABAQUS. It can be seen in this figure that the load-displacement responses are similar up to the point where the reinforcement yields and the FE model is unable to converge.

Consequently, the results of the FE analyses closely match the measured displacements for the coated and uncoated segmental concrete liners subjected to a point loading at the mid-span. This suggests that the material properties of the concrete and TSL are reliably modelled. The pattern of the load-displacement curve from FE analysis is similar to those from the tests. However, the calculated behaviour was found to be stiffer than the measured response for loads up to 40kN. The agreement between calculated and measured load-displacement performance improved as the load approached the peak or ultimate load. The difference in displacement at loads less than 40 kN is about 200% on average. However, at higher loads, the difference is reduced to less than 21%.

6.4.4.2 Comparison with measured strain

It is difficult to both measure the concrete strain and predict the strains using FE analysis due to various environmental and mechanical differences between the practical experimental conditions and the theoretical FE analysis conditions. As known, the strain gauge readings can be affected by environmental conditions such as temperature and moisture and physical conditions such as bonding, surface uniformity and the homogeneity of the segmental concrete liners used in the

experiments and the FE analysis. In light of this, the following sections compare calculated and measured strains for the uncoated and TSL coated segments.

Figure 6.22 compares the calculated and measured strains at S-4 and S-5. Based on Figure 6.22, it can be seen that there is good agreement between the calculated and measured strains for the uncoated segments up to a load of 45 kN. Between 45 and 60 kN, the measured and calculated strains diverge but the agreement improves with the load level and the measured response is very comparable to the calculated response for loads exceeding 60kN. Overall, the FE model is able to adequately simulate the load-strain response. In contrast, there is considerable difference between the measured and calculated strains for the TSL coated segments for loads between 10 kN and 65 kN where the measured strains are generally twice the calculated strains. After yielding, however, the difference between the calculated and measured strains reduces becoming insignificant at the ultimate load. Both the measured and calculated behaviour suggest that the concrete compressive strains are higher for the TSL coated specimens compared to the uncoated specimens, which tends to support the hypothesis made in Section 6.4.2.

Figures 6.23 and 6.24 compare the calculated and measured strains at S-1, S-2, S-3, S-6, S-7 and S-8. These figures show a similar trend to that shown in Figure 6.22. In general, the calculated and measured strains are comparable for the uncoated segment tests. However, for the TSL coated segments, the difference between the calculated and measured strain is significant over the segment ribs (i.e. S-1 and S3) and negligible over the bolt pockets (i.e. S-2). Unlike the behaviour seen in Figure 6.22, the difference between the calculated and measured strain at S-1

and S-3 generally increases as the load increases whereas, at the midspan, the measured and calculated strains re-converged after the segment yielded and a plastic hinge formed.

In spite of the differences between the measured and calculated strains for the TSL-coated segments, the overall trend of higher compressive strains in the TSL-coated segments compared to the uncoated segments, in spite of the stiffer load-deflection response is evident in both the measured and calculated behaviour. The reason for this trend will be examined in the following section.

6.4.4.3 Distribution of strain in the segment rib

Figure 6.25 shows the calculated strain profile (positive value represents tensile strain) in the uncoated and the TSL coated segments at 20kN, 45kN and 60kN, respectively. In particular, this plot illustrates the strain profile in the ribs through the mid-bolt pocket of the segment. As seen in this figure, the strain profiles in the uncoated and the TSL coated segments have a similar pattern at a load of 20 kN. In contrast, at a load of 45 kN, tensile strain in the TSL coated segment is slightly higher than that in the uncoated segment. Lastly, the strain profile becomes similar again at a load of 60kN.

In general, higher strain occurs in the bottom of the section (tensile strain) and higher strain occurs on top of the section (compressive strain) because TSL holds concrete cracks causing higher strain in the bottom the rib. In consequence, higher tensile strain in the tension zone of the section causes higher compressive strain in the compressive zone including the outer surface of the segment. This mechanism can be observed from the measured strain shown in Figure 6.16.

6.5 SUMMARY AND CONCLUSIONS

In this chapter, the load-deflection response of precast RC segments similar to those used in the TTC subway tunnels constructed in the 1970s was examined during simply supported flexural load tests. The effect of the TSL on the load-deflection and ultimate flexural capacity of the segments was investigated both experimentally and numerically. The numerical study was performed using a nonlinear elastic-plastic FE model developed using the FE program ABAQUS. Additionally, the cracking patterns and different crack propagation characteristics with and without TSL layers are recorded and presented in Appendix-B.

An experimental approach to evaluate a TSL layer as a support agent for the existing concrete tunnel linings was performed. According to the results obtained from the tests, the TSL layer had a significant impact on the ultimate capacity of the segments and the load-displacement response after the concrete yielded (i.e. cracking). It is shown that a nonlinear FE model based on the Concrete Damaged Plastic (CDP) model in ABAQUS is effective in predicting the displacements and the strains of the segmental concrete liner subjected to point loading notwithstanding that the FE model tended to underestimate concrete strains over the segment ribs for the TSL-coated segments. In general, the following conclusions can be made from the results of experiments and FE analysis:

1) From the results of the load-displacement and load-strain relationships, it can be observed that the segment libs carry significantly higher loads than the thinner mid-zone of the segment.
2) The 4mm TSL layer contributes to the total load capacity of the liner segments most notably after the concrete yielding.

3) The TSL effect on the segmental concrete liner with a 4 mm thick TSL coating, using the nonlinear elastic-plastic FE analysis, can be adequately simulated using ABAQUS.
4) The displacements from the FE results are slightly higher than those measured during the experiments, especially for displacements less than 10 mm. For larger displacements, there is good agreement (within 10%) between the FE calculations and displacements measured.
5) There is satisfactory agreement (within 20%) between the calculated and measured strains for the uncoated segments. Similar agreement was observed for the TSL-coated segments but only for the mid-zone of the segments over the bolt pockets.
6) The compressive strains along the segment with the TSL layer are observed and calculated to be higher than those without the TSL layer. The measured strains, however, tended to be about 2 times higher than the calculated strains for the TSL coated tests.
7) Overall, it is concluded that the TSL improves the load-displacement response and ultimate capacity of the segments by promoting development of compressive strains in a larger portion of the segment and reducing the flexural strains prior to development of a plastic hinge (i.e. the difference between the strain at the extrados and intrados)
8) Considerable differences in failure mode can be observed between the uncoated segments and the TSL coated segments (see figures in Appendix-B). It is possible, therefore, that a TSL can effectively reduce the crack propagation in tension zones. This effect causes the higher compressive strain in the extrados of the segment ribs. It is also expected that there will be spalling reduction in some conventional concrete structures when using a TSL.

Table 6.1 TTC segmental concrete liner – FE model parameters

Parameter	Material		
	Concrete	**Rebar (C45 Steel)**	**TSL**
Initial tangent elastic modulus (E)	27800 MPa	210000 MPa	100 MPa
Poisson's ratio (ν)	0.2	0.3	0.3
Density	2500 kg/m^3	8030 kg/m^3	1100 kg/cm^3
Unconfined compressive strength (f_{cu})	40 MPa		
Initial Yield Stress (σ_y)	20 MPa	280 MPa	5.5 MPa
Tensile failure stress (σ_{tf})	3.3 MPa	800 MPa	8 MPa
Model Behaviour	CDP[1]	EP-S[2]	EP-S[2]

[1]Concrete Damaged Plasticity; [2]Elastoplastic strain-hardening

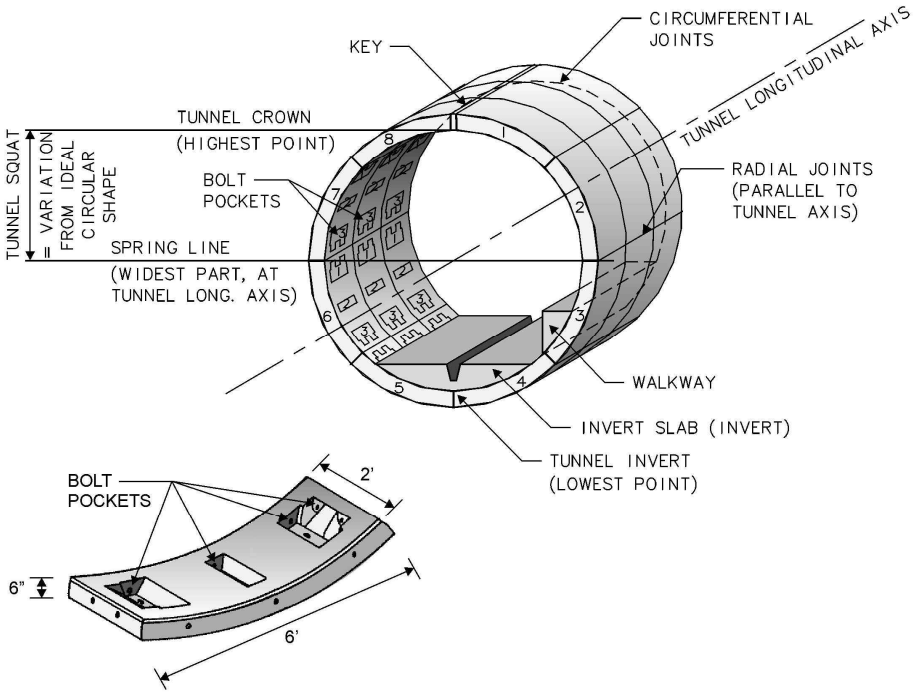

Figure 6.1 TTC segmental concrete linings

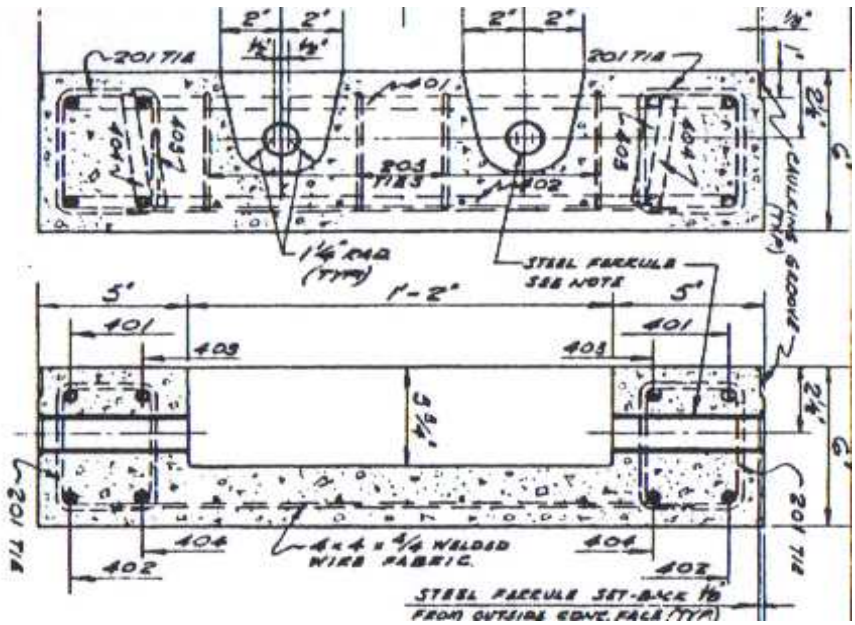

Figure 6.2 Detailed dimension and reinforcement layout

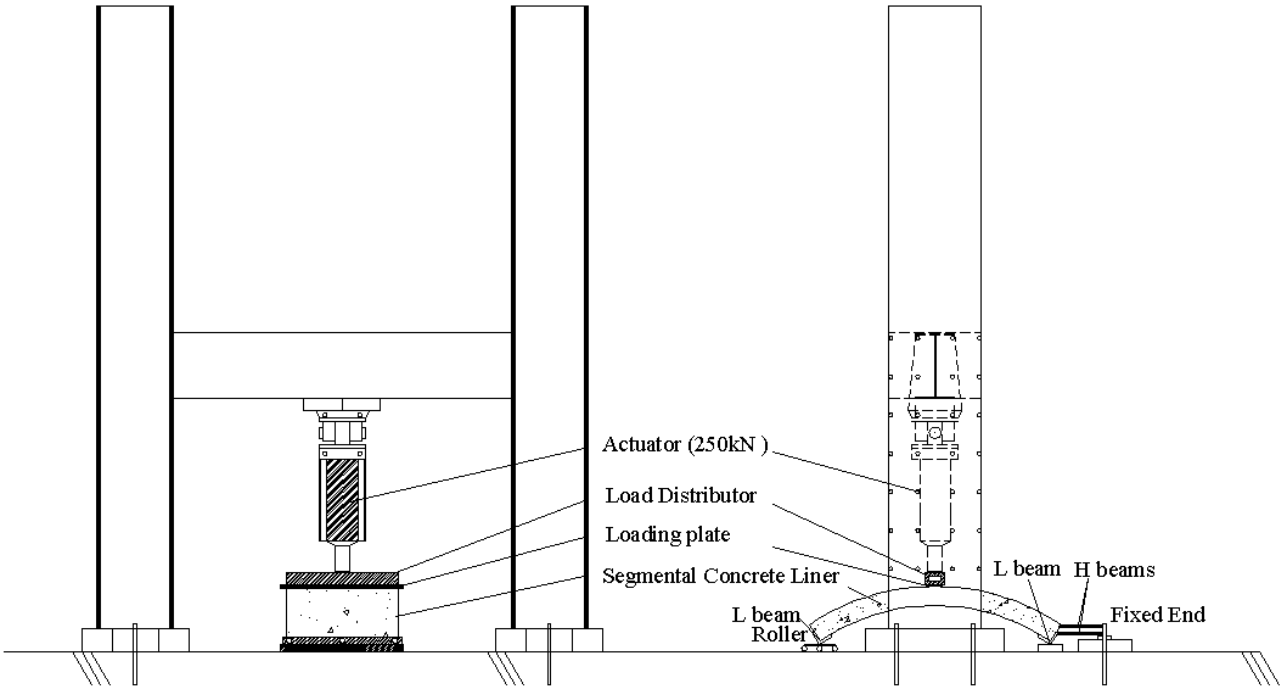

Figure 6.3 Experimental setup

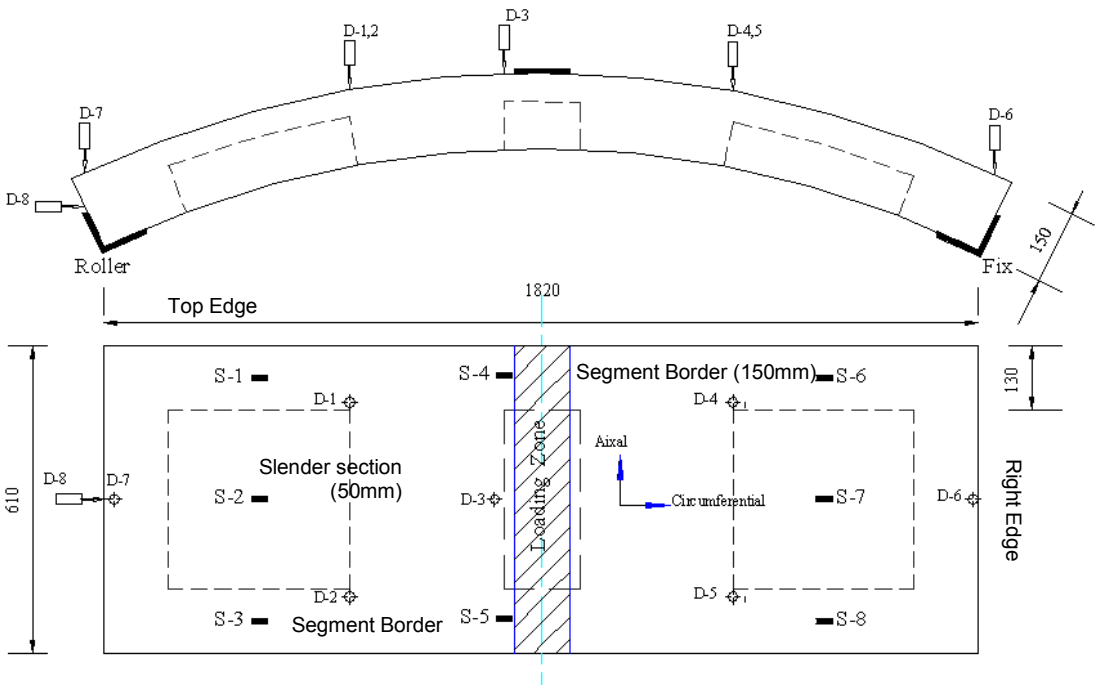

Figure 6.4 Instrumentation plan for the flexural test

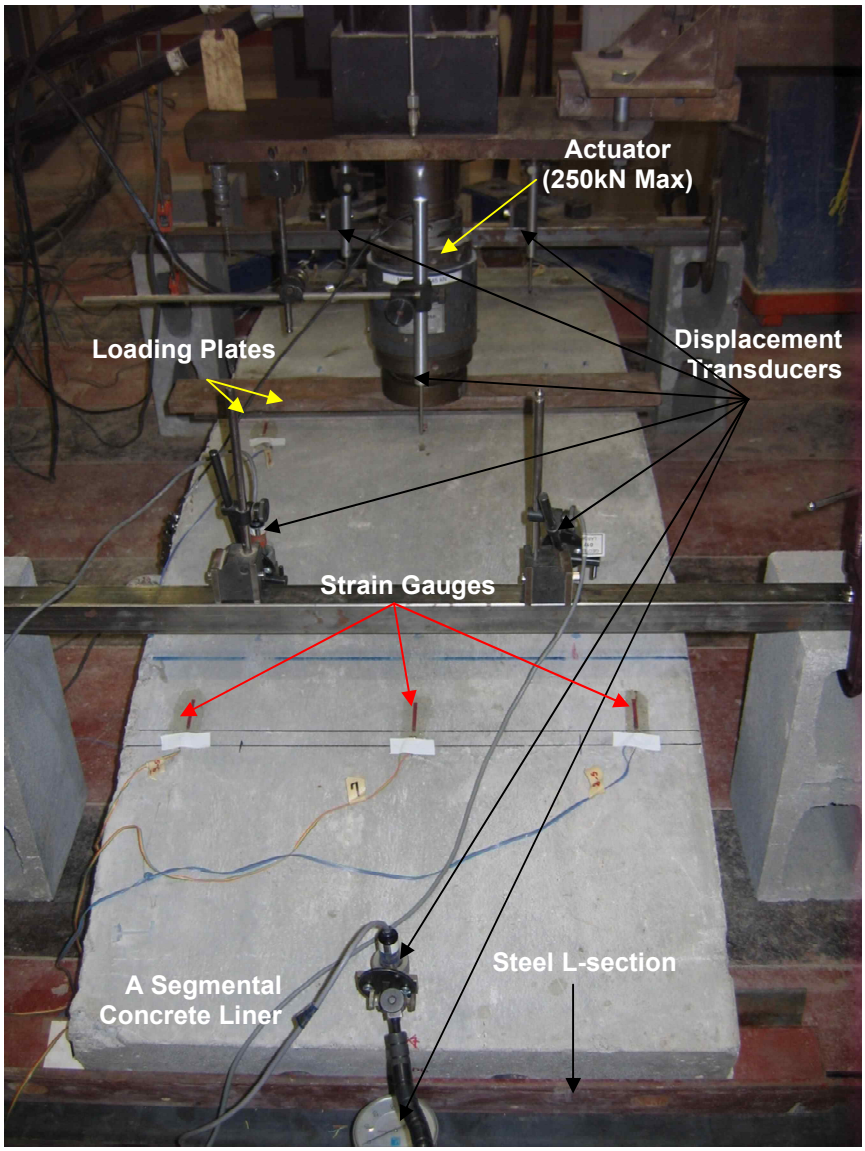

Figure 6.5 Testing setup with full Instrumentation

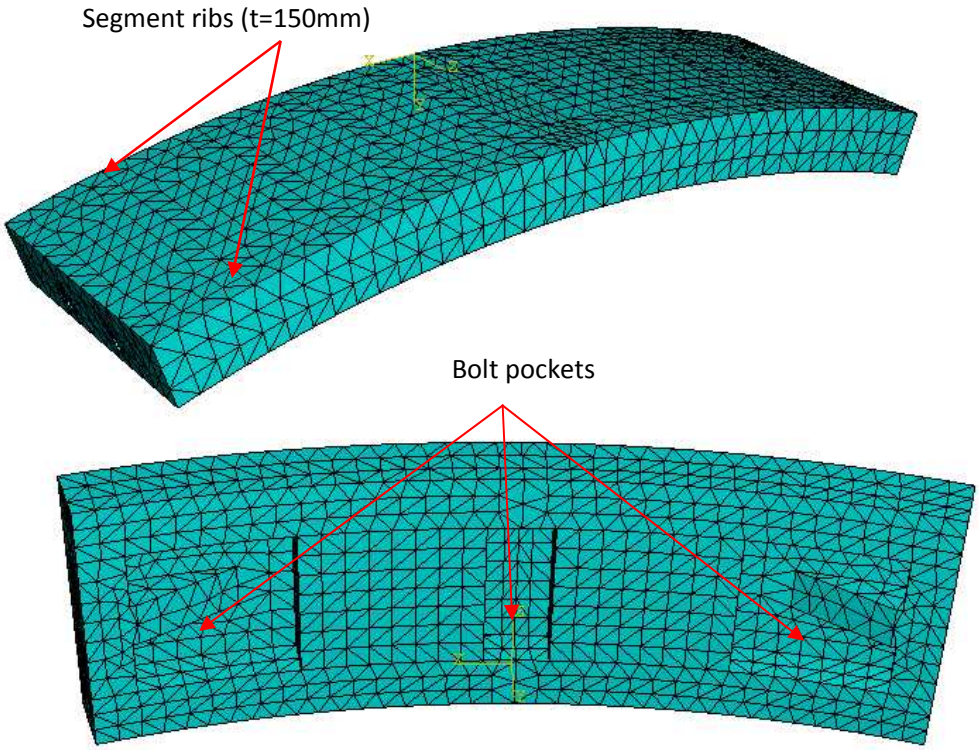

a) FE Model (without a TSL layer)

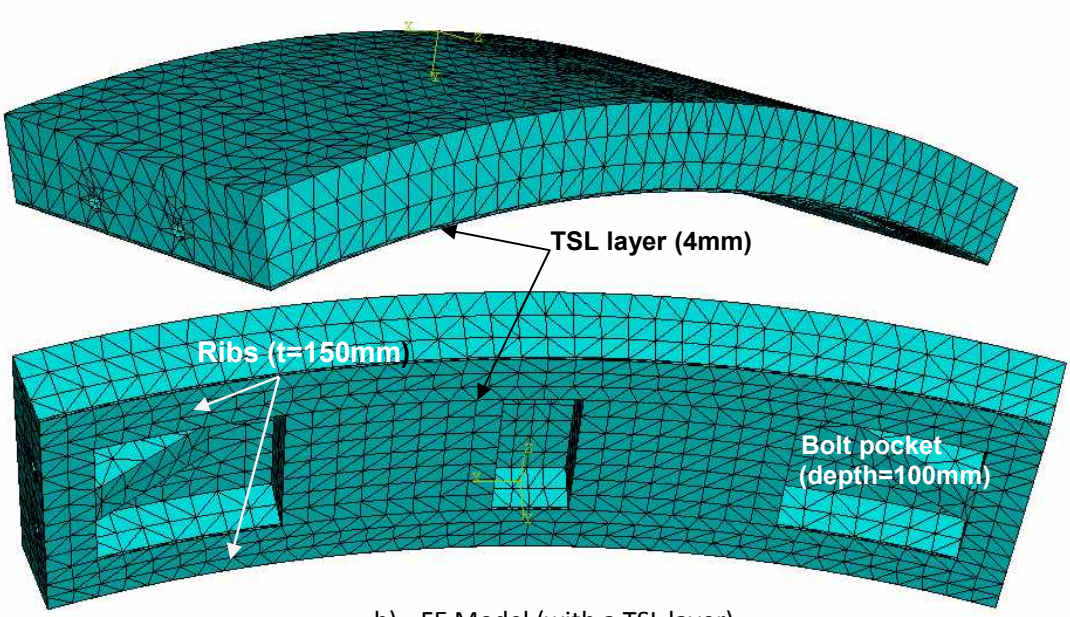

b) FE Model (with a TSL layer)

Figures 6.6 FE model of TTC segments
(12559 elements – the uncoated model; 16050 elements - TSL coated model)

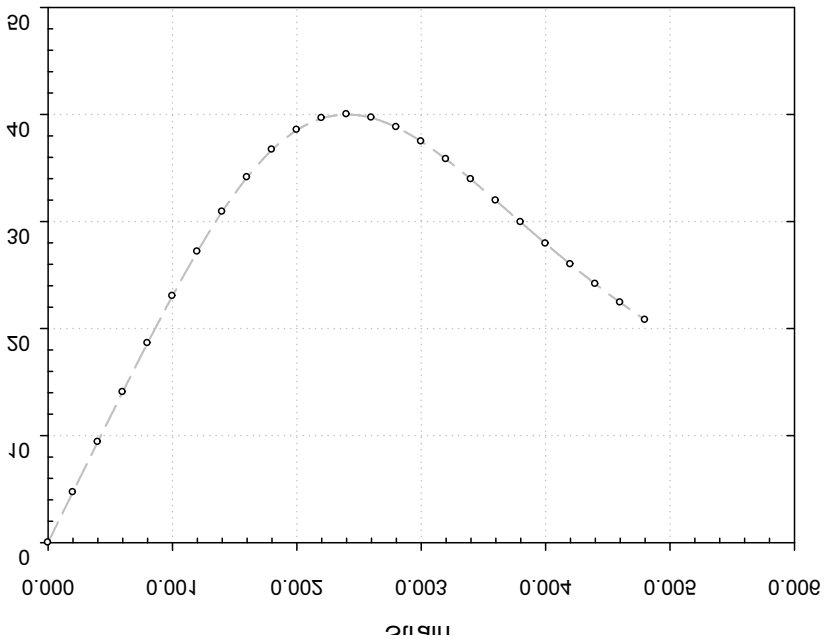

Figure 6.7 A stress-strain curve for 40 MPa concrete used in FE analyses

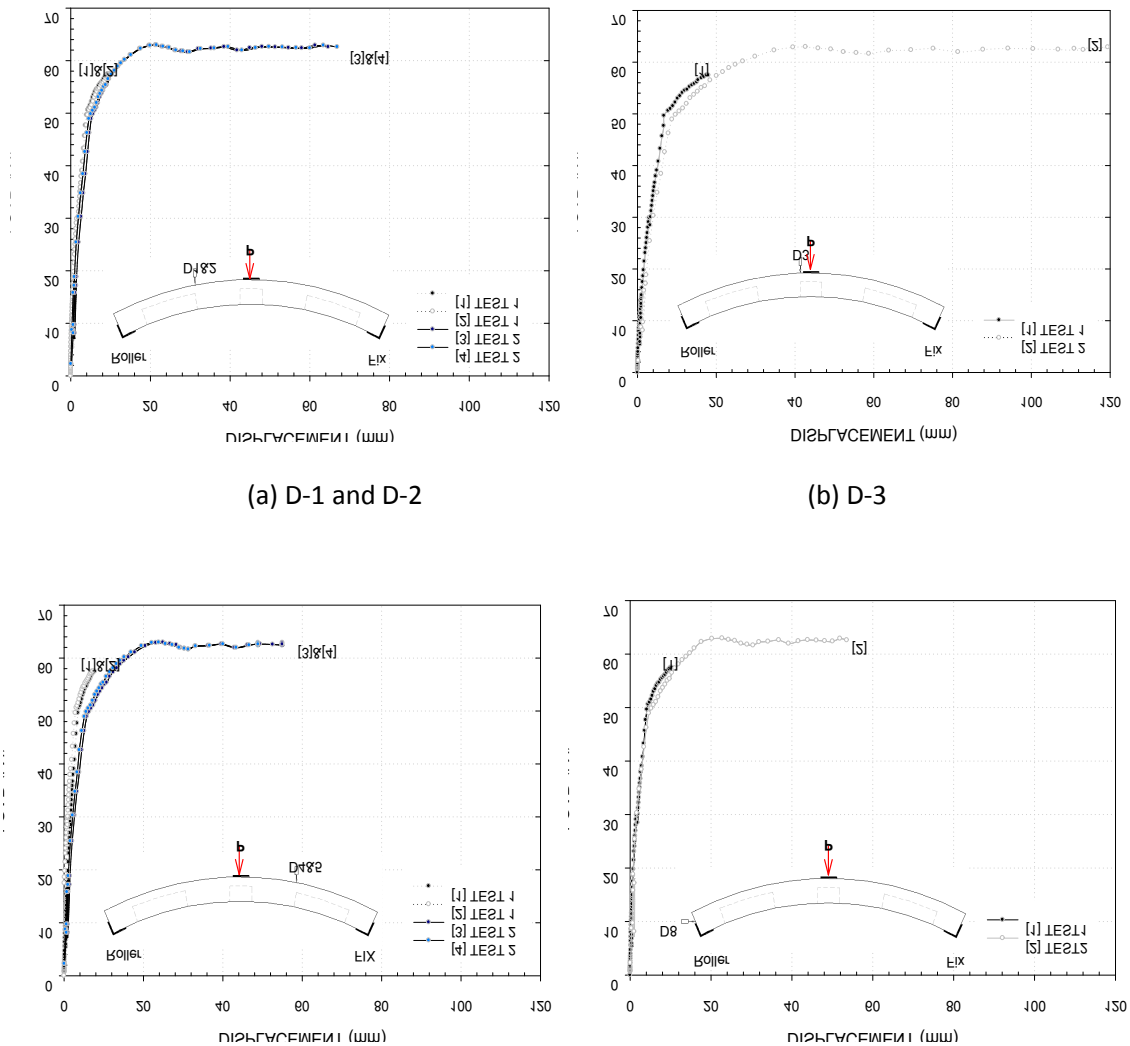

(a) D-1 and D-2

(b) D-3

(c) D-4 and D-5

(d) D-8

Figure 6.8 Load-displacement curves of the segments (no TSL)

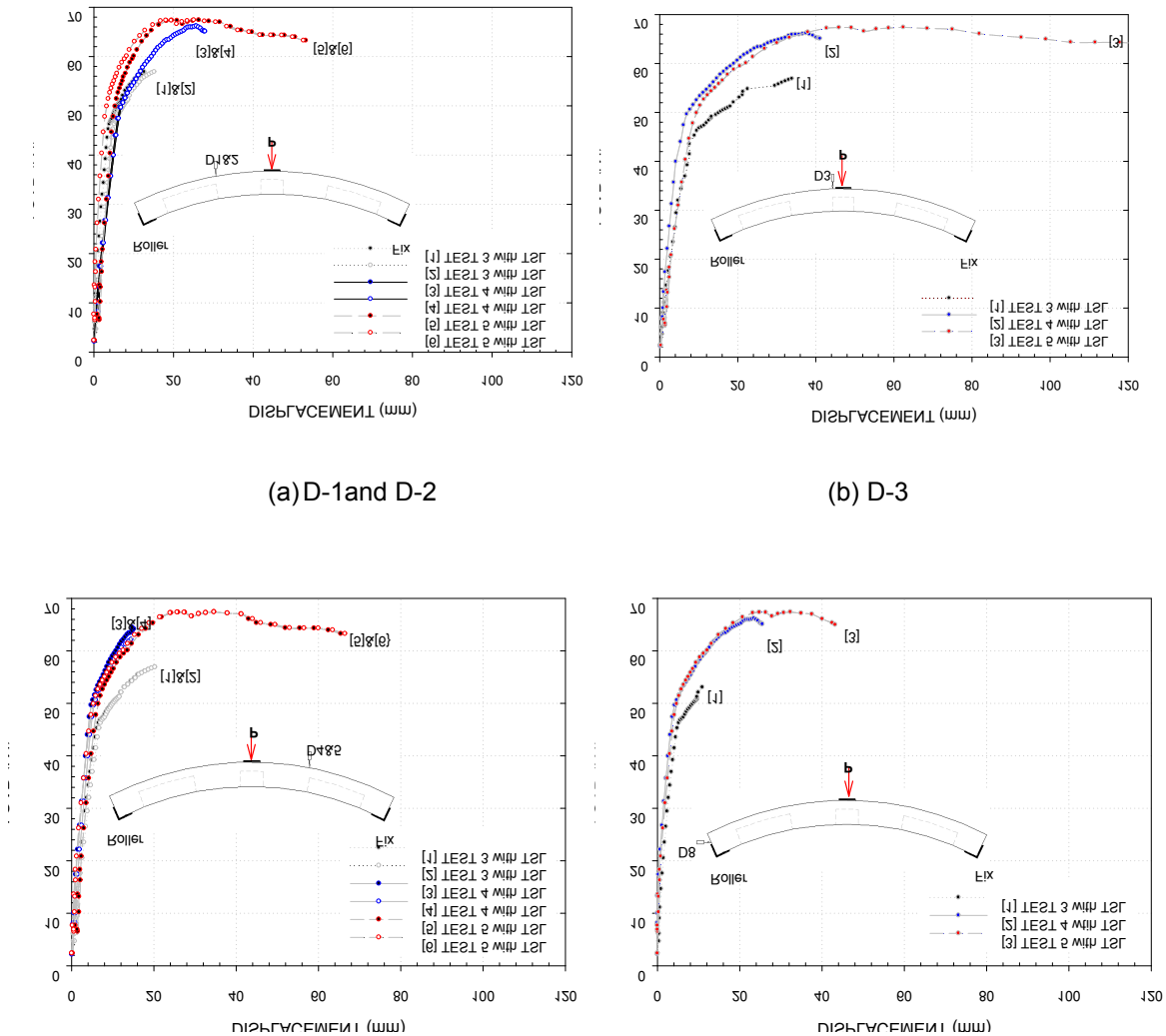

(a) D-1and D-2

(b) D-3

(c) D-4 and D-5

(d) D-8

Figure 6.9 Load-displacement curves of the segments (with TSL)

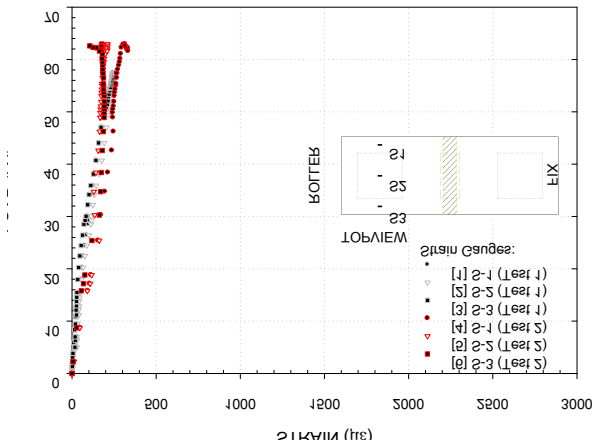

(a) S-1, S-2 and S-3

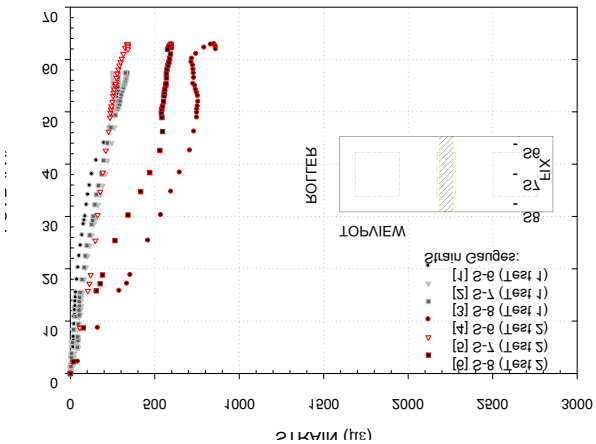

(b) S-6, S-7 and S-8

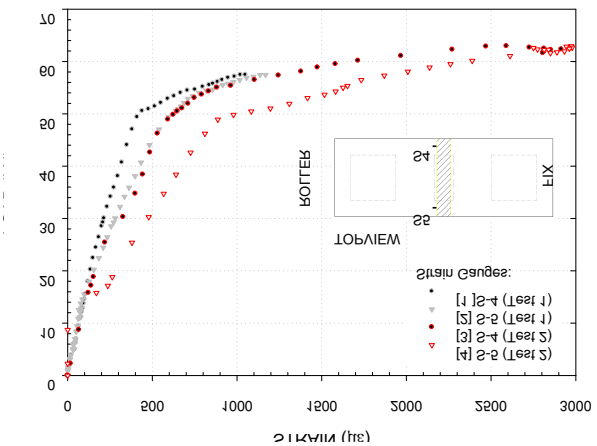

(c) S-4 and S-5

Figure 6.10Load-strain curves of the segments (no TSL)

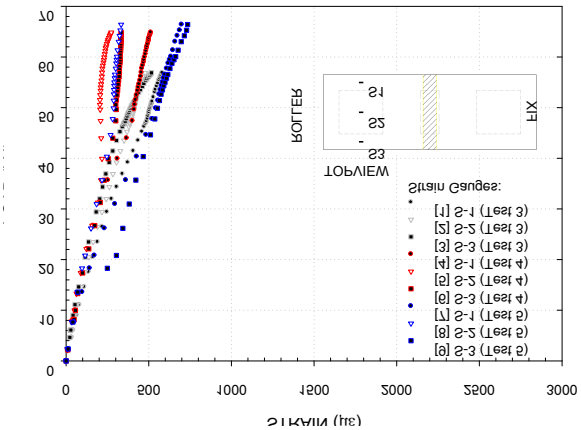

(a) S-1, S-2 and S-3

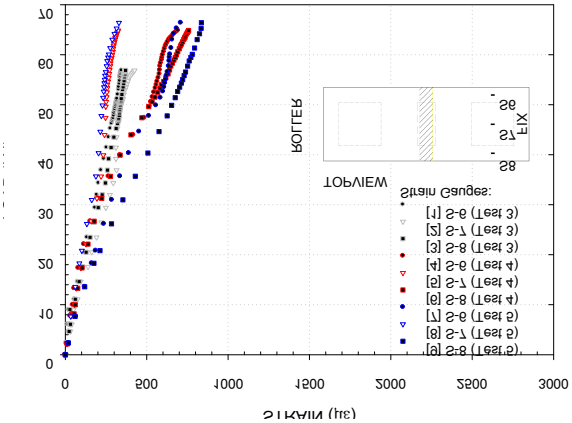

(b) S-6, S-7 and S-8

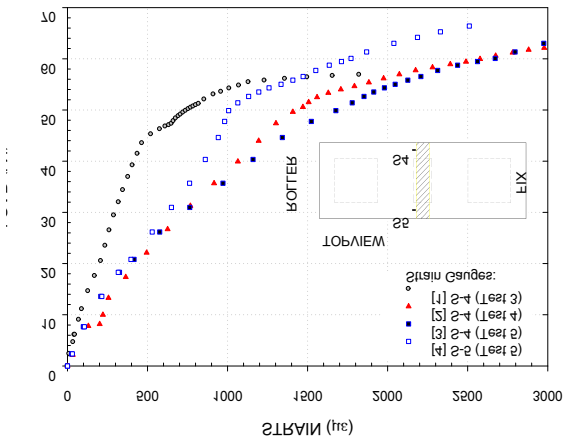

(C) S-4 and S-5

Figure 6.11 Load-strain curves of the segments (with TSL)

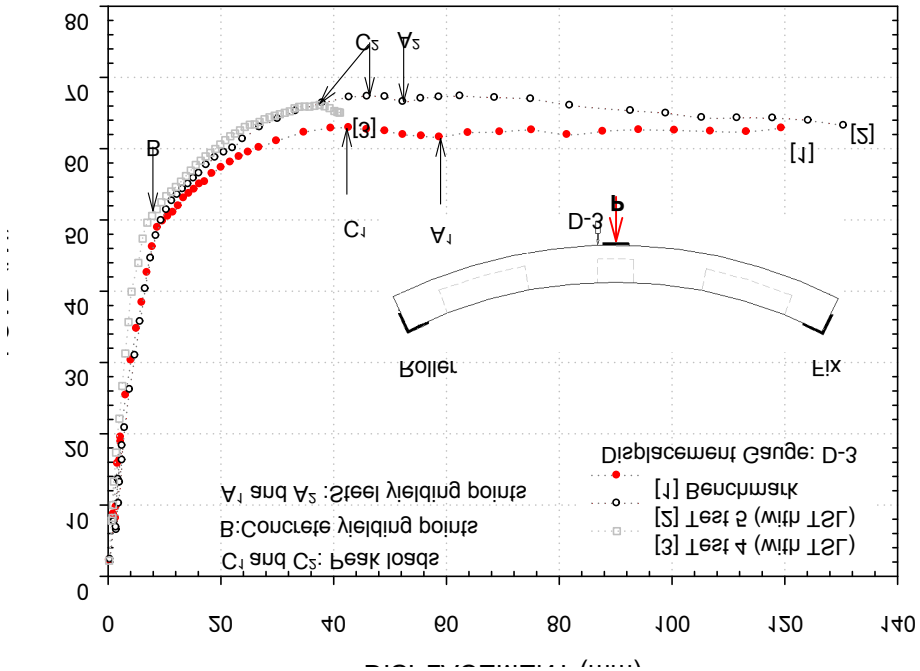

Figure 6.12 The vertical displacement comparison at D-3

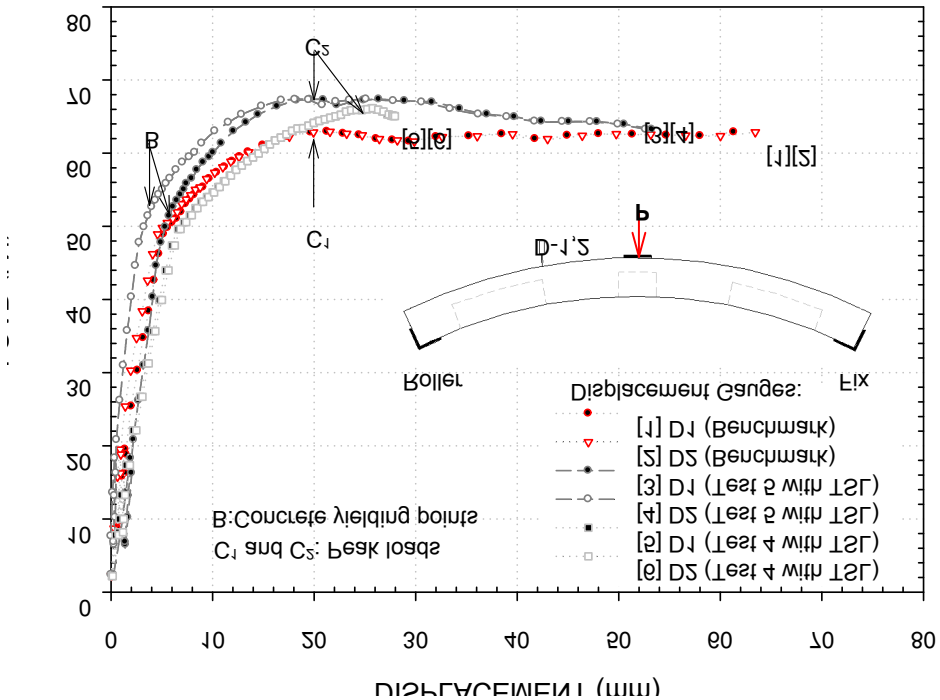

Figure 6.13 The vertical displacement comparison at D-1 and D-2

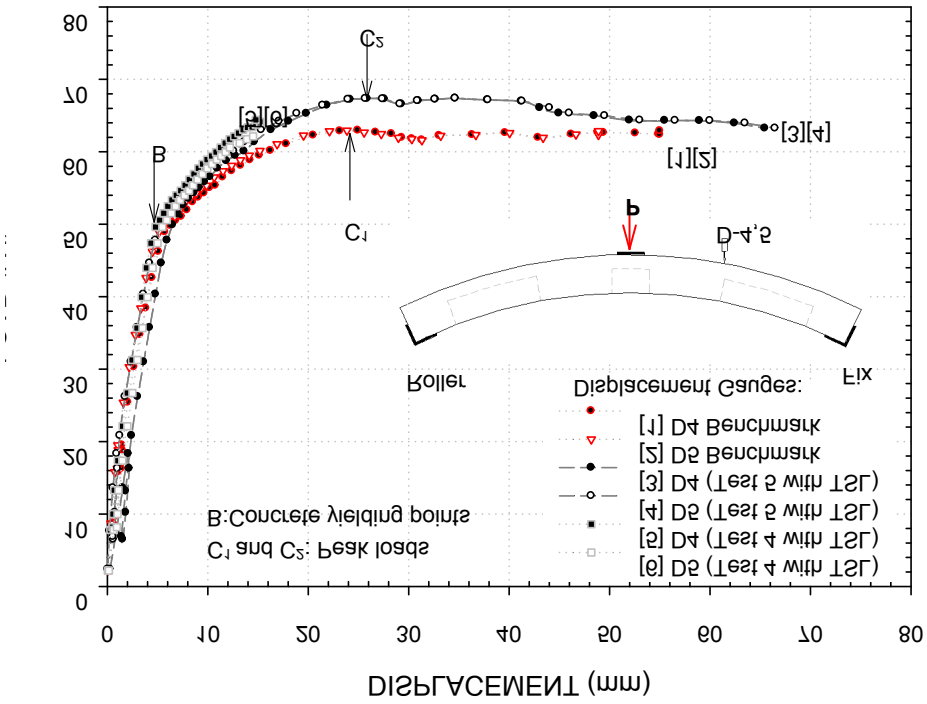

Figure 6.14 The vertical displacement comparison at D-4 and D-5

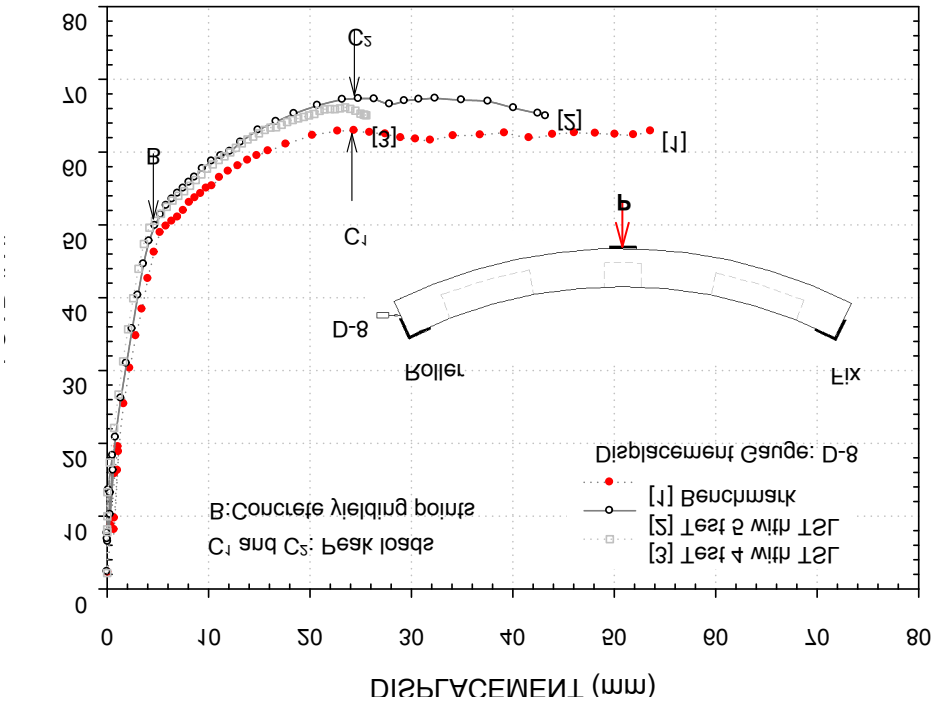

Figure 6.15 The horizontal displacement comparison at D-8

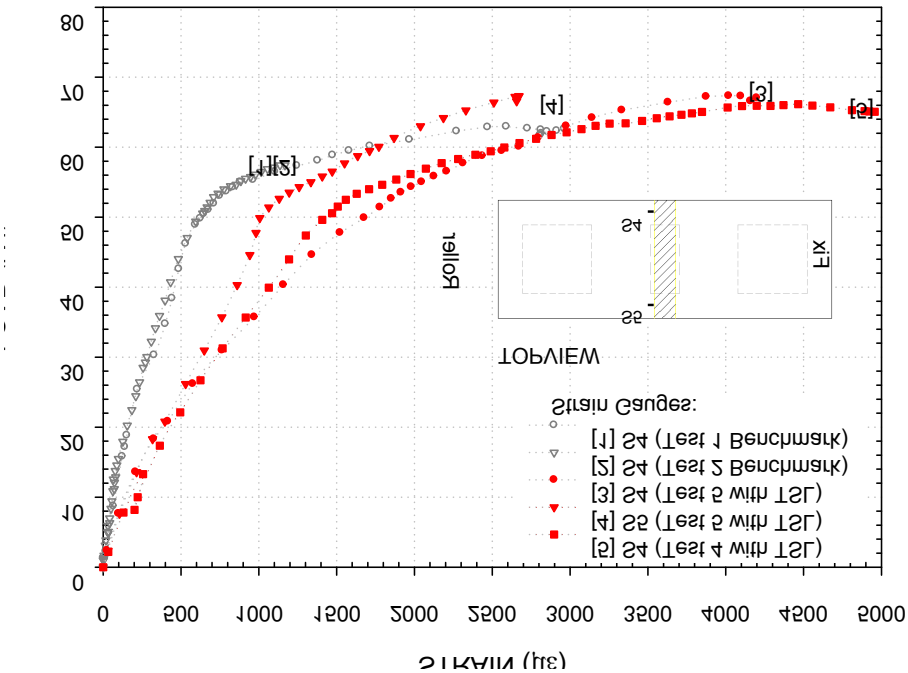

Figure 6.16 The compressive strain comparison at S-4 and S-5

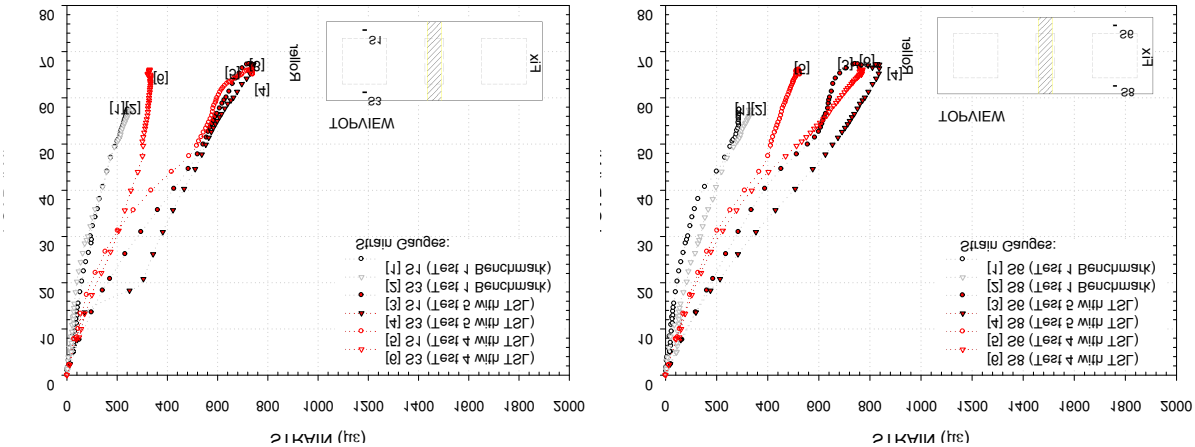

Figure 6.17 The compressive strain comparison at S-1, 3 and S-6, 8

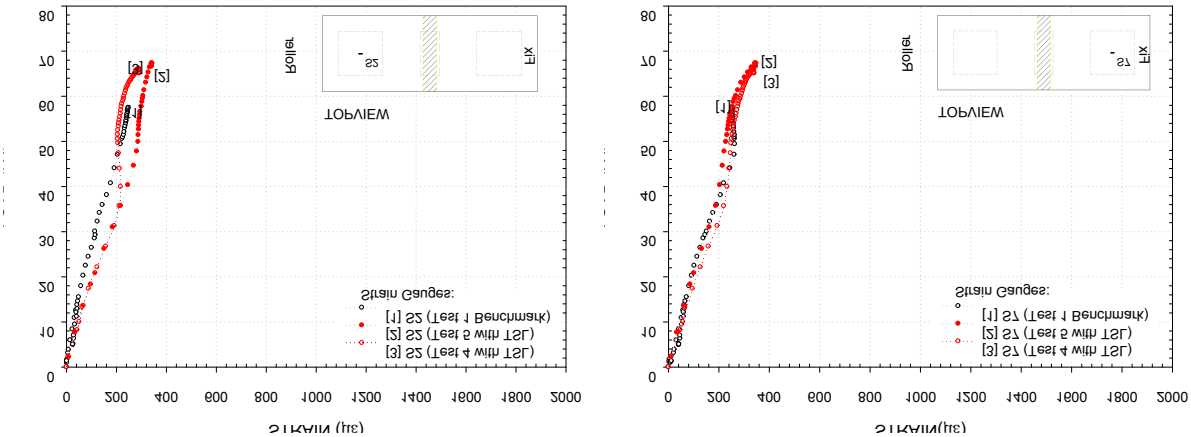

Figure 6.18 The compressive strain comparison at S-2 and S-7

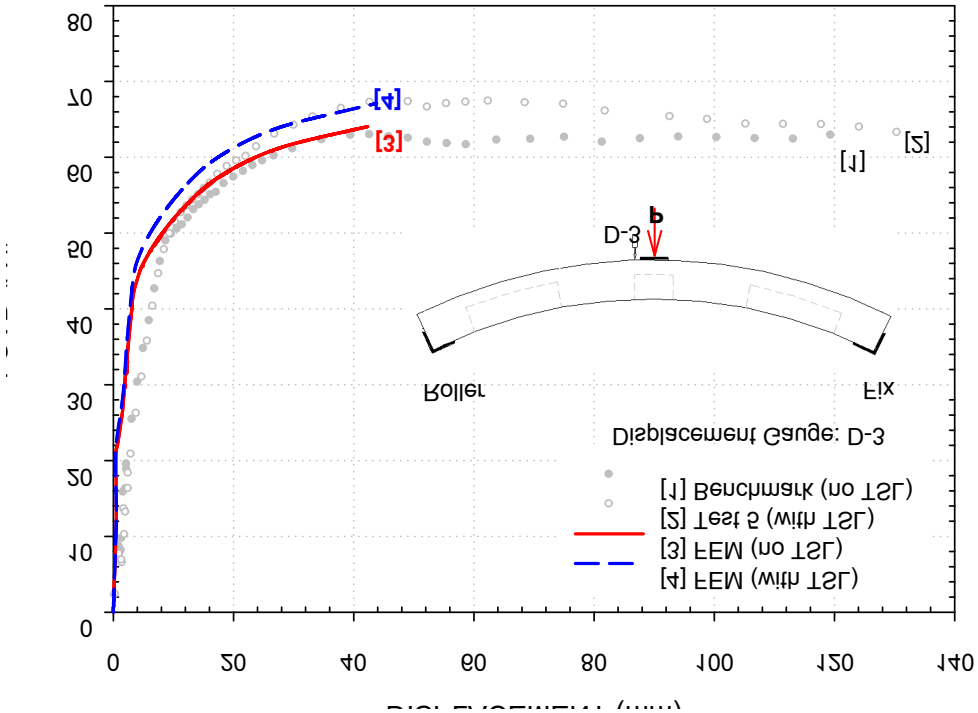

Figure 6.19 The displacement comparison between experimental and FEA results (D-3)

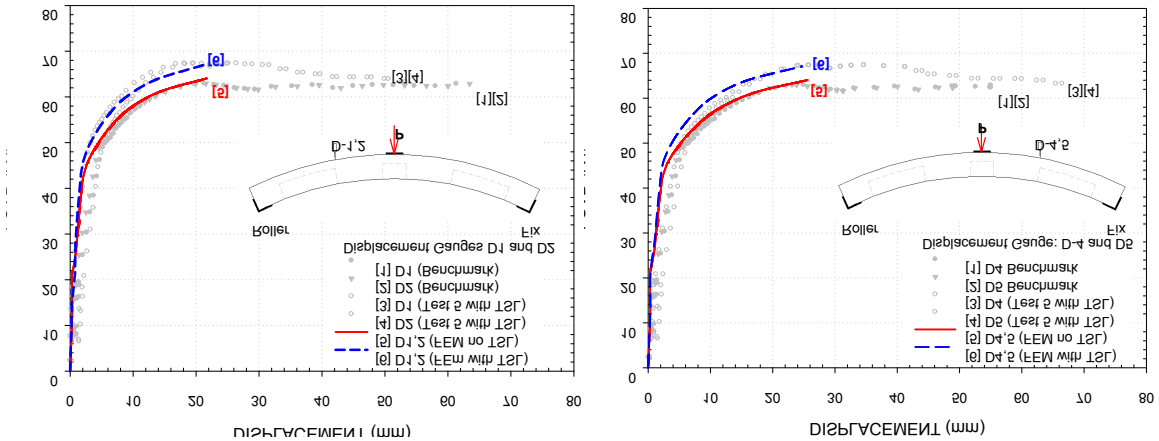

(a) D-1 and D-2 (b) D-4 and D-5

Figures 6.20 The displacement comparison between experimental and FEA results (D-1, 2 and D-4, 5)

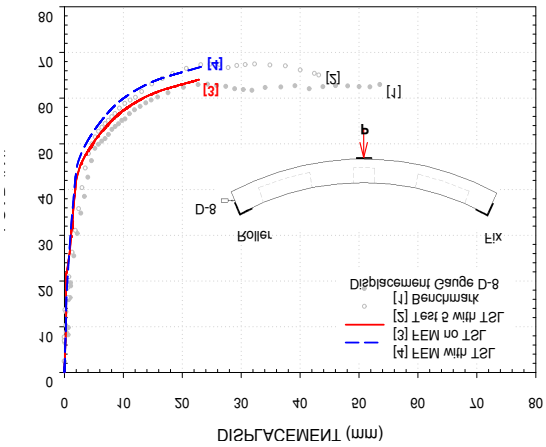

Figure 6.21 The displacement comparison between experimental and FEA results (D-8)

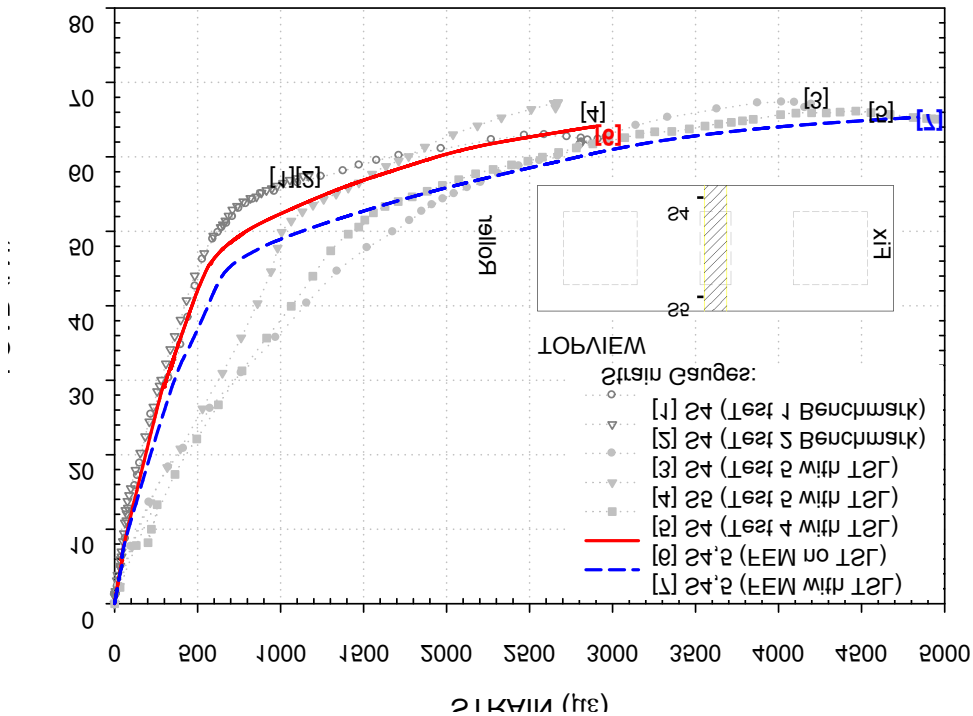

Figure 6.22 The strain comparison between experimental and FEA results (S-4 and 5)

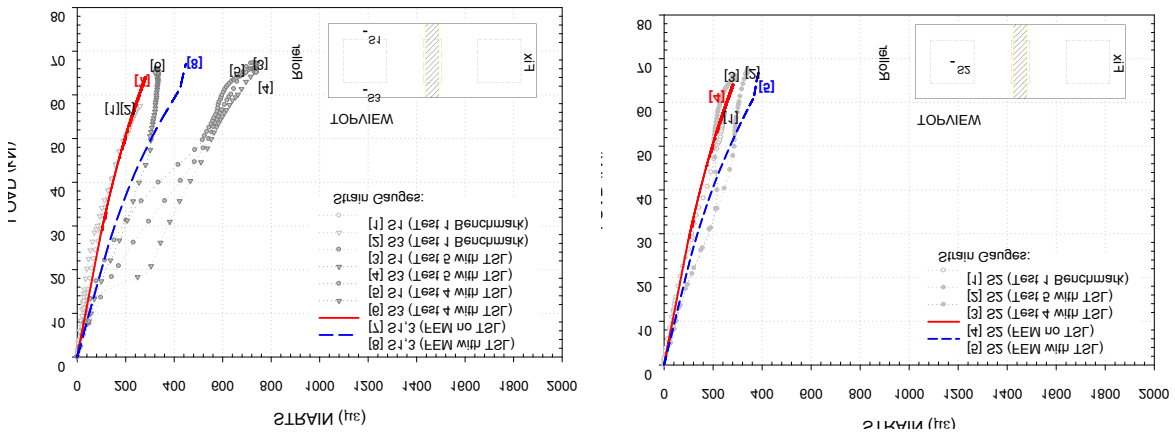

Figures 6.23 The strain comparison between experimental and FEA results (S-1, 2 and 3)

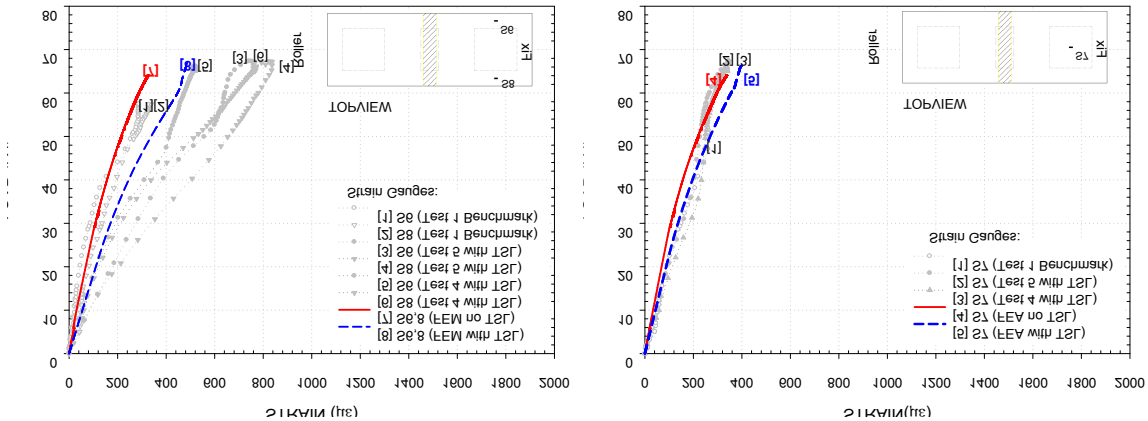

Figures 6.24 The strain comparison between experimental and FEA results (S-6, 7 and 8)

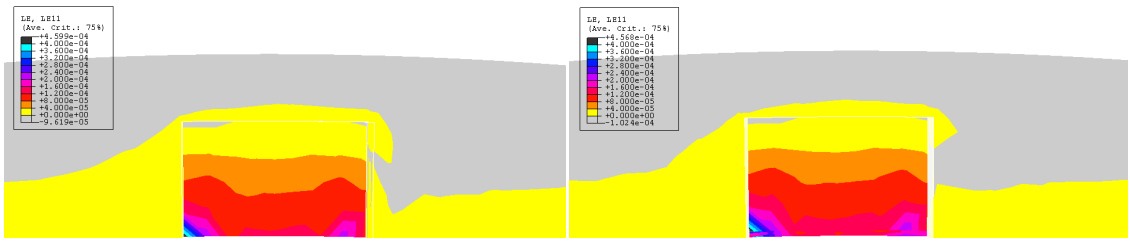

Uncoated FE model (20 kN) TSL coated FE model (20kN)

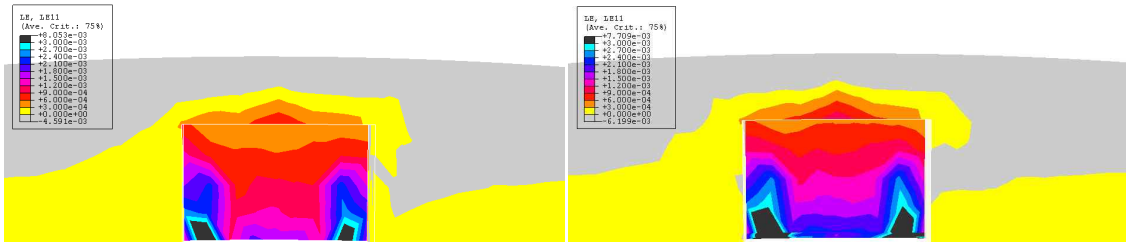

Uncoated FE model (45 kN) TSL coated FE model (45kN)

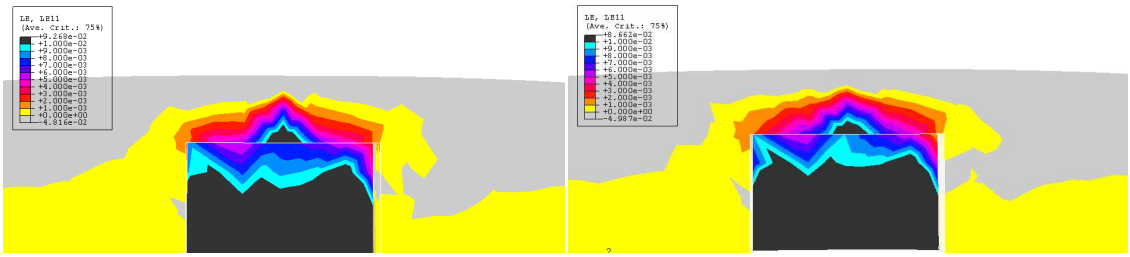

Uncoated FE model (60 kN) TSL coated FE model (60kN)

Figure 6.25 Strain distributions through the segment ribs
(Loads at 20 kN, 45 kN and 60 kN)

CHAPTER 7

NUMERICAL EVALUATION OF SEGMENTAL CONCRETE TUNNEL LINERS JOINT ROTATIONAL STIFFNESS

7.1 INTRODUCTION

Most modern subway tunnel linings are designed with segmental linings comprising precast reinforced concrete segments. In addition to enabling higher construction rates compared to cast-in-place concrete linings, the joints between liner segments can reduce bending moments in the lining reducing the amount of flexural reinforcing steel required to resist loads due to the earth pressure. Currently, designers can use either closed-form analytical solutions (Muir Wood, 1975; Einstein and Schwartz, 1979; Blom, 2002, El Naggar and Hinchberger, 2008) or Finite Element (FE) software to assess the moments and thrusts in jointed segmental tunnel linings. However, the rotational stiffness of liner joints is not well documented in the published literature.

This chapter examines the rotational stiffness of two different joint types for segmental concrete tunnel linings. The main objective is to provide useful information for consideration during tunnel lining design. The first joint examined comprises two inclined bolts per segment, polyamide bolt sockets, a single EPDM (Ethylene Propylene Diene Monomer**)** gasket at the extrados, and plywood packing between concrete-to-concrete contacts. The second joint consists of concrete segments with curved ends connected by steel bolts that pass through ferrules embedded into the segments. The rotational stiffness of this joint is evaluated assuming no

packing or gasket materials. The finite element (FE) program ABAQUS is used to model the joints and to calculate the rotational stiffness by accounting for the joint geometry, the initial thrust in the joint, geometric non-linear contact behaviour, and the non-linear stress-strain response of joint materials (i.e. reinforced concrete, plywood packing, EPDM gasket, steel bolts and polyamide bolt sockets). Lastly, a TSL layer is added to a model to evaluate the effect of the layer on the joint stiffness of flexible segmental concrete linings. To conclude, a closed-form solution (El Nagger et al. 2008) for jointed tunnel linings is used to assess the implications of joint stiffness on moments and thrust for static design.

This chapter examines the rotational stiffness of two different joint types (i.e., modern joint and flexible joint) for segmental concrete tunnel linings. The main objective is to provide useful information for tunnel design and construction. Also, subsidiary objectives of this study are to:

1) examine the feasibility of the FE model to determine the rotational joint stiffness (K_θ) using rectangular block models for both the modern joint type and the flexible joint type.
2) investigate joint stiffness changes accounting for various components of the joint, including the steel bolt, the bolt socket, EPDM gasket and plywood packing.
3) determine the range of the rotational joint stiffness for the various bending moments (M) associated with the initial thrust (T) on the linings.
4) evaluate the effect of a TSL layer on the rotational stiffness of the flexible joint.
5) finally, determine the staggered-joint stiffness and its effect on the bending moment and thrust of the tunnel lining.

7.2 JOINT GEOMETRY

7.2.1 Modern Joint

Figure 7.1 illustrates a modern joint examined in this study while Table 7.1 presents the joint component details. The segmental lining shown in Figure 7.1 has the internal diameter of 5200 mm, the width of 1000 mm and the thickness of 250 mm. A ring comprises of five concrete segments and a key segment. Each segment has an arc angle of 67.50^{o} that is equivalent to 3122mm in arc length. A small key segmental block is installed at 22.50^{o} and rotated clockwise from the crown. The joints have, therefore, unevenly distributed joint angles (i.e. $\theta = 11.25^{o}$, 33.75^{o}, 102.25^{o}, 168.75^{o}, 236.25^{o}, and 303.75^{o}) as illustrated in Figure 7.1.

As seen in Figure 7.1, the modern design consists of 250 mm thick reinforced concrete segments connected by two 28 mm diameter steel bolts counter-inclined 25° relative to the segment's circumferential axis. The joint between segments is designed as no-tension and frictional surfaces that allow slipping along and gapping between contact surfaces. The bolts are screwed into polyamide bolt sockets that are cast in the segments. In addition, the joint is equipped with one EPDM gasket offset 3cm from the extrados of the segments. This joint is examined with 3 mm thick plywood packing sandwiched between the concrete-to-concrete contacts. A packing at the joint reduces the stress concentration between concrete segments (Kramer et al. 2007).

7.2.2 Flexible Joint

The flexible joint, see Figure 7.2, is relatively flexible comprising 150 mm thick reinforced concrete segments connected by two bolts per segment. The segment ends are curved with a radius of 1520 mm. The bolts are aligned with the circumferential axis of the segments (i.e. not

inclined) and they pass through ferrules that are embedded in the segments and are offset 63.5 mm from the segment extrados. The component details can be found in Table 7.1. Hereafter, the joints will be referred to as modern and flexible joints, respectively.

7.3 NUMERICAL METHODOLOGY

As discussed in Section 7.1, the joint rotational stiffness was calculated using the FE program ABAQUS. Figures 7.3 and 7.4 show the FE meshes corresponding to the modern and flexible joints.

7.3.1 FE Models of Modern and Flexible Joints

To model the actual joint discussed in 7.2.1, a 3-D rectangular block model instead of a segmental lining model is used to determine the joint rotational stiffness for a specific thrust (T) and bending moment (M) on the joint caused by the earth pressure. Referring to Figure 7.3(a), the modern joint was modeled using a mixture of 20-noded and 10-noded quadratic brick and tetrahedron elements. The FE mesh contained 32547 elements in total. The joint was meshed in such a way that the bolts, bolt sockets, EPDM gasket, packing and concrete were modeled as separate materials assuming fully bonded contacts between (1) the bolts and bolt sockets, (2) bolt sockets and concrete, and (3) EPDM gasket and concrete. Frictional contacts that permit separation were assumed between (1) the plywood and concrete and (2) the bolt and concrete.

The flexible joint, see Figure 7.4 (a), was modeled using 17800 10-noded quadratic tetrahedron elements. Only two materials were considered for this joint: concrete and steel. For the flexible joint, a frictional no-tension contact was assumed for both (1) concrete-to-concrete and (2) bolt-

to-concrete contacts. The mesh was developed so that it modelled the exact geometry depicted in Figure 7.4 (b). In addition, a 4 mm of TSL layer was applied in the model to evaluate the TSL effects on the joint stiffness for the flexible joint linings. The TSL layer was added onto the entire inner surface of the lining except for the bolt pockets.

7.3.2 Boundary and Loading Conditions

The FE models illustrated in Figure 7.3 and 7.4 were loaded by applying: (1) an axial compressive thrust (T) at the segment ends; and (2) a uniformly distributed line load (P) at the joint. The boundary conditions were comprised of simply supported segment ends (i.e. rotation permitted, no vertical displacement, and no horizontal displacement at one end only). For such loading, the joint rotational stiffness (k_θ) is

$$k_\theta = PL^2/8\delta_v \qquad \text{[Eq. 7.1]}$$

where δ_v is the vertical displacement at the joint due to P and L is the span.

Equation 7.1 assumes that deflection due to bending in the segments is negligible compared to that caused by joint rotation. For presentation purposes, the initial thrust (T) was divided by the segment area ($A=bd$; where d is the segment depth and b is the width) to obtain (σ_o); and the joint stiffness was calculated for different values of (f_{cu}/σ_o), where f_{cu} is the unconfined compressive strength of the concrete.

7.3.3 Contacts, Constraints, and Interactions in FE Models

All contacts, constraints and interactions used in the analysis are summarized in Table 7.2. To properly simulate the joint behaviour, a number of different constraints were imposed on the model. First, interactions in the joint, for instance, between concrete and concrete and between gasket and gasket, were considered as a frictional surface. For the tangential direction, the coefficient of friction of 0.7 and 0.6 for concrete-to-concrete and gasket and gasket were used, respectively. In the normal direction, contact pressure-overclosure relationship was used at the joint contact area.

A ‘Hard’ contact was used for the concrete-concrete contact while softened contact was used for the gasket-gasket contact. The ‘Hard’ contact relationship minimizes the penetration of nodes from one into the surface of the other and does not allow the transfer of tensile stress across the interface. On the other hand, the ‘Softened’ contact relationship is one, in which the contact pressure is either an exponential or a linear function of the clearance between the surfaces. In an exponential pressure-overclosure relationship, the surfaces transmit the contact pressure when the overclosure between one surface and the other surface. For EPDM gaskets, the softened contact relationship would be applicable since it has rubber-like hyperelastic characteristics. For instance, as a gap between the segments decreases, the pressure at the gaskets exponentially increases at a point after overclosure (ABAQUS Analysis User’s Manual, 2007).

The bolt linking socket apparently embedded in the concrete block was adapted to a surface-based tie constraint. The surface-based tie constraint means two contact surfaces are jointed together and respond as one during the computation. The surface-based tie constraint can be used

to balance the translational and rotational motions as well as all other active degrees of freedom for a pair of surfaces. The bolt screwed into the linking socket was modelled using the surface-based tie constraint. The inner surface of the bolt head was also tied to the concrete surface in the bolt pocket. The frictional contact as according to its original design was considered for the bold stud.

7.3.4 FE Model Parameters

The material parameters used in FE analysis and their constitutive models are summarized in Tables 7.3 and 7.4. For all joint models, the non-linear stress-strain response of concrete was modeled using a concrete damage plasticity model. The constitutive parameters for this model are the initial tangent elastic modulus (E), Poisson's ratio (ν), unconfined compressive strength (f_{cu}), initial yield stress (σ_y) and tensile failure stress (σ_{tf}). The steel bolts were modeled as an elasto-plastic strain hardening material with initial yield stress and ultimate tensile strength. A hyper-elastic model was used for the EPDM gasket. Figure 7.5 shows the stress-strain response of the EPDM gasket. Linear elasto-plastic material properties are assumed for the polyamide socket and the plywood packing.

7.3.4.1 Concrete Damaged Plasticity (CDP)

The Concrete Damaged Plasticity (CDP) model is used in this analysis. The CDP model in ABAQUS provides a general capability for modeling concrete using concepts of isotropic damaged elasticity in combination with isotropic tensile and compressive plasticity to represent the inelastic behaviour of concrete. This model consists of the combination of nonassociated multi-hardening plasticity and isotropic damaged elasticity to describe the irreversible damage

occurring during the fracturing. The model makes use of the yield function of Lubliner et al. (1989) with the modifications proposed by Lee and Fenves (1998) to account for the evolution of strength under tension and compression. The evolution of the yield surface is controlled by the hardening variables. The yield function takes the form as follows:

$$\boldsymbol{F} = \frac{1}{1-\boldsymbol{\alpha}}(\bar{\boldsymbol{q}} - 3\boldsymbol{\alpha}\bar{\boldsymbol{p}} + \boldsymbol{\beta}(\boldsymbol{\varepsilon}^{\boldsymbol{pl}}) < \bar{\boldsymbol{\sigma}}_{\max} > -\boldsymbol{\gamma} < -\bar{\boldsymbol{\sigma}}_{\max} >) - \boldsymbol{\sigma}_{\boldsymbol{c}}(\boldsymbol{\varepsilon}_{\boldsymbol{c}}^{\boldsymbol{pl}}) = 0$$

$$\boldsymbol{\alpha} = \frac{(\boldsymbol{f}_{\boldsymbol{b0}} / \boldsymbol{f}_{\boldsymbol{c0}}) - 1}{2(\boldsymbol{f}_{\boldsymbol{b0}} / \boldsymbol{f}_{\boldsymbol{c0}}) - 1}; 0 \le \boldsymbol{\alpha} \le 0.5,$$

[Eqs. 7.2]

$$\boldsymbol{\beta} = \frac{\bar{\boldsymbol{\sigma}}_{\boldsymbol{c}}(\boldsymbol{\varepsilon}_{\boldsymbol{c}}^{\boldsymbol{pl}})}{\bar{\boldsymbol{\sigma}}_{\boldsymbol{t}}(\boldsymbol{\varepsilon}_{\boldsymbol{t}}^{\boldsymbol{pl}})}(1-\boldsymbol{\alpha}) - (1+\boldsymbol{\alpha}),$$

$$\boldsymbol{\gamma} = \frac{3(1-\boldsymbol{K}_{\boldsymbol{c}})}{2\boldsymbol{K}_{\boldsymbol{c}} - 1}$$

where, $\bar{\boldsymbol{p}} = -\frac{1}{3}\boldsymbol{trace}(\bar{\boldsymbol{\sigma}})$ is the hydrostatic pressure stress, $\bar{\boldsymbol{q}} = \sqrt{\frac{3}{2}(\boldsymbol{s} : \boldsymbol{s})}$ is the Mises equivalent effective stress $\boldsymbol{s}$ is the effective stress deviator, $\bar{\boldsymbol{\sigma}}_{\max}$ is the maximum principal effective stress, $\boldsymbol{f}_{\boldsymbol{b0}} / \boldsymbol{f}_{\boldsymbol{c0}}$ is the ratio of initial equibiaxial compressive yield stress to initial uniaxial compressive yield stress, and $\boldsymbol{K}_{\boldsymbol{c}}$ is the ratio of the second stress invariant on the tensile meridian to that on the compressive meridian at the initial yield for any given value of the pressure invariant such that the maximum principal stress in negative $\bar{\boldsymbol{\sigma}}_{\max}$. This value must satisfy the condition 0.5 < $\boldsymbol{K}_{\boldsymbol{c}}$ < 1.0, and $\frac{\bar{\boldsymbol{\sigma}}_{\boldsymbol{c}}(\boldsymbol{\varepsilon}_{\boldsymbol{c}}^{\boldsymbol{pl}})}{\bar{\boldsymbol{\sigma}}_{\boldsymbol{t}}(\boldsymbol{\varepsilon}_{\boldsymbol{t}}^{\boldsymbol{pl}})}$ is the ratio between the effective compressive cohesion stress and the

effective tensile cohesion stress. Table 7.5 presents some parameters used in CDP models (Lubliner et al. 1989)

The eccentricity of 0.1 indicates that the material has almost the same dilation angle over a wide range of confining pressure stress values. The dilation angle measuring in the *p-q* plane varies due to the percentage of steel reinforcement. The dilation angle increases rapidly as the confining pressure decreases (Lee and Fenves, 1998).

The post-failure behaviour for direct straining is modelled with tension stiffening which allows it to define the strain softening behaviour for cracked concrete. This behaviour also allows the effects of the reinforcement interaction with concrete to be simulated in a simple manner (ABQAUS Analysis User's Manual, 2006).

7.3.4.2 Gasket

The most commonly used gasket for tunnel construction is the Ethylene Polythen Diene Monomer (EPDM) compression gasket fitted around individual precast concrete tunnel lining segments. EPDM is a dense elastomeric synthetic rubber gasket installed in a preformed groove at the extrados of segment (BTS, 2004).

The EPDM gasket shows hyperelastic behaviour. The mechanical properties of the EPDM gasket cannot be simply defined without experiments such as uniaxial, biaxial, or triaxial compression tests. Hence, uniaxial compressive tests were conducted. Figure 7.5 presents the average values of three uniaxial compressive test results. It can be also seen a FE result using

hyperelastic model in ABAQUS in Figure 7.5. The FE result shows a bit higher strain at the same stress. However, the similar hyperelastic behaviour can be applied in the modern joint model.

7.3.4.3 Steel bolt

An elasto-plastic strain hardening model for the steel bolt (i.e. C45 corresponding to ASTM A307) was used in the analysis. The selected steel has the common steel properties including Young's modulus of 210 GPa and Poisson's ratio of 0.3. The initial yield stress is 350 MPa and its corresponding plastic strain is zero. Then, strain hardening occurs after the initial yielding. The stress of 800 MPa corresponding to 16% elongation is used for the tensile failure criteria.

7.3.4.4 Linking socket

The bolt linking socket is made of polyamide resin known as Nylon 66. It is common to add 20% to 50% of glass fibre to increase the strength of the material. The stress-strain response of 30% glass-filled polyamide resin is presented in Figure 7.6. The tensile strength of the linking socket is assumed at 159 MPa. Also, the flexural strength and elastic modulus are 255 MPa and 9038 MPa, respectively.

7.3.4.5 Plywood packing

The purpose for using the packing material is to avoid concrete-concrete contact due to the thrust on the lining so that it can prevent stress concentration in segments (Kramer et al. 2007). The common mechanical properties suggested in the Wood Handbook are used in this analysis

(Youngquist, 1999). The plywood has a modulus of elasticity of 13100 MPa and a compressive strength of 34.5 MPa. An initial yield stress of 20.7 MPa was used in the analysis.

7.4 STAGGERED JOINTS WITH SIMPLIFIED JOINT METHOD (SJM)

Most modern segmental concrete tunnel linings have staggered joints. Consequently, a FE model was also developed to estimate an equivalent k_θ for staggered joints. The objective was to idealize two-staggered joints as an equivalent single joint for use in analytical solutions.

A three-dimensional modern joint model is relatively complicated. Many problems, such as convergence and element distortion errors, occur during computation. For such reasons, few attempts have been made to develop a 3-D full joint model using the FE program despite the benefits of 3D-full joint models. Therefore, a simplified joint model adopting an elastic zone between concrete contact surfaces has been developed by El Nagger et al. (2008). With this method, the staggered joint model is presented in Figure 7.7. A 3mm thick elastic zone has an elastic modulus of 740 MPa while the Poisson's ratio is 0.2.

7.4.1 FE Model

Referring to Figure 7.7, the FE mesh comprised 37216 quadratic tetrahedron elements and the mesh modelled two staggered radial joints and one longitudinal joint. The segments were connected longitudinally by three fibreglass reinforced plastic dowels. A dowel has a modulus of elasticity of 3.7 GPa and a Posisson's ratio of 0.36. The yield stress of the dowel is 88 MPa (TTC, 2009). The normal contact stress on the longitudinal joint and the resultant friction between segments was ignored. The radial joints were assumed to correspond to the modern joint, which

is illustrated in Figure 7.1. The material parameters used for the staggered joint model are listed in Table 7.3.

The staggered joint model was loaded by applying a uniform stress (σ_o) at the segment ends to simulate initial thrust in the lining. Then, a uniform line load (P) was applied at the midpoint of the model and the ends were simply supported identical to that described above for the single joint models. Based on the FE results, which gave δ_v versus P, the joint stiffness was estimated using Eq. [7.1] neglecting deflections caused by the segment deformations. Evaluation of the deflected shape of the model showed that the majority of the mid-point deflection was due to the joint rotation.

7.5 FE RESULTS

7.5.1 Joint Rotational Stiffness

7.5.1.1 Modern Joint

Figure 7.8 summarizes the calculated rotational stiffness (k_θ) for the modern joint corresponding to values of f_{cu}/σ_o of 2, 10, 20, and 200. For a moment of 10 kNm, the stiffness varies from 3 MN·m/rad corresponding to f_{cu}/σ_o = 2 to 30 MN·m/rad for f_{cu}/σ_o = 20. The increase in joint stiffness with increasing f_{cu}/σ_o is caused by concrete non-linearity (yielding) and yielding of the plywood packing material. In addition to the effect of f_{cu}/σ_o , the joint rotational stiffness increases with increasing moment for moments up to 30 kN·m. Based on this figure, it can be seen that the initial lining thrust (σ_o) has a significant effect on k_θ. This can be attributed primarily to geometric non-linear effects and secondarily to the stress-strain response of the gasket material (see Figure 7.5).

7.5.1.2 Flexible joint

For comparison purposes, the rotational stiffness of the flexible joint is shown in Fig 7.9. This joint is used in the TTC subway tunnel. Values of f_{cu}/σ_o at 10, 20, and 200 and the moments between 5 kNm and 50 kNm are simulated in this analysis. Generally, it can be seen that the stiffness increases with increasing f_{cu}/σ_o. The rotational stiffness of the flexible joint increases in low moments (i.e., less than 20 kN.m) and decreases when a moment exceeds to 40kN.m. For example, the stiffness of the flexible joint increases from 1 MN·m/rad to approximately 4 MN·m/rad for values of f_{cu}/σ_o= 10 corresponding to moments between 4 and 30 kN·m. After a moment of 30 kN.m, the stiffness decreases from 4 MN·m/rad to 3MN.m/rad as the moment increases from 30 to 40 kN.m. Similar patterns can be seen in the other cases. For the case of

f_{cu}/σ_o = 20, the stiffness varies from 2 MN·m/rad to 5.5 MN·m/rad while the maximum stiffness is 5.5 MN·m/rad at the moment of 38 kN.m. Additionally, the stiffness of the joint ranges from 5.5 MN·m/rad to 7.7 MN·m/rad for the value of f_{cu}/σ_o = 200.

For both the modern and flexible joints, the moment resistance of the joint is mobilized when the joint rotates and a compressive thrust line develops at the contact, which is offset from the bolts (i.e. a force couple develops). For small values of *M*, the joint stiffness decreases as the joint rotation, consequently the distance between the compressive thrust line, and the tensile bolt force increase (referred to in Figures C-1 to C-3 in Appendix C).

The decreased stiffness is expected, given the curved segment ends. In addition, there are similar patterns of behaviour for both the flexible and modern joints i.e. the $\boldsymbol{k_\theta}$ increases with increasing moment. As noted above, this would be due to geometric non-linear effects. Rotation of the flexible joint is resisted by the formation of force couples between the tensile bolts and a compressive zone in the concrete. As the joint rotation increases, the distance between the compression and tensile regions increases and consequently the k_θ increases. There is a reduction of joint stiffness versus f_{cu}/σ_o, which is attributed to the non-linear response of the concrete.

7.5.1.3 Flexible joint with TSL

Figure 7.10 summarizes the joint stiffness for the flexible joint with 4 mm thick TSL layer. In general, the rotational stiffness with the TSL layer demonstrates higher rigidity than that of the lining without the TSL layer. For the initial lining thrust of 6 MPa (f_{cu}/σ_o = 10), an average of 10%

greater stiffness is observed for the lining with the TSL layer. For the value of f_{cu}/σ_o = 20, the stiffness differences between the lining with TSL and without TSL vary from 10 % to 25 % at moments between 4 kN.m and 50 kN.m. For the case of f_{cu}/σ_o = 200, there is an 18% difference at the moment of 5 kN.m, but the difference in the stiffness is dramatically reduced to 2% when the moment is 50 kN.m.

The TSL effects would increase as the initial lining thrust increases. The rotational stiffness difference in the joints between cases with the TSL layer and without the TSL layer becomes smaller as the ratio, $f_{cu}/\sigma_{o,}$ increases.

7.5.1.4 Staggered joint with SJM

Prior to applying SJM to the staggered joint, the simplifed joint method (SJM) was utilized with the single joint model and compared with the full joint model considering the plywood packing, gasket, two skewed bolts and two linking sockets. The results can be seen in Figure 7.11.

In general, for f_{cu}/σ_o=200, the difference in the rotation stiffness is approximately 10 MN.m/rad at the moment of 25 kN.m. and differences in the rotation stiffness reduce from 4 MN.m/rad to 0.5 MN.m/rad for $f_{cu}/\ \sigma_o$ = 20 and $f_{cu}/\ \sigma_o$ = 10, respectively. It can be seen that for the higher value of $f_{cu}/\ \sigma_o$ = 200, greater variation develops between the full joint model and the simplified joint model.

To conclude, Figure 7.12 compares the rotation stiffness of one modern joint and two staggered modern joints corresponding to $f_{cu}/\ \sigma_o$ = 10, 20 and 200. As such, these results correspond to the

joint stiffness at a low initial lining thrust. From Figure 7.12, it can be seen that the staggered joint model has essentially three times the rotational stiffness (per meter of tunnel) as the single joint. There is a coupling behaviour between the joints due to the effect of the dowels which appears to be sufficiently stiff to cause the joints to act with some composite behaviour. As a result, it is concluded that, for the modern joints shown in Figure 7.1, staggering the joints triples the equivalent single joint rotational stiffness for the case of $f_{cu}/\ \sigma_o$ = 200 and 20 and doubles it for the case of $f_{cu}/\ \sigma_o$ = 10. A decreasing value of $f_{cu}/\ \sigma_o$ causes a decrease in the rotational stiffness between the staggered joint and the single joint.

7.6 DISCUSSION

This section examines the influence of joints on moments and thrusts in a 250 mm thick, 5200 mm diameter tunnel with a 15 m cover. It is assumed that the tunnel is situated above the groundwater table. Table 6.6 summarizes the problem's geometry and material parameters.

Moments and thrusts in the lining have been calculated using the jointed liner solution of El Naggar et al. (2008) assuming (1) no joints and (2) 8 joints situated at 0°, 45°, 90°, 135°, 180° etc. with a joint stiffness of 5 MN·m/rad and 50 MN·m/rad per meter of tunnel, respectively. Figure 7.13 plots the calculated distribution of moment and thrust in the linings.

Based on Figure 7.13, it can be seen that introducing joints in closed-form solutions for tunnels in elastic soil or rock leads to a significant reduction in the moments (see Appendix-D). For the case examined in this thesis, the maximum moment in the lining caused by earth pressures varies from 24 MN·m per meter of tunnel for the case of no joints to 20 and 9.5 MN·m for k_θ values of

50 and 5 MN·m/rad per meter of tunnel, respectively. Thus, joints can be used to reduce the design moments for segmental concrete tunnel linings. However, based on Figures 7.12 and 7.13, it can be concluded that the liner moments could be comparable to those expected in a continuous lining without joints if the lining thrust is low and if staggered modern joints are used. The thrust in the linings examined in Figure 7.13 are not significantly affected by the introduction of joints in the lining.

7.6 SUMMARY AND CONCLUSIONS

This study has used a non-linear FE model to examine the stiffness of two types of joints for segmental concrete tunnel linings. The FE analysis was performed using the FE program ABAQUS taking into account the geometric non-linear contact behaviour, in addition to the non-linear stress-strain response of the various materials used in the joint designs. Based on the analysis and discussions presented, the following conclusions can be drawn:

1) The joint rotational stiffness increases with increasing M due in part to the stress-strain response of some of the joint materials, but primarily due to geometric nonlinear effects (increased distance between the compressive thrust line and the tensile bolts in the joint).
2) The modern joint has a rotational stiffness that varies from 3 to 60 MN·m/rad per meter length of tunnel depending on the $f_{cu}/\ \sigma_o$ ratio (i.e, less than 20) and M. In contrast, the flexible joint has a rotational stiffness that varies from 0.5 to 8 MN·m/rad per meter of tunnel.
3) A TSL layer applied on the flexible joint causes an increased rotational stiffness. However, the TSL effects may not be considerable, in particular, for a higher $f_{cu}/\ \sigma_o$ (i.e. 200).
4) Staggering the modern joints, as shown in Figure 7.13, will increase their equivalent rotational stiffness by factors of 2 to 3 depending on the $f_{cu}/\ \sigma_o$ ratio. For a high $f_{cu}/\ \sigma_o$ ratio, the moments in linings designed with staggered modern joints will be comparable to those for an un-jointed lining.
5) As shown in Fig 7.13, introducing joints that have a low rotational stiffness into concrete tunnel linings can significantly lower the design moments. The closed form solutions calculating the moments and thrust can be found in Appendix-'D'.

Table 7.1 Component geometry details used in ABAQUS analysis

Part Name	Dimension	Element Type	Number of Element	Material
Segments (modern)	1000mm x 1000mm x 250mm	C3D20R & C3D10M	13070(L) 13405(R) 26475(T)	Concrete (f'_c=60MPa)
EPDM Gasket	1000mm x 10mm x 35mm to 50 mm[1]	C3D20R	174	Ethylene Polythene Diene Monomer
Bolt (modern)	28mm (O.D) 370mm long	C3D10M	999	Steel (C45)
Linking socket	28mm(I.D) 80mm long	C3D10M	3240	Polyamide 30% Fibre glass
Packing	150mmx1000m X 3mm (t)	C3D10M	660	plywood
Segments (flexible)	1000mmx1000mm X 150mm	C3D10M	15950	Concrete (f'_c=40MPa)
Bolt (flexible)	25mm (O.D.) 300 mm long	C3D10M	925	Steel (C45)

[1] 35mm at the concrete contact and 50mm at the gasket contact.

Table 7.2 Contacts, constraints and interactions used in ABQAUS analysis

Positions	Constraint / Interaction Type	Conditions/Coefficient	Remarks
Concrete to concrete	Normal –hard/ Tangential - friction	allowing separation 0.7	No penetration of tensile stress
Gasket to gasket	Normal –softened/ Tangential - friction	allowing separation 0.6	Exponential
Bolt stud and concrete	Normal-hard/ Tangential - friction	allowing separation 0.5	No penetration of tensile stress
Gasket at groove	Tie	Mesh refinement	
Bolt and linking socket	Tie	Surface together	No thread
Linking socket and concrete	Tie	Mesh refinement	
Bolt head	Tie	Surface together	No washers
Gasket at groove	Tie	Mesh refinement	

Table 7.3 Modern joint – FE model parameters

Parameter	**Material**				
	Concrete	**Steel (C45)**	**EPDM Gasket**	**Polyamide Socket**	**Plywood Packing**
Initial tangent elastic modulus (E)	31800 MPa	210000 MPa	see Fig. 6.5	9308 MPa	13100 MPa
Poisson's ratio (ν)	0.2	0.3	0.4	0.3	0.18
Density	2600 kg/m^3	8030 kg/m^3	-	-	-
Unconfined compressive strength(f_{cu})	60 MPa		-	-	-
Initial yield stress (σ_y)	48 MPa	350 MPa	-	110 MPa	20.7 MPa
Tensile failure stress (σ_{tf})	4.0 MPa	800 MPa	-	159 MPa	27.6 MPa
Model behaviour	CDP[A]	EP-S[B]	Hyper-elastic	EP[C]	EP[C]

[A]Concrete Damaged Plasticity Model; [B]Elastoplastic strain-hardening; [C]Elastoplastic.

Table 7.4 Flexible joint – FE model parameters

Parameter	**Material**	
	Concrete	**Steel**
Elastic Modulus (E)	30000 MPa	210 GPa
Poisson's ratio (ν)	0.2	0.3
Density	2400 kg/cm^3	-
Compressive ultimate stress (f'_c)	40 MPa	-
Initial Yield Stress (σ_y)	18.8 MPa	350 MPa
Tensile failure stress (σ_{tf})	3.0 MPa	800 MPa
Constitutive Model	CDP[A]	EP-S[B]

[A]Concrete Damaged Plasticity; [B]Elastoplastic strain-hardening

Table 7.5 Concrete Damaged Plasticity (CDP) parameters

CDP Parameters	Values
Uniaxial Compressive strength(f'_c)	60 MPa
Dilation Angle	36.31
Eccentricity	0.1
f_{bo}/f_{co}	1.16
K_c	0.67

Table 7.6 Material parameters for example problem

Parameter	Value
Soil elastic modulus, E_s (MPa)	90
Soil Poisson's ratio, v	0.4
Coefficient of earth pressure at rest, K_o	0.7
Initial vertical stress, σ_v (kN/m^2)	344
Initial horizontal stress, σ_h (kN/m^2)	241
Lining elastic modulus, E_c (GPa)	30
Lining Poisson's ratio, ν	0.2
Cover, C (m)	15
Diameter (m)	5.2
Thickness (cm)	25

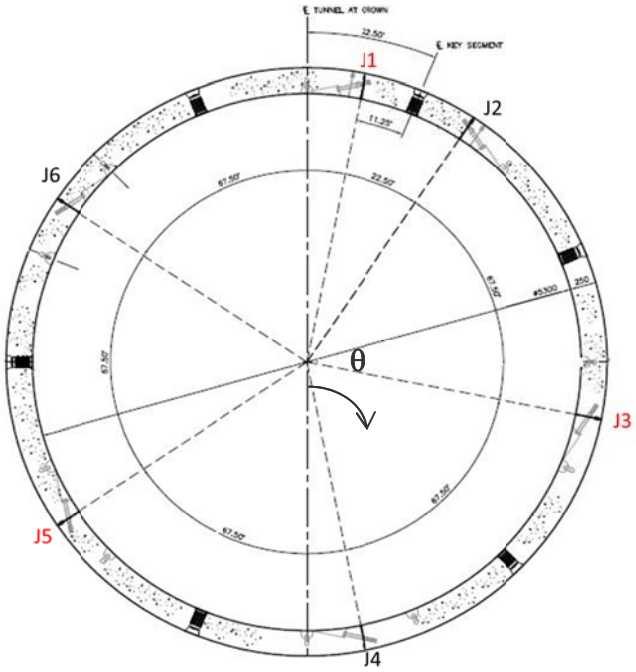

(a) Ring

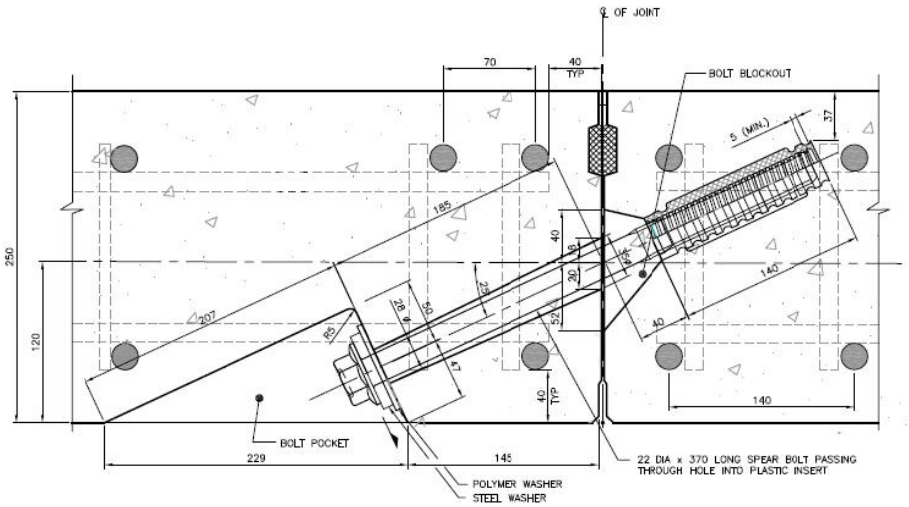

(b) Rotational Joint Geometry

Figure 7.1 The modern joint geometry

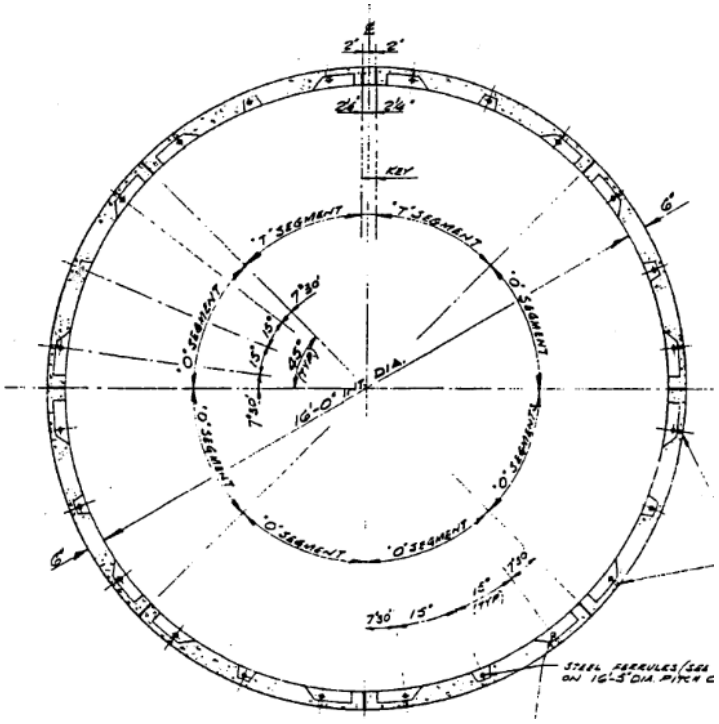

(a) Ring

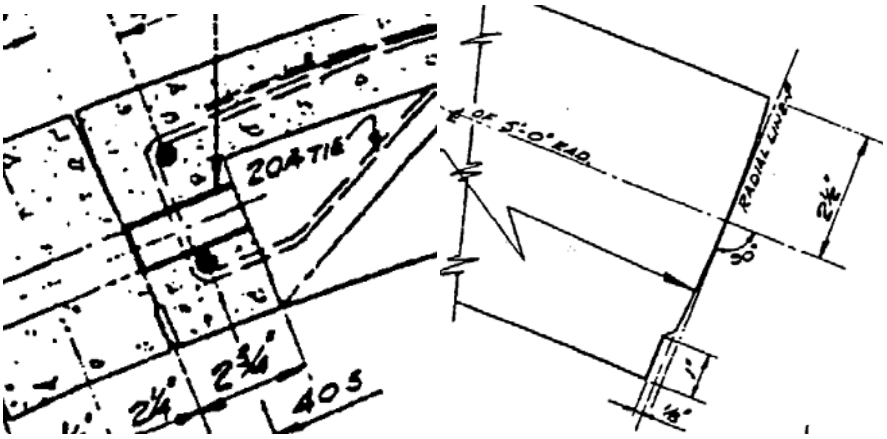

(b) Rotational Joint Geometry

Figure 7.2 The flexible joint geometry

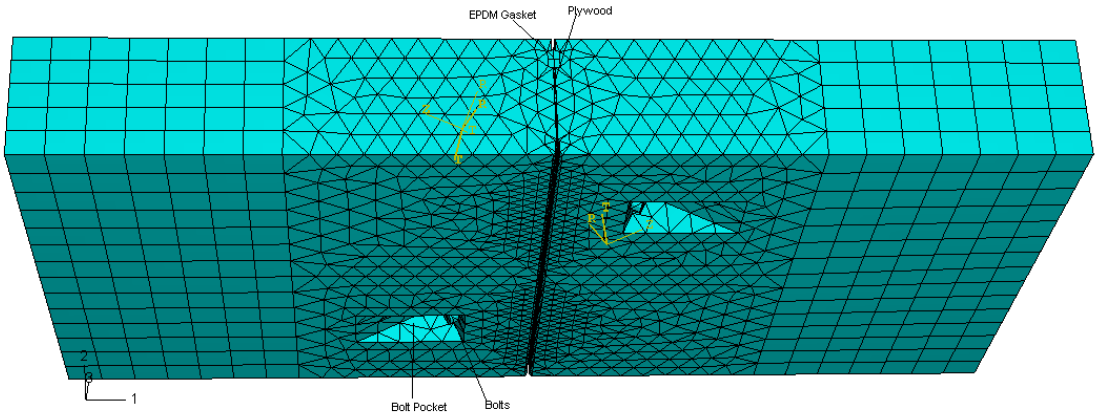

(a) 3-D FE mesh – Modern joint

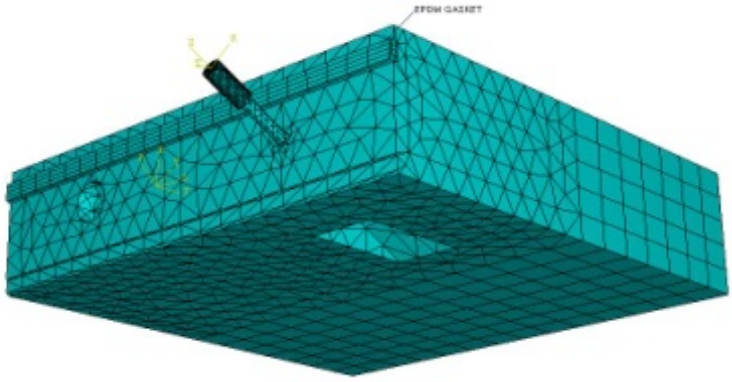

(b) Segment end detail

Figure 7.3 FE mesh – Modern joint

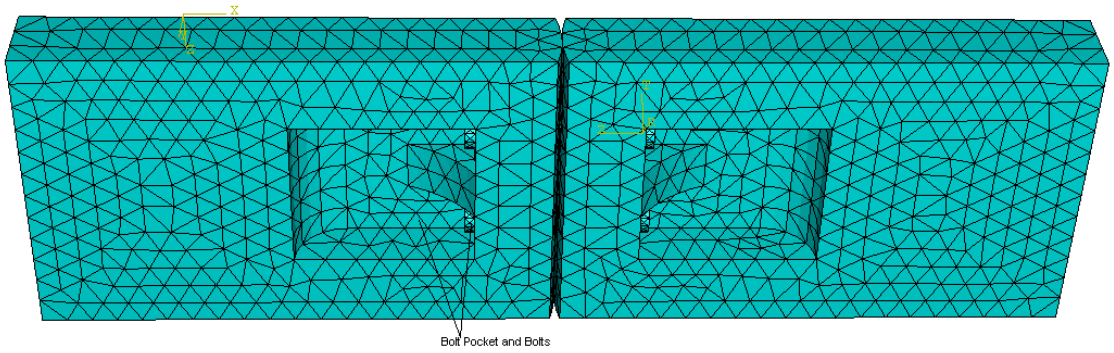

(a) 3-D FE mesh – Flexible joint

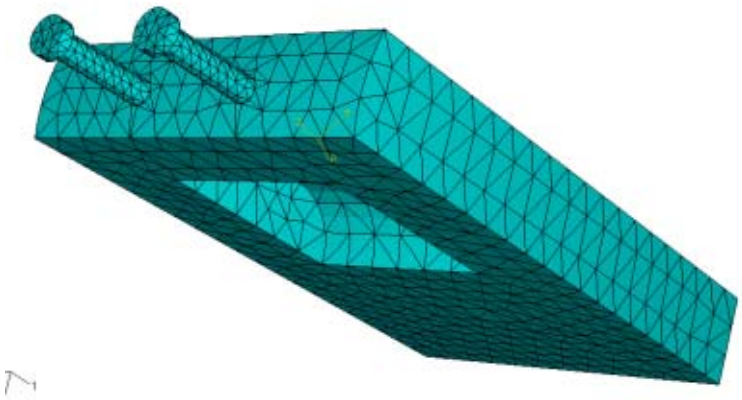

(b) Segment end detail

Figure 7.4 FE mesh – Flexible joint

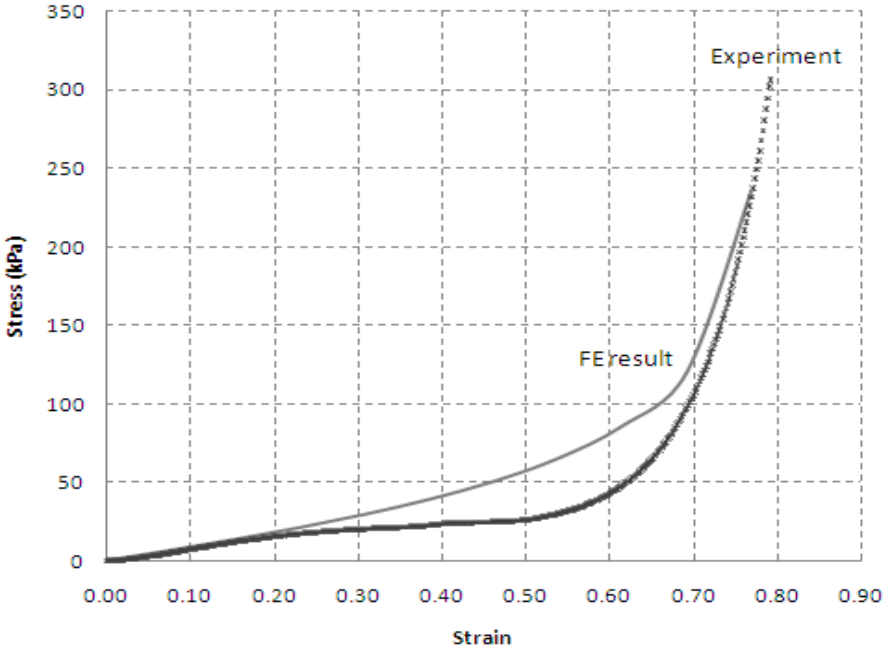

Figure 7.5 The stress-strain response of the EPDM gasket

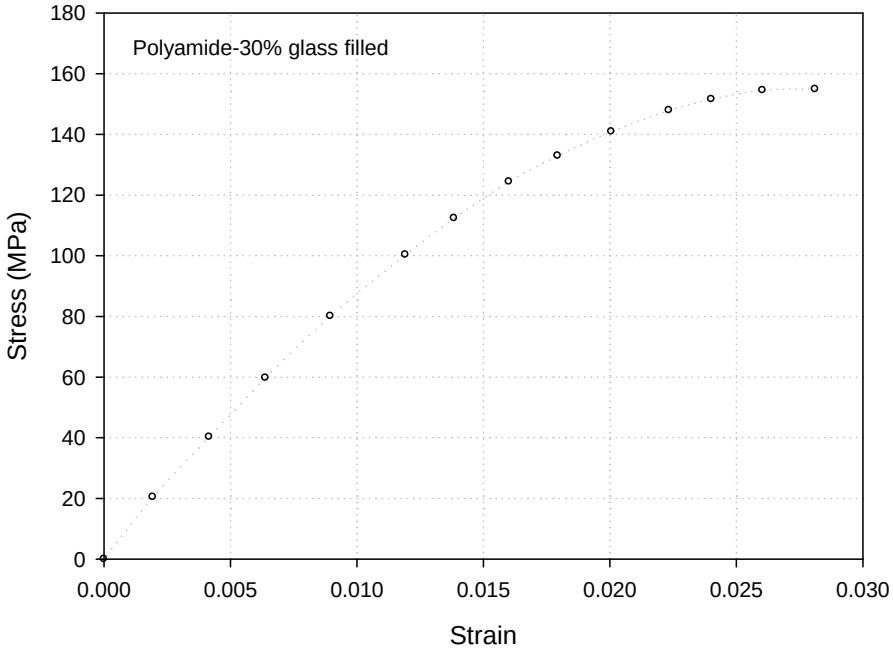

Figure 7.6 The stress-strain behaviour of 30% glass filled polyamide (RTP, 2006)

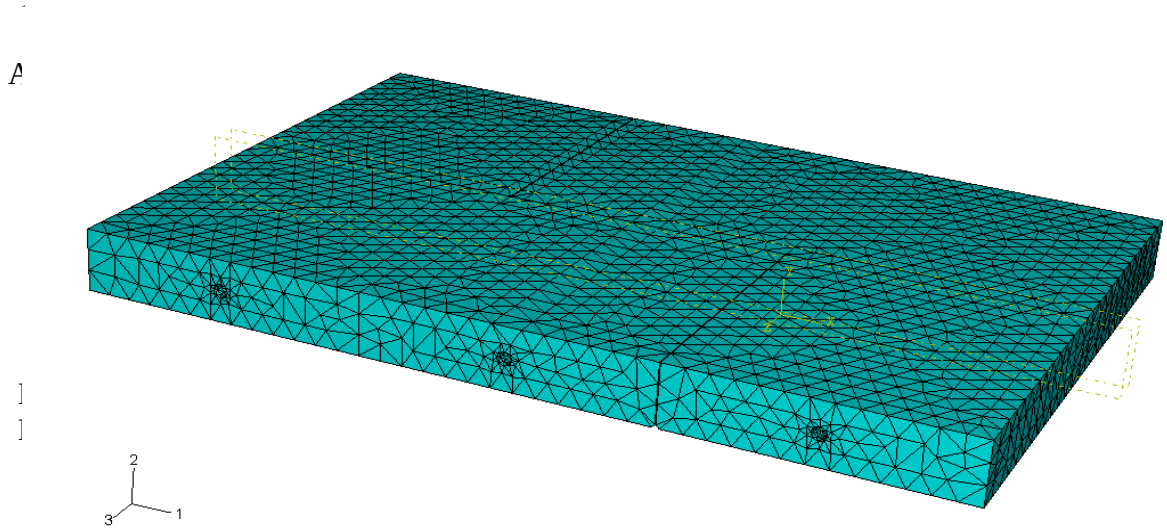

Figure 7.7 The FE mesh of staggered modern joints using simplifed joint method (SJM)

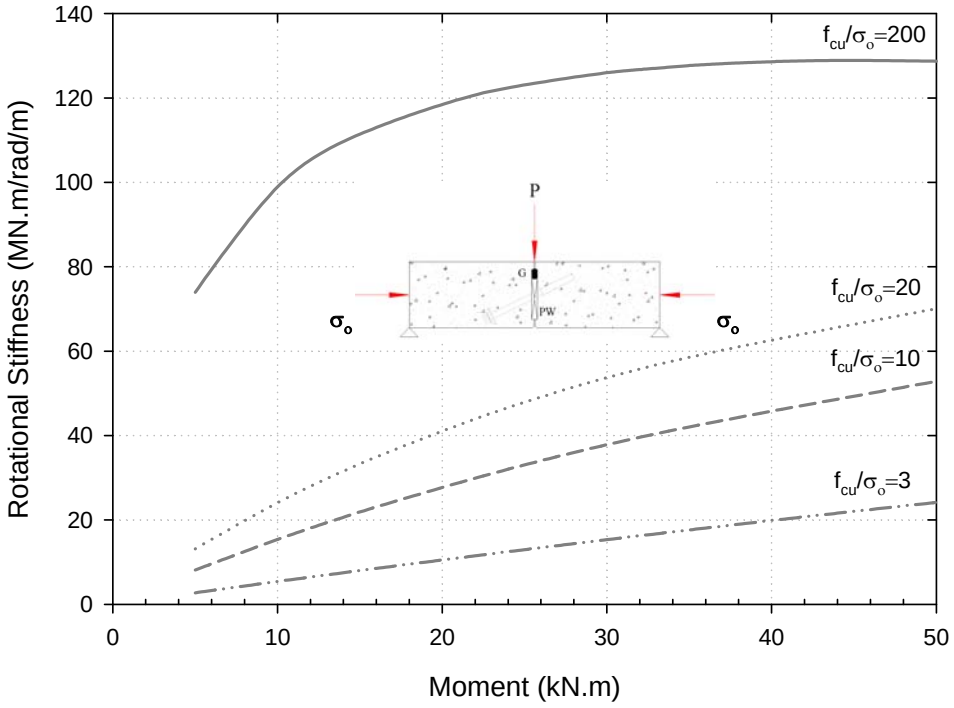

Figure 7.8 Rotational stiffness (per meter) of the modern joint

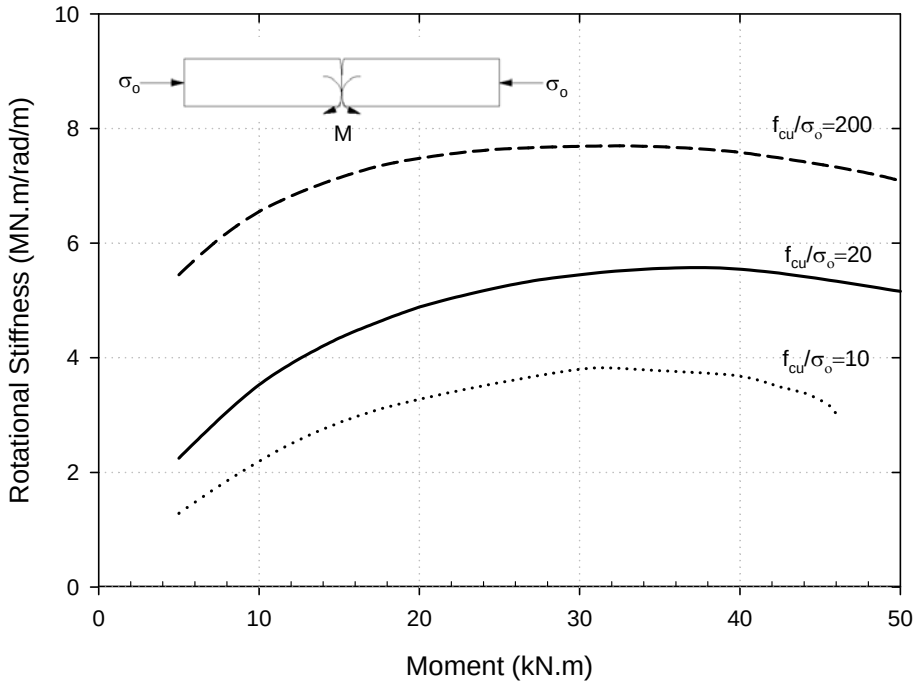

Figure 7.9 Rotational stiffness (per meter) of the flexible joint

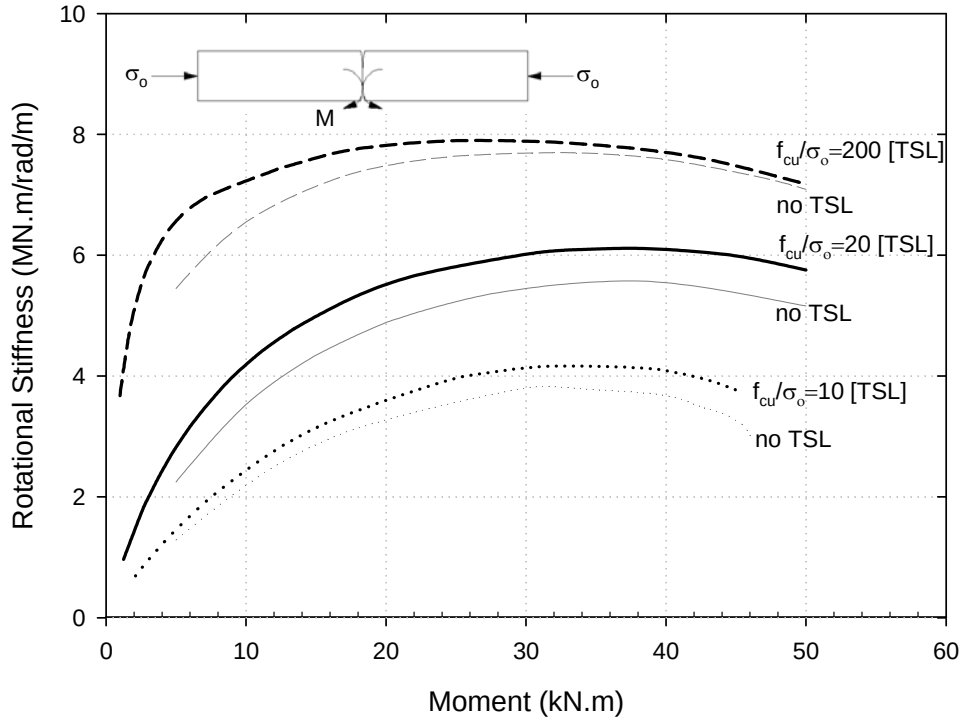

Figure 7.10 Rotational stiffness (per meter) of the flexible joint with TSL

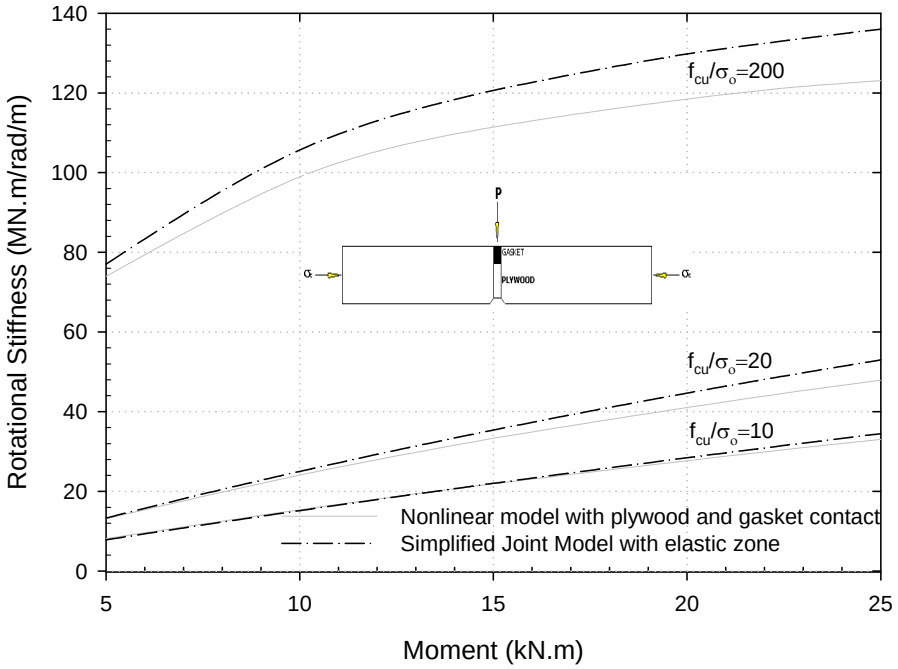

Figure 7.11 Rotational stiffness comparsion between the modern joint model and the simplifed joint

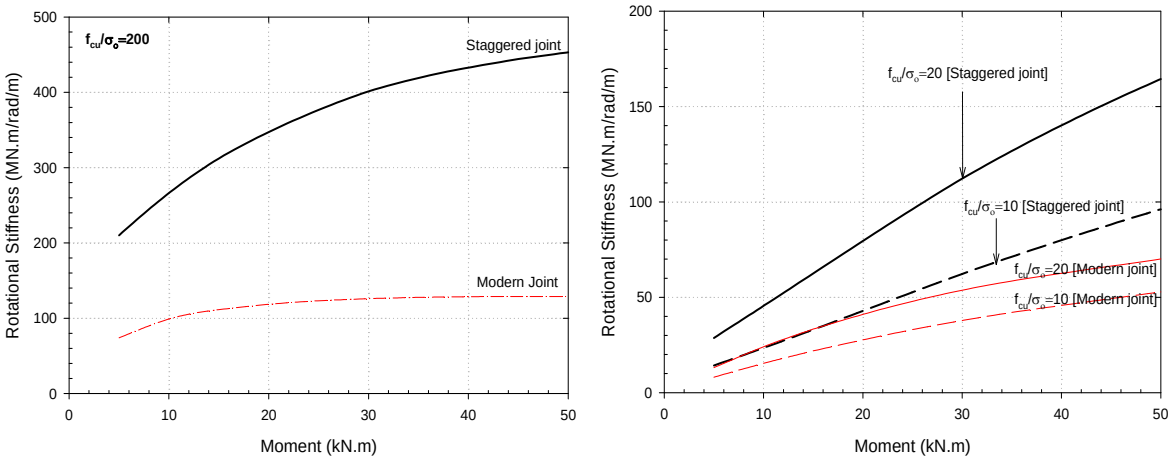

(a) f_{cu}/σ_o = 200 (b) f_{cu}/σ_o = 20 and 10

Figure 7.12 Rotational stiffness (per meter) of the staggered model using SJM

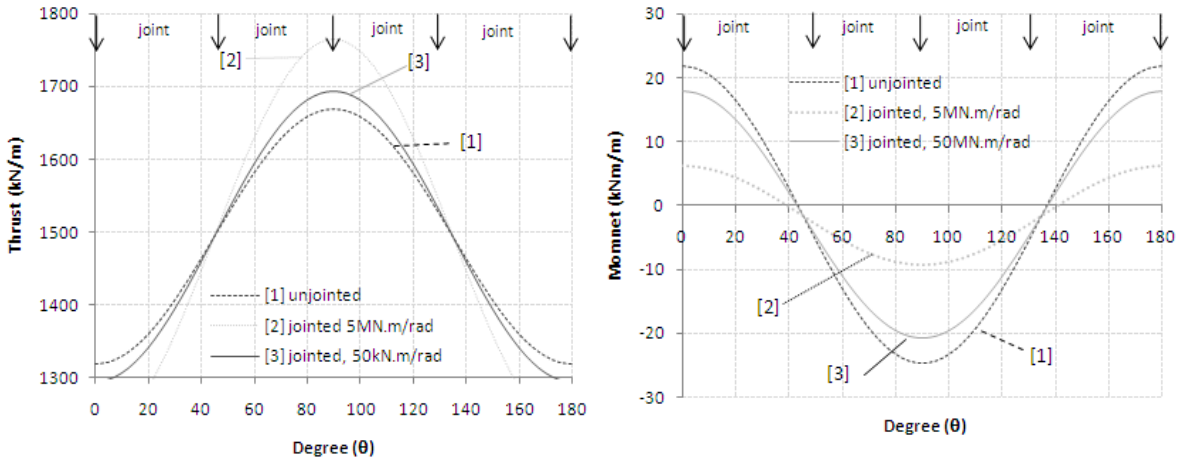

(a) Thrust (b) Moment

Figure 7.13 Thrust and moment in the example problem

CHAPTER 8

SUMMARY, CONCLUSIONS, AND RECOMMENDATIONS

8.1 GENERAL

This thesis demonstrates that an integrated study of Thin-Spray-on Lining (TSL) effects on the segmental concrete tunnel lining was successfully conducted with respect to: 1) protecting the linings due to fires, 2) limiting concrete spalling and cracking, 3) increasing the load-carrying capacity particularly after the concrete yields, and 4) increasing joint rotational stiffness thus, reducing the thrust on the linings, but increasing the moments at the joints. The major contribution of this study is to introduce, test and evaluate a TSL as an insulating material for fire and a substrate material in for reinforced concrete tunnel linings. Another contribution of this study is that such experimental approaches can be repeatable and verifiable using numerical analyses that can be utilized in concrete structures which require special treatments such as fire protection. Also, the comprehensive results obtained assure the usefulness of a TSL as a substrate material on an existing segmental concrete tunnel, in particular for the TTC subway line (Yonge and Spadina).

8.2 SUMMARY AND CONCLUSIONS

Basically, this thesis can be divided into three parts. The first part deals with the TSL as an insulating material for fire testing (i.e. CAN/ULC S102-03). Both the experimental study and its numerical analysis are presented in Chapter 3 and Chapter 4, respectively. The second part considers the TSL as a substrate material which potentially reduces concrete spalling and

cracking on the concrete lining. Also, the TSL layer increases the load carrying capacity of a segment subjected to uniaxial loading. These aspects are described in Chapter 5 and Chapter 6. The last part includes the rotational joint stiffness of the modern and flexible joints. In Chapter 7, the joint rotational stiffness changes due to geometric nonlinear effects are demonstrated. Also, the numerical results demonstrate that the TSL layer increases the rotational joint stiffness of the flexible joint. The TSL effects on the rotational joint stiffness are closely related to the initial thrust on the linings. Additionally, staggering the modern joint increases the equivalent rotation stiffness which is comparable to an un-jointed lining. The following sections delineate the major findings and conclusions drawn from this comprehensive study.

8.2.1 TSL as an Insulating Material

In Chapter 3, a total of four tests were conducted to determine the TSL effects in a planned tunnel fire. The four tests demonstrated that a specific TSL has excellent performance as an insulating material. The maximum concrete surface temperature for the TSL coated concrete slabs was approximately 60 percents less than for the uncoated concrete slabs. The TSL effects extended to crack prevention on the concrete surface when exposed to the planned fire event (i.e. less than 700 °C for 25 minutes). Overall, it is a very effective method of fire protection for existing tunnel linings compared with other methods, such as the installation of fire protection boards, spraying mortar, or a secondary liner.

Numerical analysis using TEMP/W employing a constant specific heat capacity, a constant thermal conductivity and time-dependent temperature boundaries was conducted in Chapter 4. The numerical analysis can predict the temperature distribution on the concrete slabs. The linear

FE analysis using constant thermal properties for the materials and time-dependent temperature boundary conditions corresponding to those measured during the tunnel fire tests presents good agreement to the measured concrete temperatures with TSL layers applied including the intact TSL and the char barrier. The calculated temperature versus time and with depth is close to the measured temperatures.

The analysis confirms the conclusion that the TSL causes a reduction in temperature in concrete slabs during 20 minutes of testing in CAN/ULC-S102-M88 tunnel tests due to its insulating effect (i.e. its thermal conductivity is $1/10^{th}$ that of concrete).

8.2.2 TSL as a Substrate Material

In Chapter 5, the tensile strength and the adhesion strength of a specific TSL were determined using ASTM D683-08 and the developed testing method by Archibald (Archibald, 1998). The TSL yield strength marked between 4 MPa and 6 MPa was measured and the ultimate elongation varied from 125% to 170% depending on the layer density. The adhesion strengths from the pull-off testing varied from 14 kPa to 502 kPa. Such a variation is due to the moisture content and surface roughness conditions of the concrete specimens. It is revealed that optimal conditions to maximize the adhesion strength of a TSL on concrete are clean and rough surfaces with minimum water contents that depends on the curing conditions. Consequently, with the characteristics of relative high tensile strength and relatively high adhesion strength, the TSL layer can reduce concrete spalling or crack propagation due to fire exposure or corrosion.

In Chapter 6, the load carrying capacity of concrete segments used in the TTC subway tunnel subjected to uniaxial loading was evaluated. The results from uncoated segment tests were used as a benchmark and compared with the results for the TSL coated segments. Based on the test results, the TSL layer substantially improved the load carrying capacity of the segment, in particular after concrete yielding or after cracks occurred. The TSL effect on the ultimate load carrying capacity is approximately a 5 kN improvement.

Similar results can be calculated in the nonlinear elasto-plastic FE analyses using ABAQUS. The FE results provide satisfactory predictions in both displacement and strain in terms of the applied loads. However, it is found that there is relatively high variation in the small displacements (i.e. less than 10 mm). This can be due to the differences of use between the practical concrete segments and theoretical intact FE models.

In consequence, considering all results from Chapters 5, 6, and 7, the TSL tested is an excellent substrate material for the existing reinforced concrete linings. It can increase serviceability of the TTC subway tunnel linings.

8.2.3 Joint Rotational Stiffness

In Chapter 7, the rotational joint stiffness was evaluated using ABAQUS. The analysis accounted for the joint geometry, the initial thrust in the joint geometric nonlinear contact behaviour, and the non-linear stress-strain response of the joint materials. Two different joint types, namely the modern joint type and the flexible joint type, were examined. The modern joint for the segmental concrete linings consisted of two inclined bolts per segment, polyamide bolt sockets, a single

EPDM gasket, and plywood packing between the concrete-concrete contacts. The flexible joint was comprised of a concrete segment with curved ends connected by steel bolts that passed through embedded ferrules. Neither plywood packing nor gasket material was considered.

In the analyses, general responses of the joint rotation for the moment M and the initial thrust could be evaluated. The initial thrust on the lining is one of the major attributes to determine the rotational stiffness. For steady thrust, the joint rotational stiffness increased with increasing M due to not only the stress-strain response of some joint materials, but also to primarily geometric nonlinear effects. The modern joint had a rotational stiffness varying from 3 MN.m/rad to 60 MN.m/rad.

The flexible joint has a rotational stiffness that varied from 0.5 MN.m/rad to 8 MN.m/rad. A 4 mm thick TSL layer was applied to the flexible joint model to examine the effects of the TSL on rotational stiffness. As expected, the joint stiffness increased due to the application of a TSL layer. However, the TSL effects may not be considerable, in particular, for a higher $f_{cu}/\ \sigma_o = 200$.

Finally, staggering the modern joint was investigated using the simplified joint method. The equivalent rotational stiffness was 2 to 3 times higher than for the single joint. Particularly for a high $f_{cu}/\ \sigma_o$ ratio, the moments in linings designed using staggered modern joints were comparable to those for an un-jointed lining.

8.3 RECOMMENDATIONS FOR FUTURE RESEARCH

The following outline some aspects that should be considered in future studies:

1) An extensive study is needed to evaluate the higher tunnel lining exposure temperatures which meet some European Standards (i.e. temperatures up to 1200° C for 60 minutes). Also, in order to implement the numerical analysis using the European Standards, the thermal properties of a TSL should be re-evaluated through the event of exposure to excessive heat. It is recommended that variable thermal properties of TSL with temperatures should be considered in order to predict TSL responses at higher temperatures.
2) It is recommended that the adhesion strength assessment associated with fire testing be extended. It can provide the values necessary for a TSL as a substrate material to reduce concrete spalling and cracking after a fire event. Such research can be applied to investigate load-carrying capacities of existing concrete tunnel linings when examining the impact of coupled events such as thermal and mechanical forces at work in tunnels.
3) It is also recommended that the TSL effects on the rotational joint stiffness for the modern and flexible joints be investigated in an experimental manner.
4) Finally, further studies associated with effects of nonlinear joint stiffness are recommended to investigate how they apply to the reinforcement design of precast segmental concrete tunnel linings.

REFERENCES

ABAQUS Analysis User's Manual (2007). Section18.5: Concrete, Online Manual

Ananiev, S., and Ozbolt, J. (2004). "Plastic-damage model for concrete in principal directions." Fracture Mechanics of Concrete Structures, FraMCoS-5, Vail, Colorado, USA, pp. 271–278.

ASTM Standards D638-08 (2008). Standard test method for tensile properties of plastics. ASTM International, West Conshohocken, PA, DOI: 10.1520/C0033-03, www.astm.org.

ASTM Standards E1269-05 (2005). "Standard Test Method for Determining Specific Heat Capacity by Differential Scanning Calorimetry." ASTM International, West Conshohocken, PA, 6p. www.astm.org

ASTM Standards E1461-03 (2003). "Standard Test Method for Thermal Diffusivity of Solids by the Flash Method." ASTM International, West Conshohocken, PA. 13p. www.astm.org

ASTM Standards E1530-06 (2006). "Standard Test Method for Evaluating the Resistance to Thermal Transmission of Materials by the Guarded Heat Flow Meter Technique." ASTM International, West Conshohocken, PA. 9p. www.astm.org

ASTM C684-99 (2003). "Standard Test Method for Making, Accelerated Curing, and Testing: Concrete Compression Test Specimens". ASTM International, West Conshohocken, PA, 2003, DOI: 10.1520/C0033-03, www.astm.org.

ASTM C873M-04e1 (2003). "Standard Test Method for Compressive Strength of Concrete Cylinders Cast in Place in Cylindrical Molds". ASTM International, West Conshohocken, PA, 2003, DOI: 10.1520/C0033-03, www.astm.org.

Aruga, T., Arai, Y., and Tsuno, K. (2007). "Non-linear stiffness behavior and analysis of tunnel lining with reinforcing bars." Quarterly Report, Railway Techinical Reserch Institute, Vol. 48(1), pp.44-49

Archibald, J.F. (1992). “Assessment of wall coating materials for localized wall support in underground mines.” Report of Phase 2 Investigation for the Mining Industry Research Organization of Canada (MIROC), 162 p.

Archibald, J.F. and Nicholls, T. (2000). “Comparison of reinforcement benefits of spray-on linings in side-by-side unconfined compression failure tests on rock.” Proceedings of the 103rd CIM Annual General Meeting, Quebec City, Quebec, CD-Rom Publication

Archibald, J.F. and Nicholls, T. (2001). “Assessing acceptance criteria for and capabilities of Liners for mitigating ground falls.” Proceedings of Mining Health and Safety Conference, Sudbury, Ontario, CD-Rom Publication

Archibald, J.F. and Katsabanis, P.D. (2003). "Comparative use of shotcrete, fibercrete and thin, spray-on polymer liners for blast damage mitigation ," 105th Annual General Meeting of the Canadian Institute of Mining, Metallurgy and Petroleum , Montreal, Quebec, May, 2003.

Bazant, Z.P. and Kim, S-S. (1979). “Plastic-fracturing theory for concrete.”, Journal of the Engineering Mechanical Division ASCE, 105, pp. 407–428.

Beard, A. N., and Carvel, R. (2005). The Handbook of Tunnel Fire Safety. Thomas Telford Publishing, Telford Ltd., Heron Quay, London. 536p.

Beard, A. N. (2009). “Fire safety in tunnels.” Fire Safety Journal, Vol.44 (4), pp 276-278.

Blom, C.B.M., Van der Horst, E.J., and Jovanovic, P.S. (1999). “Three-dimensional structural analysis of the shield-driven ‘Green Heart’ Tunnel of the high-speed line south.” Tunnelling and Underground Space Technology, Vol. 14(2) pp.217-224

Blom, C.B.M. (2002) Design phylosophy of segmental linings for tunnels in soft soils, Ph.D. Thesis, Delft Univ. of Technology, the Netherlands.

Both, C. (1999). “Tunnel safety- underground traffic and risks.” Technical Paper, Head TNO Centre for Fire Research. Delft, the Netherlands, 14p

Breunese A.J. and Fellinger, J.H.H. (2004). “Spalling of concrete- an overview of ongoing research in the Netherlands.” Workshop-Structure in fire, Ottawa, May 2004.

British Tunnelling Society (2004). Tunnel Lining Design Guide. Thomas Telford Drafted by the British Tunnelling Society and the Institute. 184p.

Bull A. (1944). “Stresses in linings of shield-driven tunnels.” Journal of Soil and mechanics and Foundation Division, ASCE 70:443-530

CAN/ULC-S-102-M88, (1988). “Standard method of test for surface burring characteristics of building materials and assemblies.” National Standards of Canada, Prepared and published by Underwriters’’ Laboratories of Canada, 4th Edition, 1988, 30p

Carreira, D.J. and Chu, K.H. (1985).“Stress-strain relationship for plain concrete in compression.” ACI J. Vol.82 pp.797-804

Chen, A.C.T., and Chen, W.F. (1975). “Constitutive relations for concrete.”, Journal of the Engineering Mechanical Division, ASCE 101, pp. 465–481.

Chen, E.S., and Buyukozturk, O. (1985). “Constitutive model for concrete in cyclic compression.” Journal of the Engineering Mechanics Division, ASCE 111, pp. 797–814.

De Nicolo, B., Pani, L., and Pozzo, E. (1994) “ Strain of concrete at peak comprssive stress for a wide range of compressive strengths.” Materials and Structures, Vol. 27, pp.206-210

Dragon, A., and Mroz, Z. (1979). “A continuum model for plastic-brittle behavior of rock and concrete.” International Journal of Engineering Science Vol.17, pp. 121–137.

Einstein, H. H., and Schwartz, C.W. (1979) “ Simplified analysis of tunnel support.” ASCE J. of Geotech. Engrg. Div., 105(GT4): 499-518.

El Naggar, H and Hinchberger, S.D. (2008) “Analytical solution for jointed tunnel linings in elastic soil or rock.” Can. Geotech. J., 45(11): 1572-1593.

El Naggar, H., Hinchberger, S.D., and El Naggar, M.H. (2008) “Simplified analysis of seismic in-plane stresses in composite and jointed tunnel linings.” Soil Dyn. Earthqua. Engrg, 28(12): 1063-1077.

Erdakov, P. and Khokhryachkin, D. (2005). Impact of Fire on the Stability of Tunnels. Master’s thesis, Department of Civil and Environmental Engineering, Lulea University of Technology, Sweden. 61p.

Este, G and Willam, K.J. (1994). “A fracture-energy based constitutive formulation for inelastic behavior of plain concrete.” Journal of Engineering Mechanics, ASCE 120, pp. 1983–2011.

Eurocode. (2004). Design of concrete structures, Part 1.2. General rules-Structural fire design. Commission of European Communities, Brussels.

Fellinger,T. and Both, C. (1997). “Small scale fire tests in determining the sensitivity to spalling of concrete samples of various mixtures subjected to RWS heating curves.” TNO report 97-CVB-R1463.

Gawin, D., Pesavento, F., and Schrefler, B.A. (2006). “Towards prediction of the thermal spalling risk through a multi-phase porous media model of concrete.” Computer Methods in Applied Mechanics and Engineering. Vol. 195(43), pp.5707-5729

Grassl, P., Lundgren, K., and Gylltoft, K. (2002). “Concrete in compression: a plasticity theory with a novel hardening law.” International Journal of Solids and Structures 39, pp. 5205–5223.

Gruebl, F. (2006). “Modern design aspects of segmental lining.” International Seminar on Tunnels and Underground Work. LNEC, Lisbon June 29-30, 2006.

Haack, A. (1994). Fire Protection in Traffic Tunnels –Initial Findings from Large-scale Tests. Tunneling and ground condition, Abdel Salam edition. Balkerna, Rotterdam, ISBN905410363, pp 317-326

Harmathy, T. Z., and Allen, L.W. (1973). “Thermal properties of selected masonry unit concretes.” ACI J. Proc., 70(2), 132-142.

He, W. and Wu, Z. (2005). “Comperssive failure mechanism of deformed concrete tunnel linings due to a vertically concentrated load.” Journal of Structural Mechanics and Earthquake Engineering, JSCE. Vol.22 (2), pp.73-84

Hefny, A.M., Tan, F.C., and Macalevey, N.F. (2004). “ Numerical study on the behaviour of jointed tunnel lining.” Journal of the Institute of Engineers, Singapore Vol. 44(1):108-118

Hertz, K.D. (2003). “Limits of spalling of fire-exposed concrete.” Fire Safety Journal. Vol. 38:2, pp. 103-116.

Imran, I., and Pantazopoulu, S. J. (2001). “Plasticity model for concrete under triaxial compression, Journal of Engineering Mechanics.” 127, pp. 281–290.

JSCE, Japan Society of Civil Engineers (1977). “The design and construction of underground structures.” JSCE. Tokyo.

Jasson R.M., and Bostrom L. (2010). “The influence of pressure in the pore system on fire spalling of concrete.” Fire Technology, Vol. 46 (1), pp.217-230.

Khoury, G.A. (2003). “Passive fire protection in Tunnels”, Concrete, February 1, 2003 pp.31-36

Kirkland, C.J. (2002). “The fire in the Channel Tunnel.” Tunnelling and Underground Space Technology, Vol.17 (2), pp.129-132.

Kratzig, W., and Polling, R. (2004). “An elasto-plastic damage model for reinforced concrete with minimum number of material parameters.” Computers and Structures 82 pp. 1201–1215.

Karabinis, A.I., and Kiousis, P.D. (1994). “Effects of confinement on concrete columns: a plasticity theory approach.” ASCE Journal of Structural Engineering 120, pp. 2747–2767.

Kodur, V.R., and Sultan, M.A. (1998). “Structural behaviour of high strength concrete columns exposed to fire.” Proc., Inter. Symp. On High Performance and Reactive Powder Concrete, Sherbrooke, Canada, 217-232.

Kodur, V.R. and Khaliq, W. (2011). “Effect of temperature on thermal properties of different types of high-strength concrete.” J. Mater. Civ. Eng. 23(6) pp.793-801

Koyama, Y. and Nishimura, T. (1998). “Design of lining segment of shield tunnel using a beam-spring model.” Quarterly Report of RTRI, 39(1) pp.23-27

Krahn, J. (2004) “Thermal modelling with Temp/W: An engineering methodology” Geo-Slope International Ltd. 1st Edition, 292p.

Kramer, G.J.E., Sedarat, H., Kozak, A. Liu,A., and Chai, J. (2007). “Seismic Response of Precast Tunnel Linings.” Proceedings 2007 Rapid Excavation and Tunnelling Conference, Toronto, CD-Rom

Underwriter’s, Laboratories of Canada (2003). CAN/ULC-S102-M88, Method of Test for Surface Burning Characteristics of Building Materials and Assemblies.

Lee, J and Fenves, G.L. (1998). “A plastic-damage concrete model for earthquake analysis of dams.” Earthquake Engineering and Structural Dynamics, Vol.27 pp.937-956

Lee, K.M., and Ge, X.W. (2001). “The equivalence of jointed shield-driven tunnel lining to a continuous ring structure.” Can. Geotech. J., 38, pp.461-483

Lee, K.M., Hou, X.Y., Ge, X.W., and Tang, Y. (2001). “An analytical solution for a jointed shield-driven tunnel lining.” International Journal of Analytical and Numerical method in Geomechanics, 25(4), pp.365-390.

Lubliner, J., Oliver, J., Oller, S., and Onate, E. (1989) “A plastic damaged model for concrete.” International Journal of Solids and Structures, Vol.25(3), pp.229-326

Lu, L., Lu, X. and Fan, P. (2006). “Full-ring experimental study of the lining structure of Shanghai Changjing Tunnel.” Proceedings 4th International Conference on Earthquake Engineering, Oct. 12-13 Taipei, Taiwan No.056

Mander, J.B., Priestley, M.J.N, and Park, R (1988). “ Theoretical stress-strain model for confined Concrete. J. Struct Eng. ASCE 114 (8):1804-1826

Mascia, L. (1989). Thermoplastics: Materials Engineering. Elsevier Applied Science, 2nd Edition, 537p

Mashimo, H., Isago, N., Yoshinaga, S., Shiroma, H., and Baba, K. (2002) " Experimental investigation on load-carrying capacity of concrete tunnel lining." Proceedings the 28th ITA-AITES General Assembly and World Tunnel Congress. CD-Rom

Mashimo, H., and Ishimura, T. (2003). "Evaluation of load on shield tunnel lining in gravel." Tunneling and Underground Space Technology. 18, 233-241

Menetrey, P., and Willam, K.J. (1995). "Triaxial failure criterion for concrete and its generalization." ACI Structural Journal 92, pp. 311–318.

Menzel, A., Ekh, M., Runesson, K., and P. Steinmann, P. (2005). "A framework for multiplicative elastoplasticity with kinematic hardening coupled to anisotropic damage." International Journal of Plasticity 21 (3), pp. 397–434.

Ministery of the Interior - Ministry of Equipment, Transportation and Housing (1999). Task Force for Technical Investigation of The 24 March 1999 Fire in The Mont Blanc Vehicular Tunnel - Report of 30, June 1999 (English translation version)

Morgan, H.D. (1961). "A contribution to the analysis of stress in a circular tunnel." Geotechnique 11:37-46

Muir Wood, A.M (1975). "The circular tunnel in elastic ground." Geotechnique 25(1):115-127.

Nakamura, H., Kubota, T., Furukawa, M., and Nakao, T. (2003). "Unified construction of running track tunnel and crossover funnel for subway by rectangular shape double track cross-section shield machine." Tunneling and Underground Space Technology, 18, 253-262

Nakamura, M., Yamaguchi, T., Hirosawa, N., and Nishida, K. (1998). " New mechanical joint segment tunnl lining system." Nippon Steel Technical Report No. 77 pp 40-46.

Nishikawa, K. (2003). “Development of a prestressed and precast concrete segmental lining.” Tunneling and Underground Space Technology, 18, 243-251

NFPA 130 (2000). “Standard for Fixed Guideway Transit and Passenger Rail Systems. National Fire Protection Association, Inc. Quincy, MA.

Onate, E., S. Oller, S., Oliver, S., and J. Lubliner, J. (1988). “A constitutive model of concrete based on the incremental theory of plasticity.” Engineering Computations 5, pp. 309–319.

Ono, Koichi (2006). “Fire design requirement for various tunnels.” Keynote Presentation, ITA.AITES and World Tunnel Congress and 32th General Assembly, Seoul, April 22-27 Korea.

Ortiz, . Ortiz, A (1985). “Constitutive theory for the inelastic behaviour of concrete.” Mechanics of Materials, 4 (1) (1985), pp. 67–93.

Parker, W.J., Jenkins, R.J., Butler, C.P., and Abbott, G.L. (1961). “Flash method of determining thermal conductivity, heat capacity and thermal conductivity.” J. App. Phys. 32, pp.1679-1684.

Peck, R.B., Hendron, A.J., and Mohraz, B. (1972). “State of the art of soft ground tunnelling.” 1st Rapid Excavation and Tunnel Conference, Vol.1 Illinois, pp.256-289

Pevsner, P., Levy, R., Nsieri, E., and Rutenberg, A. (2005). “Benchmark II: Numerical analyses for masonry vault.” Prohitech, WP8, 17p

RTP company (2006). Product Data Sheet & General Processing Conditions: RTP205 Nylon6/6 Glass Fiber: www.rtpcompany.com/info/data/0200/RTP205.htm

Promat (2003). Tunnel fire protection for tunnel structures and service. Tunnel brochure, Promat International NV, the Netherlands. 68p.

Spray-On Plastics (2000). RochWeb™ System. Spray-On Plastics Inc. Technical data sheet, 1p.

Schreyer, J. and Winselmann, D. (2000). “Suitability Tests for the Lining for the 4th Elbe Tunnel Tube-Results of large-scale Tests.” Tunnel, 1, pp.34-44

Tannant, D.D., Swan, G., Espley, S. and Graham,C. (1999). “Laboratory test procedures for validating the use of thin sprayed-on liners for mesh replacement.” Proceedings 101st CIM Annual General Meeting, Calgary, Alberta, CD-Rom Publication.

Technical Tunneling Components (2009). Dowelock Test Results. Westmoreland Mechnical testing & Research, Ltd., June 2nd 2009.

Troitzsch J. (2004). Plastics Flammability Handbook, 3rd Edition. Hanser Gardner Publications, Inc

Voyiadjis, G.Z, and Abu-Lebdeh, T.M. (1994). “Plasticity model for concrete using the bounding surface concept.” International Journal of Plasticity 10, pp. 1–21.

William, K.J., and Warnke, E.P. (1975). “Constitutive model for the triaxial behavior of concrete.” International Association of Bridge and Structural Engineers, Seminar on Concrete Structure Subjected to Triaxial Stresses, Paper III-1, Bergamo, Italy, May 1974, IABSE Proceedings 19.

Yan, Z.G and Zhu, H.H. (2007). “Experimental study on mechanical behavior of tunnel lining under after fire scenario.” Proceedings of the 33th ITA-AITES General Assembly and World Tunnel Congress- The 4th Dimension of Metropolises. CD-Rom

Youngquist, J.A. (1999). Wood handbook – Wood as an engineering material. Gen. Tech. Report. FPL-GTR-113. Madison. WI: U.S. Department of Agriculture. Forest Service. Forest Products Laboratory. pp.1-463.

APPENDIX-A

A.1 Concrete Strength

In the preliminary tunnel tests, the concrete was supplied by Lafarge Canada Inc. and it had an average 28-day unconfined compressive strength of 25 MPa and a unit weight of 2200 kg/m^3. For the detailed instrumentation tunnel tests, CBM (Canadian Building Materials Co.) supplied concrete which had an average unconfined compressive strength of 51 MPa and a unit weight of 2300 kg/m^3. Table A.1 summarizes the results of unconfined compressive strength tests on concrete specimens for 1, 3, 7, 14 and 28 days. The unconfined compressive strength of 51 MPa is comparable to the design strength of TTC precast concrete linings.

Table A.1 Concrete strength

Time (days)	Avg. strength (# of sample tested)	Remarks
28	25(3) MPa	Preliminary tunnel tests
1*	36(1)* MPa	Detailed Instrumented tunnel tests
3	30(2) MPa	
7	36(2) MPa	
14	49(2) MPa	
28	51(3) MPa	

*Referred to ASTM C684-99, *Standard Test Method for Making, Accelerated Curing, and Testing Concrete Compression Test Specimens*

A.2 TSL Density

The density of the TSL used was measured in each spray. A density greater than 1.025 g/cm^3 is generally required for good performance during CAN/ULC-S102-M88 tunnel tests. The density of the TSL was measured by placing coupons in pure water and sodium chloride (NaCl) solutions with concentrations of 1.025 g/ml, 1.03 g/ml, 1.05 g/ml and 1.07 g/ml. The TSL density was assumed to be equal to the density of the solution in which the coupon would just

float. For a given test, 12 coupons of TSL were used to measure the density. Table A.2 summarizes the mean density and thickness of TSL applied to the concrete slabs.

Table A.2 TSL density and thickness for the detailed instrumentation tests

Slab #	Density (g/cm^3)	Thickness of TSL (mm)	Colour variation	Remarks
TSL with density less than 1.05 g/cm^3				
1	1.010	4.8	Y	
3	1.005	4.8	N	
4	1.027	3.2	Y	blast on TSL
5	1.014	3.5	N	
6	1.046	2.7	N	
9	1.035	3.9	Y	
10	1.026	3.2-4.2	Y	boiled TSL
12	1.026	3.2-4.2	Y	
14	1.007	3.5-4.4	Y	minor cavities on the bottom of the slab
16	1.010	4.8	Y	minor cavities on a side
18	1.007	3.5-4.4	Y	
TSL with density more than 1.05 g/cm^3				
2	*1.051*	*4.5*	*N*	*Slab thickness variation*
8	*1.051*	*4.5*	*N*	
7	*1.051*	*4.0*	*N*	
11	*1.057*	*3.7*	*N*	
13	*1.057*	*3.5*	*N*	*minor cavities on the bottom of the slab*
15	*1.057*	*3.5*	*N*	*minor cavities on the bottom of the slab*
17	*1.057*	*4.0*	*N*	
19	*1.057*	*3.7*	*N*	

Italic number indicated that Huntsman Chemical based TSL

A.3 Crack Observations after the Fire Tests (PT-1 and PT-2)

Thermal cracks, after the pilot tests, are presented in Figures A.1 to A.4. The cracks developed mostly on the inner surfaces which were exposed to heat during the tests. The slabs were numbered B-1 to B-6 or S-1 to S-6 starting at the upstream end of the tunnel and going toward the downstream end. The labels ‘B’ and ‘S’ denote the uncoated (uncoated) concrete slabs and the TSL coated concrete slabs, respectively. (e.g. B-1**A** indicates the first uncoated concrete slab and **A** refers to the inner surface of the slab).

Cracks presented in Figures A.1 to A.4 were caused by heat during the tests and bending due to handling. Thermal cracks only developed in the first slab (B-1A) which was extensively exposed to high temperatures (up to 700 °C). Thermal cracks were usually generated in hairline or honeycomb patterns. Honeycomb thermal cracks were not sketched in the figures because it could not be readily observed by sight. The hairline thermal cracks had a width of less than 1.0 mm and the crack directions were either vertical or horizontal. In addition, all slabs had bending cracks due to mishandling. The bending cracks developed in various widths from 0.3 mm to 1.8 mm but all were horizontal.

Descriptions of the cracks before and after the tests can be found in Table A.3. As summarized in Table A.3, significant changes before and after each fire test can be found in slab B-1 to slab B-3 and slabs S-1, S-2, S-3 and S-4. Remarkably, S-4 showed a couple of local thermal exfoliations as shown in Figure A.4. It would occur due to lower concrete density in local areas.

Table A.3 Cracks observed in uncoated concrete slabs and TSL coated concrete slabs after the tunnel fire tests

Slab No.		Horizontal crack (Bending crack)	Thermal crack	Miscellaneous	Remarks
B-1A	Before	An original crack extended to a depth of 25mm. Location: 570mm from the upstream of the slab.	Three vertical thermal cracks appeared and one horizontal thermal crack was observed. (see Figure 2.11)	Blackened surface could be found between 200 and 350mm from the top end	
	After	A new crack appeared at 350mm from the upstream			
B-2A	After	An original crack fully extended to a depth of 35mm Location: 420mm from the upstream of the slab	No thermal crack	Blackened surface was observed over the surface	
B-3A	After	An original crack located in the middle of the slab fully extended (40mm)	No thermal crack	Locally blackened spots were observed	
S-1A	Before	An original crack fully developed with a depth of 33mm Location: 620mm from the upstream	No thermal crack	TSL were completely burned out. Char could be easily removed	A new crack developed just above the drilled holes. (see Figure 2.13)
	After	A new crack appeared at 700mm from the upstream.			
S-2A	After	An original crack extended to a depth of 36mm. Location: 700mm from the upstream	No thermal crack	Most TSL was burned out. But small amount of TSL can be found	
S-3A	After	An original crack extended to a depth of 28mm Location:450mm from the upstream	No thermal crack	TSL still remained at minimal thickness	
S-4A	After	An original crack extended to a depth of 15mm. Location: 300m from the upstream			

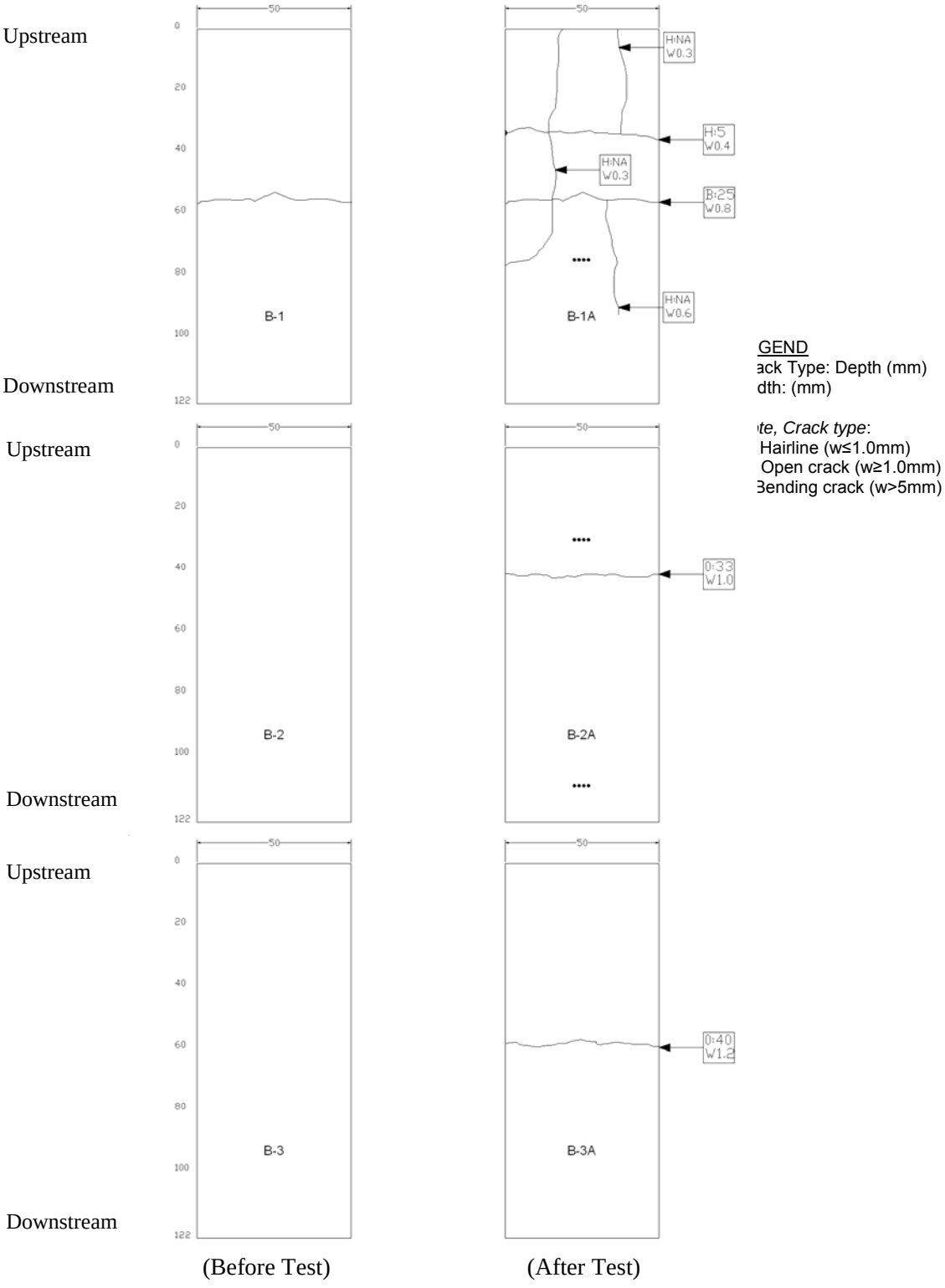

Figure A-1 Crack observations-Uncoated concrete slabs B-1, B-2 and B-3

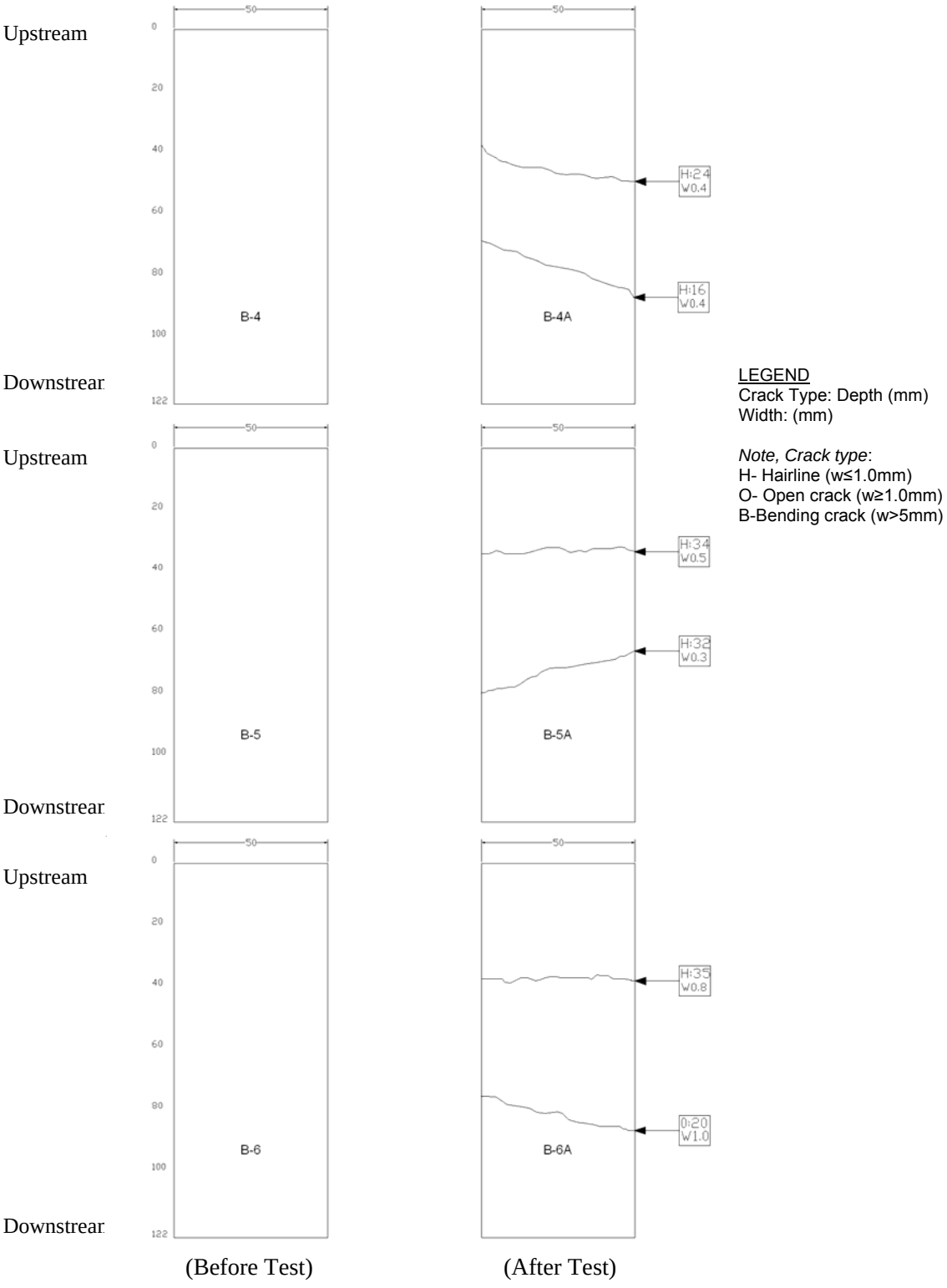

Figure A-2 Crack observations-Uncoated concrete slabs B-4, B-5 and B-6

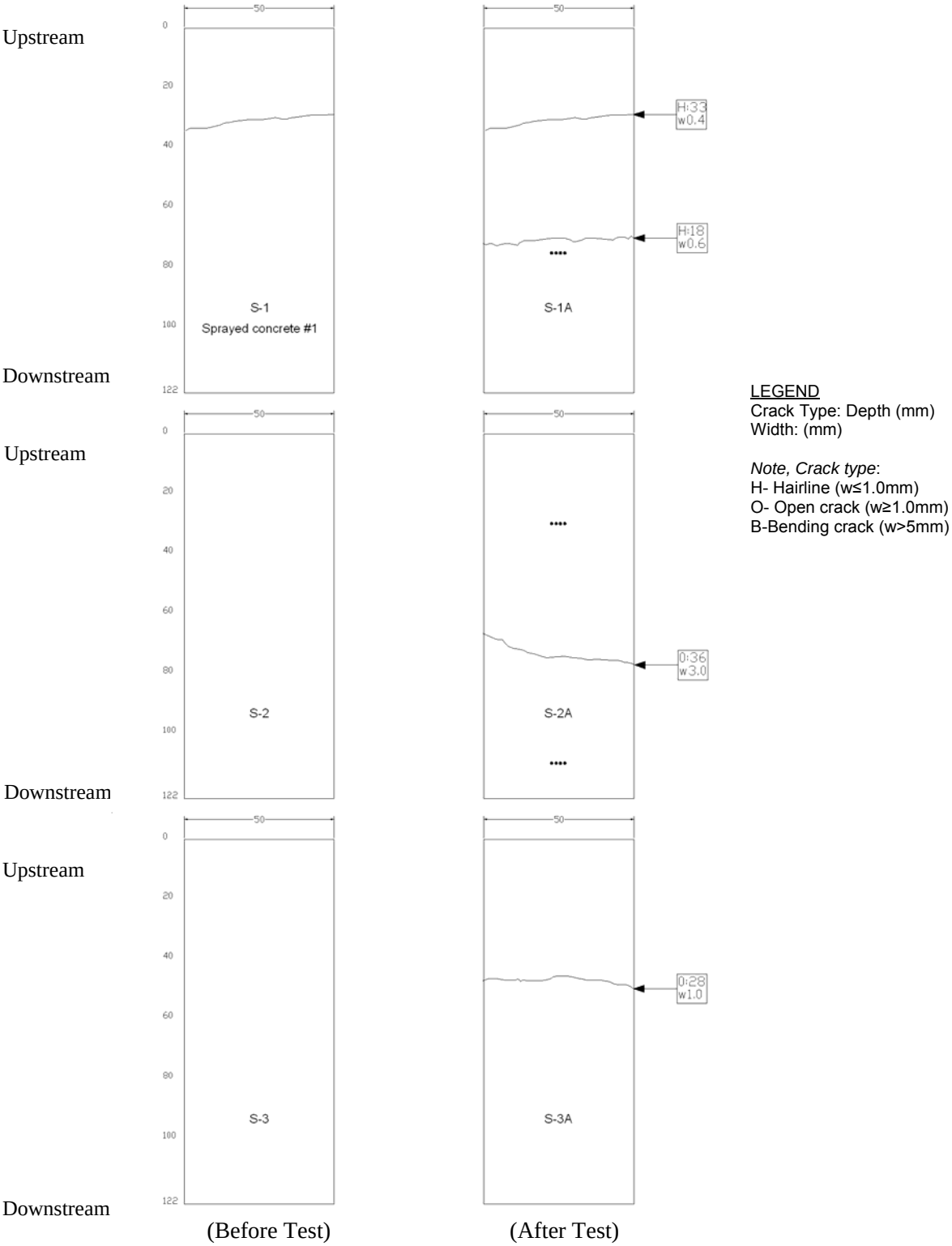

Figure A-3 Crack observations-TSL coated concrete slabs S-1, S-2, and S-3

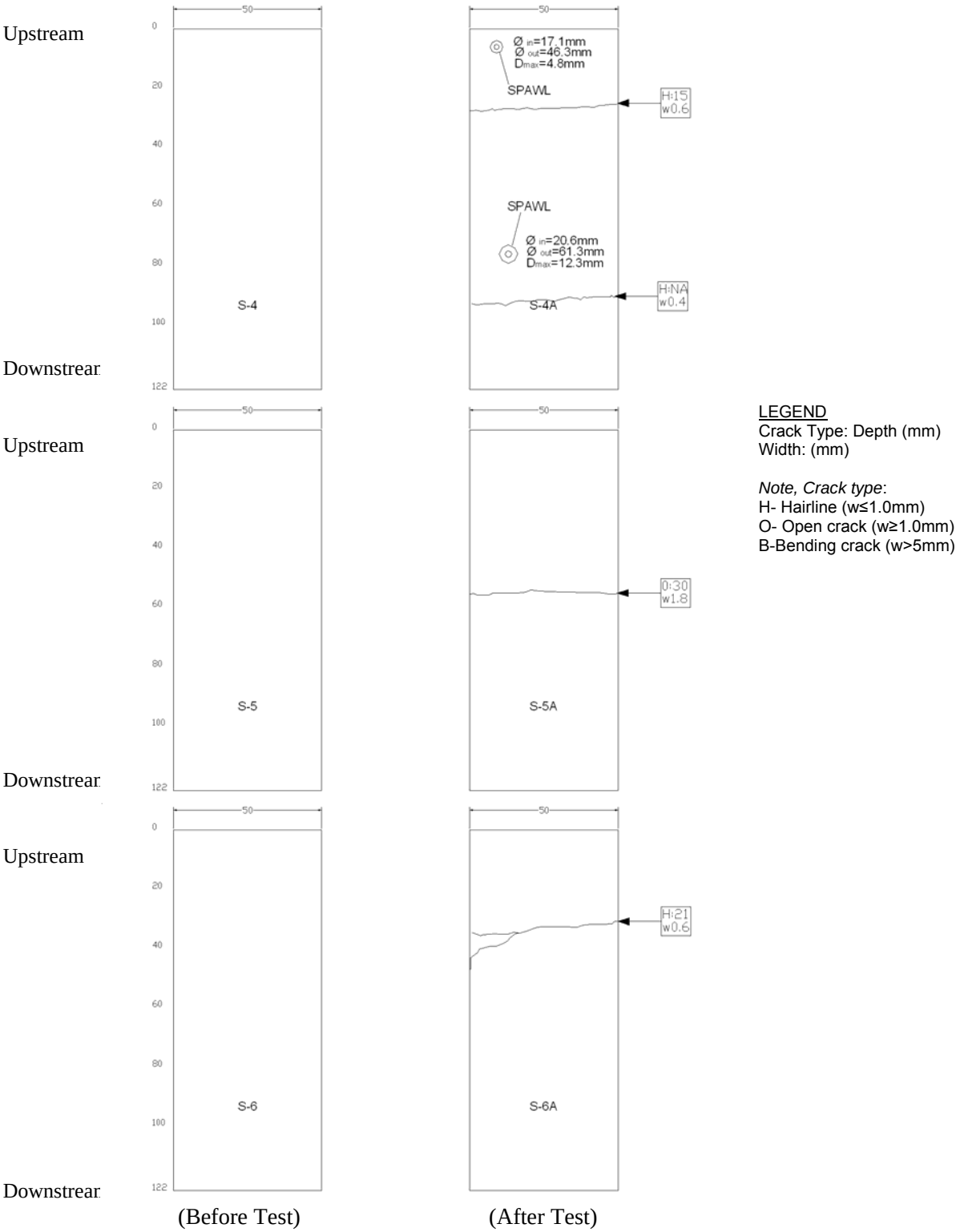

Figure A-4 Crack observations-TSL coated concrete slabs S-4, S-5, and S-6

APPENDIX – B

B.1 Crack Mapping during the Flexural Tests

Test 1: Max. Load 57 kN and Max. Displacement 19 mm

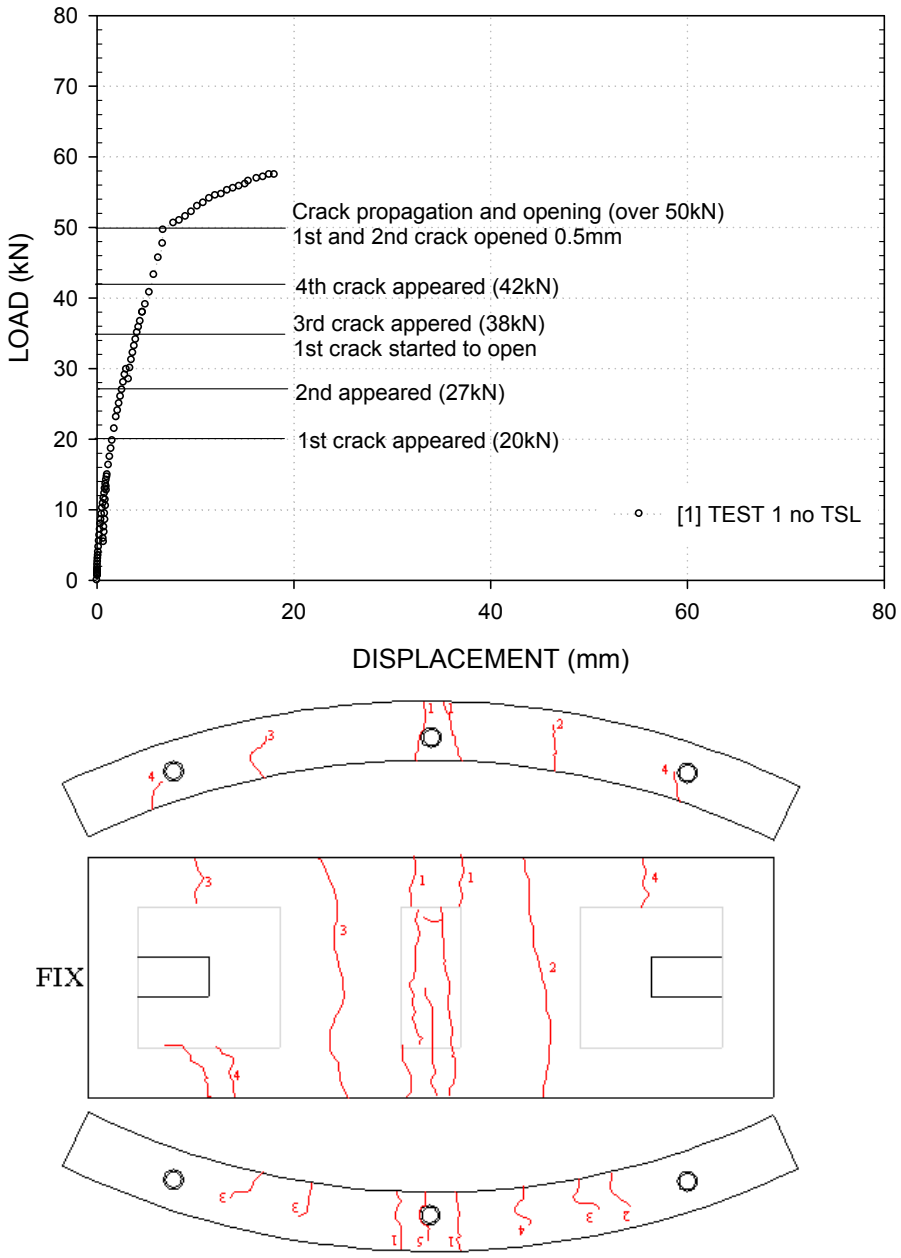

Figure B-1 Crack map and corresponding loads in Test 1

Test 2: Max. Load 63 kN and Max. Displacement 120 mm (Benchmark)

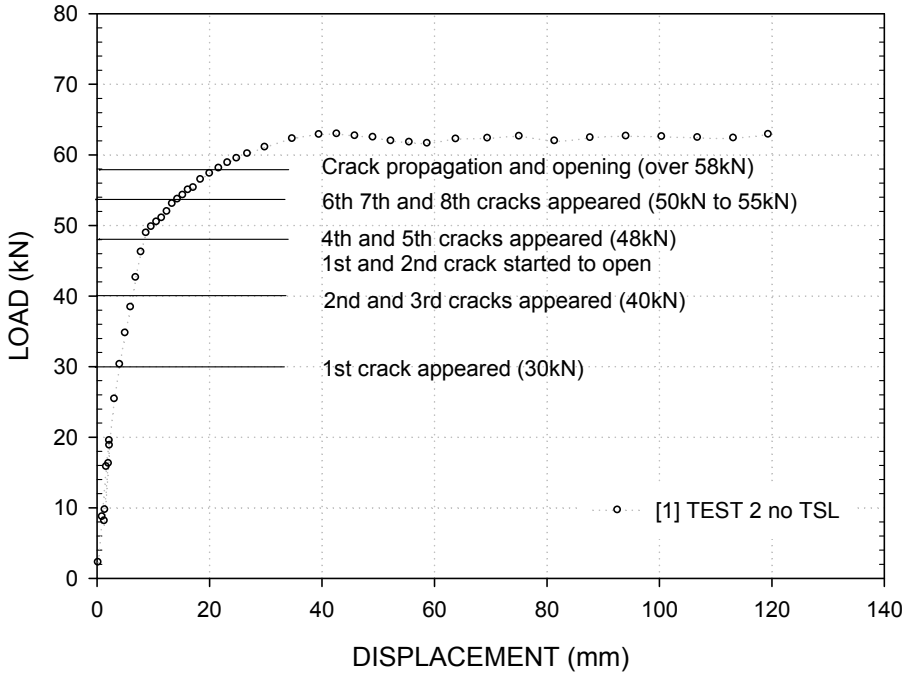

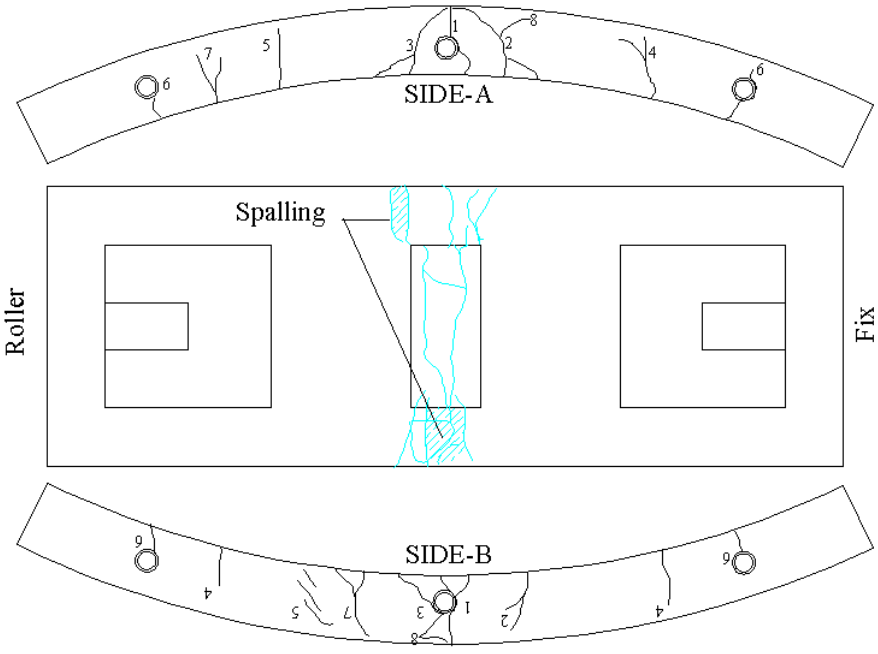

Figure B-2 Crack map and corresponding loads in Test 2

Test 3 (with TSL): Max. Load 56 kN and Max. Displacement 29 mm

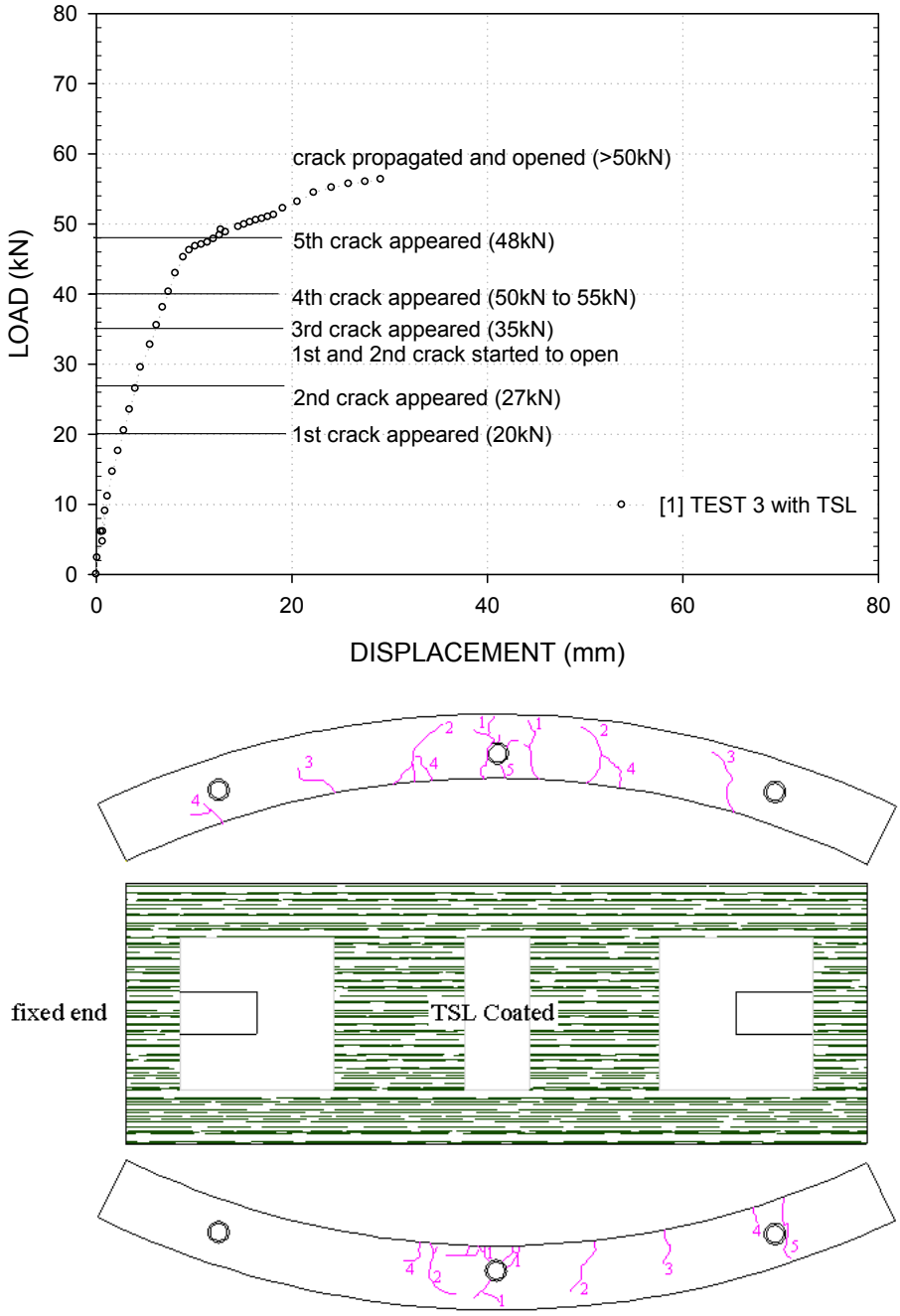

Figure B-3 Crack map and corresponding loads in Test 3

Test 4 (with TSL): Max. Load 63 kN and Max. Displacement 42 mm

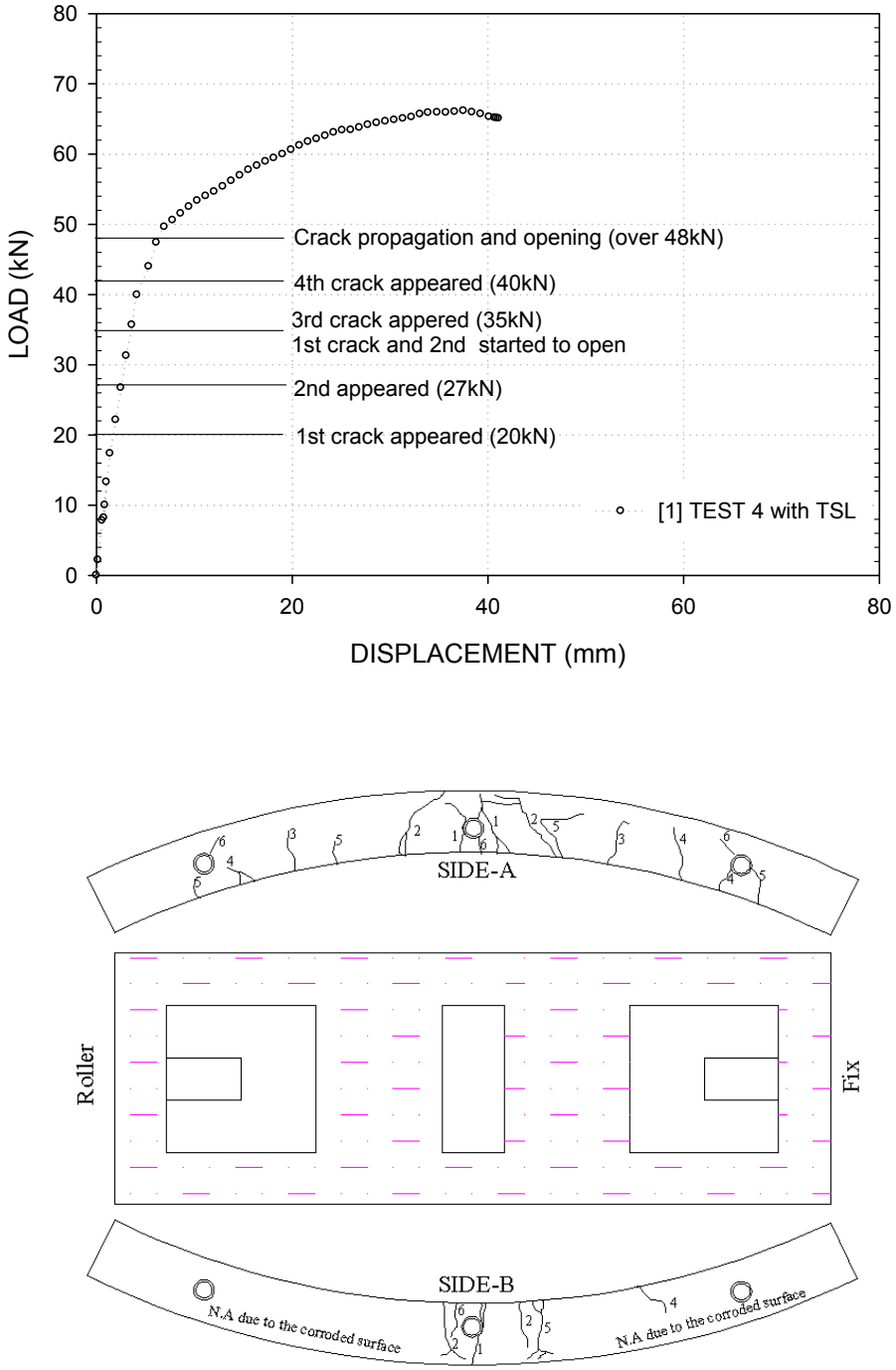

Figure B-4 Crack map and corresponding loads in Test 4

Test 5 (with TSL): Max. Load 67 kN and Max. Displacement, 138 mm

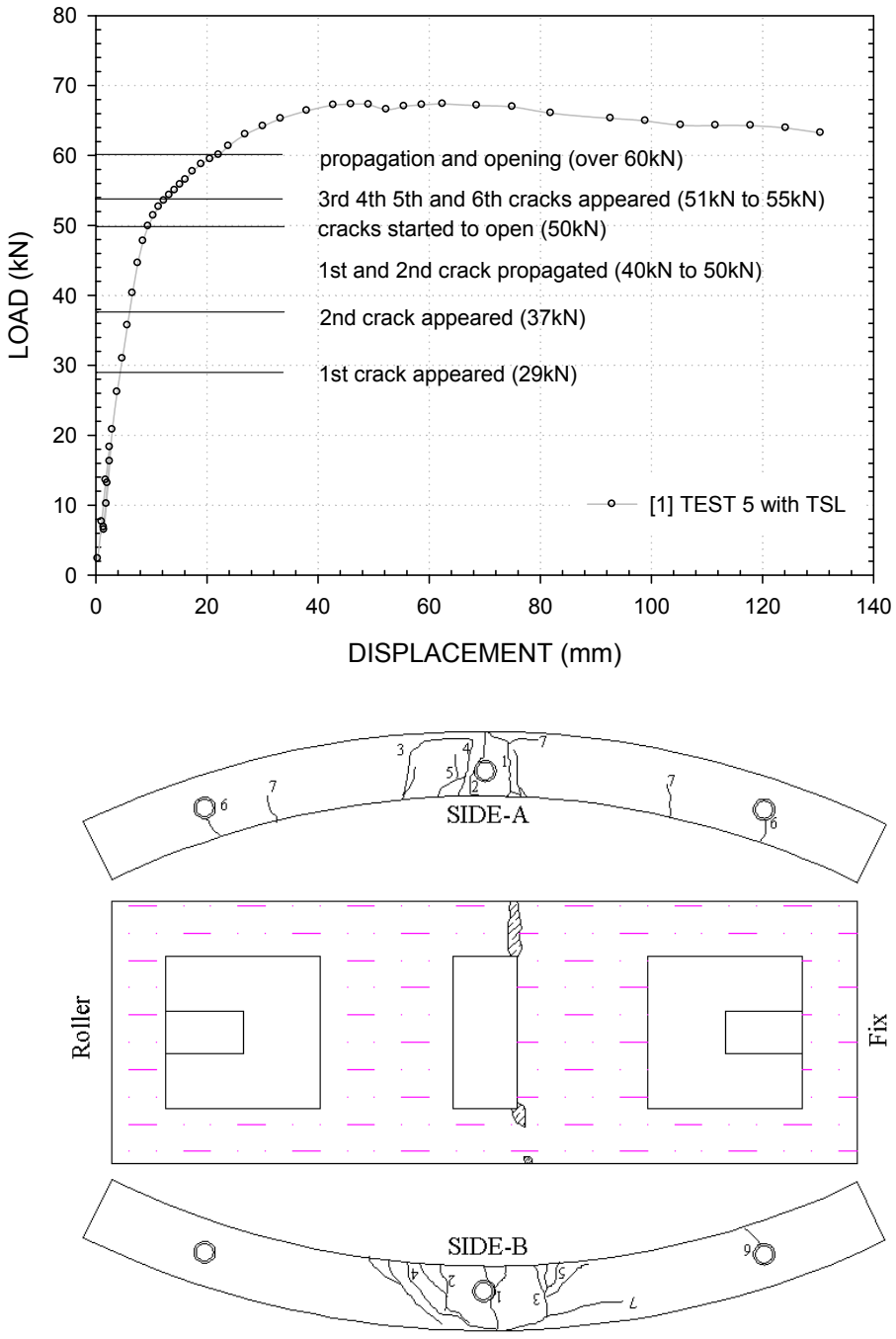

Figure B-5 Crack map and corresponding loads in Test 5

B.2 Crack Profile

Failure profiles in various loads are presented for Test 2 and Test 5. The TSL effects can be observe in the following figures. The test with an uncoated segment generated three large cracks at the middle of the segment shown in Figure B-6. On the other hand, it can be seen from Figure B-7 that many and relatively small cracks can be observed for the test with the TSL coated segment.

Figure B-6 Failure profile (the uncoated segment, Test 2)

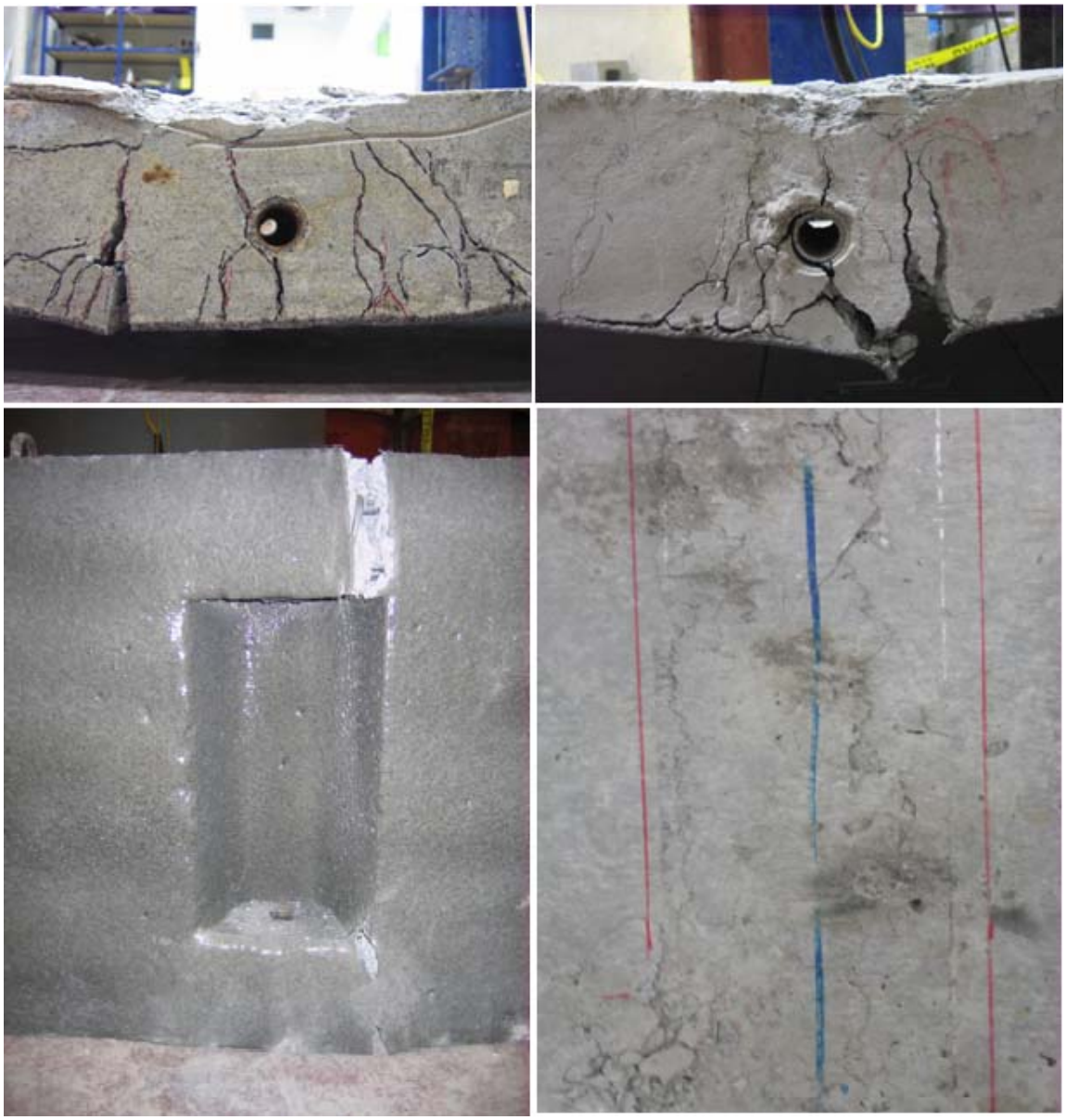

Figure B-7 Failure profile (the TSL coated segment, Test 5)

From the figures, it is revealed that resisting crack propagation by TSL caused higher tensile strains in the intrados of the segments. As a consequence, the higher compressive strain occurred in the extrados of the segments. It is agreeable with the strain distribution through the rib shown in Figure 6.25.

APPENDIX - C

C.1 The Effect of Joint Components on Stress Distribution

Figures C-1 and C-3 present S_{11}, which is the stress in the circumferential direction (hereafter named *x*-direction). The positive value indicates tension in *x*-direction. These figures depict the different mechanisms of stress distribution in terms of the different joint components considering 1) plywood-gasket contact, 2) plywood contact only, and 3) concrete contact only.

As seen in Figure C-1, the joint with plywood and gasket and the joint with only plywood have a similar stress distribution. Thus, the similar rotational stiffness between the joint with plywood and gasket contact and the joint with plywood contact can be obtained. However, the joint with the concrete-concrete contact presents a much smaller tension zone than the other two joints. Moreover, the tension in the bolt can be seen in these figures. The joint with concrete-concrete contact, therefore, shows a relatively low rotational stiffness compared with the other two joints. In the cases of initial thrust of 3 MPa and 6 MPa (see Figures C-2 and C-3), three different joint models show a similar stress distribution which results in a similar rotational stiffness.

For a low initial thrust (i.e., 0.3 MPa ; $f_{cu}/\ \sigma_o$=200), the joint geometry would be the important factors to determine the joint rotational stiffness. In contrast, the higher the initial thrust (i.e. 6 MPa; $f_{cu}/\ \sigma_o$=10), the less effect on the joint geometry (see Figure C-3) can be seen. As a consequence, the joint rotational stiffness is related to the joint geometry in a low thrust condition. It is concluded that the joint geometry is an important factor in a relatively low thrust condition.

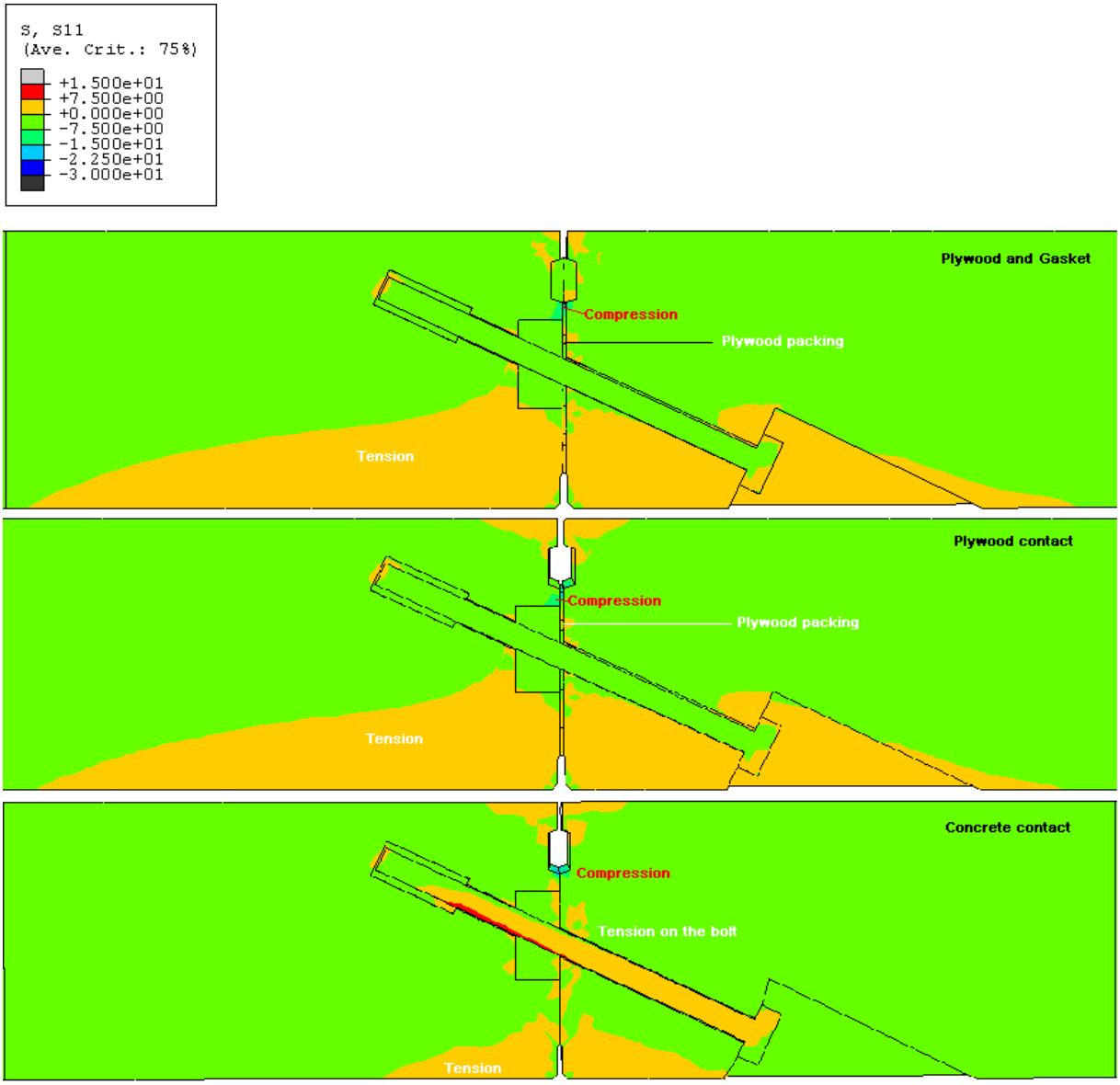

Figure C-1 Stress (S_{11}) on the modern joint: f_{cu}/σ_o=200

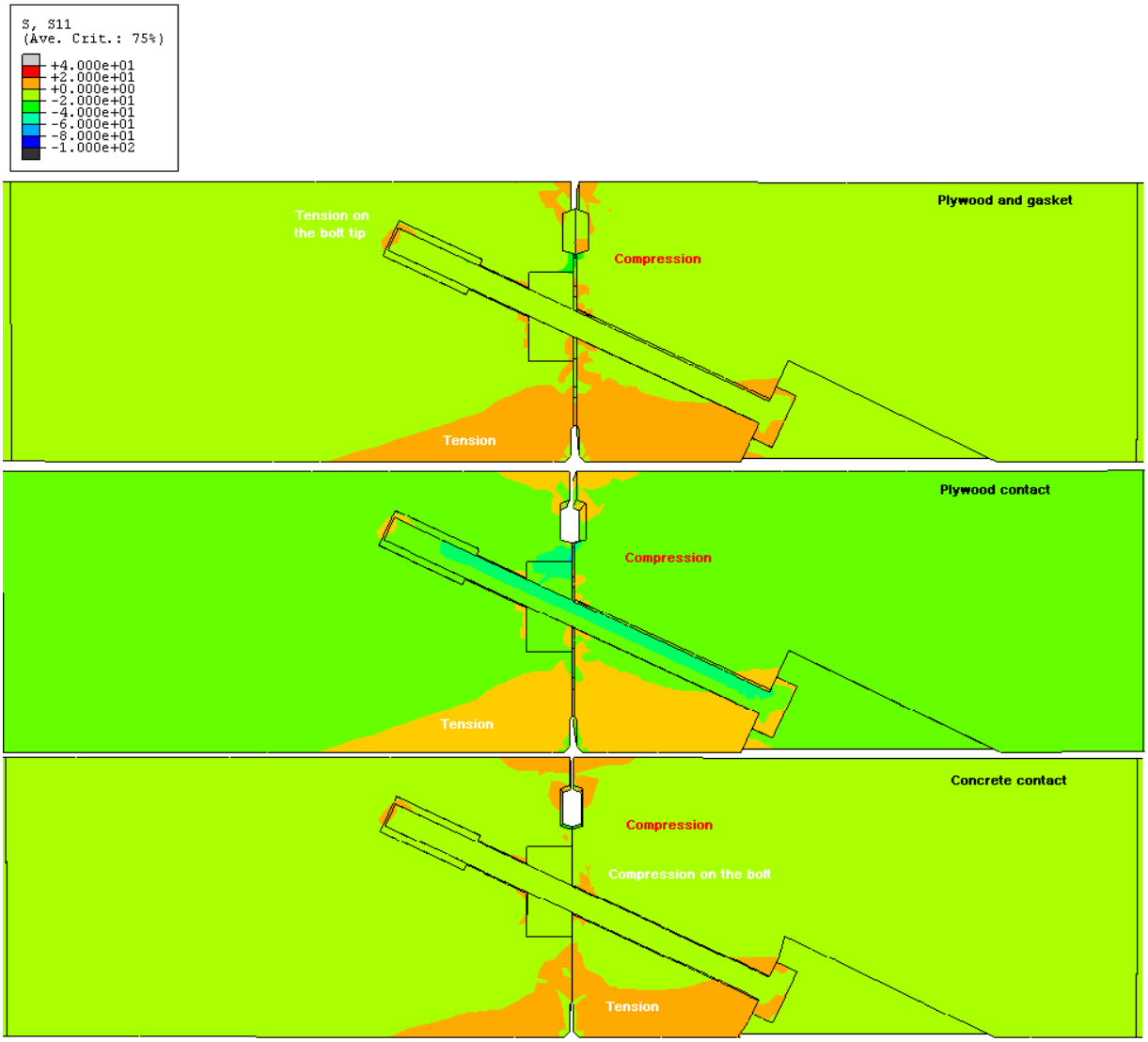

Figure C-2 Stress (S_{11}) on the modern joint: f_{cu}/σ_o=20

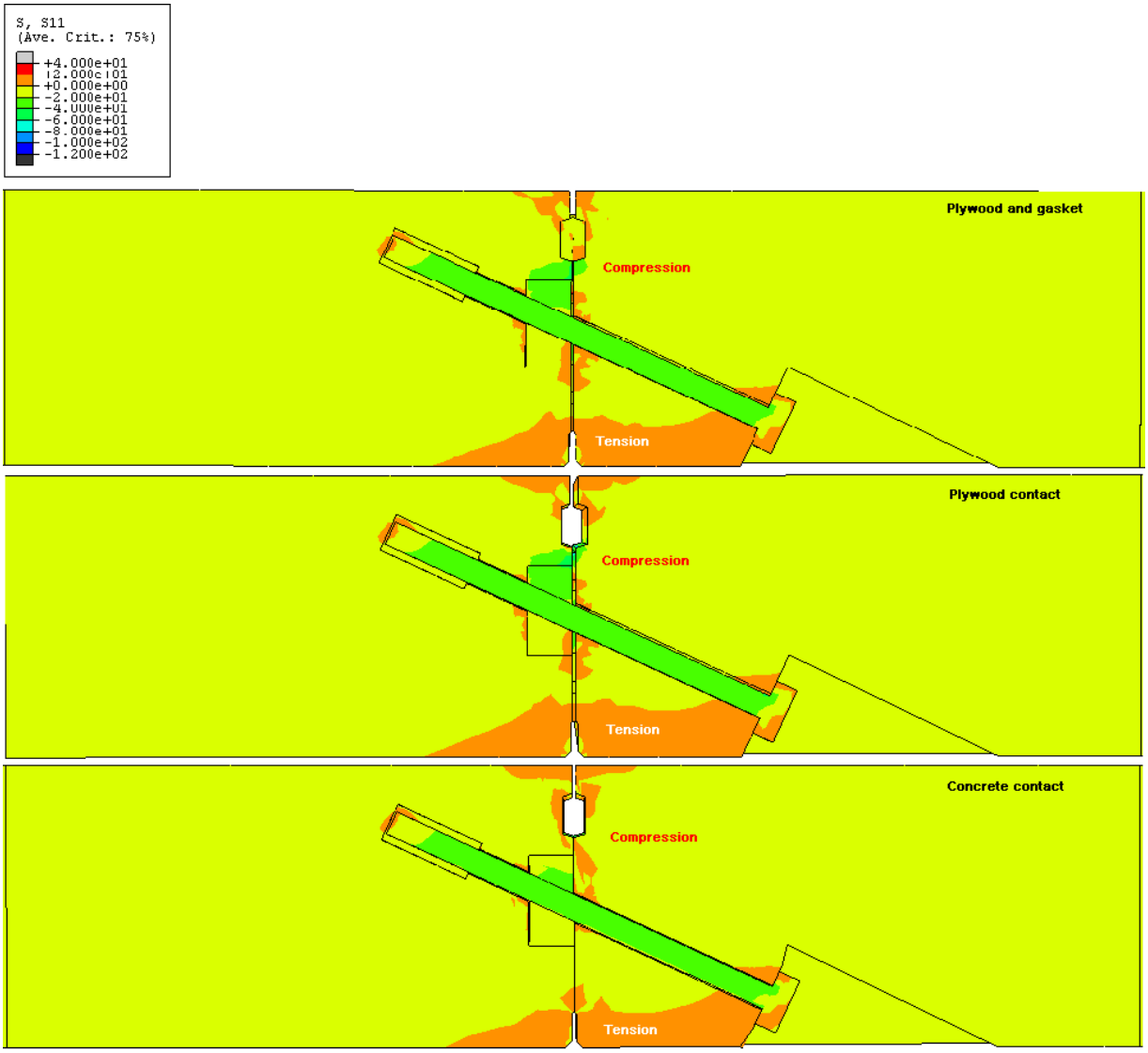

Figure C-3 Stress (S_{11}) on the modern joint: f_{cu}/σ_o=10

C.2 The Effect of Plywood Packing and Gasket on Joint Rotational Stiffness

This section describes the effects of the plywood packing and gasket on the rotational stiffness for the modern joint. It concludes that the plywood packing and the gasket increase the rotational stiffness for the modern joint. The results can be seen in Figures C-4 to C-7.

As seen in Figure C-4, the rotational stiffness increases as the plywood packing is added and so does the addition of the EPDM gasket. The rotational stiffness increase is due to the improvement in contact between concrete-plywood-concrete. The plywood packing makes good contact and it is related to the concrete yielding point. It is affirmed that the plywood packing increases the concrete non-linearity yielding. Consequently, the plywood packing increases the rotational stiffness. However, as the initial thrust increases, the plywood packing effects gradually diminish and become minimal as presented in Figure C-7.

Although the effects of the EPDM gasket are not as great as with the plywood, the rotational stiffness increases due to the installation of the gasket. A 5% increase in the rotational stiffness can be found when the f_{cu}/σ_o ratio is 200. Similar to the effects of the plywood packing, the variation in the rotational stiffness reduces as the f_{cu}/σ_o decreases.

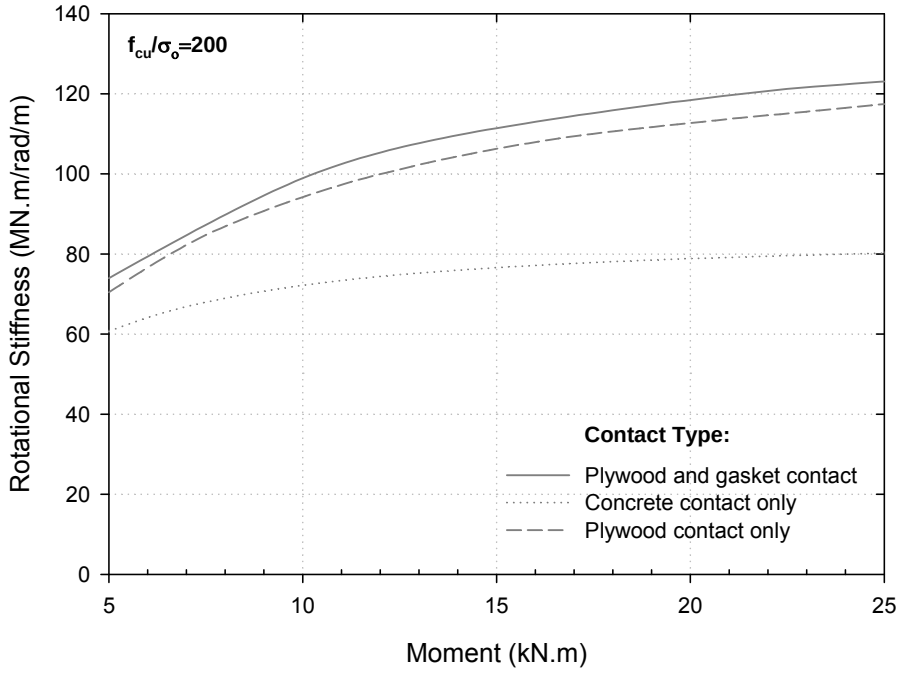

Figure C-4 The effects of the plywood packing and gasket on K_θ: f_{cu}/σ_o=200

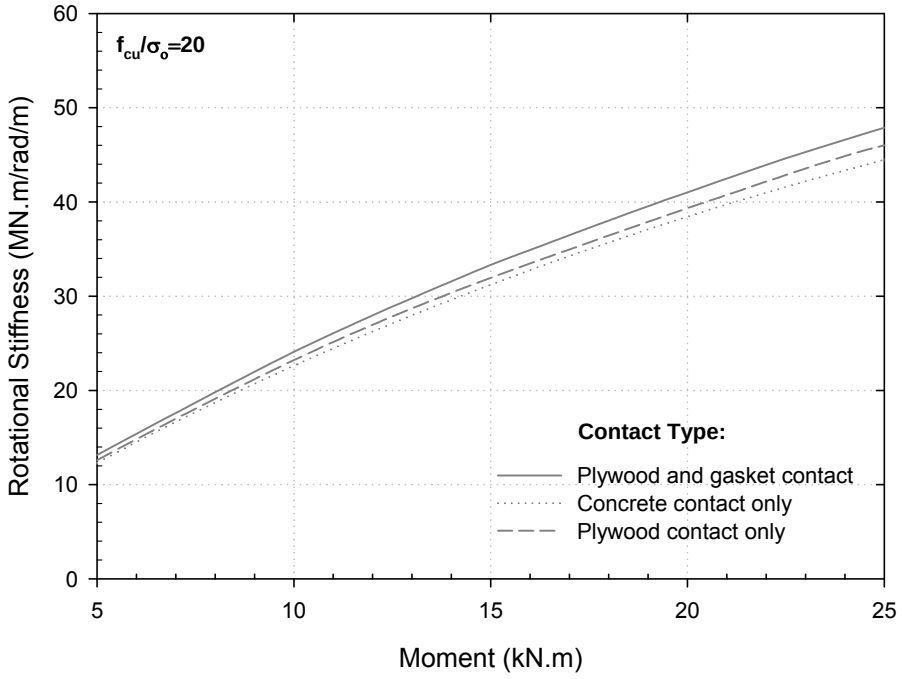

Figure C-5 The effects of the plywood packing and gasket on K_θ: f_{cu}/σ_o=20

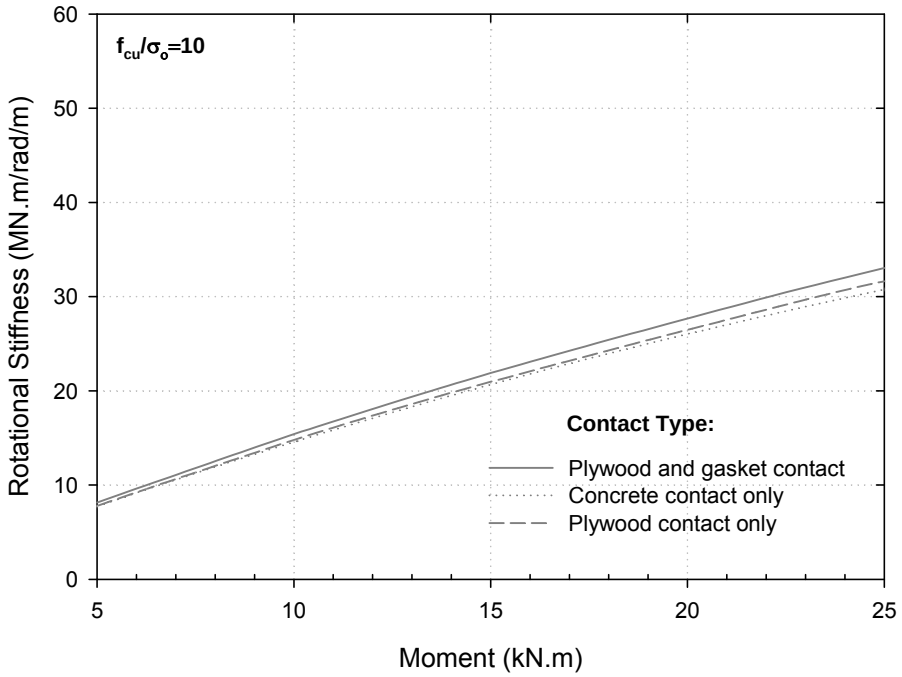

Figure C-6 The effects of the plywood packing and gasket on K_θ: f_{cu}/σ_o=10

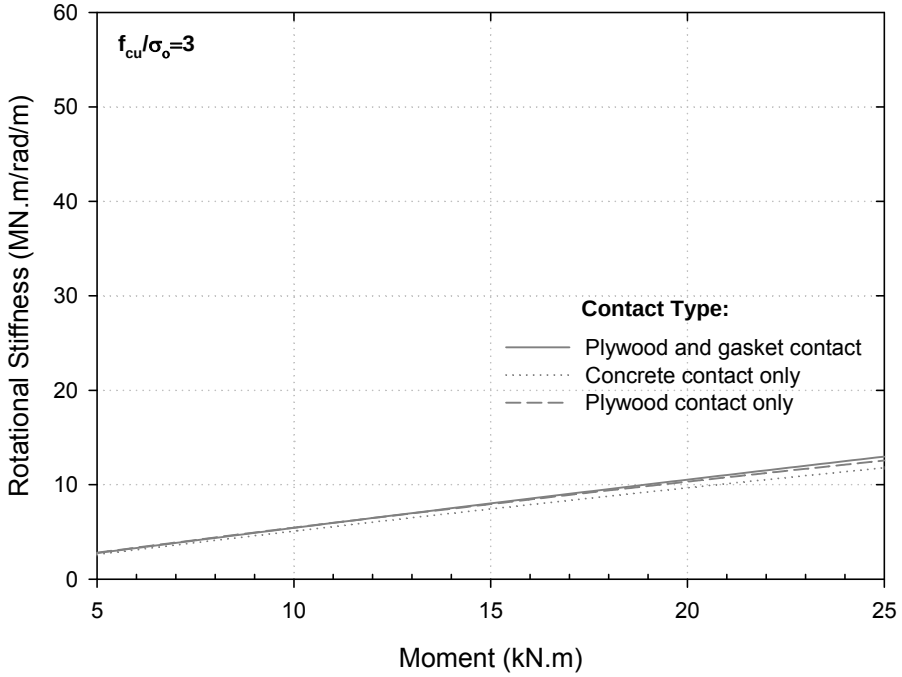

Figure C-7 The effects of the plywood packing and gasket on K_θ: f_{cu}/σ_o=3

APPENDIX –D

D.1 Moment and Thrust on the Tunnel Lining (closed form solution)

The lining structures of tunnels are solely affected by earth and water pressure so that it is the total stress matter. In this study, an analytical solution for an inner-jointed thin wall shell and an outer thick wall cylinder embedded in homogenous soil was used. According to El Nagger and Hinchberger (2008), earth and water pressure distribution on the lining can be divided into two parts namely, moment (***M***) and thrust (***T***). Assuming that a segmental tunnel lining is a continuum, a circular ring, moment and thrust can be calculated at any angle. These equations are given by:

$$\boldsymbol{M}^{\boldsymbol{H}} = -\frac{\boldsymbol{D}_{f1}\boldsymbol{R}_{c1}^{2}}{\boldsymbol{D}_{c1}\boldsymbol{R}_{c1}^{2} + \boldsymbol{D}_{f1}}\boldsymbol{\sigma}_{N1}^{\boldsymbol{H}} \qquad \text{[Eq.C-1]}$$

$$\boldsymbol{M}^{\boldsymbol{D}} = -\frac{\boldsymbol{R}_{c1}^{2}}{3}\left(\boldsymbol{\sigma}_{N1}^{\boldsymbol{D}} + \frac{\boldsymbol{\tau}_{T1}}{2}\right)\cos 2\boldsymbol{\theta} \qquad \text{[Eq.C-2]}$$

where, $\boldsymbol{D}_{c1} = \boldsymbol{E}_1\boldsymbol{A}_1/(1-\boldsymbol{\nu}_1^2)$, $\boldsymbol{D}_{f1} = \boldsymbol{E}_1\boldsymbol{I}_1/(1-\boldsymbol{\nu}_1^2)$ and E_1, A_1, I_1, and v_1 are the elastic modulus of concrete, cross-sectional area, moment of inertia and Poisson's ratio, respectively. Meanwhile, hydrostatic and deviatoric thrusts on the liner can be expressed by:

$$T^{H} = \frac{D_{c1}R_{cl}^{\ 3}}{D_{cl}R_{cl}^{\ 2} + D_f}\sigma_{N1}^{H} + \frac{M^{H}}{R_{cl}} \qquad \text{[Eq.C-3]}$$

$$T^{D} = -\frac{R_{cl}}{3}(\sigma_{N1}^{D} - 2\tau_{T1})\cos 2\theta \qquad \text{[Eq.C-4]}$$

From Eqs. B-1 to Eq. B-4, subscriptions, *cl*, *N1*, and *T1*, mean centre line, the radial reaction and the tangential reaction between the inner and outer liners, respectively. Superscriptions, *D* and *H* mean deviatoric and hydrostatic component.

Combined with the Equations B-1 and B-4, moment and thrust can be calculated for the linings. Details for deriving the equations can be found in El Naggar and Hinchberger (2008).

CURRICULUM VITA

NAME:	Taesang Ahn
POST-SECONDARY EDUCATION:	Hanyang University Seoul, Korea 1999 B.Sc. (Eng.) The University of Western Ontario London, Canada 2003 M.E.Sc. The University of Western Ontario London, Canada 2011 Ph.D.
RELATED WORK EXPERIENCE:	Teaching and Research Assistant The University of Western Ontario London, Canada 2005-2010 Geotechnical Specialist exp Services Inc. Brampton, Canada 2011-Present Civil Engineer Chun-Il Engineering Inc. Seoul, Korea 1999-2000

PUBLICATIONS:

- Hinchberger, S.D., **Ahn, T** and Lo, K.Y. (2010). "Numerical evaluation of segmental tunnel liner joint stiffness" Proceedings, 36th General Assembly, ITA. AITES and World Tunnel Congress 2010, Vancouver, Canada

- **Ahn, T**., Allouche, E.N. and Yanful, E.K. (2007). "Detection of heavy metal and hydrocarbon contamination using a miniature resistivity probe." Environmental Technology. Vol. 28, pp. 701-711.

- **Ahn, T**., Allouche E.N. and Yanful E. K. (2006). “A multipurpose platform for horizontal investigation.” Geotechnical Testing Journal ASTM. Vol. 29, No. 3. pp. 181-192.

- Allouche, E.N. and **Ahn, T**. (2003). “Horizontal subsurface investigation using a smart innovative geoprobe.” Proceedings, International No-dig Conference 2003, Las-Vegas, Nevada, U.S.A

- **Ahn, T**., Allouche, E.N. and Yanful, E.K. (2002). “Miniature resistivity probe deployed from the Smart Subsurface Horizontal Investigation Probe (SSHIP).” Proceedings 55th Canadian Geotechnical Society Conference, Niagara Falls, Ontario, Canada.

- Allouche, E.N., El Naggar, M. H., Yanful, E. K., **Ahn, T**. and Devaux M. G (2002). “An Innovative device for sampling and logging directionally drilled horizontal bores” Geotechnical Research Centre Report GEOT-04-02, ISSN 0847-0626, January, 47p.